Organizational Results Research Report

May 2006
OR06.014

Steel Free Hybrid Reinforcement System for Concrete Bridge Decks – Phase 1

Prepared by Missouri Transportation Institute and Missouri Department of Transportation

TECHNICAL REPORT DOCUMENTATION PAGE

1. Report No. OR06-014	2. Government Accession No.	3. Recipient's Catalog No.
4. Title and Subtitle Steel-Free Hybrid Reinforcement System for Concrete Bridge Deck		5. Report Date May 2006 6. Performing Organization Code University of Missouri-Columbia (UMC) and University of Missouri-Rolla (UMR)
7. Author(s) Vellore S. Gopalaratnam, John Meyer and Kenny De Young – UMC Abdeldjelil Belarbi and Huanzi Wang - UMR		8. Performing Organization Report No.
9. Performing Organization Name and Address University of Missouri-Columbia Dept. of Civil and Environmental Engineering E2509 Engineering Building East Columbia, Missouri 65211-2200 University of Missouri-Rolla Dept. of Civil, Architectural and Environmental Engineering 1870 Miner Circle Rolla, Missouri 65409		10. Work Unit No. 11. Contract or Grant No.
12. Sponsoring Agency Name and Address Missouri Department of Transportation Organizational Results P. O. Box 270-Jefferson City, MO 65102		13. Type of Report and Period Covered Final Report, June. 2002 – Dec. 2005 14. Sponsoring Agency Code MoDOT

15. Supplementary Notes
The investigation was conducted in cooperation with the U. S. Department of Transportation, Federal Highway Administration.

16. Abstract
Use of nonferrous fiber-reinforced polymer (FRP) reinforcement bars (rebars) offers one promising alternative to mitigating the corrosion problem in steel reinforced concrete bridge decks. Resistance to chloride-ion driven corrosion, high tensile strength, nonconductive property and lightweight characteristics make FRP rebars attractive. However, there are design challenges in the use of FRP reinforcement for concrete including concerns about structural ductility, low stiffness, and questions about their fatigue response and long-term durability. The report presents results from a three-year collaborative investigation conducted by the University of Missouri-Columbia (UMC) and the University of Missouri-Rolla (UMR). Details of the investigation, results and discussions from static and fatigue studies are presented including experimental programs on bond, flexural ductility, accelerated durability, and full-scale slab tests. Based on the results from this investigation, the use of a hybrid reinforced concrete deck slab is recommended for field implementation. The hybrid reinforcement comprises a combination of GFRP and CFRP continuous reinforcing bars with the concrete matrix also reinforced with 0.5% volume fraction of 2-in. long fibrillated polypropylene fibers. A working stress based flexural design procedure with mandatory check for ultimate capacity and failure mode is recommended.

17. Key Words Bridges Fatigue Behavior Fiber Reinforced Concrete Fiber Reinforced Polymer Testing Steel-Free Bridge Deck	18. Distribution Statement No restrictions. This document is available to the public through National Technical Information Center, Springfield, Virginia 22161		
19. Security Classification (of this report) Unclassified	20. Security Classification (of this page) Unclassified	21. No. of Pages 274	22. Price

Form DOT F 1700.7 (06/98)

FINAL REPORT

RI02-002

Steel-Free Hybrid Reinforcement System for Concrete Bridge Decks

Prepared for the
Missouri Department of Transportation

Written by

Vellore S. Gopalaratnam (PI)
Professor of Civil Engineering
John Meyer and Kenny De Young
Graduate Research Assistants
University of Missouri-Columbia

and

Abdeldjelil Belarbi (PI)
Distinguished Professor of Civil Engineering
Huanzi Wang
Graduate Research Assistant
University of Missouri-Rolla

May 2006

ACKNOWLEDGEMENTS

The authors from both the University of Missouri-Columbia (UMC) and the University of Missouri-Rolla (UMR) would like to gratefully acknowledge financial support from the Missouri Department of Transportation (MoDOT) for the research project. UMR researchers would like to additionally acknowledge support from the UMR University Transportation Center.

The Principal Investigators on both campuses are also thankful to Doug Gremmel of Hughes Brothers and Richard Smith, SI Concrete Systems for their participation as well as the generous in-kind material donation to this project. Support for the full-scale slab tests from UMC undergraduate honors students Kendall Tomes and Sarah Craig are also acknowledged. The authors would also like to thank the following individuals for numerous discussions during quarterly meetings for the project : Michele Atkinson, Tim Chojnacki Bryan Hartnagel, Paul Porter, and Shyam Gupta (all of MoDOT) and Peter Clogson (FHWA).

Early discussions with Prof. Aftab Mufti of ISIS, Canada also helped develop ideas for the project described in this report. These contributions from Prof. Mufti are gratefully acknowledged.

EXECUTIVE SUMMARY

New materials and design methods are being investigated for the design of bridge components to alleviate the current devastating corrosion problems. A research project was initiated at the University of Missouri (UM) and the Missouri Department of Transportation (MoDOT) to develop a nonferrous hybrid reinforcement system for concrete bridge decks by using continuous fiber-reinforced-polymer (FRP) rebars and discrete randomly distributed polypropylene fibers. This hybrid system may eliminate problems related to corrosion of steel reinforcement while providing requisite strength, stiffness, and desired ductility, which are shortcomings of FRP reinforcement system in reinforced concrete.

The overall study plan includes: (1) development of design procedures for an FRP/FRC hybrid reinforced bridge deck, (2) laboratory studies of static and fatigue bond performances and ductility characteristics of the system, (3) accelerated durability tests of the system, and (4) static and fatigue tests on full-scale hybrid reinforced composite bridge decks.

The test results showed that with the addition of fibers, structural performances of the system are improved. Although polypropylene fibers do not increase the ultimate bond strength, they provide enhanced ductile bond behavior. Also, with the addition of fibers, the flexural behaviors are improved with the increase of the ductility index μ by approximately 40%, as compared to the plain concrete beams. In addition, with the addition of polypropylene fibers, the durability of the system was improved.

The large-scale slab tests revealed that crack widths were smaller for hybrid slab than for GFRP slab and were more readily comparable to that for steel reinforced slab, even while the global stiffness of the hybrid slab was more comparable to the GRFP slab. Design guidelines for steel-free bridge deck are proposed based on a similar design equations provided by ACI440. These equations were calibrated using the results of the above test program. Contrary to the current design methods, it is recommended that flexural design of deck slabs be carried out using working stress approach with mandatory checks on ultimate capacity and mode of failure. This approach is more practically relevant for hybrid reinforced FRP slabs. The large-scale tests proved that the proposed design guidelines for such hybrid system are adequate and are ready for implementation in the design a hybrid steel-free bridge deck.

TABLE OF CONTENTS

LIST OF FIGURES

LIST OF TABLES

LIST OF NOTATIONS

a	distance from the support to the point load applied, in.
A	effective tension area per bar, in.^{2}
A_{CFRP}	area of CFRP reinforcement
A_{GFRP}	area of GFRP reinforcement
A_f	area of rebars, in.^{2}
A_{split}	concrete splitting area, in.^{2}
b_e	effective beam width, in.
C	cover depth, in.
C_E	environmental reduction factor
d	distance from the extreme compression fiber to centroid of the tension reinforcement
d_b	diameter of rebar, in.
d_c	thickness of concrete cover measured from extreme tension fiber to the center of the closest layer of longitudinal bars
d_{CFRP}	effective depth of CFRP reinforcement
d_{GFRP}	effective depth of GFRP reinforcement
E_c	modulus of elasticity of concrete, psi
E_{CFRP}	elastic modulus of CFRP reinforcement
E_{GFRP}	elastic modulus of GFRP reinforcement
E_f	modulus of elasticity of FRP rebar, psi
E_t	total energy of the system, kips-in.
E_e	elastic energy, kips-in.
$E_{0.75Pu}$	energy corresponding at 75% of the ultimate load, kips-in.
F	friction force on deformation with unit area, psi
f_c'	concrete compressive strength, psi
f_{ct}	concrete splitting tensile strength, ksi
f_{CFRP}	elastic stress in the CFRP reinforcement
f_{GFRP}	elastic stress in the GFRP reinforcement
$\overline{f}_{CFRP}$	allowable stress in the CFRP reinforcement for working stress design

$\overline{f}_{GFRP}$	allowable stress in the GFRP reinforcement for working stress design
f_f	stress in the FRP reinforcement, ksi
f_{fu}	tensile strength of FRP bars, ksi
$f_{fu(CFRP)}$	design tensile strength of CFRP with environmental reduction applied
$f_{fu(GFRP)}$	design tensile strength of GFRP with environmental reduction applied
h_r	height of deformation, in.
I_e	effective moment of inertia of the section, in.^{4}
I_g	gross moment of inertia of the section, in.^{4}
k_b	coefficient that accounts for the degree of bond between the FRP bar and the surrounding concrete
L	span length, in.
l_d	embedment length, in.
l_{db}	basic development length, in.
l_e	effective splitting length, in.
M_a	moment applied to the section, kips-in.
M_{cr}	cracking moment including rebars' contribution, kips-in.
$M_{cr\text{-}exp}$	cracking moment measured from experiments, kips-in.
M_{DL}	moment induced by deal loads, kips-in.
M_{LL+I}	moment induced by live load and impact, kips-in.
M_u	ultimate flexural strength, kips-in.
$M_{\varepsilon=0.001}$	flexural strength at concrete strain of 0.001, kips-in.
n_i	number of cycles applied at a particular stress level
$N_{max,i}$	number of cycles which cause fatigue failure at a certain stress level
P	normal stress on deformation, psi
R	resultant stress of P and F, psi
R_r	radial component of R, psi
S	crack spacing
S_m	slip at peak bond strength, in.
S'_m	slip at second peak bond strength, in.
S_r	residual slip after fatigue loading, in.
T	pullout force, kips

T_{CFRP}	tensile force in the CFRP reinforcement
T_{GFRP}	tensile force in the GFRP reinforcement
u	bond strength (longitudinal component of R), psi
$u^{'}$	bond strength at second peak, psi
$u_{0.002}$	bond strength at the slip of 0.002 in. at the free end, psi
$u_{0.01}$	bond strength at the slip of 0.01 in. at the loaded end, psi
u_{design}	design bond strength , psi
$u_{b,f}$	bond strength of FRP rebar to concrete, psi
$u_{b,s}$	bond strength of steel rebar to concrete, psi
u_{test}	bond strength based on test results, psi
$u_{theo.}$	theoretical bond strength, psi
w	crack width at tensile face of the beam, in.
V_f	volume fraction of fibers
α	rib angle
β	coefficient to converse crack width corresponding to the level of reinforcement to the tensile face of beam
β_d	modification factor for FRP reinforced beam
Δ_{mid}	mid-span deflection, in.
ε_{CFRP}	elastic stress in the CFRP reinforcement
ε_{cu}	ultimate concrete strain
ε_{GFRP}	elastic stress in the GFRP reinforcement
$\psi_{\varepsilon=0.001}$	curvature at concrete strain of 0.001
ψ_u	curvature at ultimate
γ	adjustment factor for different embedment length
μ	friction coefficient
μ_E	ductility index
ρ_f	reinforcing ratio of FRP reinforced concrete
ρ_{fb}	balanced reinforcing ratio of FRP reinforced concrete

1. INTRODUCTION

1.1. BACKGROUND AND PROJECT OVERVIEW

There are approximately 592,000 bridges in the United States. Of this total, approximately 78,000 bridges are classified as structural deficient, 80,000 bridges are functionally obsolete (FHWA 2003). These numbers indicate that in excess of 25 percent of the bridges listed in the National Bridge Inventory Databases are in need of repair or replacement. Steel reinforcement corrosion is the primary reason for the structural deficiency of reinforced concrete (RC) bridges. The annual direct cost of corrosion for highway bridges is estimated to be \$8.3 billion, consisting of \$3.8 billion to replace structurally deficient bridges over the next ten years, \$2.0 billion for maintenance and cost of capital for concrete bridge decks, \$2.0 billion for maintenance and cost of capital for concrete substructures (minus decks), and \$0.5 billion for maintenance painting of steel bridges. Life-cycle analysis estimates indirect costs to the user due to traffic delays and lost productivity at more than ten times the direct cost of corrosion maintenance, repair, and rehabilitation. (CorrosionCost.com 2004).

Limited service life and high maintenance costs are associated with corrosion, fatigue and other degradation of highway bridges and RC structures. Corrosion problems began to appear in steel reinforced concrete in the 1960s. De-icing salt used in colder climates, and associated chloride penetration is a major cause of this corrosion in highway structures. Expansion, cracking, and eventual spalling of the concrete cover are the results of salt-related damage. Additionally, loss of bond between steel and concrete also occurs, resulting in structural damage to RC members.

The long-term integrity of RC structures is of major concern. Repair and/or replacement of deteriorating structures constitute an enormous task that involves prohibitively high cost. For example, in the state of Missouri 10,533 bridges are classified as deficient (corrosion.com 2004), which amounts to 46% of its total number of bridges. In the late 1970s, the Federal Highway Administration (FHWA) funded extensive research to probe into various ways of overcoming this problem.

Bridge decks reinforced with conventional steel reinforcing bars generally perform well when sound concrete practices are used. These include use of quality constituent materials, good construction and curing procedures, and a design procedure that minimizes the potential for cracks due to mechanical and thermal loads and from time-dependent influences such as restrained shrinkage and creep. In such cases, the passive layer of protection provided to the steel reinforcing bars in the concrete matrix is adequate, and the risk of corrosion due to ingress of chloride ions either from the atmosphere or from the deicing salts is minimal. However, if concrete cracks or there is a breakdown in the passive layer of protection, corrosion of steel can lead to a rapid deterioration of the reinforced concrete deck. There has been limited success with the use of epoxy coated steel reinforcing bars, stainless steel reinforcing bars, penetrating sealers, and corrosion inhibiting admixtures. However, the long-term field performance data is yet to conclusively establish any one of these materials as the solution to the corrosion problem.

Use of Fiber Reinforced Polymer (FRP) reinforcing bars to reinforce concrete bridge decks offers another promising alternative. Presently available FRP reinforcing bars are made using glass fibers (GFRP), carbon fibers (CFRP), or aramid fibers (AFRP) bound together in a polymer matrix. CFRP and AFRP reinforcing bars offer the advantage of higher stiffness, better fatigue performance, and better durability compared to GFRP, which is the most popular among the three types of FRP reinforcement in large measure due to its cost-effectiveness. Among the advantages of using GFRP reinforcing bars are its resistance to chloride corrosion, high strength-to weight ratio, transparency to magnetic and radio frequencies, and electrical/thermal nonconductance. Design challenges while using GFRP, resulting from its low strain capacity, elastic-brittle response, low stiffness, low shear strength, higher initial cost, and reduction of strength and stiffness at moderately elevated temperatures, need to be understood and satisfactorily addressed before these materials can routinely be used in bridge decks. Other concerns include long-term durability in an alkaline environment (particularly if there is a breakdown in the polymer matrix protecting the glass fibers) and fatigue performance of GFRP. CFRP and AFRP reinforcing bars also share somewhat similar if not identical merits and concerns. It is very likely that the synergistic effects of including hybrid nonferrous reinforcement (combinations of different types of continuous reinforcing bars, or combinations of continuous reinforcing bars with short discrete fibers) may provide cost-effective and technically viable solutions to some of the design challenges.

It is proposed here that a hybrid steel-free reinforcing system that utilizes continuous fiber reinforced polymer (FRP) bars in conjunction with randomly oriented fibrillated polypropylene fibers be used for the bridge deck slab. Short, polypropylene fibers provide resistance to plastic and drying shrinkage, and improve resistance to crack growth, impact loading, fatigue loading and freeze-thaw durability. The fibers also improve the static and fatigue bond characteristics of continuous reinforcement in a concrete matrix by mitigating secondary cracking and reinforcing the weak interface zone. The combination of FRP reinforcement with use of polypropylene fibers offers an innovative hybrid bridge deck system that can eliminate problems related to corrosion of steel reinforcement while providing requisite strength, stiffness and desired ductility.

1.2. OBJECTIVES AND SCOPE

The main objective of this collaborative research project involving the University of Missouri-Columbia (UMC), University of Missouri-Rolla (UMR) and the Missouri Department of Transportation (MoDOT) is to develop nonferrous hybrid reinforcement system for concrete bridge decks using continuous FRP bars and discrete randomly distributed polypropylene fibers with a view to eliminate corrosion in bridge decks. A typical steel girder bridge is used to study implementation of this innovative bridge-deck system, although it is anticipated that similar innovation can also be implemented for other bridge types (like prestressed concrete I-girder bridges and concrete slab bridges). Enormous savings in maintenance effort and costs can accrue from this hybrid composite bridge deck application.

The specific research objectives include: (1) development of procedures for the design of a deck slab system using a combination of FRP bars and polypropylene fibers, (2) fundamental laboratory study to evaluate the bond, ductility and fatigue performance of small specimens made of such materials, and (3) static and fatigue tests on full-scale hybrid reinforced composite slab systems to evaluate mechanical performance of the slab system and compare it to the performance of a conventional slab design.

Following successful completion of Phase I of this project comprising the above three objectives, Phase II of the project will be undertaken. Field implementation and performance monitoring of the steel-free bridge deck system on one typical steel girder bridge will constitute Phase II of the project.

Phase I of the project described in this report was accomplished using the following nine tasks. UMC and UMR research teams jointly completed Tasks 3, 6 and 9. All other tasks were completed either at UMC or UMR as designated below.

1. Review current MoDOT and AASHTO procedures for design of deck slab (UMR)
2. Review design information from Canadian "Steel-free" bridge and study service performance information (UMC)
3. Develop analysis/design procedures for new FRP/FRC hybrid reinforced bridge deck system (UMC and UMR)
4. Conduct laboratory tests to establish static and fatigue tensile pull-out and bond splitting characteristics (UMR)
5. Conduct laboratory tests to establish static and fatigue flexural bond characteristics (UMC)
6. Conduct laboratory tests on FRP/FRC reinforced beams to evaluate ductility performance and validate analytical/design model (UMR and UMC)
7. Conduct accelerated durability tests on FRP/FRC hybrid reinforced concrete specimens (UMR)
8. Conduct static and fatigue tests on full-scale hybrid reinforced deck slab system (UMC)
9. Analyze test results and prepare recommendations for Phase II implementation (UMC and UMR)

1.3. RESEARCH SIGNIFICANCE

Cracking in concrete decks under service loads and consequent ingress of chlorides from de-icing salts is common in most states requiring snow removal. When chlorides reach the steel bars, local electrochemical cells are set up due to potential differences. Oxidation and pitting of steel bars results from electrochemical action. Oxidation (rusting) of steel bars has two detrimental effects. Firstly, the bars loose cross-sectional area, and hence it's tensile capacity due to rusting. Secondly, the rust products have a volume of 600-800% of the volume of steel that they replace, resulting in extremely large tensile pressures on the concrete at the location of steel reinforcement. These pressures cause splitting failures and spalling of concrete. Thus, corrosion of reinforcing steel in concrete decks constitutes the most common and expensive component of bridge maintenance. Associated maintenance effort is also perhaps very time-intensive. It is expected that when steel bars are replaced with a hybrid system of FRP bars and short discrete polypropylene fibers, the problem of corrosion in reinforced concrete bridge decks can be greatly mitigated. This would result in enormous savings in maintenance efforts and costs. Inconvenience from frequent lane closures and associated costs can also be avoided.

1.4. IMPLENTATION AND ORGANIZATION

Even while the individual tasks identified in Section 1.2 were necessary to successfully accomplish the project objectives, a cohesive analysis of research observations and associated presentation is better accomplished using a format that collates several tasks with somewhat related themes. For this reason, this report is organized in the following sections (instead of a task-specific discussion):

1.4.1. Design of Bridge Decks, Steel-Free Deck Designs and Related Background

The MoDOT and AASHTO procedures for the design of deck slabs in steel girder bridges are reviewed to understand the current approaches in the design of concrete decks. Canada has developed and implemented a steel-free bridge deck system using a somewhat different reinforcing system than the one proposed here. Deck slabs in the Canadian design are assumed to act as tied arches. The steel-free deck slab system uses polypropylene fibers in the slabs. There is no embedded continuous reinforcement in the slab. Steel straps at the bottom of the concrete deck slab tie steel girders at the top-flange level. These straps act as ties that carry horizontal thrust forces and prevent horizontal movement of the girders. The Canadian design approach has evolved in recent years from the original design based on their experience with several steel-free bridge deck and other similar structures as described in Chapter 2. The approach proposed in this study where the deck slab is reinforced with a non-ferrous hybrid reinforcement system comprising continuous FRP bars and short discrete randomly oriented fibers is somewhat different from the Canadian concept. Nevertheless, it is beneficial to study and understand the Canadian experience in steel-free bridge deck designs. The innovative Canadian approach is also reported on. The above reviews facilitated design emphasis on parameters that will be useful in the current effort to develop design procedures for a non-ferrous hybrid reinforced concrete bridge decks.

1.4.2. Bond Performance of FRP Reinforcement in an FRC Matrix

Good bond performance is essential to ensure effective use of bar strength and avoid undesired brittle failures. While deformed steel bars develop mechanical bond resistance by means of steel lugs on concrete, FRP bar develop bond resistance either by mechanical resistance (helical patterns mimicking deformed steel bars) or by frictional resistance between concrete and the uneven bar surface. Types of FRP bar, their shape and their surface treatment dictate their bond performance. Several studies have addressed this issue in recent years.

Unique to this proposed work is combining FRC, made of short polypropylene fibers as discrete reinforcement, with FRP as primary continuous reinforcement. The short fibers tend to improve the mechanical properties of the concrete matrix by enhanced resistance to crack growth. Thus, by mitigating secondary cracking and reinforcing the weak zone around FRP bars, FRC improves the bond characteristics of the hybrid reinforcing system.

Three test methods are commonly used to study bond behaviors: namely, pullout bond test, splitting bond test, and flexural bond test. These different test configurations provide different information with regard to bond behaviors. Pullout tests represent the concept of anchorage and are usually adopted to study the bond behavior between rebar and concrete. Although pullout test causes concrete to be in compression and the reinforcing bar to be in tension, a stress condition not exhibited in real structures, a reasonable correlation has been found between structural performance and measures of performance in the pullout test (Cairns and Abdullah, 1992). Splitting bond tests are often used to study the splitting bond behavior under different cover thicknesses. The effect of the transverse reinforcement on bond behavior can be avoided when properly designed. Splitting bond tests simulate the stress field of real structures to some extent - while it can simulate the shear stress field it does not represent the stress gradient induced by bending. Flexural bond tests have the advantage of representing actual stress fields in beams and the cover effects on bond. However, it requires considerable confining reinforcement to avoid a shear failure. All three test configurations were investigated and compared to provide a complete picture of interface interactions in FRP reinforced concrete.

1.4.3. Ductility Characteristics in FRP Reinforced FRC Systems

Ductility is an important design requirement in many structures and minimum levels of ductility are mandated by design codes. In reinforced concrete structures, when using conventional materials (i.e. steel and concrete) ductility is provided by the proper combination of the two materials cross-sectional ratios allowing the ductile material (steel) to yield first. In FRP reinforced concrete members, both the FRP and concrete exhibit relatively brittle behavior. Traditional definitions of ductility used in conventional steel reinforced concrete structures are not appropriate for FRP reinforced concrete. However, in FRC, the short fibers tend to increase the toughness of concrete allowing for a significant increase in the total energy absorption of the system, which can be regarded as inducing ductility in concrete.

More recently energy-based (Naaman and Jeong, 1995) and deformation-based (Jaeger et al., 1995) approaches have been developed and successfully used for reinforced concrete structural elements. These approaches will be reviewed for application in the context of the hybrid reinforcement system used in this investigation. In addition to being phenomenologically more appropriate for FRP reinforced systems, the presence of fibers in the concrete matrix and its contribution to enhanced toughness and crack growth resistance will make newer measures of ductility even more relevant.

1.4.4. Accelerated Durability Tests on Hybrid Reinforced Systems

Composite materials offer many advantages such as corrosion resistance, and their use in bridge decks have become more technically attractive and economically viable. However, long-term performances have to be clearly understood before it can be applied in the field with confidence.

Much research has been completed on the durability issue regarding individual FRP components, but there is a paucity of literature on the durability of FRP and concrete system. The durability characteristics depends more on the interrelation between the materials than on the individual component’s property. In addition, the mechanical properties of a hybrid material system may deteriorate much faster than that suggested by the property degradation rates of the individual components making up the hybrid system (Schutte, 2004). The FRP/FRC hybrid system is relatively new and hence published literature on durability characteristics of this hybrid system is not currently available. Thus, accelerated durability tests on the FRP/FRC system are necessary. Specimens were subjected to cycles of freeze-thaw and high temperature while in contact with salt water. Bond characteristics and flexural performance were evaluated, and results were compared to those without environmental effects.

1.4.5. Static and Fatigue Tests on Hybrid Reinforced Slab Specimens

Three full-scale tests on conventionally and hybrid reinforced slab systems designed using the procedures and data developed in this study were tested under static as well as fatigue loading conditions. Results from these tests allow understanding of the fatigue characteristics and potential failure modes in such hybrid reinforcing systems compared to the deck of conventional design.

2. BACKGROUND INFORMATION

2.1 BOND PERFORMANCE OF FRP IN A CONCRETE MATRIX

One of the major parameters affecting the performance of reinforced concrete members is the bond characteristics of the reinforcement in concrete. Bond strength governs development length, crack width, crack spacing, and member deflection. Since bond is a governing design criterion, much effort has been expended researching the subject and developing constitutive models of the bond mechanism, for steel reinforcement and, more recently, for FRP reinforcement.

Since its development around 1950, the deformed steel bar has become ubiquitous, and its bond characteristics have been determined fairly precisely by a vast number of experiments. Steel reinforcing bar has the advantage of uniformity: a grade 60 bar has stringently controlled yield strength, regardless of the manufacturer. Steel also exhibits isotropy, having equal strength in all directions. In bond failure between concrete and steel, it is the concrete that fails by crushing, leaving the steel undamaged.

Fiber reinforced polymer, however, represents a wide range of materials and hence has a range of performance characteristics, which poses many design challenges. Composites have been under development since the 1960's, but much of the technology is still new, and it is rapidly changing. The term FRP describes a wide range of fibers and polymers, including glass fiber reinforced, carbon fiber reinforced, aramid fiber reinforced, and others. Each of these types of FRP has very unique properties, which make the bond behavior unique. When considering GFRP bars only, the properties can still vary widely according to manufacturer. Also, the same bar can undergo different surface treatments to improve bond, leading to very different bond strengths. Unlike steel, FRPs demonstrate shear lag, producing lower values of ultimate tensile stress for larger cross-sectional areas, a characteristic that affects bond. As a result of these factors, the study of bond of FRP must still be carried out with regard to a particular type of bar. No broad generalizations on bond behavior can be made for such a varied collection of materials.

The vast majority of the research that has been conducted on FRP reinforcement has focused on GFRP, which consists of what is commonly known as fiberglass. Compared to the other types of FRP, it is cheaper and much more widely available. In fact, most of the literature refers to GFRP simply as FRP. GFRP has a modulus of elasticity which is less than one-quarter that of steel. This lack of stiffness leads to larger deflections and crack widths. A three-fold increase in both deflections and crack widths compared to conventional steel rebars can be expected. CFRP, on the other hand, has a much higher modulus, and is approximately two-thirds of that of steel. Thus, CFRP reinforced concrete will have less deflection and smaller crack widths than GFRP reinforced concrete members. These improvements come at a price, though, as CFRP is much more expensive than GFRP.

2.1.1 Bond Testing Configurations and Related Observations

Many different tests have been devised to study the bond of reinforcement to concrete. These include concentric pullout tests (direct, rod-rod, and pretensioned rod), cantilever beam, hinged beam, trussed beam, and others. As noted by Nanni, Bakis, and Boothby (1995a) in a comprehensive review of the methods for testing the bond of FRP, all of these methods have been used to study the bond of steel reinforcement to concrete, and are now being implemented to study the FRP bond. Although there is no standard test to determine bond strength, the two most common types of testing are the direct pullout test and the hinged beam test.

2.1.1.1 <u>Direct Pullout Tests</u>

In 1991, the American Society for Testing and Materials developed a standard direct pullout test, found in ASTM C 24-91a. It has the distinct advantage of simplicity: a single reinforcement bar is cast into a concrete specimen, then pulled out as the concrete is restrained (Fig. 2.1). The free end of the reinforcement bar is accessible for measurement of free-end slip. The value of bond strength can be delineated as the bond stress at a certain level of free-end slip, or as the ultimate bond stress developed before pullout.

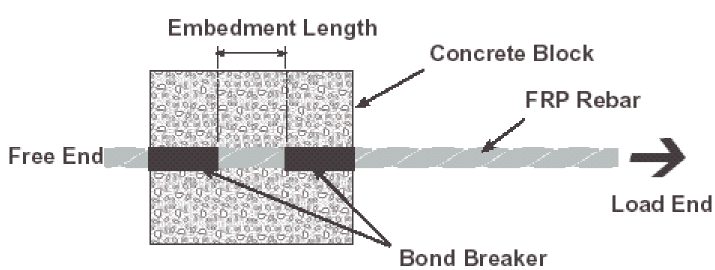

Figure 2.1 – Direct Pullout Test

This test method has several disadvantages as well. The concrete samples tend to split during testing, affecting the results obtained. Also, the concrete at the free end of the reinforcement is subjected to compression due to the restraint, which can affect the results obtained. These drawbacks can be minimized with proper selection of the test parameters. Results from the direct pullout test are limited to the ultimate bond strength and the bond stress-slip curves. The free-end slip is readily measured, and internal instrumentation can be used to gauge embedded-end slip. Internal strain gauges can capture the strain in the reinforcement itself. Modifications of this test have included varying the confining pressure surrounding the concrete sample, as in the study by Malvar (1995). To solve the problem of compression in the concrete sample, the rod-rod pullout test was developed. In this test, two separate reinforcement bars are embedded in the sample, one with a shorter embedment length. The reinforcement bar with the longer embedment length is held, and the shorter reinforcement bar is pulled out. Since the concrete itself is not restrained, no compression is introduced, giving more realistic bond strengths. Other modifications have been made to the pullout test for individual studies. Malvar in 1995 added concentric confinement to the standard pullout setup to study the effect of concrete cover on bond strength of FRP. The tests used cracked samples with varying confining stresses.

2.1.1.2 Flexural Bond Tests

Although simple and versatile, pullout tests cannot replicate the stresses found in a real beam, so beam tests are also used. The broad category of beam tests includes hinged beam, cantilever, P/C type, and many other test setups. Each attempts to reproduce the conditions found in a typical beam, with combined shear and moment causing strain gradients along the reinforcement.

The most common type of beam test for bond is known as the flexural bond test, or the hinged beam test. A typical experimental setup for this type of test is shown in Figure 2. Specimens are cast in two halves, joined at the top by a steel hinge and at the bottom by the reinforcing bars. When the load is applied, the hinge is subjected to compression and the reinforcement bars are subjected to tension. The bonded length of the reinforcement is under combined shear and pullout forces with this arrangement, as it would be in an actual beam.

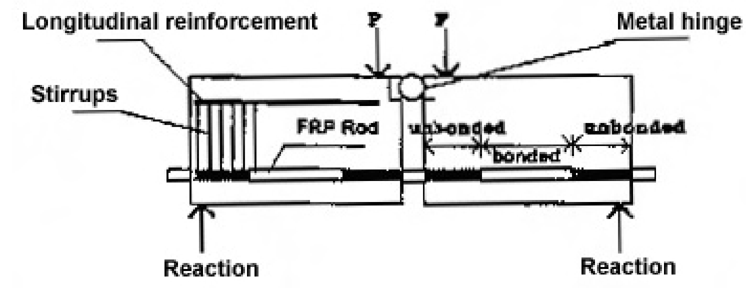

Figure 2.2 – Flexural Bond Test

Since this test accurately replicates conditions in a beam, the results given are more representative of bond strength than those given by the pullout test. The split in the middle of the beam makes it possible to instrument both ends of the reinforcement, loaded and unloaded, allowing strain gradients to be obtained. Also, it is possible to obtain two sets of results from each specimen, if the reinforcement that slips first is clamped to prevent further slip.

A modification of the flexural bond test is the cantilever bond test. The cantilever test setup, shown in Figure 2.3, is basically half of a hinged-beam test, with a load cell providing the resistance instead of the other half of the beam. The advantages of this test are relative simplicity, since it is only half of the full test, and ease of instrumentation.

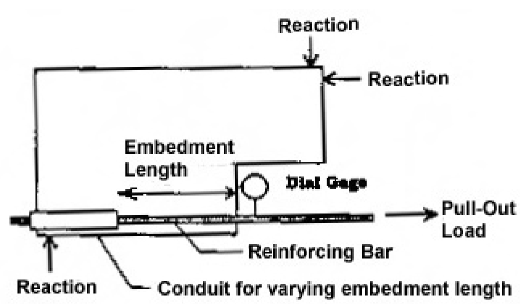

Figure 2.3 – Cantilever Test

2.1.2 Experimental Results from Bond Tests

Due to the increasing interest in corrosion-resistant reinforcement for concrete structures, the amount of research being conducted on the bond of FRP with concrete has been increasing steadily. As a fairly new field, the earliest research on the topic dates back less than ten years. The earlier studies sought to provide basic information on bond behavior, and the more recent studies have built on this information and have dealt with more aspects of the behavior of the FRP. A number of these studies are presented here, beginning with the earliest and simplest.

2.1.2.1 Static Loading

Faza and GangaRao (1990) performed a number of experiments involving FRP reinforcement, including bending tests and cantilever bond tests, in order to determine the stress-strain behavior, load-deflection variations, load-carrying capacities, crack patterns, modes of failure, and bond strength. A total of twenty-two bending tests were performed, on beams with different combinations of FRP reinforcement, smooth and ribbed rebar, and steel and FRP stirrups. The specimens were subjected to four-point bending, resulting in pure moment in the mid-span. High-strength concrete was utilized in order to take advantage of the higher tensile strength of the FRP. In all of the tests, crack widths were observed to be uniform, indicating that there was no loss of bond between the FRP tension reinforcement and the concrete prior to failure. Bond failure of the smooth FRP stirrups, however, did result in lower beam capacity.

Twelve bond tests were also performed, using a cantilever test setup. The authors note that "bond strength is a complicated phenomenon," influenced by many factors. As a result of the small number of tests performed, no conclusions regarding bond are made, only that "more tests are necessary before determining the minimum development length for FRP."

For the No.8 bars used in the study, the bond stress was found to be close to 400psi for each test. In every test using No.3 bars, the bars failed prior to bond failure, giving only an estimate of the minimum bond strength. This minimum shear stress varied from under 400psi to over 900psi, showing greater strength with less embedment length.

Most useful from this study was the finding that sand-coated FRP reinforcement increased the cracking moment of the beams by forty percent, due to improved bond. Smooth FRP reinforcement was found to be inadequate in developing bond to concrete, and is not recommended for use as tension reinforcement or as stirrups. Crack widths were consistent over the length of the beam specimens, showing good bond with the concrete, but were roughly four times wider than cracks in beams with steel reinforcement. This is due to the lower stiffness of the FRP, and must be addressed in design.

Ehsani, Saadatmanesh, and Tao (1996) conducted a broad study on the bond behavior of FRP reinforcement to concrete, using glass FRP. This study noted that the lack of design criteria for FRP reinforcement is one of the major factors restricting the use of this corrosion-resistant material. It had the very practical aim of providing general guidelines for the bond of glass fiber reinforced plastic reinforcement to concrete, under a wide range of influencing factors.

A total of 102 specimens were prepared and tested, including 48 beam tests, 18 pullout specimens, and 36 hooked-bar specimens. Reinforcing bars were No.3, No.6, and No.9. In this test, as with others, the pullout tests gave higher values of bond strength, due to the concrete being in compression.

With traditional steel bars, the critical bond stress is defined as the stress at a free-end slip of 0.002 inches or a loaded-end slip of 0.01 inches, whichever occurs first. In the case of GFRP reinforcement, these slip conditions cannot be utilized, due to the lower modulus of elasticity. With this in mind, the authors developed new slip conditions governing the reported bond strength of GFRP. The recommended slip is 0.0025 inches at the free end and 0.015 inches at the loaded end.

With practical goals in mind, the authors compared the behavior of the FRP reinforcement to traditional steel. The American Concrete Institute (ACI) guidelines for concrete design with steel reinforcement were then modified appropriately, according to the results of the study. These proposed modifications will be discussed further later. It must be noted that the recommendations given are applicable only to this one type of FRP, and only with similar conditions.

Malvar (1995) studied the influence of confining stress on the bond of GFRP reinforcing bars to concrete. Four unspecified commercially available GFRP bars comprised the test specimens, each having a diameter of ¾-inch. Each bar used a different method of improving the bond characteristics: Type A had an external helicoidal tow, Type B had large indentations from a surface tow, Type C had only a spiral strand glued to the surface, and Type D was similar to Type B, with smaller indentations. Each bar was cast into a concrete cylinder, with a development length of 2.64 inches, equivalent to five bar lugs. A steel pipe, split into eight sections longitudinally, enclosed the concrete, for the purposes of applying the confining stress. Before the pullout tests began, the concrete was cracked by means of applying tension to the reinforcing bar, allowing the confining pressure to be controlled externally.

Type A, with an external layer of matrix material, failed in longitudinal splitting. Weak fiber-matrix interface caused this type of failure, which allowed the core of the bar to pull out while leaving the exterior in the concrete. The second type of bar, with deep indentations, failed by cracking at the kinks induced by the deformations. Type C, with only an exterior strand and no deformations, lost its bond strength when the strand separated from the bar surface, leaving it smooth. Failure of Type D was also in the bar, occurring at higher levels than the other three samples.

In addition to bond strength data, information on the stress-slip performance of the samples was also obtained for each level of confining stress. Bar type A showed a response similar to steel reinforcement, with stress that peaks rapidly and falls off slowly as slip increases. Increased confining pressure led to increased peak values of bond stress. Type B showed more scatter, with the highest value being three times the value at the lowest confining pressure. The variation in indentation depth contributed to this uncertainty. For bar type C, the concrete remained uncracked under the initial loading, and carried the confining pressure applied during pullout testing as hoop stress. Thus, the responses under different confining pressures were the same. Type D showed the most promise, giving high peak values corresponding to high confining stresses, and having high residual stresses after peak, showing increased energy dissipation.

As a result of the study, Malvar developed an analytical model for the stress-slip behavior of FRP reinforcement to concrete. This model will be discussed further later. Malvar concluded with this study that small surface deformations, similar to those of steel reinforcement, are sufficient to yield bond strengths equivalent to those of steel. Surface deformations and indentations provided by a helicoidal wrapping are deemed acceptable for bond. Also, the bond strengths of steel bars under identical confining stresses were from 1.2 to 1.5 times higher than those of FRP bars. Bond strength increased threefold with increased confining pressure, pointing out the need for adequate concrete cover.

Benmokrane, Tighiouart, and Chaallal (1996) investigated the bond of GFRP reinforcement to concrete. For this study, twenty beam tests and five pullout bond tests were done, using GFRP and steel reinforcement in order to form a comparison. Extensive testing was performed on the GFRP bars to determine the specific material properties, including tensile strength and modulus of elasticity. Normal strength concrete was used for each specimen.

Three GFRP bars and two steel bars were used in the pullout tests. Extensive instrumentation recorded strains at six locations along the bars, as well as other strains and reactions. In both types of bars, the tensile stress distributions in the bar varied exponentially, decreasing as the distance from the loaded end increased. As the load increased, the bond stress distributed itself further from the loaded end, with the maximum bond stress moving away from the loaded end due to progressive loss of bond starting at that end. It was found that chemical adhesion and mechanical interlock give bond strength before slip; friction provides bond strength after slip begins.

In the beam test, the results showed bond strengths of GFRP to be in the range of sixty to ninety percent of the strengths given by steel bars. As with steel bars, the bond stress decreases as bar diameter increases. Additionally, the relative slip of the two ends of the bar was shown to be roughly the same under similar stresses as the slip experienced by the steel bars.

The bond of concrete and steel reinforcement comes largely from concrete bearing against the deformations in the steel bar. Thus, the loss of bond comes from concrete shear failure and crushing in this bearing zone, and not from the steel bar being deformed. GFRP bars have a lower bond strength, due mainly to the fact that the deformations on their surface, unlike those on steel bars, do not have the strength to cause concrete shear and crushing failure. In this study, the concrete surfaces adjacent to the GFRP bars were observed to be undamaged following the tests, pointing to low induced bearing stresses in the concrete. The authors conclude that adhesion and friction are the two main bond stress components of GFRP rebar to concrete; concrete bearing is an insignificant factor.

Results from the beam tests and the pullout tests were compared, showing the pullout tests giving much higher values for bond strength. In the pullout test, the concrete is placed in compression, disallowing tensile cracking, which in many cases precipitates bond failure. Thus the bond strengths given by this test ranged from 5 to 82 percent higher than those from the beam tests. The beam tests replicate actual conditions and strain gradients much closer, giving better estimates for the bond strength.

Tighiouart, Benmokrane, and Gao (1998) studied the bond of GFRP reinforcement to concrete. A total of 64 beam tests were performed, using four different bar diameters for each of the two types of GFRP, along with similar steel bars for comparison. The embedment lengths used were six, ten, and sixteen times the bar diameter. Bond strength was measured for each specimen, using the standard hinged beam test.

Bond strength arises from three sources: friction, adhesion, and mechanical bearing. With deformed steel bars, mechanical bearing provides the majority of the bond strength, as the steel has excellent transverse stiffness. GFRP bars do not exhibit high transverse strength, and thus their bond performance in concrete depends on adhesion and friction between the materials. As a result, the bond strengths given by the polymer bars used in this test are lower than those for the steel bars. Additionally, the authors discussed ACI code provisions, and modified the analytical model proposed by Malvar for FRP. These topics will be presented later.

A study done by Katz (1999) formed the basis of the work done later by Katz (2000) on the effect of high temperature and cyclic loading the bond of FRP bars in concrete. Five different GFRP bars were utilized in this test. The bars had some combination of sand coating, helical wrapping of strands, deep dents, and resin deformations to improve bond. A steel bar was also tested as a comparison.

Pullout tests were performed on each bar, using a specimen cut in two to form two pullout specimens. Each had a bonded length of 60 mm. All specimens were statically loaded to failure, and bond strength was calculated based on the maximum load applied.

Two types of bar exhibited very poor bond characteristics. The third bar, R3, had sand coating, a helically wrapped strand, and deep deformations, yet showed negligible bond strength. In testing, a gap between the concrete and the reinforcement bar was noticed. The polyester resin dissolved at the surface of the bar, leaving no mechanical interlock between the materials. Bond strength then came solely from the weak friction between the protruding sand particles and the concrete. Also showing low strength was bar number five, the smooth polyester bar. The smooth surface did not have any interlock with the concrete, and the polyester material, with poor wetting properties, reduced the strength of the concrete at the bar surface.

The remaining three types of bars all exhibited bond strengths greater than that of the steel bar. Bar number one, with sand coating and helical wrapping, gave a maximum bond strength of 1987psi, bar number two gave 1769psi, and bar number four exhibited 2118psi, and the steel bar gave 1755psi. In the case of the FRP bars, the damage during pullout was limited to the bar itself; with steel, the concrete alone was damaged.

Three modes of post-peak behavior are presented. Mode I represents combined matrix-reinforcement damage, typical of bars with good exterior mechanical properties. The decrease in load with increased slip is fairly uniform. In Mode II, there is a rapid decrease in load once the peak loading is reached, representing a rapid and brittle failure of bond. Bars with poor mechanical properties exhibited this type of behavior. Mode III shows slip-hardening, as the load falls off slowly with increasing slip. The smooth bar was the only one to exhibit this type, as the wedging effect caused increased resistance.

In conclusion, Katz states that the mechanical and physical properties of the reinforcement bars have every effect on bond strength. When the external layer of the reinforcement bar consisted of a polymer with good mechanical properties, adequate bond was obtained, on the order of the bond strength of steel rebar. Bars with exterior layers of weaker polymers exhibited inferior strengths. The polyester resin was shown to be inferior to the vinyl ester.

2.1.2.2 <u>Fatigue Loading</u>

The studies that have been discussed thus far have all involved testing in static loading to failure, giving the short-term response of the bond between the concrete and the FRP. However, a real-life structure is subjected to repeated loadings of a small magnitude relative to the ultimate strength. The long-term bond behavior must be understood in order to design against fatigue failure, especially in structures such as bridge decks, where FRP is likely to be used. To gain understanding of the long-term behavior of the bond between FRP and concrete under fatigue loading, several studies have been conducted.

Bakis et al. (1997) discuss the effect of cyclic loading on bond of GFRP bars to concrete. Their study utilized a hinged beam test, which the authors referred to as the RILEM flexural beam bond test. Two types of commercially available reinforcement bars were tested, along with a machined E-glass vinyl ester reinforcement bar.

Cyclic loading was applied to each specimen, with the magnitude of the loading and the number of cycles determined according to the maximum bond strength of the virgin beam. The first machined reinforcement bar, with lugs spaced at approximately one inch, was tested to 100,000 cycles. When the bond strength actually showed an increase, the second specimen was tested to 1,000,000 cycles of the same stress level. In all cases, the fatigue loading increased the available shear strength of the bars with lugs, due to the "seating in" of the lugs against the concrete. The virgin bond strength was measured to be 1,630psi after loading; the average bond strength was 2,180psi.

The first of the two commercially available reinforcement bars had a sand-coated exterior, with a helical fiber causing deformations on the surface. All three specimens underwent 100,000 cycles, under three different stress levels of up to fifty percent of the ultimate strength of the virgin specimen. Before cyclic loading, a maximum bond stress of 2,260psi was measured. The repeated loading increased the ultimate bond strength of all three specimens, from one to twenty-six percent. The authors theorize that the cyclic loading squeezes the reinforcement bar into smaller spaces in the concrete, improving the mechanical interlock between the materials.

For the third type of reinforcement bar, also commercially produced, 100,000 cycles were applied with stresses ranging from 25 to 75 percent of the ultimate bond strength in the virgin sample. One reinforcement bar, undergoing testing at 75% loading, failed at 28,000 cycles. The other two reinforcement bars completed the testing, and gave residual bond strengths greater than the virgin sample. Again, the increase is attributed to increased mechanical interlock due to the fatigue loading.

The increase in strength of all types of bars tested in this study must be qualified. The specimens were designed to prevent longitudinal splitting of the concrete, a failure mechanism obviously susceptible to damage accumulation under fatigue loading. Damage in these tests was limited to the FRP bars and the surrounding concrete. The bond strengths after loading ranged from 2,000-2,600psi, close to the bond strength of a virgin steel bar specimen.

Although the actual strength increased, the cyclic loading did cause increased slip of the reinforcement bars, which must be considered. This additional slip would cause increased crack widths and deflections in a member subjected to repeated loading, and thus must be considered for serviceability. The long-term slip is governed by the transverse stiffness and surface properties of the individual reinforcement bars, so no design recommendations are given. Also noted in the study is the need for additional testing of specimens under cyclic loading at 10 to 20 percent of the tensile capacity of the bar, the typical design loading.

Having previously studied the bond behavior of statically loaded FRP specimens to concrete, Katz (2000) subjected FRP specimens to cyclic loading, determining the bond durability as well as strength. Five types of FRP reinforcement bars were used, including a smooth bar and four bars with bond-improving characteristics such helical-wrapped strands and sand coatings. As a comparison, tests were also performed on a steel reinforcing bar.

In addition to the cyclic loading, the test was also modified by subjecting the test specimens to environmental conditioning. Two different curing temperatures were used when casting the samples: 20 C and 60 C. This provided two sample sets, each of which was subjected to 450,000 cycles of loading, in three stages of 150,000 cycles followed by immersion in a water bath for three weeks. A control sample containing specimens with each type of reinforcement bar was not subjected to loading prior to pullout testing.

Two types of reinforcement bar, the helically wrapped smooth bar and the bar with excess resin, failed at a small number of cycles. A third bar, with sand coating, failed at 282,000 cycles, and the remainder of the samples survived all loading cycles. All of the failed bars ruptured under the helical strand, which evidently initiates the failure under repeated loading.

Bond strength for the surviving bars was tested, and found to be fairly uniform for the unloaded samples. Three of the FRP samples, all with bond-enhancing coatings, gave values for the shear stress that were higher than for the steel bar. Not surprisingly, the other two bars, one smooth and the other with excess resin, gave very low values for bond strength.

After loading, all of the FRP bars exhibited lower bond strength, although not for the same reasons. Reinforcement bar with sand coating and helical strands, lost only 20% of its original bond strength. Similarly, the reinforcement bar with only a helical strand had a decrease in bond strength of 20%. The bar with excess resin performed poorly when not subjected to loading, giving only 580psi of shear stress, and had a strength reduction of 35% after the small number of cycles it withstood. For the bar with deformations shaped like those of a steel bar, the bond strength decreased by 50%, and for the smooth bar, a reduction of 70% was seen.

As an explanation for the behavior of the samples, Katz presented various methods of bond failure. For reinforcing bars with good mechanical properties at the core and on the surface, both the surface of the bar and the surrounding concrete were damaged. In this form of failure, bond strength can be maintained over short slip distances, but then falls off rapidly as each bulge in the reinforcement bar reaches the previously failed zone of concrete.

Two reinforcement bars exhibited failure of the polymer at the surface of the reinforcement bar. In both cases, the interior layer sheared away from the exterior, leaving the bond with the concrete intact. The reinforcement bar with a stiff outer layer with large deformations gave high unloaded strength, but as a result of the damage to the outer layer under cyclic loading, gave much lower bond strengths after loading. Entrapment of sand particles between the two surfaces gave the smooth FRP bar much of its bond strength, but this wedging action was not sustained under cyclic loading, and the reinforcement bars gave very little bond strength after loading.

In conclusion, Katz noted that the method of failure for all FRP bars is unlike that of steel reinforcement. Steel bars cause failure by crushing of the surrounding concrete; FRP bars themselves fail. The surrounding concrete may be damaged by the FRP bar, but the concrete is not the sole contributor. The composition and manufacture of the FRP has every effect on the bond strength, and no broad conclusions can be drawn that apply equally to all types of FRP.

2.1.2.3 Environmental Conditioning

As discussed previously, static loading tests only reveal short-term bond behavior. Long-term behavior depends on both repeated loading and exposure to environmental conditions. The preceding two studies dealt with fatigue loading, and the second study (Katz 2000) involved both of the factors. Other studies have focused on the long-term behavior of the bond between FRP and concrete under accelerated weathering, using environmentally conditioned samples.

One such study is the work of Bank, Puterman, and Katz (1998). The bond of FRP to concrete is governed, quite obviously, by the outermost layer of the reinforcement, which is the only part in contact with the concrete. The resin matrix is responsible for transferring the forces from the concrete into the bar, and thus its long-term susceptibility to degradation must be a concern when considering bond strength. The purpose of this study was to determine if this degradation could be observed and measured, and to gain a fundamental understanding of the process.

Degradation of the bond properties relates directly to the polymer resin matrix, meaning that this study applies equally well to all types of high-fiber-content polymers, included GFRP and CFRP. Only GFRP bars were used in this research, though, with various types of resin matrices. The cost of the E-glass FRP, with both polyester and vinyl ester resins, is much lower than the alternative types of FRP available, so this type of FRP is considered the most promising material.

In the study, embedded-reinforcement bar test specimens were used. Each reinforcement bar was encased in concrete, which was then sawed into three parts: a pullout specimen with the bar protruding, a splitting specimen, and a smaller slice specimen for microscopic analysis. Prior to the slicing, each sample was environmentally conditioned by submersion in alkaline water for either 14 or 84 days. This conditioning regimen simulated exposure to concrete, which produces alkalinity. A control group was left at room temperature unsubmerged for the same period of time.

As would be expected, both types of smooth bars, with polyester and vinyl ester resins, offered no measurable initial bond strength, although as the reinforcement bar was pulled out, the strength did increase somewhat. Examination of the splitting samples revealed that the damage to the bar resulted in debris wedging against the concrete as the bar was extracted, causing resistance. This bond strength did not develop, however, until relatively large values of slip had occurred, and thus cannot be used in design calculations. Smooth bars were not recommended for use in actual applications.

Bar number three, made of a vinyl ester resin and containing deformations, exhibited much better bond strength. The damage from submersion in the alkaline solution was noticeable, and caused a decrease in the maximum bond stress. The pullout tests resulted in circumferential cracks developing around the bar, underneath the helical strands. To the authors, this was “troublesome,” as this sort of failure could allow the outer layer to remain bonded to the concrete while the inner layer of unidirectional fibers pulled away. Although the pullout tests did not give ultimate bond strength values due to the concrete cracking prematurely, the observation is made that the bond stiffness compared favorably to other commercially produced FRP bars.

The fourth bar, also with deformations, contained polyester resin and was coated with sand to improve the bond characteristics. The control bar, unexposed to the alkalinity, performed satisfactorily, but the other two samples exhibited dramatic losses of strength.

The bar that had been exposed for 84 days actually had the sand coating peel off when the bar was pulled out, leaving the coating in the concrete. Two of the pullout specimens failed in this manner; the remainder failed by concrete splitting. In both bars that had been exposed, a decrease of up to fifty percent in the bond stiffness occurred, changing the mode of failure, which clearly points to degradation of the resin matrix as the failure mechanism.

In conclusion, the exposure to harsh environmental conditions decreased not only the bond strength but also the bond stiffness of the FRP bars. The resin matrix, as the link between the fibers and the concrete, was found to be the cause of the failure. In design with steel reinforcement, bond strength is considered the governing factor; with FRP reinforcement, it was shown that both bond strength and bond stiffness, as well as the time-dependence of these characteristics, must be included in design parameters.

A study by Conrad, Bakis, Boothby, and Nanni (1998) exposed various types of FRP reinforcement bars to corrosive environments, and then tested the bond strength of the samples. Two carbon fiber reinforced polymer reinforcement bars and one aramid FRP reinforcement bar, all used in prestressed concrete, were tested, along with an E-glass FRP bar used only in cast-in-place construction. Three of the four types, with the exception of one CFRP reinforcement bar, were commercially produced, making this a very practical study.

Before casting, all reinforcement bars were placed in a saturated calcium hydroxide (alkaline) solution, which was kept at a constant 80 C for 28 days. After this conditioning, they were allowed to dry for 14 days before being cast into the concrete specimens. Each type of reinforcement bar was cast into a concrete cylinder, with bond lengths being multiples of the nominal reinforcement bar diameter (2.5D, 5D, 10D, and 15D). Each specimen was tested in direct pullout, giving maximum bond strength.

The Leadline specimens (CFRP) gave between 2,600psi and 3900psi of bond strength for the 5D and 10D specimens, which failed by a complete shearing of the surface FRP material between indents. For the 15D sample, the reinforcement bar failed in the grips, giving only a low estimate of the bond strength. The aramid fiber reinforcement bars, made by Technora, exhibited a constant 1,450-1,740 psi of bond strength, failing when the external windings sheared and slipped.

The one non-commercial reinforcement bar was made of carbon fiber and epoxy. The ultimate bond strength given by these reinforcement bars were all close to 1,300 psi, regardless of embedment length. A shallow waffle pattern was impressed on the surface of these reinforcement bars, which did not result in good bond capacity. In every test, the surrounding concrete removed these indentations upon pullout. The lone GFRP sample, known as C-Bar (no longer commercially produced), produced shear strengths between 2,300 and 2,750psi for the shorter embedment lengths, and failed in the grips at the two longer embedment lengths. The authors conclude that the grips used are inadequate.

Only the Technora reinforcement bars were affected significantly by the conditioning regimen. Conditioned reinforcement bars of this type showed highly variable bond strengths, for unexplained reasons. The other types of reinforcement bars showed no appreciable decrease in bond strength as a result of the conditioning. As in other tests, the slip and subsequent failure of all FRP bars was governed by shear failure of the bar material, not the concrete.

Both the Leadline and C-Bar specimens provided bond strength superior to that of the epoxy-coated steel bar tested. Although the Technora bar had deeper indentations, they did not translate to increased bond strength. More research was advised on the effects of FRP material properties, surface treatments, and geometric parameters on bond strength.

2.1.3 Computational and Analytical Investigations

With FRP development thus far, much of the impetus has been toward practical research, aimed at the civil engineering designer and focusing on structural performance and safety. However, there is also a need for computational models of FRP reinforced systems. It has been noted that the most pressing need is to provide computational models that will advance the research on these types of structures (Cox 1999). An increasing amount of work has been done on this front recently.

With any type of composite system modeling, both the materials themselves and the interaction between them (bond) must be modeled. Analytical models of the bond behavior of steel reinforcement in concrete are well developed, since the materials involved have not changed much in fifty years. The work that is now being done with the bond of FRP to concrete uses these existing models as a starting point, making required modifications.

According to Cox, computational models exist on several scales. Experimental data provide relationships between bond stress and slip, which can be used to form mathematical models. These empirical relationships are referred to as member-scale, with the bar being modeled one-dimensionally. At the opposite extreme is the rib-scale model, which involves a three-dimensional analysis of an individual rib of the deformations on the surface of the bar. In between the two scales is the bar-scale model, in which the bar is continuously modeled, but the failure mechanisms are not modeled explicitly.

Cox has presented an overview of the work that has been done on the various scales of modeling. The model proposed by Malvar is presented as a member-scale model. Using the data and the family of curves for each specimen in his test, Malvar proposed analytical expressions for the monotonic bond stress-slip curves. The peak stress is defined as a function of confinement thus

$$\tau_m / f_t = A + B(1 - e^{-C\sigma / f_t}) \tag{2.1}$$

$$\delta_m / \varnothing = D + E\sigma / f_t \tag{2.2}$$

where

τ_m = bond strength (peak bond stress)

σ = confining axisymmetric radial pressure

f_t = tensile strength

δ_m = slip at peak bond stress

$\varnothing$ = nominal bar diameter

A, B, C, D, E = non-dimensional empirical constants.

The complete bond stress-slip curve is then expressed as

$$\tau = \tau_m \frac{F(\delta / \delta_m) + (G-1)(\delta / \delta_m)^2}{1 + (F-2)(\delta / \delta_m) + G(\delta / \delta_m)^2} \tag{2.3}$$

where F and G are non-dimensional empirical constants.

Equations 2.1 through 2.3 are valid for the range of confining pressures tested, and can serve as a modeling tool when doing simple numerical modeling. A more complete representation of bond behavior would include the effects of the radial dilation that accompanies slip.

Tighiouart et al. (1998) proposed changes to the work by Malvar. The authors suggested one modification to Malvar’s model, in the representation of the ascending branch of the bond-slip relation, where the slip is greater than the slip at maximum stress. They propose the following expression

$$\tau / \tau_m = (1 - e^{4s})^{0.5} \tag{2.4}$$

where s = slip corresponding to the bond stress (τ). This model correlates well with the data obtained in their tests. It is only applicable, however, to this particular type of GFRP under similar conditions.

These member-scale models are quite useful in addressing realistic structural problems, as they deal with larger structural systems. The chief limitation of these models is not that they are empirical, but what Cox refers to as the "scale of empiricism," which restricts the application of these models to problems with similar or identical elements, under similar conditions. Smaller scale models, such as the rib-scale, have much greater predictive capacity, meaning they can be used to predict the results of untested material combinations more effectively.

In a rib-scale model, the surface intricacies of a deformed bar are explicitly modeled, leading to great complexity. Thus, few attempts at modeling at this scale have been done. With the greater complexity, though, comes a greater understanding of the mechanics involved in the bond. Cox reviewed several rib-scale analyses in his paper. The first, done by Yonezawa (1993), who attempted to optimize the surface characteristics of FRP bar to maximize bond strength. A two-dimensional finite element model was constructed of a trapezoidal deformation on the surface of a bar, leading to qualitative conclusions on how changing the rib geometry influenced bond strength. Due to the simplicity of the model, the conclusions were not widely applicable.

Cox also presented the analysis by Boothby et al (1995). Axissymmetric finite element models of a bar with a single rib were developed, and it was concluded that the transverse strength and stiffness of the FRP material could change the failure mechanism of the bond. Also, as was proven with so many experiments, the failure was shown to be likely the result of material failure of the FRP, rather than crushing of the concrete.

The conclusion was made that while potentially useful, the rib-scale models are currently too computationally demanding to accurately depict the effect of bond at a large scale. Also, there is great difficulty in modeling two anisotropic materials, FRP and concrete, at a small scale, where modeling either as homogeneous could cause significant error. The intermediate scale of modeling, bar-scale, provides a reasonable compromise, and can both predict failure and be used to model larger scale problems.

The one bar-scale model presented by Cox was based on a model developed for the interaction of steel reinforcement and concrete, and was only slightly generalized. It was based on the work of Malvar. A very brief yet still detailed version of this model is given. For a complete version, the reader is directed to the work of Guo and Cox (2000). This model has been calibrated to several experimental results, and in each case has correlated with the actual data to within 20 percent.

As previously mentioned, each of these models evolved from those produced for the interaction of steel reinforcement and concrete. Each scale of model has distinct advantages and applications. The smaller scale is best for gaining insight into the underlying mechanics, while the larger scale is best for modeling experimental data. All of the models can be useful tools in the study of the bond behavior of FRP.

2.1.4 Design Recommendations

However useful the models and the research may be, the designer still relies on design recommendations and code guidelines to arrive at a practical design. The American Concrete Institute collects research, developing guidelines to be implemented by the designer. As has been done for steel reinforcement, guidelines and codes for design with FRP have been developed by ACI. The most recent publication on the design of FRP-reinforced concrete structures is ACI 440.1R, the guide for the design and construction of concrete reinforced with FRP bar.

The main consideration in design involving bond is development length, the length required to fully develop the ultimate strength of the bar. An expression for the development length is:

$$\ell_{bf} = K_2 \frac{d_b^2 f_{fu}}{\sqrt{f_c^{'}}} \tag{2.5}$$

where K_2 is an empirical constant. Several researchers have given values for this constant. Ehsani et al. (1996) suggested 1/21.3; Tighiouart et al. (1998) put forth a value of 1/5.6.

In lieu of the previous equation, which is more applicable to steel reinforcement, Ehsani also suggested an alternative equation for development length, given here:

$$\ell_{bf} = \frac{d_b f_{fu}}{K_3} \tag{2.6}$$

where K_3 is a different empirical constant. Studies by both Ehsani and Gao recommend a K_3 value of 2850.

In consideration of these recommendations, the ACI Report specifies the development length for FRP reinforcement is to be, conservatively,

$$\ell_{bf} = \frac{d_b f_{fu}}{2700} \tag{2.7}$$

In SI units,

$$\ell_{bf} = \frac{d_b f_{fu}}{18.5} \tag{2.8}$$

with units of mm and MPa.

2.2 CANADIAN AND US STEEL-FREE DECK SLABS AND OTHER STRUCTURES

Several types of nonferrous hybrid reinforcement systems can be engineered for concrete bridge decks, some of which are illustrated in Fig. 2.4. Combinations of these systems also offer viable design alternates for nonferrous bridge deck reinforcing systems. The tied-arch approach used in Canada is illustrated in Fig. 2.4a. The tied-arch behavior of the deck slab is not very much unlike arch action (shaded region in Fig. 2.4b) in conventional reinforced concrete beams after sufficient flexural cracking has occurred. The arch action becomes effective only after the deck slab cracks due to flexural tensile stresses. A layered hybrid composite system where the deck slab comprises of precast prestressed panels or precast stay-in-place forms on the bottom, topped with cast-in-place concrete containing FRP rebar is shown in Fig. 2.4c. A hybrid reinforcement system using both continuous FRP reinforcing bars and fiber reinforced concrete matrix shown in Fig. 2.4d represents the type of hybrid reinforcing system being studied in an ongoing project at the University of Missouri.

The Salmon River Bridge in Nova Scotia, Canada is the first known steel-free concrete bridge deck and was built in 1995 (Bakht and Mufti, 1996). This design shown in Fig. 2.4a uses a deck slab reinforced only with short discontinuous polypropylene fibers (Vf = 0.55%). Steel straps provided outside the deck slab tie the top flanges of the steel girders supporting the deck. The tied arch behavior is engineered through the use of shear studs (providing composite action between the deck slab and the steel girders) and steel straps. Fibers in the deck slab provide resistance to early-age plastic shrinkage cracking and resistance to crack growth in the hardened state. More recent Canadian steel-free bridge decks have used refined versions of this original design concept details of which are summarized in Table 2.1.

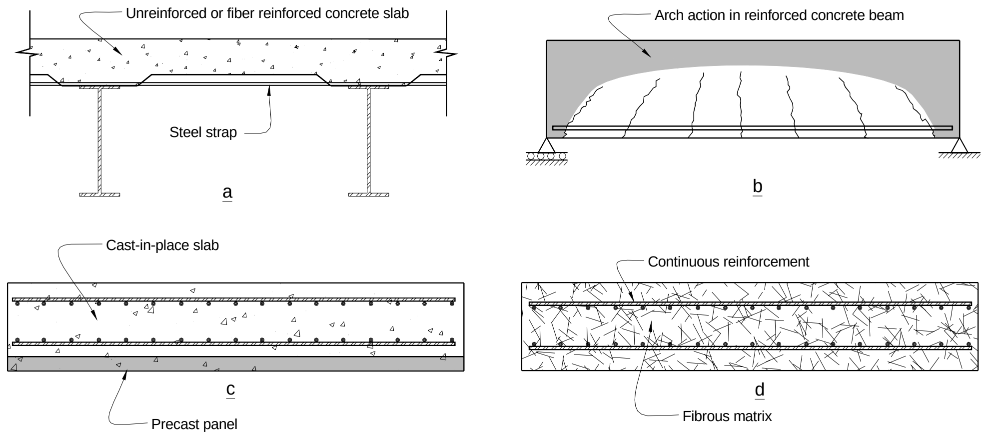

Fig. 2.4 Bridge deck slab reinforcement systems (a) Early Canadian steel-free deck slabs, (b) Arch action in reinforced concrete beam, (c) Layered hybrid composite system, and (d) Continuous/discrete hybrid reinforcement system

Table 2.1 – Summary Of Canadian Steel-Free Bridge And Wharf Deck Slabs

Structure	Year	Span (ft)	Girders	Spacing (ft)	Slab Thickness (in.)	f'_c (psi)	Strap Reinforcement Ratio (%)	Fiber Content /(%) Volume	Additional Reinforcement
Salmon River Bridge, NS	1995	102.4	Steel	8.86	8	5,000	0.50%	Polypropylene / 0.55	None
Chatham Bridge, ON	1996	42.6	Steel	6.89	7	5,000	0.70%	Polypropylene / 0.55	CFRP Grid
Crowchild Trail Bridge, AB	1997	98.4	Steel	6.56	7	*	0.45%	Polypropylene / 0.45	GFRP Bars
Waterloo Creek Bridge, BC	1998	82	Precast Prestressed Concrete	9.22	7.5	*	0.50%	Polypropylene	GFRP Bars
Lindquist Bridge, BC	1998	78.7	Steel	11.48	6 + Precast Panel	*	0.80%	Polypropylene	None
Hall's Harbour Wharf, NS	1999	*	*	*	*	*	*	Polypropylene	GFRP Bars

AB – Alberta, BC - British Columbia, NS – Nova Scotia, ON – Ontario

* *Information unavailable*

Recently, there has been a lot of activity in use of FRP reinforcement in concrete bridge decks in the United States. US Department of Transportation's Federal Highway Administration web site provides a convenient database (US DOT FHWA, 2003) of the numerous recent US projects using FRP reinforcing bars in concrete bridge decks. Even though the list is not exhaustive and includes decks that use conventional steel reinforcement in addition to FRP reinforcement (i.e. not strictly nonferrous reinforced slabs), this site provides a good overview of the types of concrete slab reinforcement systems used in the US. Brief reviews of details from two recent FRP rebar reinforced concrete bridge decks provide general idea of the designs currently used in the US.

Worth noting is the first FRP bar reinforced bridge deck constructed across buffalo creek in McKinleyville, West Virginia. The McKinleyville Bridge is a 177-ft (54-meter) long, 3 span, continuous structure accommodating 2 lanes of traffic. The design of the FRP reinforced concrete deck was based on a design method developed at the Constructed Facility Center at West Virginia University. The design method is similar to the procedure described in the American Association of State Highway Transportation Officials' Standard Specifications for Highway Bridges working stress design of transversely reinforced concrete decks. The design requires a deck thickness of 9in. and No.4 FRP bars as the main transverse reinforcement of 6in. spacing. The main reinforcement is tied to No.3 FRP bars for distribution reinforcement, also at 6in. spacing. The clear cover for top and bottom reinforcements was 1 1/2in. and 1in., respectively.

The Miles Road Bridge in Bentleyville, Ohio is a two span (45 ft spans) steel girder bridge, 38 ft. in width and carries two lanes of traffic (Huckelbridge and Eitel, 2003). The conventionally reinforced concrete deck, which had deteriorated was replaced with an 8.5in. thick cast-in-place GFRP reinforced concrete deck. The GFRP reinforced concrete deck slab used No.5 (16 mm) and No.6 (19 mm) diameter bars (depending on the moment capacity desired at various sections), spaced on 3in. centers in each direction. Two layers of this reinforcement were provided with a cover of 1.5in. Deck reinforcement ratio were 0.0182 for the top reinforcement, 0.0167 for the bottom reinforcement, and 0.0083 for temperature and shrinkage reinforcement. The top of the deck was sealed with a high molecular weight methacrylate rapid-curing penetrating sealant. The overhangs supporting the barrier curb were also reinforced using custom bent GFRP bars.

The Sierrita de la Cruz creek bridge in Potter County, Texas, recently had two of its seven spans redecked with an FRP cast-in-place reinforced concrete deck slab, where the top mat is of GFRP bars (No.6 bars, at 5.5in. centers in both directions), and the bottom mat of epoxy-coated steel rebars (Bradberry, 2001). The composite deck slab also uses stay-in-place forms made of concrete precast panels reinforced with epoxy-coated steel rebars at the bottom. This is the type of construction is illustrated in Fig. 2.4c.

More recently, a new FRP reinforced bridge deck is built inWaupum, Wisconsin. The uniqueness of this bridge is the combination of three different FRP materials. The FRP reinforcing system is made up of three different components: a stay-in-place FRP pultruded deck panel, standard FRP bars, and a bi-directional FRP pultruded grid panel, as shown in Figure 2.5 (Bank et-al. 2004). The deck is 8in. thick and with 1.5in. of cover at the top. The deck panels serve as the bottom tensile reinforcement for the deck in the transverse direction. Standard FRP reinforcement bars serve as the temperature and shrinkage reinforcement. The grid serves as the top reinforcement of the concrete deck.

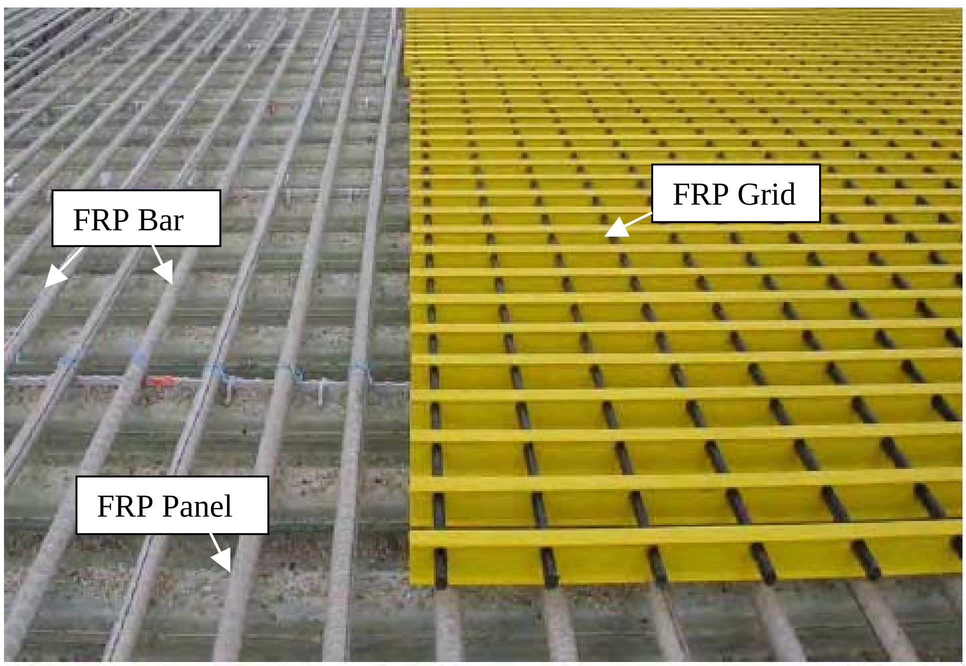

Figure 2.5. FRP panels, FRP bars and FRP Grid used in Wisconsin

2.3 AASHTO AND MODOT DECK SLAB DESIGN PROCEDURES

Decks are the platform of a roadway extending horizontally over a crossing. Decks have many functions. In addition to provide the riding surface for vehicular traffic, they also serve several structural purposes. The bridge deck distributes the vehicular wheel loads to the girders, which are the primary load-carrying members on a bridge superstructure. And the deck is often composite with the main girders and, thus, helps to increase the flexural strength and torsional rigidity of the bridge. For most new bridges, cast-in-place concrete bridge decks are chosen as the most appropriate deck type. Typically, these types of precast panel concrete decks are designed as a transverse beam supported by the main longitudinal girders. While cast-in-place concrete decks designed as transverse beams have been the standard for decades, bridge deck type and design is continuing to evolve.

2.3.1 Loads Relative to Deck Slab Design

From the construction stage to the whole service life, the bridge deck must sustain various loads. The bridge engineer must take into account a wide variety of loads which vary based on duration (permanent or temporary), deformation (concrete creep, thermal expansion, etc.), and effect (shear, bending, compression, torsion, etc.).

- **Permanent Loads**

  (a) Dead Load. The dead load on a deck slab is the aggregate weight of all elements. This includes the deck, wearing surface, stay-in-place forms, sidewalks and railings, parapets, signing, and utilities.

  (b) Superimposed Dead Load. Superimposed dead loads are those loads added onto the deck after it has cured. From the list of elements mentioned previously, the designer should treat items such as sidewalks, railings, parapets, signing, utilities and the wearing surface independently.

- **Temporary Loads**

  (a) Vehicle Live Load. To help designers accurately model the live load on a structure, hypothetical design vehicles based on truck loading, such as HS 20, were developed by AASHTO.

  (b) Impact. In order to account for the dynamic effects of the loading of a moving vehicle onto a structure, an impact factor is used as a multiplier for certain structural elements.

  (c) Construction Loads. During the construction period, large stresses in the structural members may be induced. It is the engineers' responsibility to consider this effect.

- **Deformation and Response Loads**

  (a) Shrinkage. Shrinkage is the natural change in volume of concrete. Besides limiting the effects of shrinkage by better curing the concrete, reinforcement is added perpendicular to the main reinforcement to account for tensile stresses induced by shrinkage.

(b) Thermal Forces. The effects of thermal forces on a structure are significant and should not be underestimated by the designer. In general, thermal forces are caused by fluctuations in temperature. Reinforcements are required on the top of the deck to withstand the tensile stresses induced by temperature change.

2.3.2 Detailed Design Procedures

AASHTO Standard Specifications, MoDOT Bridge Manual, and AASHTO LRFD design procedures for a typical girder bridge deck will be discussed in detail in the following sections. Herein, only the following conditions are considered:

- Steel girders as supports
- Main reinforcement perpendicular to traffic
- Slab continuous over 3 or more supports

2.3.2.1 AASHTO Standard Specifications

The American Association of State Highway and Transportation Officials (AASHTO) has promulgated design specifications for many decades. These specifications, adopted throughout the United States, have been updated periodically. AASHTO's 17th Edition, Standard Specifications for Highway Bridges, published in 2002, is the latest specification.

STEP 1: Choose the general parameters

(1) slab thickness; (2) girder spacing; (3) girder type; (4) reinforced steel; (5) concrete strength; (6) future wearing surface (FWS).

STEP 2: Compute the effective span length

S= Distance between Edges of Top Flange + ½ Top Flange Width

(AASHTO 3.24.1.2 (b))

STEP 3: Compute moment due to dead load

(a) Dead Load:

(1) slab; (2) FWS; (3) barrier curb; (4) median; (5) railing; (6) pedestrian curb and fence

(b) Moment calculation:

CASE A: slabs continuous over more than 2 supports:

$M_{DL}=\frac{wS^2}{10}$,

where w=dead load

S=effective span length

(AASHTO does not give specific dead load moment equations. This is the generally accepted expression).

CASE B: cantilever slabs:

Compute the moments induced by different loads and add them together.

STEP 4: Compute moment due to live load + impact

<u>(A). Interior Spans.</u>

(1) Calculate M_{LL}

Slabs continuous over more than two supports

$M_{LL}=0.8(\frac{S+2}{32})P$ ***(AASHTO 3.24.3.1)***

where P=Live load

=12,000lb for H15 & HS15 loading or

=16,000lb for H20 & HS20 loadings

=20,000lb for HS20 (modified)

(2) Compute M_{LL+I}

$M_{LL+I}= M_{LL}\times(1+I)$

where: I= Impact coefficient

$=\frac{50}{L+125}\leq 0.3$ ***(AASHTO 3.8.2.1)***

L=Length in feet of the portion of the span that is loaded to produce the maximum stress in the member.

<u>(B). Cantilever Spans</u>

(a) Truck Loads

$M_{LL}=P\times X/E$ (foot-pounds)

where: P= Wheel load

E=the effective length of slab resisting post loadings

=0.8X+3.75

X = the distance in feet from load to point of support ***(AASHTO 3.24.5.1.1)***

(b) Railing Loads

M_{LL}=Py/E

where: P=Highway design loading=10kips

y= moment arm

E=0.8X+3.75 feet, where no parapet is used

=0.8X+5.0 feet, where a parapet is used

X=the distance is feet from the center of the post to the point under investigation

Railing and wheel loads shall not be applied simultaneously.

(AASHTO 2.7; AASHTO 3.24.5.2)

STEP 5: Compute factored bending moment

M_u= 1.3(M_{DL}+1.67M_{LL+I})

$M_u \geq 1.2 M_{cr}$ (This requirement may be waived if the area of reinforcement provided at a section is at least one-third greater than that required by analysis based on the loading combinations)

STEP 6: Protection against corrosion

The minimum cover for the slab in inches is shown in Table 2.2.

Table 2.2. Minimum Cover per AASHTO 8.22 (inches)

	Concrete deck slabs in mild climate	**Concrete deck slabs which have no protective corrosion protection and are frequently exposed to deicing salts**
Top Reinforcement	2	2.5
Bottom reinforcement	1	1

(AASHTO 8.17.1)

STEP 7: Compute the main reinforcement

$$\phi M_n = A_S f_y (d - \frac{a}{2})$$

$$a = A_s f_y / (0.85 f'_c b)$$ ***(AASHTO 8.16.3.2.1)***

$$\rho_s \leq 0.75 \rho_b$$ ***(AASHTO 8.16.3.1.1)***

$$\rho_b = \frac{0.85\beta_1 f'_c}{f_y}\left(\frac{87{,}000}{87{,}000 + f_y}\right)$$ ***(AASHTO 8.16.3.2.2)***

STEP 8: Compute distribution steel in bottom of slab

To provide for the lateral distribution of the concentrated live loads, reinforcement shall be placed transverse to the main steel reinforcement in the bottom of the slabs except culvert or bridge slabs where the depth of fill over the slab exceeds 2 feet.

(AASHTO 3.24.10.1)

Percentage= $\frac{220}{\sqrt{S}} \leq 67\%$

where S=the effective span length in feet ***(AASHTO 3.24.10.2)***

STEP 9: Shrinkage & temperature reinforcement

Reinforcement for shrinkage & temperature stresses shall be provided near exposed surfaces of slabs not otherwise reinforced.

$A_s \geq 1/8 in^2/ft$ in each direction

Spacing $\leq 3h_{slab}$

$\leq 18in$ ***(AASHTO 8.20)***

STEP 10: Negative moment reinforcement over supports

In the negative regions of continuous spans, the minimum longitudinal reinforcement, including the longitudinal distribution reinforcement, must equal or exceed 1 percent of the cross sectional area of the concrete slab. Two-thirds of this required reinforcement is to be placed in the top layer of the slab within the effective width.

(AASHTO 10.38.4.3)

STEP 11: Check serviceability

(a) compute f_s at service load

$$f_s = \frac{M}{A_s jd};$$

(b) compute allowable $f_{s,allow}$

$$f_{s,allow} = \frac{z}{(d_c A)^{1/3}} \leq 0.6 f_y$$ ***(AASHTO 8.16.8.4)***

where A=effective tension area, in square inches, of concrete surrounding the flexural tension reinforcement and having the same centroid as that reinforcement, divided by the number of bars or wires. When the flexural reinforcement consists of several bar or wire sizes, the number of bars or wires shall be computed as the total area of reinforcement divided by the largest bar or wire used. For calculation purposes, the thickness of clear concrete cover used to compute A should not be greater than 2 inches.

d_c=distance measured from extreme tension fiber to center of the closest bar or wire in inches. For calculation purposes, the thickness of the clear concrete cover used to compute d_c should not be taken greater than 2 inches.

$z \leq$ 170kips/in for members in moderate exposure conditions

$\leq$ 130kips/in for members in severe exposure conditions

(c) check

$f_s \leq f_{s,allow}$

2.3.2.2 <u>MoDOT Bridge Design Specifications</u>

The MoDOT Bridge Manual, developed for the design of bridges in the state of Missouri, builds on and references the latest AASHTO Standard specifications. It has more restricted conditions on design than AASHTO LFD. Load Factor Design methods for all bridges (both steel and concrete) are used.

STEP 1: Choose the general parameters

(1) slab thickness ((a)h_s=8.5in. cast-in-place concrete slab with conventional forming may be selected by the contractor; (b) 3in. P/S concrete panels with 5-1/2in. minimum cast-in-place concrete will be the standard slab); (2) concrete strength (f_c'=4000psi, f_c=1600psi); (3) reinforcing steel (f_y=60,000psi); (4) modular ratio of elasticity (n=8); (5) future wearing surface (F.W.S).(future wearing surface =35 lb/ft^2) (6) girder type & spacing;

(BM Sec 3.30.1.2-1; 3.30.1.2-2)

STEP 2: Compute the effective span length

slab supported on steel stringers over more than two supports

S= Distance between Edges of Top Flange + ½ Top Flange Width

(AASHTO 3.24.1; BM Sec3.30.1.2-1)

STEP 3: Moment over interior support

(a) Compute moment due to dead load

CASE A: slabs continuous over more than 4 supports:

M_{DL}=-0.100wS^2

CASE B: slabs continuous over more than 5 supports:

M_{DL}=-0.107wS^2,

where w=dead load

S=effective span length ***(BM Sec 3.30.1.2-1)***

(b) Compute moment due to live load

Slabs continuous over more than two supports

$$M_{LL}=0.8\left(\frac{S+2}{32}\right)P$$

where P=Live load

= 12,000lb for H15 & HS15 loading or

= 16,000lb for H20 & HS20 loadings

= 20,000lb for HS20 (modified) ***(AASHTO 3.24.3, BM Sec 3.30.1.2-1)***

(c) Compute moment due to live load + impact

$M_{LL+I}= M_{LL}\times(1+I)$

where I= Impact coefficient

$= \frac{50}{L+125} \leq 0.30$ ***(AASHTO 3.8.2.1)***

L=For continuous spans, ***L*** to be used in this equation for negative moments is the average of two adjacent spans at an intermediate bent or the length of the end span at an end bent. For positive moments, ***L*** is the span length from center to center of support for the span under consideration.

STEP 4: Cantilever moment

(a) Compute moment due to dead load

Dead load =Moment due to slab, future wearing surface (F.W.S) and safety barrier curb (S.B.C)

(b) Compute moment due to live load + impact

Wheel Loads

M_{LL+I}=P×X/E

where: P=wheel load (apply impact factor)

E=the effective length of slab resisting post loadings

= 0.8×+3.75

X = the distance in feet from load to point of support ***(AASHTO 3.24.5.1.1)***

Collision Loads

M_{COLL}=P×y/E

where: P= 10 kips (collision force)

y=Moment arm (curb height + 0.5 slab thickness)

E= 0.8X + 5.0

where: X = Dist. from C.G. of S.B.C. to support

Find the greater of the two (wheel load & collision load) for design load

$M_u = 1.3(M_{DL}+1.67M_{LL+I})$ ***(BM Sec 3.30.1.2-1)***

STEP 5: Determine the design moment

Use the bigger one of the cantilever moment and the interior moment as the design moment.

STEP 6: Protective against corrosion

3 inches clear cover preferred minimum for cast-in-place, 2-3/4 inches clear cover preferred minimum for prestressed panels to accommodate No.8 bars over supports and 2-1/2 inches clear cover absolute minimum by AASHTO 8.22.1.

(BM Sec 3.30.1.2-1A)

STEP 7: Determine the top transverse reinforcement

(1) $\phi M_n = A_S f_y (d - \frac{a}{2})$

$a = A_s f_y /(0.85 f'_c b)$ ***(AASHTO 8.16.3)***

(2) Check ρ_{max} & ρ_{min}

$$\rho_{max} = 0.75\rho_b = 0.75[\frac{0.85\beta_1 f'_c}{f_y}(\frac{87,000}{87,000+f_y})]$$ ***(AASHTO 8.16.3)***

The minimum reinforcement shall provide:

$$\rho_{min} = 1.67(\frac{h}{d})^2 \frac{\sqrt{f'_c}}{f_y}$$

STEP 8: Bottom transverse reinforcement

For design of the bottom transverse reinforcement, the following applied:

(a) Assume the positive moment is the same as the negative moment

(b) Remove 1.0 inch of wearing surface from the effective depth.

Note: When using prestressed panels, P/S panels replace the bottom transverse reinforcement. ***(BM Sec. 3.30.1.2-1)***

STEP 9: Longitudinal distribution reinforcement

(a) Top of Slab

Use No.5 bars at 15in. cts. for temperature distribution.

(BM Sec. 3.30.1.2-1A)

(b) Bottom of Slab

$$\text{Percentage}=\frac{220}{\sqrt{S}} \leq 67\%$$

where S=the effective span length in feet ***(AASHTO 3.24.10)***

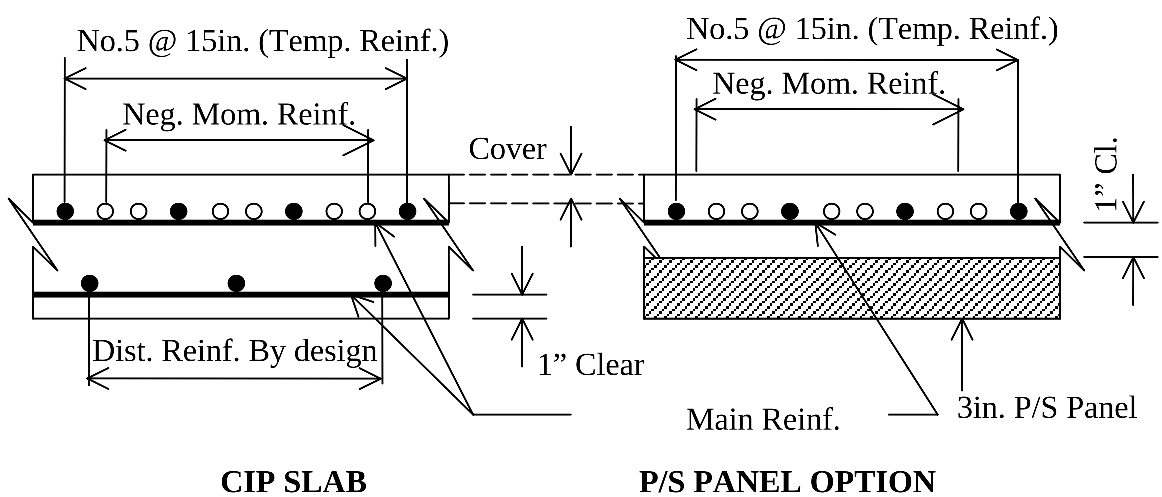

Figure 2.6. Distribution Reinforcement

STEP 10: Negative moment reinforcement over supports

For slabs on steel girder, add No.6 bars at 5in. between No.5 bars.

(AASHTO 10.38.4, BM 3.30.1.2-1A)

STEP 11: Serviceability requirement

(1) Allowable Stress

$$f_{sa} = \frac{z}{(d_c A)^{1/3}} \leq 0.6 f_y$$

where: z=130 k/in.

d_c= Dist. From extreme tension fiber to center of closest bar (concrete cover shall not be taken greater than 2 in.)

A= Effective tension area of concrete

=$2d_cs$

s= Bar spacing ctr. to ctr.

(2) Actual Stress

$$f_s = \frac{M_w}{A_s \times j \times d};$$

where: M_w=Service load moment;

A_s=Area of steel;

j=moment arm coefficient

$$k = \sqrt{(n\rho)^2 + 2n\rho} - n\rho;$$

$$\rho = \frac{A_s}{bd};$$

b= Effective width;

d= Effective depth;

(3) Check

$f_s \leq f_{sa}$

(BM Sec. 3.30.1.2-1A)

2.3.2.3 <u>AASHTO LRFD Specifications</u>

AASHTO LRFD Bridge Design Specifications, first published in 1994, is based on load resistance factors and employs the load and resistance factor design (LRFD) methodology. The factors have been developed from the theory of reliability based on current statistical knowledge of loads and structural performance.

STEP 1: Determine the deck thickness

The minimum required deck thickness, excluding provisions for grinding, grooving, and sacrificial surface is t_{deck} =7.0in.

(LRFD 9.7.1.1)

STEP 2: Compute the effective length

STEP 3: Determine unfactored dead loads

For simplicity, the deck will be designed as a one-foot wide one way slab. Therefore, all loads will be determined on a per foot width.

(LRFD 9.7.2.3)

STEP 4: Determine unfactored live loads

(a) Wheel load:

Truck axle load=32 kips/axle

The axle load of 32 kips is distributed equally such that each wheel load is 16 kips.

(LRFD 4.6.2.1, 3.6.1.3.3, 3.6.1.2.2)

(b) Calculate the number of live load lanes

Generally, the number of design lanes should be determined by taking the integer part of the ratio w/12.0, where w is the clear roadway width in FT between curbs and/or barriers.

(LRFD 3.6.1.1.1)

(c) Determine the wheel load distribution

Type of Deck	Direction of Primary Strip Relative Traffic	Width of Primary Strip (in)
Concrete:		
	Overhang	45.0+10.0X
• Cast-in-place	Perpendicular	+M: 26.0+6.6S -M: 48.0+3.0S
• Cast-in-place with stay-in-place concrete formwork	Perpendicular	+M: 26.0+6.6S -M: 48.0+3.0S
Precast, post-tensioned	Perpendicular	+M: 26.0+6.6S -M: 48.0+3.0S

S=girder spacing; X=dist. from load to point of support

(LRFD 4.6.2.1, Table 4.6.2.1.3-1, 4.6.2.1.3)

(d) Determine the live loads on 1-ft strip:

The unfactored wheel loads placed on a 1-ft strip based on the width of the strips, that is, 16kips/w_p, where w_p=the width of primary strip.

STEP 5: Determine the wheel load location to maximize the live-load moment

Apply the unfactored loads to a continuous 1-ft-wide beam spanning across the girders and find the maximum moment value. The design section for negative moments may be taken as follows: one-quarter the flange width from the centerline of support for steel beam.

(LRFD 4.6.2.1.6)

STEP 6: Determine the load factors

$$Q = \sum \eta_i \gamma_i q_i$$

where Q=factored load

η_i=load modifier

γ_i=load factor

q_i=unfactored loads

(LRFD 1.3.2.1, 3.4.1)

(a) Load modifier

$\eta_i = \eta_D \eta_R \eta_I > 0.95$

For Strength Limit State

η_D>=1.05 for non-ductile components and connections

=1.0 for conventional designs and details

>=0.95 for ductile components and connections

η_R >=1.05 for non-redundant members

=1.0 for conventional levels of redundancy

>=0.95 for redundant members

$\eta_I \geq 1.05$ if a bridge is deemed of operational importance

=1.0 for typical bridges

$\eta_I \geq 0.95$ for relatively less important bridges

For other limit states

$\eta_D = \eta_R = \eta_I = 1.0$

(LRFD 1.3.3, 1.3.4, 1.3.5)

(b) Load factor

	Maximum Load Factor	Minimum Load Factor
Slab and barrier rail	γ_{DCmax}=1.25	γ_{DCmin}=0.90
Future wearing surface	γ_{Dwmax}=1.50	γ_{Dwmin}=0.65

γ_{LL}=1.75

γ_{IM}=1.75 (Strength-1 Load Combination)

(LRFD Table 3.4.1-1, Table 3.4.1-2, 3.4.1, 3.3.2)

(c) Multiple presence factor

$m_{1lane=1.20}$, m_{2lane}=1.00, m_{3lane}=0.85, $m_{>3lane}$=0.65 ***(LRFD Table 3.6.1.1.2-1)***

(d) Dynamic load allowance

IM=0.33 ***(LRFD 3.6.1.2, 3.6.2)***

STEP 7: Calculate the factored moments

$$M_u = \eta_i[\gamma_{DC}(M_{DC}) + \gamma_{DW}(M_{DW}) + (m)(1+IM)(\gamma_{LL})(M_{LL})$$

As specified in ***LRFD 4.6.2.1.1***, the entire width of the deck should be designed for these maximum moments.

For overhang- Calculate Extreme Event II

$$M_u = \eta_i[\gamma_{DC}(M_{DC}) + \gamma_{DW}(M_{DW}) + 1.0(M_{CT})]$$

STEP 8: Determine the slab reinforcement detailing requirements

(a) Determine the top deck reinforcement cover

The top deck requires a minimum cover of 2 in. over the top mat reinforcement (when exposing to deicing salt, 2.5 in.), unless environment conditions at the site require additional cover. This cover does not include additional concrete placed on the deck for sacrificial purposes, grooving, or grinding.

The cover of the bottom of the cast-in-place slabs is 1.0 in for steel bar up to No.11 and 2.0 for No.14 to No.18. ***(LRFD Table 5.12.3-1)***

(b) Determine deck reinforcement spacing requirements

$s \le 1.5 \times t$. (t=thickness of slab) and $s \le 18in.$

The minimum spacing of reinforcement is determined by ***LRFD 5.10.3.1*** and is dependent on the bar size chosen and aggregate size. ***(LRFD 5.10.3.2)***

(c) Determine distribution reinforcement requirements

Reinforcement is needed in the bottom of the slab in the direction of the girders in order to distribute the deck loads to the primary deck slab reinforcement.

Reinforcement should be placed in the secondary direction in the bottom of the slabs as a percentage of the primary reinforcement for positive moment as follows:

$220 / \sqrt{S} \le 67\%$

where S= the effective span length taken as equal to the effective length specified in Article 9.7.2.3 (FT) ***(LRFD 9.7.3.2)***

(d) Determine the minimum top slab reinforcement parallel to the girders

Reinforcement for shrinkage and temperature stresses should be provided near surfaces of concrete exposed to daily temperature changes and in structural mass concrete.

The top slab reinforcement should be a minimum as required for shrinkage and temperature of $0.11A_g/f_y$. And it should not be spaced farther than either 3.0 times the slab thickness or 18in. ***(LRFD 5.10.8.2)***

STEP 9: Check serviceability

$$f_{sa} = \frac{z}{\left(d_c A\right)^{1/3}} \le 0.6 f_y$$

where A=effective tension area, in square inches, of concrete surrounding the flexural tension reinforcement and having the same centroid as that reinforcement, divided by the number of bars or wires. When the flexural reinforcement consists of several bar or wire sizes, the number of bars or wires shall be computed as the total area of reinforcement divided by the largest bar or wire used. For calculation purposes, the thickness of the clear concrete cover used to compute A should not be taken greater than 2 inches.

d_c=distance measured from extreme tension fiber to center of the closest bar or wire in inches. For calculation purposes, the thickness of the clear concrete cover used to compute d_c shall not be taken greater than 2 inches.

$z \leq$ 170kips/in for members in moderate exposure conditions

$\leq$ 130kips/in for members in severe exposure conditions ***(LRFD 5.7.3.4)***

2.3.2.4 <u>Summary of the Design Procedures</u>

A summary of the design procedures of the typical girder bridge deck is shown in Table 2.3.

Table 2.3. Bridge Deck Design Procedures

AASHTO LFD	**AASHTO LRFD**	**MODOT**	**NOTES**
Step1: Choose general parameters	Step1: Choose general parameters	Step1: Choose general parameters	***MoDOT***: 8.5in. for C.I.P
Step 2: Compute effective span length	Step 2: Compute effective span length	Step 2: Compute effective span length	
Step 3: Compute moment due to dead load	Step 3: Determine unfactored dead load	Step 3: Determine moment over interior support	**1.** ***LFD***: $M_{LL} = 0.8 * \left(\frac{S+2}{32}\right) P$; ***LRFD***: Based on structural analysis. Loads are applied to a continuous 1-ft-wide beam spanning across the girder. Wheel load= 16 kips/W, where W is the width of primary strip. **2.** ***LFD***: $I = \frac{50}{L+125} \le 0.3$; ***LRFD***: IM=0.33 **3.** ***LFD***: $M_u = 1.3(M_{DL}+1.67M_{LL+I})$; ***LRFD***: $M_u = \eta_i[\gamma_{DC}(M_{DC}) + \gamma_{DW}(M_{DW}) + (m)(1+IM)(\gamma_{LL})(M_{LL})]$
Step 4: Compute moment due to live load + impact	Step 4: Determine unfactored live load	Step 4: Determine cantilever moment	
Step 5: Compute factored bending moments	Step 5: Calculate unfactored moments	Step 5: Determine design moments	
	Step 6: Determine the load factors		
	Step 7: Calculate factored moments		
Step 6~10: Determine reinforcement in details (main reinforcement, bottom distribution reinforcement, shrinkage and temperature reinforcement, reinforcement over supports	Step 8: Determine reinforcement in details	Step 6~10: Determine reinforcement in details	**1.Temperature reinforcement:** ***AASHTO***: $A_S \ge 1/8$ $spacing \le 3 \times h_{slab} \le 18''$. ***MODOT***: #5 @ 15” **2. Negative reinforcement over support:** ***AASHTO***: $A_S \ge 0.01 A_g$ ***MODOT***: #6 @ 5” between # 5 bars **3. Cover** ***AASHTO***: 2.5” for exposing to deicing salts. ***MODOT***: 3” for C.I.P
Step 11: Check serviceability	Step 9: Check serviceability	Step 11: Check serviceability	

Table 2.4 MoDOT LFD and MoDOT LRFD Bridge Design Procedures

<table>
<tr><th>MODOT LFD</th><th>MODOT LRFD</th><th>NOTES</th></tr>
<tr><td><u>Step1</u>: Choose general parameters</td><td><u>Step1</u>: Choose general parameters</td><td></td></tr>
<tr><td><u>Step 2</u>: Compute effective span length</td><td><u>Step 2</u>: Compute effective span length</td><td></td></tr>
<tr><td><u>Step 3</u>: Determine moment over interior support</td><td><u>Step 3</u>: Determine unfactored dead load</td><td rowspan="5">1. LFD: $M_{LL} = \frac{S+2}{32}P$;
LRFD: Based on structural analysis and separate into continuous slab case and discontinuous slab case:
Continuous Slab
Positive: E_{Cont} =26+6.6S
Negative: E_{Cont}=48+3.0S (S is the center to center of the supporting components)
M_{LL} refer to AASHTO LRFD.
Discontinuous Slab
$E_{Discont}$=0.5XE_{Cont} + dist. between transverse edge of slab and edge of beam if any
$M_{LL+IM-Discont.} = M_{LL+IM-Cont}\left(\frac{IM_{Discont}}{IM_{Cont}}\right)\left(\frac{E_{Discont}}{E_{Cont}}\right)$
2. LFD: $I = \frac{50}{L+125} \le 0.3$;
LRFD: IM=0.33
3. LFD: M_u= 1.3(M_{DL}+1.67M_{LL+I});
LRFD:
$M_u = \eta_i[\gamma_{DC}(M_{DC}) + \gamma_{DW}(M_{DW}) + (m)(1+IM)(\gamma_{LL})(M_{LL})]$</td></tr>
<tr><td><u>Step 4</u>: Determine cantilever moment</td><td><u>Step 4</u>: Determine unfactored live load</td></tr>
<tr><td><u>Step 5</u>: Determine design moments</td><td><u>Step 5</u>: Calculate unfactored moments</td></tr>
<tr><td></td><td><u>Step 6</u>: Determine the load factors</td></tr>
<tr><td></td><td><u>Step 7</u>: Calculate factored moments (including both interior section and overhang)</td></tr>
<tr><td><u>Step 6~10</u>: Determine reinforcement in details</td><td><u>Step 8</u>: Determine reinforcement in details</td><td><u>1.Temperature reinforcement:</u>
LFD: #5 @ 15”LRFD: $spacing \le 3 \times slab \le 18''$
and $A_s \ge \frac{0.11A_g}{f_y}$, where A_g=gross area of slab section
<u>2. Negative reinforcement over support:</u>
LFD: #6 @ 5” between # 5 bars
LRFD: Min= #5 bars @7.5”cts between temp. bars
Max= #8 bars@ 5” cts between temp. bars</td></tr>
<tr><td><u>Step 11</u>: Check serviceability</td><td><u>Step 9</u>: Check serviceability</td><td></td></tr>
</table>

2.4 DUCTILITY REALTED ISSUES FOR FRP REINFORCED CONCRETE

Ductility is a design requirement in most civil engineering structures and is mandated by most design codes. In steel reinforced concrete structures, ductility is defined as the ratio of deflection (or curvature) values at ultimate to deflection (or curvature) at yielding of steel. Due to the linear-strain-stress relation of FRP bars, the traditional definition of ductility can not be applied to the structures reinforced with FRP reinforcement. Thus, there is a need for developing a new set of ductility indices to both quantitatively and qualitatively evaluate the FRP reinforced structures. Furthermore, some design guidelines could be developed for FRP reinforced structures to make their performances comparable to the traditional steel reinforced structures.

Ductility calculation related to FRP reinforced structures has been widely studied. Two approaches have been proposed in the literature to address this problem.

2.4.1 Deformation Based Approach

The deformation based approach was first introduced by Jaeger et al. (1995). It takes into account the increase of moment as well as the increase of deflection (or curvature). Both the moment factor and the deflection (or curvature) factor are defined as the ratio of respective moment or deflection (or curvature) values at ultimate to the values corresponding to a concrete compressive strain of 0.001.

Deformability factor= moment factor × deflection (or curvature) factor

Moment factor= (moment at ultimate)/ (moment at concrete stain of 0.001)

Deflection factor= (deflection at ultimate)/ (deflection at concrete strain of 0.001)

2.4.2 Energy Based Approach

Based on the energy definition, ductility may be defined as the ratio between the elastic energy and the total energy, as shown in Figure 2.2.

Naaman and Jeong (1995) proposed the following equation to compute the ductility index, μ_E:

$$\mu_E = \frac{1}{2}\left(\frac{E_t}{E_e} + 1\right)$$

where E_t is the total energy computed as the area under the load deflection curve and E_e is the elastic energy. The elastic energy can be computed as the area of the triangle formed at failure load by the line having the weighted average slope of the two initial straight lines of the load deflection curve, as shown in Fig. 2.2.

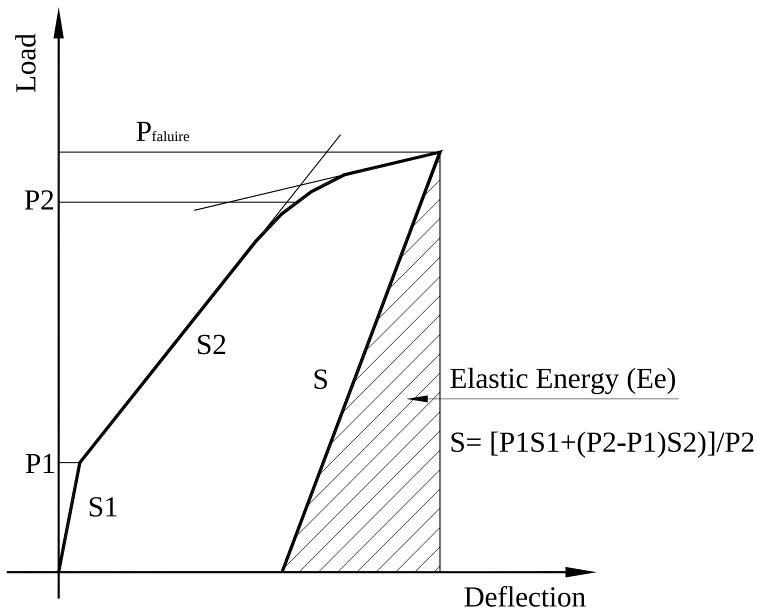

Figure 2.7: New Definition of Ductility Index (Naaman and Jeong, 1995)

Spadea et al. (1997) suggested that the ductility index be expressed as:

$$\mu_E = \frac{E_t}{E_{0.75pu}}$$

where E_t is the total energy computed as the area under the load deflection curve and $E_{0.75pu}$ is the area under the load-deflection curve up to 75% of the ultimate load.

Vijay and GangaRao (2001) introduced DF, which is a unified approach to account for ductility deflection and crack width in the form of energy absorption. The DF is defined as the ratio of energy absorption at ultimate to energy absorption at a limiting curvature value. The limiting value of curvature is based on the serviceability criteria of both deflection and crack width (hence, unified) as specified by ACI 318/318R-99 as follows:

- The serviceability deflection limit of span/180 (ACI 318/318-99) and
- The crack width limit of 0.016in. (ACI 318/318R-99).

Based on experimental data, Vijay and GangaRao determined that the maximum unified curvature at a service load that satisfies both deflection and crack width serviceability limits should be limited to 0.005/d radians/in., where d is the effective depth.

With the addition of fibers, the toughness of concrete will be increased. Thus, a noticeable increase in the energy absorption capacity of the whole system is expected. In this report, the energy-based approach will be adopted to study the ductility characteristics of this FRP/FRC hybrid system.

3. DETAILS OF THE EXPERIMENTAL PROGRAM

3.1 INTRODUCTION

This chapter includes descriptions of the objectives, scope and details of the various components of the exhaustive experimental investigation. The overall objective of the experimental program is to better understand the static and fatigue behaviors of nonferrous hybrid reinforced concrete comprising continuous FRP reinforcing bars and discrete randomly distributed polypropylene fibers. The various tests have been logically grouped into five classes including: (1) tests to establish constituent material properties (2) static and fatigue tests to characterize bond performance; (3) static and fatigue tests to characterize flexural ductility response; (4) accelerated durability tests of the hybrid system; and (5) static and fatigue tests on full-scale hybrid reinforced composite bridge decks.

3.2 TESTS FOR CONSTITUENT PROPERTIES

3.2.1 Tensile Response of Reinforcing Bars

Nine FRP reinforcing bars, 3 - #4 GFRP (nominally ½ inch diameter), 3 - #8 GFRP (nominally 1 inch diameter), and 3 - #4 CFRP (nominally ½ inch diameter), were used in the program to obtain the tensile response of FRP reinforcing bars . A 5 in. Shaevitz 3002 XS-D LVDT was used to measure displacement in each specimen over a gage length of 9 in. for the #4 CFRP and GFRP bars and a 5 in. gage length for the #8 GFRP bar. A Riehle 300 kip hydraulic machine was used to load each specimen quasi-statically until failure. The test was controlled using a custom-built LabView program. Data was acquired for ram displacement, load, and LVDT displacement.

Each specimen consisted of the FRP bar embedded at the ends in steel tubes that served as tensile grips. These tubes were bonded to the FRP using expansive cement. The steel tube-ends allowed the 300 kip hydraulic testing machine to grip the FRP without crushing the FRP bars. FRP bars cannot be gripped directly because of it’s low lateral strength. Figure 3.1 shows the steel tube grips at the ends of a GFRP bar.

Figure 3.1 GFRP Tensile specimen with bonded steel tubes for gripping

After the LVDT was in place, the specimen was loaded in a 300 kip universal testing machine using two sets of wedge grips. These grips grabbed the steel tubing at the ends of the specimen and held the specimen in place for testing. A close up view of the specimen loaded into the 300 kip machine can be seen in Figure 3.2. Results from the constituent materials tests are summarized in Appendix I.

Figure 3.2 CFRP Tensile specimen in the test fixture showing gripping and displacement measurement details

3.2.2 Compressive Response of the Concrete and Fiber Reinforced Concrete Matrix

MoDOT high performance concrete bridge deck mixture (MB2) with a 28-day design strength specified at 5,000 psi was used for all the specimens in the test program. The mixture was adjusted to incorporate 0.5% by volume of 2 in. long fibrillated randomly distributed polypropylene fibers. The fibrous matrix as observed later in the next several chapters greatly enhances the post-cracking strength and toughness of the concrete. The addition of fibers also has the tendency to lower the compressive strength as a result of significantly larger air-contents. The air content in fiber mixes for actual bridge deck placement needs to be controlled by significantly reducing the use of additional air entraining admixtures. Table 3.1 includes the basic design mixture used for the test program. However, since the specimens for the exhaustive experimental program had to be made in approximately 9 different castings using concrete from a local ready-mix company, the actual mixtures were somewhat different from the design mixture (due to practical variations in constituent properties over the extended fabrication period and practical constraints in maintaining very strict control on quality of concrete supplied).

Table 3.1 Details of the basic concrete mixture design used

Batch weights per cubic yard of concrete	
Cement (Type I)	550 lbs.
Fly ash (Class C)	100 lbs.
State rock (MoDOT Gradation D used for bridge decks)	1,820 lbs.
Sand (MoDOT Class C)	1,150 lbs.
Water	29 gal.
Superplasticizer (slump of 3-4 in. for plain and fiber concrete mixes)	varies
Air entraining agent	8 oz.

The target slump was 3 in. for plain and fiber concrete mixes (with a maximum acceptable slump of 4.5 in.). The unit weights typically obtained with the lime-stone aggregates used ranged from 142-148 lb/ft^3. Even while the air content was specified as 5 ± 2%, some of the fiber mixtures had as much as 10% air which resulted in lower compressive strengths. This also reduced the unit weight of some of the fiber mixes to approximately 130 lb/ft^3.

Two test configurations were used for compression tests. Small 4 in. (diameter) x 8 in. (length) cylinders were tested in a closed-loop machine to obtain the complete stress-strain response and standard 6 in. (diameter) x 12 in. (length) were tested in a open-loop configuration typically used by most commercial testing labs for obtaining strength and elastic modulus information. Six of each size of specimens was made with each casting using disposable plastic molds. Due to the extended time period of the various test programs, compression tests were conducted at several ages. In some instances where test results at 28-days were unavailable due to scheduling and logistical problems, projected 28-day strength values are reported

A 110-kip MTS servo-controlled testing machine was used for conducting these closed-loop tests (Figure 3.3) on the 4 in. cylinders. The test was controlled using circumferential strain as the feedback parameter. The confining influence of fibers could then be established from the complete stress-strain response of the concrete and fiber concrete specimens and appropriate analytical models of confined concrete. Three LVDTs mounted 120º apart along the circumference over a 6 in. gage length allowed monitoring of average axial strains during the test. A load-cell was used to monitor the compressive load applied during the tests. PC-Based data acquisition system using a custom-written LabView program was used to record the data for later analysis.

Figure 3.3 Overall view (left) and a close-up view of the closed-loop compression test

A Forney 600-kip compression testing machine was used for the tests on 6 in. cylinders (Figure 3.4). Three LVDTs mounted 120º apart along the circumference over a 10 in. gage length allowed monitoring of average axial strains during the test. A load-cell was used to monitor the compressive load applied during the tests. PC-Based data acquisition system using a custom-written LabView program was used to record the data for later analysis.

Figure 3.4 Compression test on standard 6 in. diameter cylinders

Results from the compression tests are summarized later in Appendix I.

3.3 STUDIES ON BOND PERFORMANCE

Interface bond between the reinforcing bar and the concrete matrix is among one of the important that governs the mechanical behavior and type of failure in reinforced concrete. Three test configurations are commonly used to study the bond characteristics: namely, pullout test, splitting bond test, and flexural beam test.

The pullout test simulates anchorage stress behavior and is popular because of the fundamental nature of the associated analysis required. Although in some pull-out test configurations, the test puts concrete in compression and the reinforcing bar in tension, a stress condition that is not representative of an RC beam or bridge deck, a reasonable correlation has been observed between structural performance and measures of performance in the pullout test (Cairns and Abdullah, 1995).

The splitting bond test can be used to study the splitting bond behavior for different concrete cover thicknesses. The effect of the transverse reinforcement on bond behavior can be avoided when properly designed. The splitting bond test simulates the realistic stress field observed at beam-ends even if analysis of actual stress field is complicated by the multiaxial nature of stress in this region.

The flexural bond test has the advantage of representing the actual stress field in real beams and slabs and the cover effects on bond. However, it requires considerable confining reinforcement to avoid a shear failure, and so bond-splitting failures may not occur (Cairns and Plizzari, 2003). Even while each of the three test configurations described have respective merits and drawbacks, collectively the bond information obtained, as in this test program, is valuable to understand the overall flexural performance of the hybrid reinforced deck slab system.

3.3.1 Pull-Out Bond Test

3.3.1.1 <u>Experimental Program</u>

The objectives of this component of the test program are to: (1) study the bond-slip response of the hybrid reinforced specimen by the pullout test method; (2) investigate the effect of fibers on bond performance, and (3) investigate the effect of static and fatigue loading on bond performance.

A total of 45 pullout specimens were studied. The experimental variables included FRP rebar type (CFRP and GFRP), FRP rebar size (#4 and #8), concrete with and without polypropylene fibers, embedment length, and loading conditions (static or fatigue). The scope of the pull-out test program is outlined in Table 3.2.

The notation for specimens is as follows: the first character indicates the matrix type (“P” for plain concrete and “F” for fiber reinforced concrete); the second character denotes the rebar type, (“C” for CFRP and “G” for GFRP); the third character is the bar size (#4 or #8 representing appropriate nominal bar diameter per standard US designation); the fourth character refers to the embedment length in multiples of the bar diameter d_b (05 or 10); the last character represents the loading type (“M” for monotonic static or “F” for fatigue).

Table 3.2 Details of pullout test program

Loading Conditions	Specimen I.D.	Materials	V_f (%)	l_d/d_b
Plain Monotonic	PC405M	#4 CFRP	0	5
	PG405M	#4 GFRP	0	5
	PG805M	#8 GFRP	0	5
FRC Monotonic	FC405M	#4 CFRP	0.5	5
	FC410M		0.5	10
	FG405M	#4 GFRP	0.5	5
	FG410M		0.5	10
	FG805M	#8 GFRP	0.5	5
	FG803M		0.5	3
Plain Fatigue	PC405F	#4 CFRP	0	5
	PG405F	#4 GFRP	0	5
	PG805F	#8 GFRP	0	5
FRC Fatigue	FC405F	#4 CFRP	0.5	5
	FG405F	#4 GFRP	0.5	5
	FG805F	#8 GFRP	0.5	5

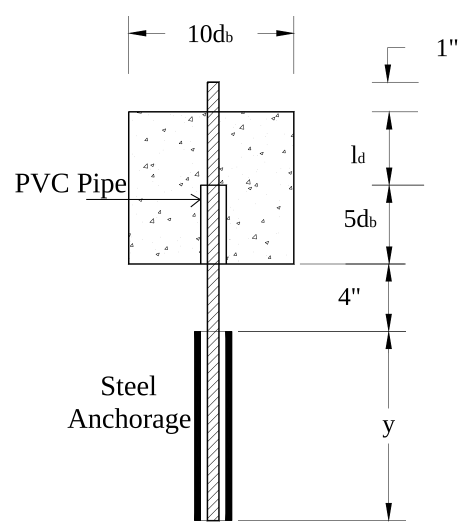

y=10" (14")for #4 (#8)specimens;

Figure 3.5. Pullout specimens

3.3.1.2 Test Specimens

Test specimens are designed according to RILEM recommendations with a 5 d_b embedment length (some with 10 d_b to study the effect of different embedment lengths).

FRP reinforcement bars are embedded in concrete to a predetermined length, l_d, in the concrete block. PVC pipe is used as a bond breaker at the first 5d_b length to minimize the restraint effect of the bottom plate on the rebar and to eliminate any undesirable confinement that may affect the bond characteristics. Figure 3.5 includes a schematic set-up for pullout test providing dimensional and other details.

3.3.2 Splitting Bond Tests

3.3.2.1 Experimental Program

The objectives of this component of the test program are to: (1) study the bond-slip response of the hybrid reinforced specimen using the splitting bond test configuration; and (2) investigate the cover depth effect on bond performance.

A total of 24 specimens were investigated under the splitting bond tests. The experimental variables include FRP rebar size (#4 and #8), concrete cover depth, and concrete with and without polypropylene fibers. Table 3.3 includes research scope of this component of the test program.

The notation for the specimens is as follows: the first character represents the bar size (#4 or #8 representing appropriate nominal bar diameter per standard US designation); the second character indicates the matrix type ("P" for plain concrete and "F" for fiber reinforced concrete); the third character denotes the rebar type, ("C" for CFRP and "G" for GFRP); the last character refers to the clear cover depth in multiples of the bar diameter, d_b (1 or 3).

3.3.2.2 Test Specimens

Specimens are designed based on ASTM A944 specifications. Specimens with a nominal rebar diameter of 0.5 in. (including #4 CFRP and #4 GFRP) had dimensions of 9 in. ×14 in. ×24 in.. Specimens with a nominal rebar diameter of 0.75 in. had dimensions of 9 in. ×17 in. ×24 in. PVC pipes were used to cover the two ends of the rebar being tested (to serve as bond breakers) so as to adjust the test embedment length to 10 d_b, as shown in Figure 3.6. Four closed stirrups were used to increase shear strength of the #8 GFRP specimens. The stirrups were oriented parallel, rather than perpendicular, to the side of the specimens to eliminate their effect on a splitting bond failure.

Table 3.3 Details of the splitting bond test program

Specimen I.D.	REBARS	Embedment length l_d (in.)	Volume fraction V_f (%)	Cover C_b (in.)
4PG1	#4GFRP	$10d_b=5$	0	$1d_b=0.5$
4PG3		$10d_b=5$	0	$3d_b=1.5$
4FG1		$10d_b=5$	0.5	$1d_b=0.5$
4FG3		$10d_b=5$	0.5	$3d_b=1.5$
4PC1	#4CFRP	$10d_b=5$	0	$1d_b=0.5$
4PC3		$10d_b=5$	0	$3d_b=1.5$
4FC1		$10d_b=5$	0.5	$1d_b=0.5$
4FC3		$10d_b=5$	0.5	$3d_b=1.5$
8PG1	#8GFRP	$10d_b=10$	0	$1d_b=1$
8PG3		$10d_b=10$	0	$3d_b=3$
8FG1		$10d_b=10$	0.5	$1d_b=1$
8FG3		$10d_b=10$	0.5	$3d_b=3$

Note: Each series has two replicate specimens.

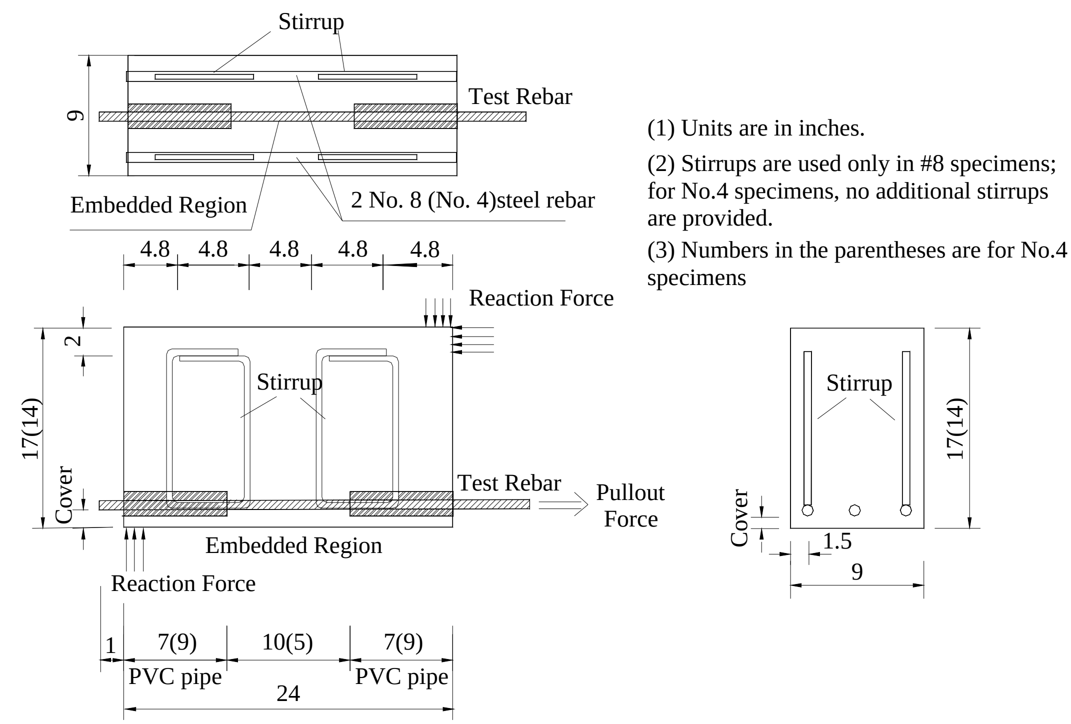

Figure 3.6. Splitting bond specimen configuration

This kind of specimen is not representative to duplicate the testing of bond strength in bridge deck systems, where no stirrups are usually used. Steel bars were also used as auxiliary flexural reinforcement (two #4 steel bars were used in #4 specimens and two #6 steel bars for #8 specimens) to increase the flexural capacity of the specimens, so that the failure of the specimens would be controlled by bond. The specimens also contained two transverse #5 steel rebars for ease of fabrication and testing.

3.3.3 Flexural Bond Tests

3.3.3.1 <u>Experimental Program</u>

A total of 56 specimens were tested for studying the flexural bond. The experimental variables include FRP rebar type and size (#4 GFRP, #4 CFRP and #8 GFRP), concrete matrix (with or without polypropylene fibers), bonded length (10 d_b versus 20 d_b), fatigue stress level (upper limit fatigue stress of 60% and 80% of nominal static strength). Static tests were conducted on all three types of FRP bars while fatigue tests were limited to #4 CFRP and #8 GFRP bars to reduce the number of tests required. Table 3.4 includes details of the test program involving flexural bond tests.

The specimen identification numbers for the flexural bond tests are made up of 6 characters. The first character represents the concrete matrix type (fiber mixes are denoted with "F" and plain concrete mixes are denoted with "N". The second character describes the bar size of the FRP reinforcement (#4 or #8). The third character denotes the reinforcement material type ("G" for GFRP or "C" for CFRP). The fourth character denotes the bonded length with a 1 indicating that the bonded length is 10d_b and 2 indicating that the bonded length is 20d_b. The fifth character denotes the test type (Static –S, Low upper limit fatigue stress level –L, High upper limit fatigue stress level H. The final character represents the specimen number (1 or 2 as two replicate tests were completed for each series)

3.3.3.2 <u>Test Specimens</u>

Specimens were constructed in wooden molds as shown in Figure 3.7. A schematic of the flexural bond test specimen is shown in Figure 3.8. The specimens measured 53 in. in length. A 1.5 in. gap in the middle of the beam split the specimen in two halves. The beams were 6 in. wide and 9.5 in. deep. The reinforcement was placed 1.5 in. from the bottom of the beam (measured from the centerline of the bar) and was horizontally centered.

Table 3.4 Details of the flexural bond test program

Matrix V_f (%)	Reinforcement Type	Bonded Length α	Test type	Specimen ID
0.0	#4 GFRP	10	Static	N4G1S1, 2
		20	Static	N4G2S1, 2
	#4CFRP	10	Static	N4C1S1, 2
			Low - Fatigue	N4C1L1, 2
			High - Fatigue	N4C1H1, 2
		20	Static	N4C2S1, 2
			Low - Fatigue	N4C2L1, 2
			High - Fatigue	N4C2H1, 2
	#8 GFRP	10	Static	N8G1S1, 2
			Low - Fatigue	N8G 1L1, 2
			High - Fatigue	N8G 1H1, 2
		20	Static	N8G 2S1, 2
			Low - Fatigue	N8G 2L1, 2
			High - Fatigue	N8G 2H1, 2
0.5	#4 GFRP	10	Static	F4G1S1, 2
		20	Static	F4G2S1, 2
	#4CFRP	10	Static	F4C1S1, 2
			Low - Fatigue	F4C1L1, 2
			High - Fatigue	F4C1H1, 2
		20	Static	F4C2S1, 2
			Low - Fatigue	F4C2L1, 2
			High - Fatigue	F4C2H1, 2
	#8 GFRP	10	Static	F8G1S1, 2
			Low - Fatigue	F8G 1L1, 2
			High - Fatigue	F8G 1H1, 2
		20	Static	F8G 2S1, 2
			Low - Fatigue	F8G 2L1, 2
			High - Fatigue	F8G 2H1, 2

Figure 3.7 Casting operations for the flexural bond specimens

A continuous reinforcing bar connected the bottom portions of the beam halves while the top portions of the beam halves were connected by a 1 in. hinge that allowed free rotation, but not vertical or horizontal displacements between the two halves of the test specimen. The FRP bars were de-bonded from the concrete matrix at each end of the two specimens-halves (Figure 3.8) using plastic sleeves that allowed for free movement of the bars through the unbonded regions. This assured precise prescribed length of the bonded interface. Specimens were constructed with bonded lengths of both $10d_b$ and $20d_b$ where d_b is the FRP bar diameter. During specimen construction, a 1.5 in Styrofoam block was used to separate the two beam halves.

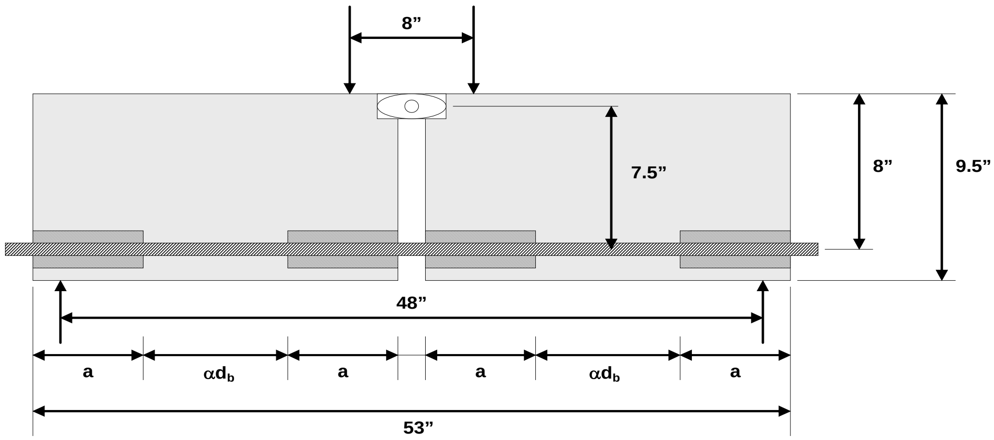

All measurements are in inches, α = 10 or 20 and d_b = bar diameter

Figure 3.8 Schematic of the flexural bond specimen

The rotary mechanism comprises two parts. The first is a steel angle with three 6 in. long steel rebar pieces welded to it for anchoring to the mechanism to the concrete beam-halves. The second part of the rotary mechanism is the steel hinge. During the casting process, transportation to the curing chamber and transportation to the loading machine it was not desirable for the rotary mechanism to be in place. This would result in loads being applied inadvertently to the specimen before the test program began. In order to stabilize the specimen during these times, a stiff steel plate was used in place of the steel hinge. The plate rigidly connected the two beam halves and did not allow rotation or translation at the midpoint of the beam. The plate stabilized the specimen until it was placed into the loading machine, at which time the plate was removed and the hinge was put in place.

3.3.3.3 Instrumentation and Test Procedures

Instrumentation for the flexural bond test included a load cell and four LVDTs. The load cell measured the applied load during the flexural bond tests. LVDTs were used to measure vertical deflection at the midspan of the beam (midspan LVDT), crack mouth-opening deflection (CMOD LVDT) in the longitudinal direction, and rebar end slip at the ends of the specimen (north end slip and south end slip LVDT). The distance between load points was 8 in. and the distance between support points was 48 in. The distance between the centerline of the hinge and the centerline of the FRP reinforcement was 7.5 in.

The midspan LVDT measured the deflection of an aluminum plate bonded to the underside of the specimen. For mounting the CMOD LVDT, two aluminum plates were bonded to the inside of the beam opening. One plate was drilled and tapped, into which the LVDT was fixed. The other plate provided the contact surface for the LVDT core. Figure 3.9 shows a detail of the midspan and CMOD LVDTs.

The north and south end slip LVDTs were attached to the end of the reinforcing bar, which extended 1.5 in beyond the edge of the concrete. Figure 3.10 details the end slip LVDT configuration.

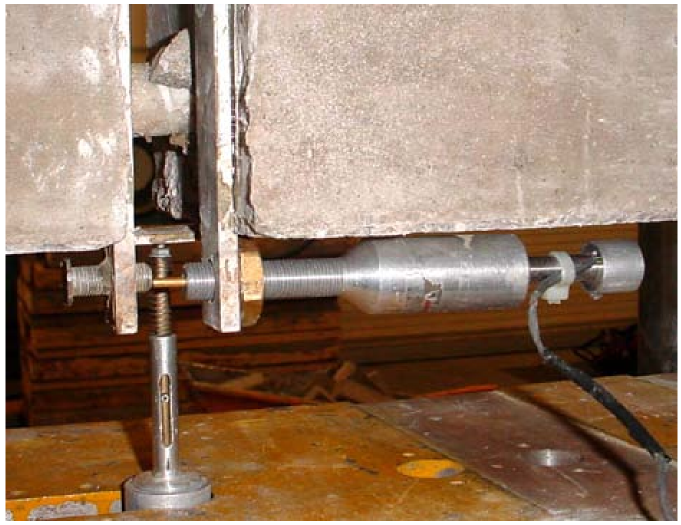

Figure 3.9 Close-up photograph of midspan deflection and CMOD LVDTs

Figure 3.10 Close-up photograph of end-slip LVDT

A 100-kip load cell was used to measure the applied load during the tests. Static tests were ram displacement controlled with a loading rate of 0.00025 in/sec. Fatigue tests were load controlled and ran in two stages. The specimen was subjected to fast cyclic loading at a rate of 5 Hz for 40 minutes (12,000 cycles). Every 12,000 cycles, the loading rate was slowed to 0.1 Hz for 50 seconds (5 cycles). The slow loading rate allowed for more specific monitoring of the specimen than what is possible at the 5 Hz loading rate. The cycle was repeated 100 times (presuming failure had not occurred by that point) for a total of 1.2 million cycles. If the specimen survived the fatigue loading program, it was then loaded statically to failure. Fatigue tests load limits were defined as a percentage of ultimate static strength of the specimen. Tests were run at a low-end limit of 5% - 65% of ultimate and a high-end limit of 5% - 85% of ultimate. Figure 3.11 shows the test setup used for the flexural bond tests.

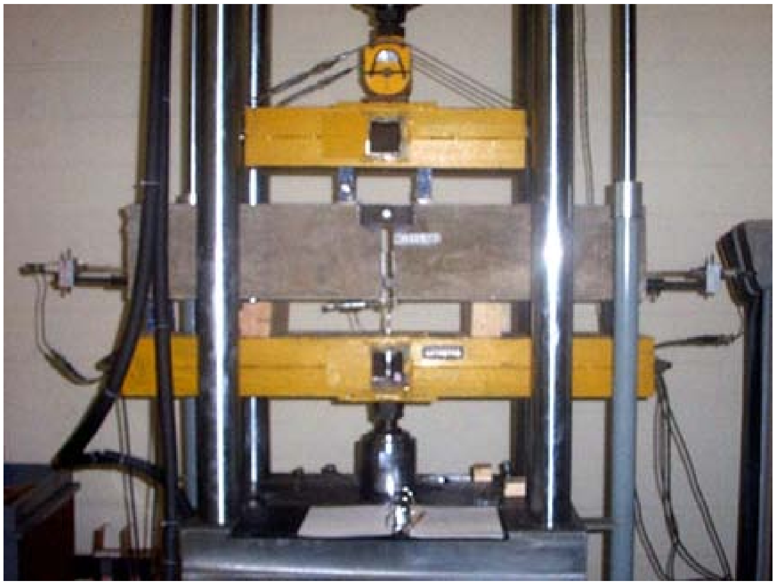

Figure 3.11 Test setup used for the flexural bond test

3.4 STUDIES ON FLEXURAL DUCTILITY RESPONSE

Ductility is a structural design requirement in most design codes. In conventional steel reinforced concrete systems ductility is often defined as the ratio of ultimate post-yield deformation at ultimate capacity to yield deformation. Traditional definitions of ductility used for steel reinforced concrete such as this is obviously not suited for application in FRP reinforced concrete primarily because of the limited inelastic post-cracking response. There is need for a better characterization of ductility requirement in such reinforcement systems that exhibit elastic-brittle constituent behavior. With the addition of fibers as used in this investigation, the post-cracking response of concrete is significantly enhanced. Thus, an increase in the ductility of the hybrid system is expected.

Three different types of beam geometries were used for the ductility studies. Two sets ensured flexural failure and were tested at UMR. These are denoted Beam Types 1 and Type 2, respectively. The third set had a shear dominant failure mode such as one would expect in a bridge deck slab (without shear reinforcement). These beams designated Type 3 flexural beams were tested at UMC. Types 1 and 2 beams were tested under static loading whereas Type 3 beams were tested under static and fatigue loading.

A total of twelve Type 1 beams were tested in this study. During the ductility study, several issues were investigated, including mid-span displacement, curvature, crack width, crack distribution, and ultimate capacity. Also, the energy absorption capacity of this hybrid system was studied by loading/unloading at load level of 45% and 90% of its capacity.

Type 2 beams were 7 in. wide, 9 in. high, and 80 in. long. To avoid shear failure, traditional #3 steel U-shape stirrups with spacing of 3.5 in. were used as shear reinforcement. To minimize the shear reinforcement's confining effect on the flexural behaviors, no stirrups were used at the testing regions (pure bending regions). A 1.5 in. concrete clear cover was used for all the beams. All beams were designed to fail by concrete crushing, which was recommended by the current ACI 440 document. This was accomplished by using reinforcement ratio greater than the balanced reinforcement ratio, ρ_b.

Type 2 beams were also subjected to a four-point flexural testing. These beams were instrumented with three LVDTs at the testing region (pure bending region) to monitor the mid-span deflection and curvature. FRP reinforcing bars were installed with stain gauges to measure deformation. Two LVDTs with high resolution were mounted at the top surface of the beam to record the concrete strain. In the testing region, Demec gages were bonded to the beam surface 1.5 in. above the bottom (the same level as the longitudinal reinforcing bars) to measure the crack widths. A microscope was also used to measure the crack width. Load was applied in stages by hydraulic jacks and measured with a load cell. Three stages were taken up to the initiation of cracking and ten steps up to failure. At the end of each step, the load was held constant and crack patterns were photographed, and near mid-span crack widths were measured.

A total of twenty-eight Type 3 beams were tested (twelve under static loading and the rest subjected to fatigue loading). Four-point bending configuration was used for these beam tests. Load, midspan deflection, end slip were measured using automated data acquisition system in both the static and fatigue load tests. Fatigue tests were conducted using 5 Hz sinusoidal constant amplitude loading. The lower limit fatigue load was fixed at a stress level equal to 10% of the static strength. Two different upper limit fatigue stress levels were studied (60% and 80% of static strength). Specimens that did not fail after the limiting fatigue cycles of 1 million, were tested to failure in a static mode of loading and compared to similar static tests on virgin specimens.

Type 3 beams were 6 inches wide, 9.5 inches deep and 56 inches long. The effective reinforcement depth was 8 inches. The outer span in the four-point flexural configuration was 48 inches and the inner span was 16 inches. This geometry allowed a shear span to effective depth ratio of 2 which makes the failure shear dominant.

3.4.1 Flexure-Sensitive Beam Specimens (Type 1 and 2 beams)

Issues with regard to flexural behavior are addressed, including mid-span deflection, curvature, crack width, crack distribution, and relative slip of the longitudinal rebar from the concrete. The energy absorption capacity of the hybrid reinforcement system was studied by loading/unloading at load level of 45% and 90% of its ultimate capacity. The residual deflection and crack width caused by the loading/unloading cycles are also discussed.

A total of 12 beams with 6 testing groups were tested. The experimental variables included FRP rebar size (#4 or #8) and concrete with and without polypropylene fibers. The details of the specimens are shown in Table 3.5.

The notation for the specimens is as follows: the first character V means the virgin specimens without subjecting accelerated environmental tests; the second character, "P" or "F", indicates the plain concrete or FRC; the third character is the rebar diameter US designation; the fourth character, "C" or "G", indicates the rebar type, CFRP or GFRP, and the last character represents the first beam or the second beam in the testing group;

3.4.1.1 <u>Experimental Program and Test Specimens</u>

The beams were 7 inches wide, 9 inches high and 80 inches long. Each testing group included two identical beams. To avoid shear type of failure, traditional #3 steel rebars with spacing of 3.5 inches were used as shear reinforcement. To minimize the shear reinforcement's confining effect on the flexural behaviors, no stirrups were used at the testing regions (pure bending regions). A concrete clear cover of 1.5 inches was used for all the beams. All beams were designed to fail in concrete crushing, which is recommended in the current ACI 440. This was accomplished by using a reinforcement ratio greater than the balanced reinforcement ratio ρ_b. Specimen details are shown in Figure 3.12.

Table 3.5 Flexural ductility test specimens

I.D.	f`c (psi)	A_f (in^2)	ρ_f/ρ_{fb}	V_f (%)
VP4G-1	7000	5#4=1.12	3.51	0
VP4G-2	7000	5#4=1.12	3.51	0
VP8 G-1	7000	2#8=1.67	3.6	0
VP8G-2	7000	2#8=1.67	3.6	0
VP4C-1	7000	2#4=0.34	3.16	0
VP4C-2	7000	2#4=0.34	3.16	0
VF4G-1	4400	5#4=1.12	4.71	0.5
VF4G-2	4400	5#4=1.12	4.71	0.5
VF8 G-1	4400	2#8=1.67	4.83	0.5
VF8G-2	4400	2#8=1.67	4.83	0.5
VF4C-1	4400	2#4=0.34	4.24	0.5
VF4C-2	4400	2#4=0.34	4.24	0.5

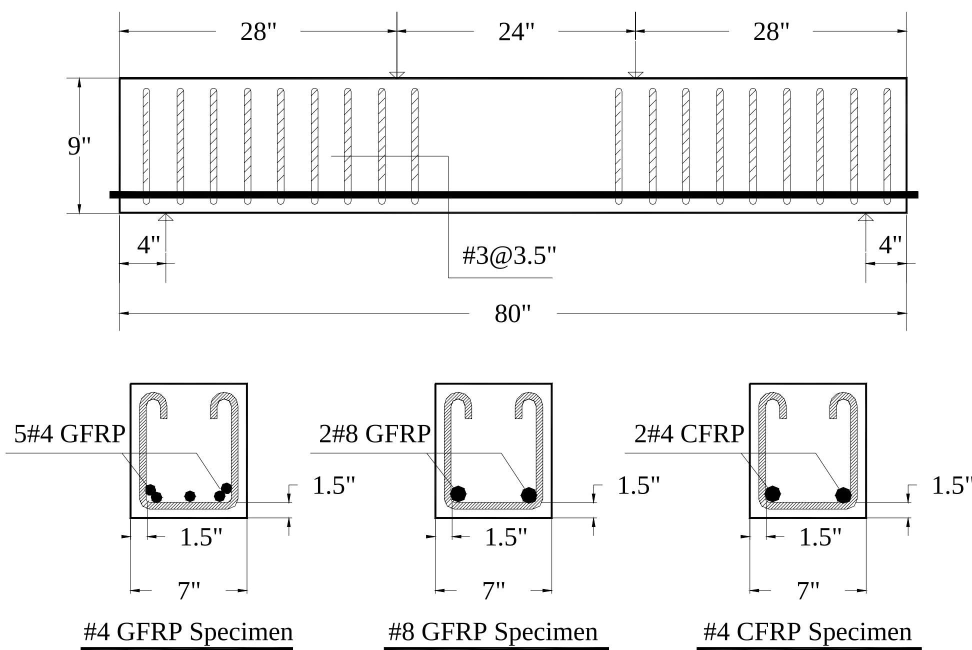

Figure 3.12. Beam details

3.4.2 Shear Sensitive Beam Specimens (Type 3 beams)

3.4.2.1 Experimental Program and Test Specimens

Type 3 beams were all 6 in. wide and were tested according to the experimental program included in Table 3.4. Other geometric details of the Type 3 beams are included in Figure 3.13. Half of the beams were plain concrete and half included 0.5% by volume polypropylene fibrillated fibers in the concrete mix. Two of the cured beams, for each type of beam, were first tested under quasi-static displacement controlled loading to determine the initial strength and stiffness properties. The fatigue tests were load controlled test that continued over a period of 1.2 million cycles. Two beams were tested at the low upper limit fatigue stress level (termed “low fatigue”) and two beams were tested at high upper limit fatigue stress level (termed “high fatigue”). During the low fatigue tests the specimens were loaded to 60% of the ultimate strength of that type of beam as determined by the previous static tests. The value of 60% was chosen because under current load and resistance factor design criteria for steel reinforced concrete, the design service loads are typically close to 60% of the final design strength. During the high fatigue tests, the specimens were loaded to 80% of their ultimate strength. These tests were performed to determine what, if any, fatigue capacity the specimens may have had at high levels of repetitive loading.

There were three reinforcement type tested in the experimental process and each type was tested with and without the additional of 0.5% by volume fibrillated polypropylene fibers. The types of beams were differentiated based on the type and amount of FRP flexural reinforcement included. The reinforcement ratios and number of bars for each type of beam are indicated in Table 3.4. All reinforcement ratios are reported in terms of the balanced reinforcement ratio.

Table 3.6 Experimental program for Type 3 beam test

I.D.	Test type	A_f (in^2)	ρ_f / ρ_{fb}	V_f (%)
N4GS1 N4GS2	Static	0.449	1.61	0.0
N4GL1 N4GL2	Low	0.449	1.61	0.0
N4GH1 N4GH2	High	0.449	1.61	0.0
N4CS1 N4CS2	Static	0.336	1.96	0.0
N4CL1 N4CL2	Low	0.336	1.96	0.0
N4CH1 N4CH2	High	0.336	1.96	0.0
N8GS1 N8GS2	Static	0.834	2.99	0.0
N8GL1 N8GL2	Low	0.834	2.99	0.0
N8GH1 N8GH2	High	0.834	2.99	0.0
F4GS1 F4GS2	Static	0.449	1.61	0.5
F4GL1 F4GL2	Low	0.449	1.61	0.5
F4GH1 F4GH2	High	0.449	1.61	0.5
F4CS1 F4CS2	Static	0.336	1.96	0.5
F4CL1 F4CL2	Low	0.336	1.96	0.5
F4CH1 F4CH2	High	0.336	1.96	0.5
F8GS1 F8G S2	Static	0.834	2.99	0.5
F8G L1 F8G L2	Low	0.834	2.99	0.5
F8G H1 F8G H2	High	0.834	2.99	0.5

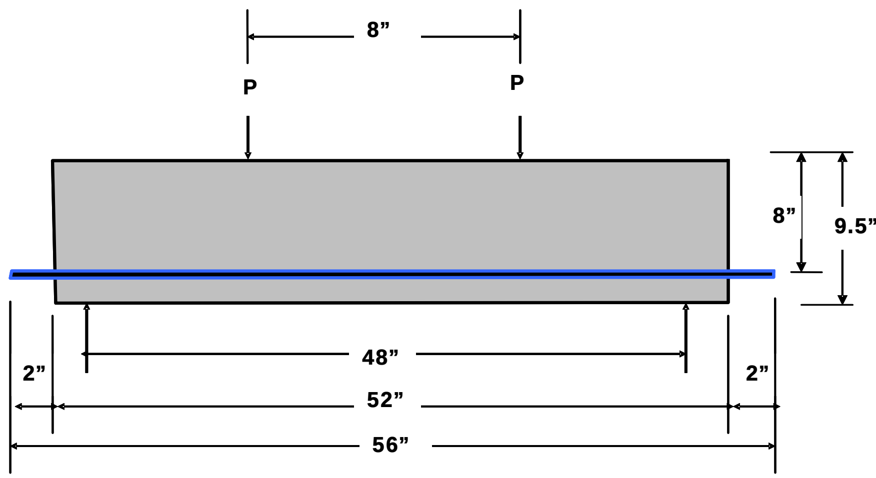

Figure 3.13 Geometric details of the shear-sensitive beam (Type 3 Beam)

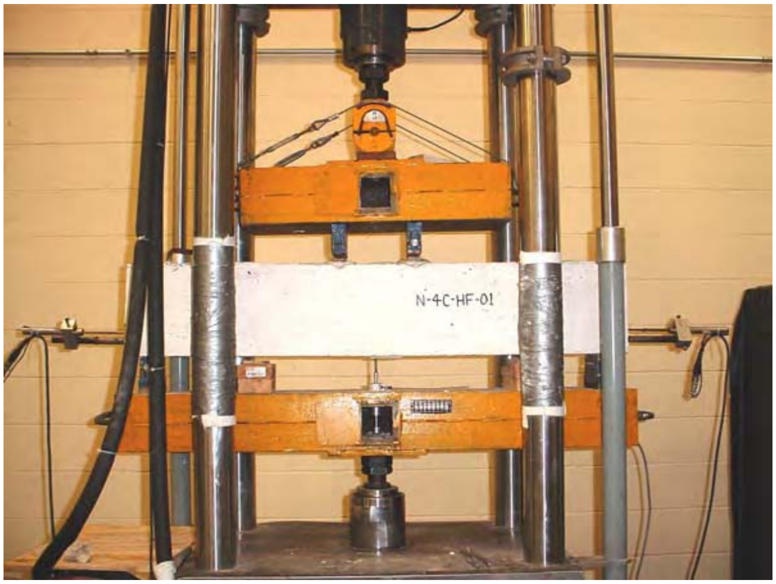

Figure 3.14 Set-up showing Type 3 beam in the test fixture

3.4.2.2 <u>Instrumentation and Test Procedures</u>

During the beam tests, load, rebar end slip, mid-span deflection, and ram deflection data were all recorded. Figure 3.14 shows the test setup including associated instrumentation.

Data were recorded using a customized LabView program and associated PC based data acquisition system. The tests were conducted on a servo-controlled testing machine using a 220 kip hydraulic actuator. Ram deflection was recorded using an integral linear variable displacement transducer (LVDT). Rebar end slip was recorded through two LVDT mounted at the ends of the rebar which protruded 2 in. outside of the specimens (Figure 3.14). Mid-span deflection was also monitored with an LVDT. Load was measured using a strain-gage based 100 metric ton load cell. An additional LVDT was used for the direct measurement of the specimen mid-span deflection.

3.5 STUDIES ON DURABILITY CHARACTERISTICS

Composite materials offer many advantages, such as corrosion resistance, and their use in bridge decks has become more technically attractive and economically viable. However, long-term performances have to be clearly understood with confidence before its application in the field. The objectives include:

- To investigate bond degradation for the FRP/FRC hybrid system
- To propose a reduction coefficient accounting for the environmental effect on the bond strength of the FRP/FRC system
- To investigate flexural degradation for the FRP/FRC hybrid system
- To propose a reduction coefficient to account for the environmental effect on the flexural behavior of the FRP/FRC system

3.5.1 Bond Specimens

3.5.1.1 <u>Experimental Program and Test Specimens</u>

Dimensions of test specimens were the same as the specimens described earlier. Chemical agents will attack the reinforcing materials as well as the bond between the concrete and reinforcing materials. In RC structures, cracks exist under service conditions. The degradation effect is expected to be more pronounced at the places where cracks exist. In most cases, cracks develop at the places with high stress levels (the loaded end), and concrete is intact at low stress level (the free end). To better simulate the real situations, the portion at the loaded end of the bond specimens was directly exposed to salt water, while the portion at the free end was coated with waterproof epoxy to protect it from direct attack from salt water. Since the epoxy could induce unwanted mechanical anchorages and thereby change the bond behavior when rebar being pulled out, all the epoxy that stuck to the rebar was removed before bond tests.

The notation for specimens is as follows: the first character, "V" or "D", means the virgin specimen or durability specimen; the second character, "P" or "F", indicates the plain concrete or FRC, the third character (#4 vs. #8) is the bar size in US designation, and the fourth character, "C" or "G", indicates the rebar type, CFRP or GFRP; Specimen details are shown in Table 3.7.

Table 3.7 Durability testing for bond performance

Specimen I.D.*	Number of Specimens	Materials	V_f (%)	l_d/d_b
VP4C	3	#4 CFRP	0	5
VP4G	3	#4 GFRP	0	5
VP8G	3	#8 GFRP	0	5
VF4C	3	#4 CFRP	0.5	5
VF4G	3	#4 GFRP	0.5	5
VF8G	3	#8 GFRP	0.5	5
DP4C	3	#4 CFRP	0	5
DP4G	3	#4 GFRP	0	5
DP8G	3	#8 GFRP	0	5
DF4C	3	#4 CFRP	0.5	5
DF4G	3	#4 GFRP	0.5	5
DF8G	3	#8 GFRP	0.5	5

3.5.2 Beam Specimens

3.5.2.1 <u>Experimental Program and Test Specimens</u>

Dimensions of the beams specimens were the same as earlier. Cracked structures will be much more susceptible to environmental attack than intact ones. To represent the realistic conditions, three artificial cracks for each beam were induced. Those cracks were 0.024 in. wide (a limitation of 0.020 in. for exterior exposure by ACI 440), 1.5 in. deep (cracks reaching the rebars) and 8 in. in spacing. This was accomplished by putting 0.024 in.

thick and 1.5 in. wide stainless steel sheets underneath the longitudinal rebars before casting the concrete. Once the concrete hardened, the steel plates were pulled out. Artificial seams were thus created to simulate the concrete cracks.

The notation for the specimens is as follows: the first character, “V” or “D”, means the virgin specimens or durability specimens; the second character, “P” or “F”, indicates the plain concrete or FRC; the third character is the rebar diameter in US designation; the fourth character, “C” or “G”, indicates the rebar type, CFRP or GFRP;

Table 3.8 Durability testing for flexural performance

I.D.	Number of Specimens	$f`_c$ (psi)	A_f (in^2)	ρ_f / ρ_{fb}	V_f (%)
VP4G	2	7000	5#4=1.12	3.51	0
VP8 G	2	7000	2#8=1.67	3.6	0
VP4C	2	7000	2#4=0.34	3.16	0
VF4G	2	4400	5#4=1.12	4.71	0.5
VF8 G	2	4400	2#8=1.67	4.83	0.5
VF4C	2	4400	2#4=0.34	4.24	0.5
DP4G	2	7000	5#4=1.12	3.51	0
DP8 G	2	7000	2#8=1.67	3.6	0
DP4C	2	7000	2#4=0.34	3.16	0
DF4G	2	4400	5#4=1.12	4.71	0.5
DF8 G	2	4400	2#8=1.67	4.83	0.5
DF4C	2	4400	2#4=0.34	4.24	0.5

3.6 FULL-SCALE SLAB TEST

3.6.1 Experimental Program and Test Specimens

Three full-scale slabs were tested under static, fatigue and static failure tests to obtain information on stiffness characteristics in the pre and post cracking regimes, degradation of stiffness due to fatigue loads in the post-cracking regime and to establish the mechanisms of failure in the deck slabs at ultimate loads. The first slab tested had conventional epoxy coated steel reinforcing bars, Figure 3.15 in a plain concrete matrix that used the MoDOT high performance concrete bridge deck mix (MB2, detailed in Table 3.1).

Figure 3.15 The conventional deck slab with steel reinforcement ready for plain concrete matrix placement

The second slab had GFRP reinforcing bars (Figure 3.16) in a fiber reinforced concrete matrix. MoDOT's conventional bridge deck mix MB2 was modified to incorporate 0.5% V_f fibrillated polypropylene fibers (with no other changes to the mix).

Figure 3.16 The all GFRP second deck slab is ready for FRC matrix placement

The third slab used a hybrid reinforcing system comprising alternate GFRP and CFRP reinforcing bars for all four layers of reinforcement (transverse and longitudinal reinforcements in the top and bottom mats) and the same MB2 mix with fibers as used for the second slab.

Figure 3.17 The CFRP/GFRP hybrid deck slab is ready for FRC matrix placement

Details of the rebar spacings used for the three slabs are detailed in Table 3.9. The concrete deck slab was 14 ft. 6 in. in length (transverse to traffic direction) and 5 ft. in width (along traffic direction). It was supported on two W 16 x 57 steel girders 8 ft. long at 9 ft. center to center transverse spacing, Figure 3.18. The two steel girders were supported at their two ends on concrete pedestals with roller supports using a 6 ft. 6 in. span so as to simulate the bending rigidity of a typical steel-girder bridge span. The slab was supported on the top at the two ends by roller line supports so as to create negative moments directly over the steel girder lines (Figure 3.19). These supports were located approximately near the inflection points due to transverse bending of a deck loaded with normal design loads. The steel girders had two rows of shear connectors spaced at 8 in. welded along the length of the girder so as to provide the necessary composite action expected in a typical MoDOT steel girder bridge. A total of 14 studs were required for each girder.

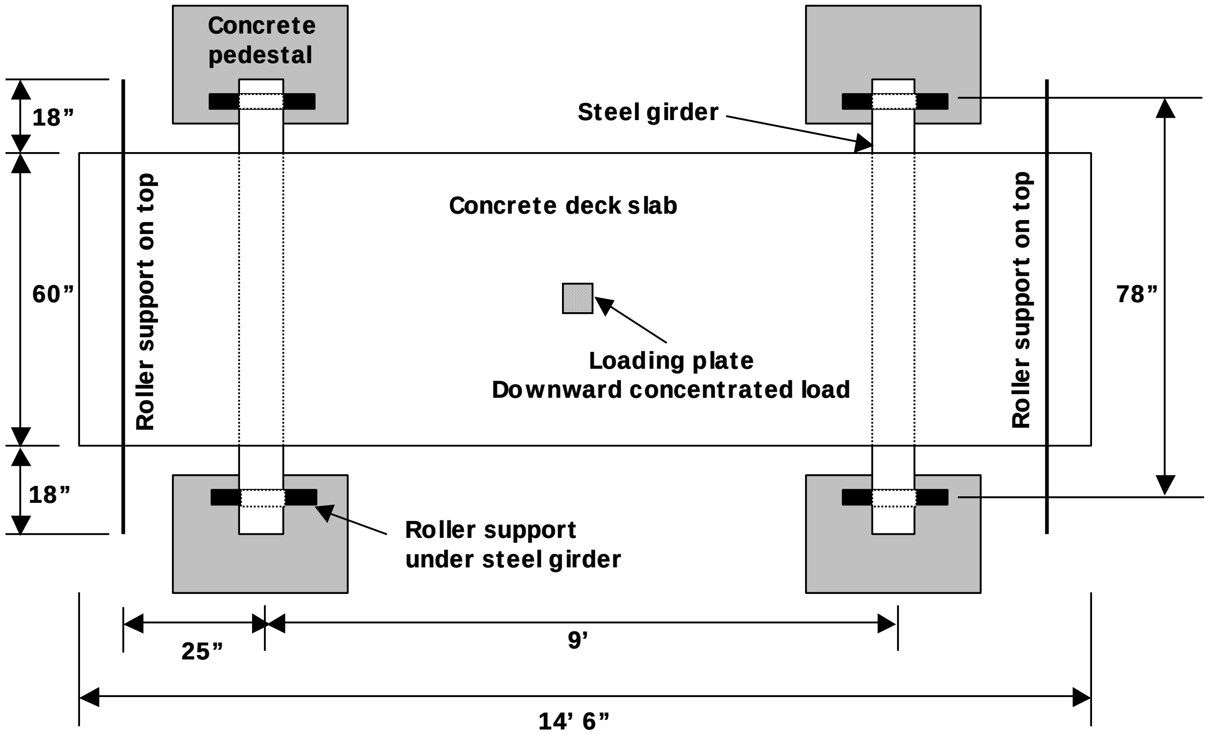

Figure 3.18 Schematic plan view of the deck slab test configuration

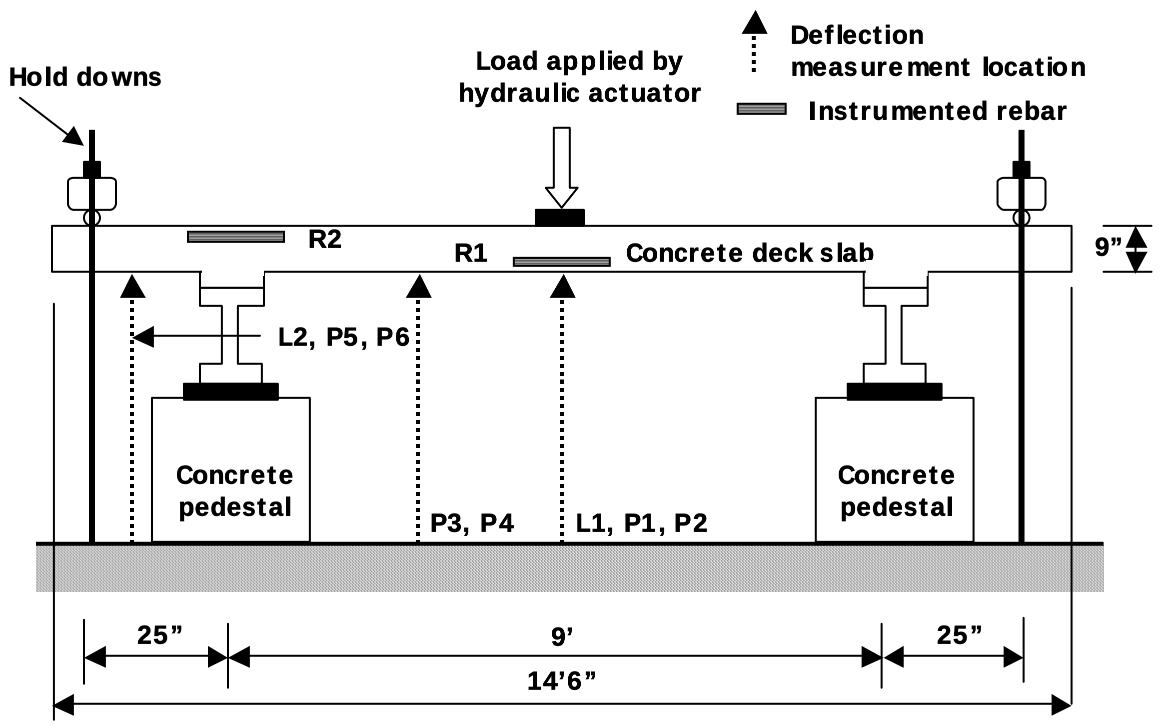

Figure 3.19 Schematic side elevation of the deck slab test configuration

Table 3.9 Reinforcement and spacing details for the three test slabs

Reinforcement	Matrix	Top mat		Bottom mat	
		Transverse	Longitudinal	Transverse	Longitudinal
Epoxy-coated steel rebars	Plain concrete	#6 Bars at 6 in. centers	#5 Bars at 15 in. centers	#5 Bars at 6.5 in. centers	#5 Bars at 9 in. centers
GFRP rebars	Polyprop. FRC (V_f 0.5%)	#6 Bars at 5 in. centers	#6 Bars at 8 in. centers	#6 Bars at 5 in. centers	#6 Bars at 9 in. centers
GFRP/CFRP Hybrid reinforcement*	Polyprop. FRC (V_f 0.5%)	Alternate* bars at 5 in. centers	Alternate* bars at 10 in. centers	Alternate* bars at 6 in. centers	Alternate* bars at 10 in. centers

* *#4 CFRP and #6 GFRP rebars were placed alternately in all the four layers of reinforcement*

The deck slab thickness was 9 in. excluding a 1 in. haunch provided over the steel girder flanges to represent typical MoDOT deck slab design. Additional details with regard to the deck slab design and geometry are discussed later in Chapter 7 where results from the deck slab tests are reported. Figure 3.20a and b show the casting of a typical deck slab. Slabs were steam cured for approximately 24 hours starting from approximately 12 hours after casting operations were completed. Test on wet concrete were conducted including unit weight, air content and slump. 6 in. cylinders for compression tests were also fabricated and cured along with the slab. Results from these tests are summarized in Chapter 7 where slab test results are reported and discussed.

Figure 3.20 Fabrication of the conventionally reinforced slab (a) concrete consolidation, and (b) concrete finishing operations

3.6.2 Instrumentation and Test Procedures

Two LVDTs (L1 - L2), six potentiometers (P1 - P6) and two instrumented rebars (R1 - R2) at locations shown in Figure 3.19 were used to monitor displacement (L1, L2, P1 – P6) and internal strains (R1 – R2), respectively for all the three slabs. Transducers L1, L2, R1, R2, P1, P3, and P5 were placed along the centerline of the slab at the locations indicated in Figure 3.19. Potentiometers P2, P4 and P6 were placed along the edge of the slab at the locations indicated in Figure 3.19. In addition to these transducers, ram deflection and applied load were monitored. LabView based data acquisition programs were custom written for the slab tests to acquire data from static, fatigue and ultimate load tests.

Static loading/unloading tests were conducted on each of the three slabs where a ramp loading function was used to obtain the load deflection response of the slab before beginning any fatigue testing. Such static tests were also conducted several times during the fatigue test protocol so as to facilitate monitoring of progressive stiffness degradation after desired numbers of fatigue cycles were completed. Static tests were carried up to a midpoint load of approximately 20 kips which was close to the first cracking load. Complete load deflection characteristics were recorded for the static tests.

A 3-Hz sinusoidal loading was used for the fatigue tests. The lower limit load was approximately 10 kips and the upper limit load was approximately 20 kips. Fatigue tests were conducted under ram-displacement controlled mode. To avoid collecting a lot of data of little practical significance, only maximum and minimum load and maximum and minimum deflection/strain responses were recorded during the fatigue tests. This facilitated monitoring of stiffness degradation versus number of fatigue cycles during the application of fatigue loading. Fatigue tests were stopped after 1 million fatigue cycles were completed. Following fatigue testing, all the slabs were tested to failure under static loading rate using a ramp loading function. Complete load deflection histories were recorded during these tests.

In addition to automated digital data acquisition, visual observations of the cracking patterns and crack widths were completed at regular intervals. Following the failure test, cracking in the slab along the underside as well as at the top surface were recorded using a template of the deck slab. Details of the failure mechanism and crack patterns/widths are discussed in Chapter 7.

4. STATIC AND FATIGUE BOND TEST RESULTS

4.1 INTRODUCTION

It is generally understood that the three primary mechanisms of bond resistance result from chemical adhesion, mechanical interlock, and friction resistance. Each component contributes to the overall bond performance in varying degrees depending on the type of rebar. Typical bond mechanisms for the deformed rebars are shown in Figure 4.1 (Hamad, 1995).

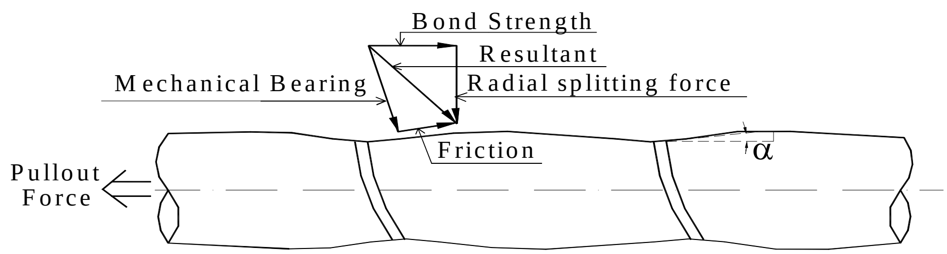

Figure 4.1 Bond mechanisms for deformed GFRP rebar (Hamad, 1995)

Based on its overall performance, bond can be divided into two categories, average bond and local bond, as shown in Figure 4.2. The average bond is the average bond over a specific length of embedment (or between the cracks), and its value is generally varied with the embedment length. The local bond is an inherent property of the rebar and the concrete. It is independent of the embedment length and is determined by its constitutions (the concrete and the rebar) and the interaction between the constitutions.

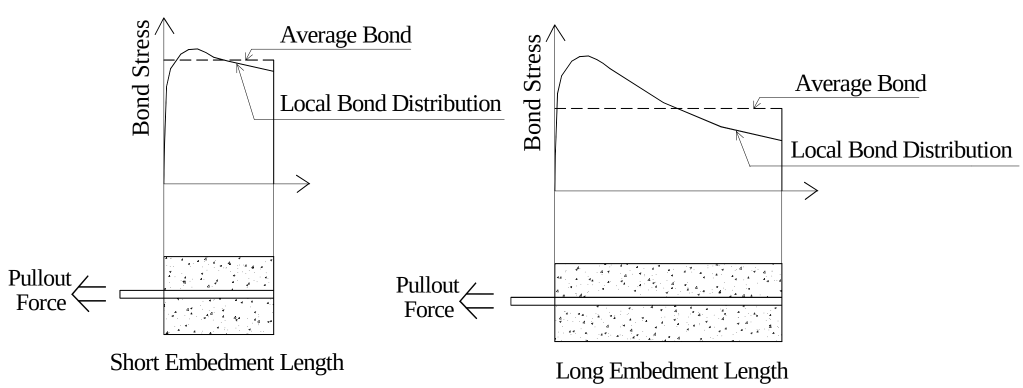

Figure 4.2. Average bond and local bond

Considerable studies have been conducted on the bond behavior of the Glass Fiber Reinforced Polymer (GFRP) rebar in plain concrete. Different types of the FRP rebars have quite different bond characteristics, which are strongly dependent on the mechanical and physical properties of external layer of FRP rods (Ehsani et al., 1997; Kaza, 1999). On the other hand, because no accepted manufacturing standards for FRP are available, bond research is far from satisfactory. For the deformed GFRP rebar having similar surface to rebar GFRP, as shown in Figure 3.9, the bond strength is equivalent to or larger than those of ordinary deformed steel (Cosenza et al., 1997; Kaza, 1999). Research also showed that for some smooth surface rebars, the bond strength can be as low as 145 psi (Nanni at al., 1995), which is about 10% of that of steel. As for Carbon Fiber Reinforced Polymer (CFRP) rebar, relatively fewer experimental data are available in the literatures. Four types of CFRP rods were tested by Malvar et al. (2003) and they found that when there was sufficient surface deformation, a bond strength of 1,160 psi or more could be reached.

Compared to relatively other materials and/or monotonic bond tests, literature on fatigue bond tests is very limited and the testing results are also controversial. Test results by Katz (2000) indicated that there was a reduction in the bond strength after cyclic loading, while Bakis et al. (1998) found that the bond strength in cyclically loaded beams increased as compared to the bond strength in the monotonic tests.

Fibers may improve the properties of concrete, although there is no strong opinion on the effect on the strength (ACI 544, 1996). As a consequence, with the addition of fibers, bond performance will change due to the alteration of the concrete properties. Bond between the traditional steel bars and the FRC was investigated by several researchers and the test results indicated the addition of fibers significantly improved the post-peak bond behavior. However, no agreement was reached on its effect on bond strength. As for bond behavior of the FRP bars embedded in the FRC, open literature does not provide any published information.

Three test methods are commonly used to study bond behaviors: namely, pullout test, splitting bond test, and flexural beam test. These test methods provide different information to the bond behaviors. Pullout tests can clearly represent the concept of anchorage and is usually adopted to study the bond behavior between rebar and concrete. Although pullout tests cause concrete to be in compression and the testing bar to be in tension, a stress condition not exhibiting in real structures, a reasonable correlation was found between structural performance and measures of performance in the pullout test (Cairns and Abdullah, 1995). Splitting bond tests can be used to study the splitting bond behavior under different cover thicknesses. The transverse reinforcement's effect on bond behavior can be avoided when properly designed. Splitting bond tests can simulate the stress field of real structures to some extent; it can simulate the shear stress field but not the stress gradient induced by bending. Flexural beam tests have the advantage to represent actual stress fields in real beams and the cover effects on the bond. But, it requires considerable confining reinforcement to avoid a shear failure and so bond-splitting failures are unlikely (Cairns and Plizzari, 2003). In this program, all three types of tests were investigated and compared to each other. In this Chapter, bond characteristics, studied by pullout test method and splitting bond test method, are presented.

4.2 PULL-OUT BOND TESTS

4.2.1 Test Results and Discussions

The average bond strength was calculated as the pullout force over the embedded area of the rebar. The slip at the loaded end was calculated as the value recorded by LVDT2 minus the elastic deformation of the FRP rebar between the bond zone and the location of LVDT2 (see Chapter 3). It should be mentioned that the deformation of the steel frame was very small (because of its high stiffness), less than 1% of the slip (approximately 0.0015 in. when the pullout load equals to 45 kips), which the total slip was larger than 0.30 in., thus it was ignored in all calculations. When the bond strength of specimens was compared with different concrete strengths, bond strength was normalized based on the square root of f_c', which is adopted in the current ACI 318-02.

4.2.1.1 <u>Monotonic Static Tests</u>

The monotonic test results are listed in Table 4.1. Most of the test results shows repeatability with small variations for the same testing group. In the case of PG405M and FG405M, there was a combination of both pullout and splitting failure modes. Since the slip at failure was very different for different failure modes, the coefficients of variance for slip in these two groups were large.

Table 4.1. Summary of results from static pullout bond test

Specimen I.D.	Bond Strength First (Second)Peak $u/\sqrt{f_c^{'}}$ ($u^{'}/\sqrt{f_c^{'}}$) ($psi/\sqrt{psi}$)		Slip at First (Second)Peak S_m ($S_m^{'}$) (in.)		0.002 in. Bond Strength $u_{0.05}/\sqrt{f_c^{'}}$ ($psi/\sqrt{psi}$)		Mode[1]
	Average	COV (%)	Average	COV (%)	Average	COV (%)	
PC405M	11.40 (15.24)	6.01 (5.33)	0.03 (0.69)	9.77 (4.42)	11.52	7.49	P
PG405M	32.88	7.80	0.36	40.57	15.12	6.95	S/P
PG805M	30.6	2.95	0.34	9.31	11.88	5.09	S
FC405M	14.04 (13.20)	14.20 (1.54)	0.04 (0.67)	11.11 (9.57)	13.92	13.57	P
FC410M	16.68 (15.12)	14.26 (3.97)	0.07 (0.66)	3.68 (16.92)	16.32	13.14	P
FG405M	31.92	5.16	0.41	23.22	17.64	23.38	S/P
FG410M	28.2	4.44	0.37	16.23	24.36	4.53	S
FG805M	26.04	7.25	0.54	6.21	13.08	12.13	P
FG803M	29.28	5.92	0.48	6.52	13.20	12.26	P

1. *P=Pullout failure; S=Splitting failure;*
2. *Two peak values were observed only in CFRP specimen (Figure 3.4). The numbers in the parenthesis are second-peak values.*
3. *Values are the average of three duplicate specimens;*

Effect of Rebar Surface Conditions: Due to their significant surface differences, bond behavior of the GFRP and the CFRP are not the same, as shown in Figure 4.3. The bond strength of the GFRP was about twice as much as that of the CFRP. The bond failure of the CFRP was controlled by rebar pullout and, providing more ductile behavior.

(a) Bond-slip behavior of CFRP: During the pullout of the CFRP rebars, the surface of the rebar was severely rubbed and the resin was scratched off (see Figure 4.4). The surface of the CFRP used in this study was very smooth. As a result, a very low mechanical bearing force can be expected. Thus, for the CFRP rebar, the mechanical bearing can be neglected. Load-slip response for the CFRP can be roughly divided into four phases, as shown in Figure 4.5.

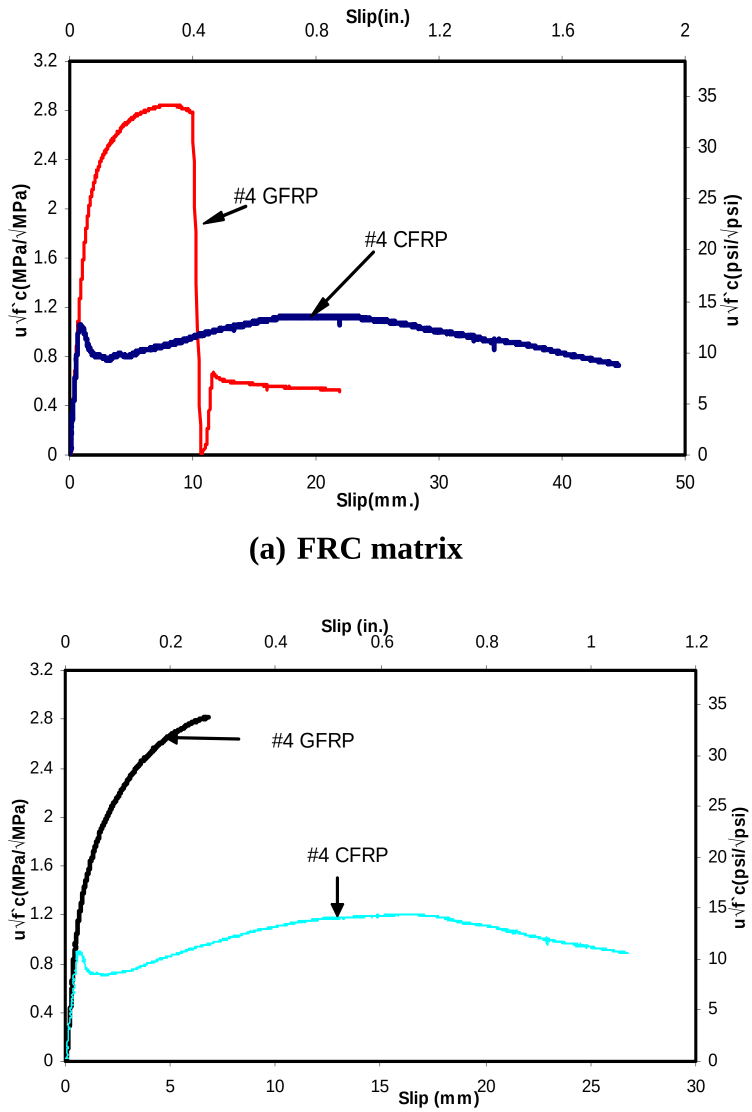

(a) FRC matrix

(b) Plain concrete matrix

Figure 4.3. Bond-slip relationship of GFRP and CFRP specimens

Phase I *(as described in Figure 4.5 in portion O~A):* At Phase I, the chemical bond and friction force resisted pullout force together, which resulted in a very high bond stiffness. *Point A (refer to Figure 4.5):* Chemical bond was broken at the loaded end first, and then extended to the free end. The peak value of chemical adhesion was reached at Point A. After this point, chemical bond was completely lost along the whole rebar.

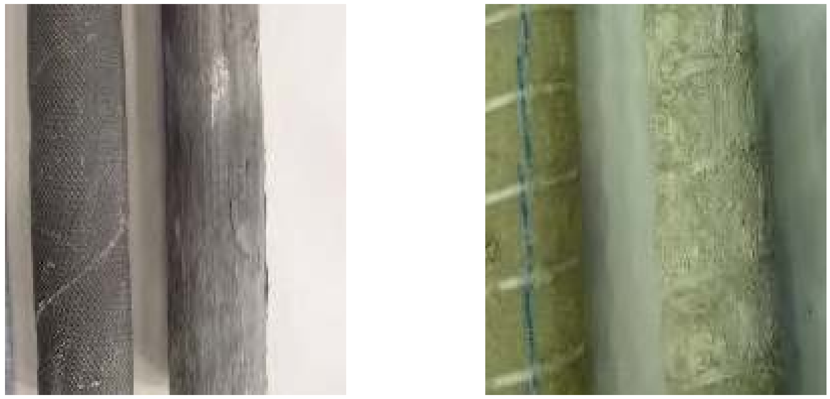

(a) CFRP **(b) GFRP**

Figure 4.4. Surface conditions of rebars (left before and right after test in each case)

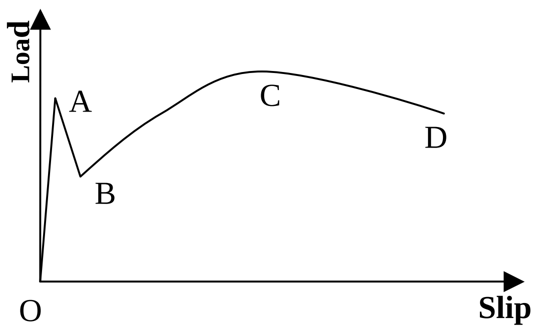

Figure 4.5. Idealized load-slip curve for CFRP rebar embedded in concrete

Phase II *(as described in Figure 4.5 in portion A~B):* After the chemical bond was broken, only the friction component was present. The total resisting force provided only by the friction decreased suddenly. Because the tests were controlled by the slip at the loaded end, the slip between the rebar and concrete continued increasing constantly. As a result, the pullout load had to be reduced to maintain the increasing rate of the slip. If the specimen was load-controlled, this drop would have been omitted. When the pullout load dropped to Point B, a new equilibrium was reached. The chemical bond component can be calculated by the difference of the bond strength at Point A and Point B *minus* the increase of the friction bond component from Point A to Point B. For the CFRP rebar used in this study, the chemical bond strength was 150 to 200 psi. Chemical cohesion between deformed steel bars and concrete was reported, ranging from 150 to 300 psi by Choi et al. (2002).

Phase III *(as described in Figure 4.5 in portion B~C):* As the slip continued to increase, friction force increased accordingly, and the load-slip curve went up again. Due to the loss of chemical bond, the curve B~C was much flatter than O~A. At this phase, microcracks occurred and propagated. *Point C (refer to Figure 4.5):* At Point C, friction reached its maximum value.

***Phase IV** (as described in Figure 4.5 in portion C~D):* With the increasing of slip, more and more microcracks developed. It caused the confinement from concrete to rebar to reduce. Thus, the friction force between rebars and concrete also decreased. The load-slip curve was softened.

Based on the bond-slip curve, two peak bond values were observed for each specimen. (1) In Phase I, chemical adhesion and friction resistance dominated bond behavior. The first peak occurred when maximum local chemical bond stress spread to the free end. (2) In phase II, friction force dominated the bond behavior. The second peak value occurred when friction force reached its maximum.

(b) Bond-slip behavior of GFRP: At failure, the surface of the GFRP rebar was damaged, and resin was rubbed off from the rebar surface. Some small pieces of resin scale were noticed in the concrete, and helical fiber strands were broken in several specimens. However, the overall shape of the rebar remained intact. The deformation created by the helical fiber strand could still be seen, which suggested that the deformation was not transversely crushed or sheared off by the bearing force from the concrete. In other words, the resin acted as a good cover to protect the glass fibers, as shown in Figure 4.4b. Previous work carried out by other researchers (Katz, 1999; Chaallal and Benmokrane, 1993) showed that the shearing of the rib is the main reason for the bond failure in the deformed FRP bars. This kind of failure phenomenon was not observed in this study. That may be due to the different surface characteristics of the FRP rebar. In the studies conducted by Katz et al. and Chaallal and Benmokrane, the ratio of the projected area that was normal to the bar axis to the shearing area of the rib was much smaller than that of the rebar used in this study, as shown in Figure 4.6.

Consequently, when the bearing forces on the projected deformation are the same (i.e., deformation heights, h_r, are the same), the rebar as shown in Figure 4.6b will induce much larger shearing stresses on the rib. Thus, it is easier for the rib to be sheared off. In other words, rib deformation like Figure 4.6a is more desirable to prevent such shearing off failure. This factor is more important for the FRP rebar than it is for the traditional steel rebar, since the ribs of the FRP rebar are made of resin, which is much weaker in shear-resisting capacity. At this point, the bond is strongly relative to the FRP manufacturer.

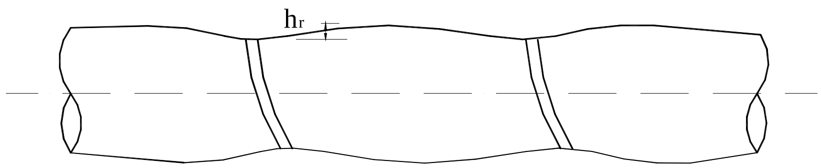

(a) Deformation pattern of GFRP used in this study

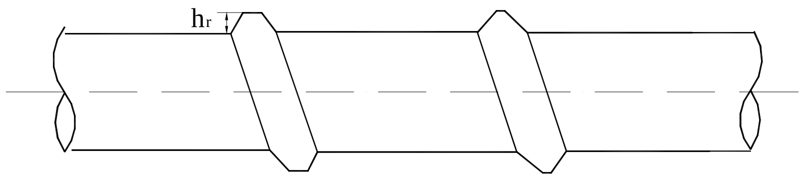

(b) FRP with other deformed patterns

Figure 4.6. Deformation patterns available in FRP rebars

Chemical bond played a much less important role for the GFRP specimens than for the CFRP specimens. It was the mechanical bearing and friction force that dominated the bond behavior. Due to the GFRP's relatively rough surface, internal cracks (crack unnoticeable at concrete surface) were created, even at a very low load level. It was thought that chemical adhesion had been lost at these portions (Goto, 1971). Since the CFRP had a very smooth surface, no internal cracks, or very few, were formed at the initial loading. Chemical cohesion was almost intact until the relative slip between the rebar and concrete was too large, and then it was broken abruptly.

Embedment Length Effect: Similar to the traditional steel rebar, bond stresses along the FRP rebar are also nonlinearly distributed along the embedded portion (Benmokrane et al., 1996). The bond mechanisms for the CFRP and GFRP bars in this study were different, therefore, the embedment length effect on bond strength was also different.

(a) GFRP: As mentioned earlier, mechanical bearing dominated the bond. The bond stresses were nonlinearly distributed along the embedment portion. High bond stresses concentrated at the portions near the loaded end, and the bond stresses decrease sharply toward the free end. In the case of the longer embedment length, a relatively smaller portion of the embedded area had large bond stress. Consequently, the average bond strength with a longer embedment length would have a lower value, as shown in Figure 4.7. Also, the slope of the bond-slip curve of the specimens with shorter embedment length was steeper than that of the specimens with longer embedment length. That was due to the fact that the higher bond stress concentrated near the loaded end and lower bond stress developed far away the loaded end. Thus, when the average bond stress was calculated based on the pullout load divided over the whole embedment length, the specimens with longer embedment would have lower bond stiffness.

(b) CFRP: As mentioned previously, all the bond strength came from friction resistance at ultimate (the second peak). The friction resistance was a function of the friction coefficient and normal pressure on the rebar. Obviously, the friction coefficient was the same along the rebar. Also, the normal pressure was the same along the embedment portion, except that the portions near the ends had lower values due to less confinement at the ends. As a result, the bond stress distribution was almost uniformly distributed along the embedment length. The average bond strength over the whole embedment length would not decrease with the increasing of the embedment length. It could even get a higher value due to the relative small portion of rebar near the ends. A 14% increase of the bond strength was observed in this study, when the embedment length increased from 5 d_b to 10 d_b, as shown in Figure 4.7a.

Diameter Effect: As shown in Figure 4.8, the bond strengths of the #4 specimen were about 8% and 23% higher than the #8 embedded in the plain concrete and the FRC, respectively. One explanation is that the possibility of defect (voids created by concrete bleeding—Tighiouart et al., 1998) is higher for a larger rebar, a phenomenon similar to the size effect on the behavior of various brittle materials. Another possible explanation is the Poisson effect; as there is elongation in the longitudinal direction, the transverse direction tends to contract. Consequently, the confinement from the concrete to the rebar will be reduced to some extent. This effect is more significant for a larger rebar; thus, a rebar with a bigger diameter will have smaller bond strength.

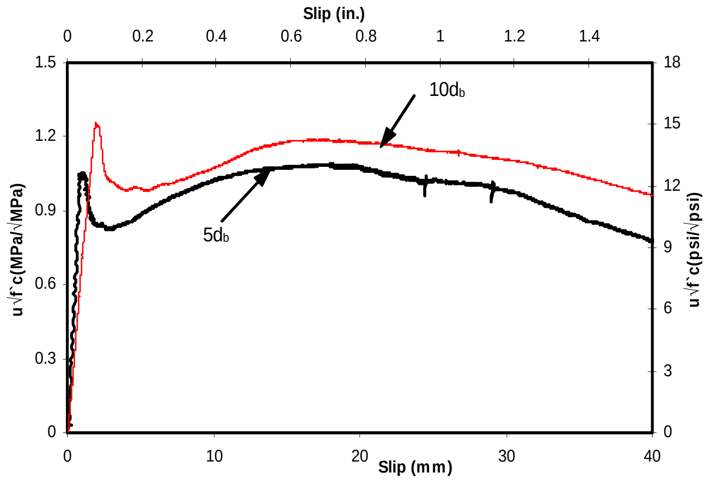

(a) #4 CFRP

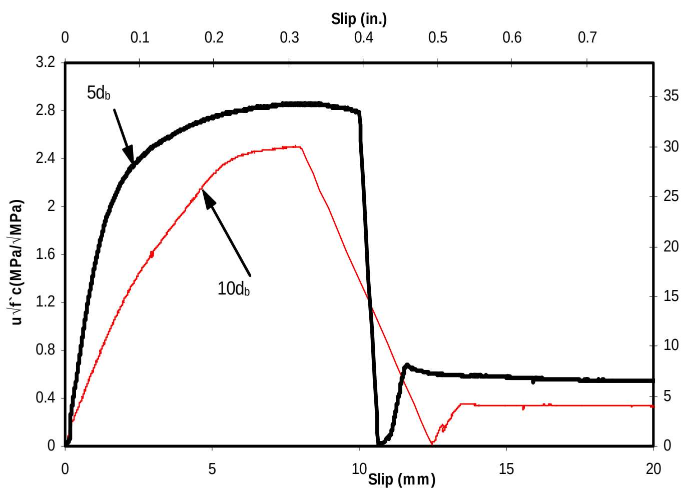

(b) #4 GFRP

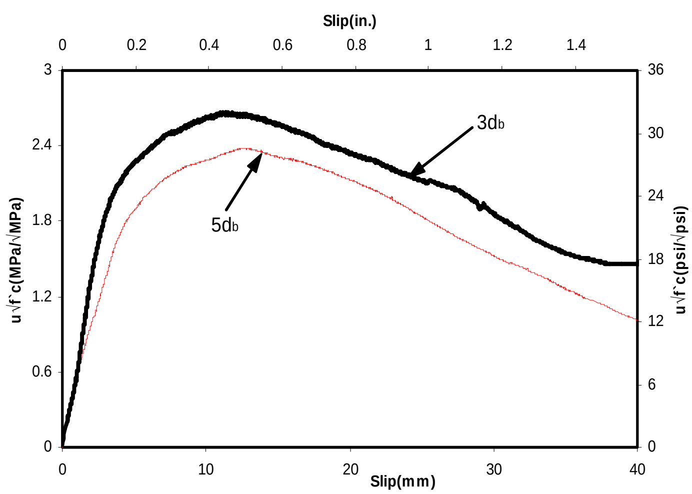

(c) #8 GFRP

Figure 4.7. Effect of embedment length on bond-slip curves

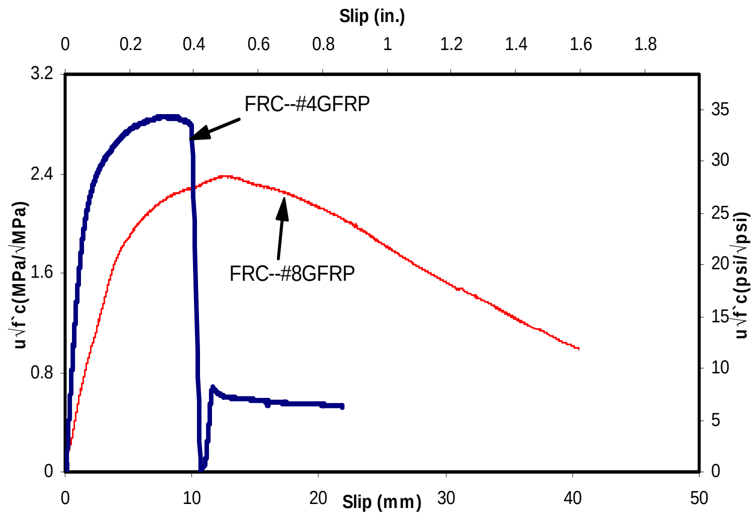

(a) Fiber reinforced concrete

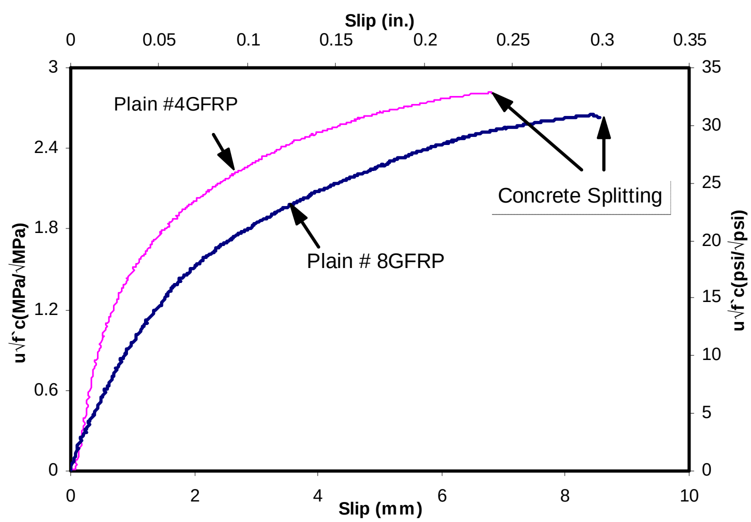

(b) Plain concrete

Figure 4.8. Effect of bar diameter on bond-slip curve

Effect of Polypropylene Fibers: The following remarks are made:

(a) The ultimate bond strength slightly decreased with the addition of the polypropylene fibers. The reduction ranged from 3% to 16% (see Table 4.1 and Figure 4.9).

(b) The slip corresponding to the ultimate bond strength increased significantly with the addition of fibers for the GFRP specimens and less for the CFRP specimens. As discussed previously, in the case of the GFRP, internal microcracks were created due to the mechanical bearing; however, fewer internal cracks existed in the case of CFRP, due to its

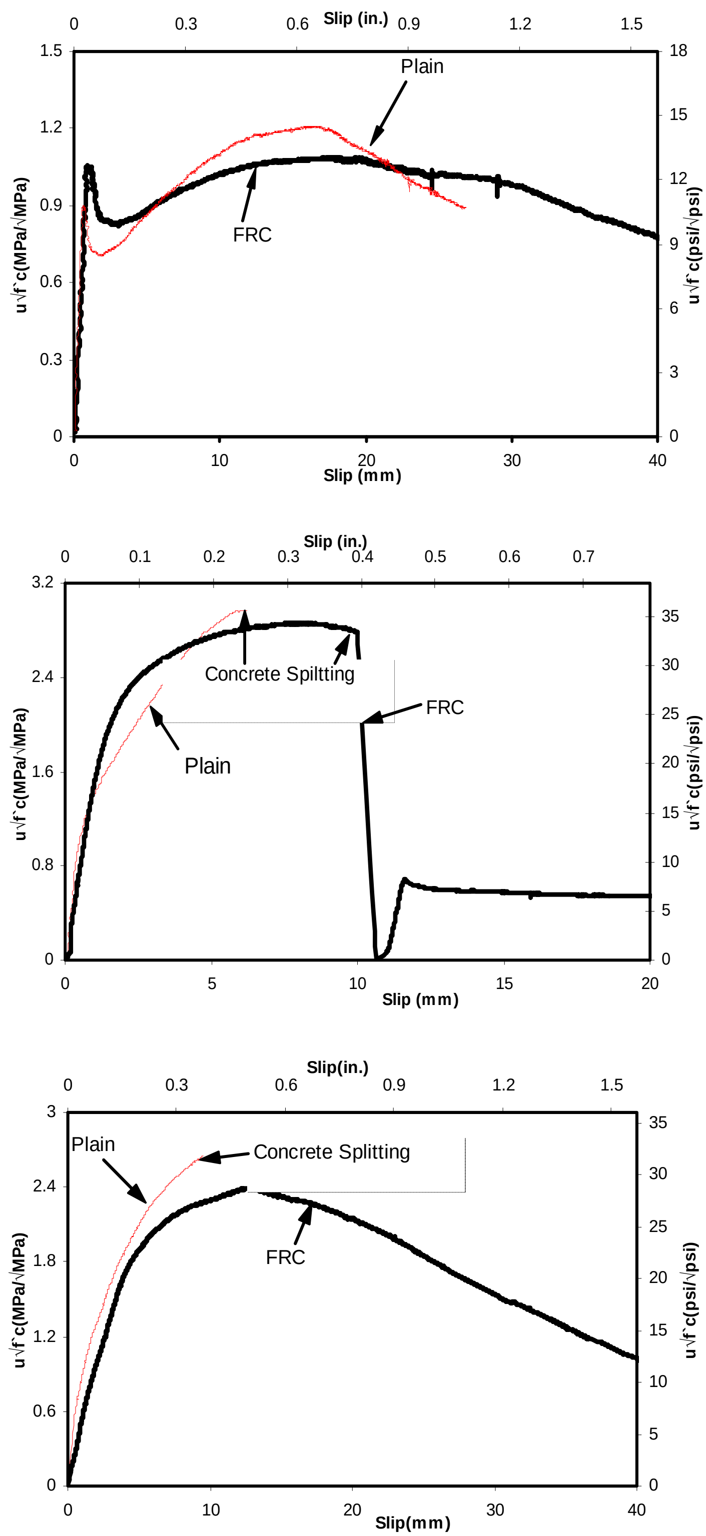

Figure 4.9. Effect of polypropylene fibers on bond-slip curves (a) Top - #4 CFRP, (b) Middle - #4GFRP and (c) Bottom - #8 GFRP

negligible mechanical bearing. Only when the microcracks developed could the polypropylene fibers behave effectively to limit the opening of microcracks and thus decreased the rate of microcracks propagation. Since many more microcracks existed in the GFRP specimens, the contribution from the polypropylene fibers was more noticeable.

(c) The addition of fibers changed the failure mode; most specimens that failed in concrete splitting changed to pullout failure.

(d) When specimens failed in splitting, the failure for the plain concrete specimens was much more brittle than that of the FRC specimens. As shown in Figure 4.10, the plain concrete specimens usually failed by breaking the concrete into several pieces; while, in the case of the FRC specimens, splitting cracks developed along the splitting plane. With the presence of the polypropylene fibers, the specimens were held together and remained integrated.

Figure 4.10. Failure for FRC and plain concrete specimens

4.2.1.2 <u>Fatigue Pull-Out Test Results</u>

Fatigue loading will produce a progressive deterioration of bond caused by the propagation of microcracks and the progress of micro-crushing of concrete in front of the irregularity of the rebar surface (ACI 408-99). The damage accumulation can be observed by measuring the relative slip between the concrete and the rebar.

<u>General Observations:</u> Different remarks were drawn for different specimens when they were subjected to the fatigue loading. The #4 CFRP and the #8 GFRP specimens withstood one million cycle fatigue loading, while, the #4 GFRP specimens failed because the concrete split prematurely. It should be noted that ranges of fatigue loading were 10% to

60%, 10% to 60%, and 0% to 40% of their ultimate monotonic bond strengths for #4 CFRP, #4 GFRP, and #8 GFRP specimens, respectively.

Because the #4 GFRP and the #8 GFRP had similar surface conditions and bond mechanisms, we may regard that their fatigue bond behaviors were also the same. Based on the limited test data, 10% to 60% and 0% to 40% can be conservatively considered as the fatigue bond limit to sustain one million cycle loading for the CFRP and the GFRP, respectively.

Residual Slip Accumulation: The commonly accepted hypothesis to determine the damage accumulation due to fatigue loading is the Miner's hypothesis. According to the rule, failure occurs if $\sum n_i/N_{max,i} = 1$, where n_i is the number of cycles applied at a particular stress level, and $N_{max,i}$ is the number of cycles which cause fatigue failure at that same stress level. Test results have shown that this hypothesis is only partly suitable for FRP fatigue bond behavior.

As shown in Figure 4.11, the residual slips accumulated gradually with the increasing number of cycles, but the rate of increase was not constant. Micro-voids between rebar and concrete existed at the time of the specimen fabrication; i.e., rebar was not in full contact (100 %) with the concrete. When the specimens were subjected to fatigue loading, some of the micro-voids would have gradually closed. At the beginning, relatively large amounts of voids existed; thus, the residual slips were easier to develop. After a certain number of fatigue cycles, most of the voids were closed and the system became stabilized. At that point, the accumulation rate of the residual slip slowed down. Figure 4.11 shows slip vs. cycle-number curve can be roughly divided into two phases. The first approximately 10,000 cycles may be regarded as the first phase. The rest of the curve is the second phase. During the first phase, the fatigue damage accumulated much faster than it did in the second phase. After the first phase, the slip increased linearly with a much lower rate.

Fatigue Loading Effect on Residual Bond-Slip Behavior:

(a) **Fatigue Loading Effect on Bond Stiffness:** Fatigue loading can increase bond stiffness (Figure 4.12). This was also reported by Gylltoft et al. (1982) based on a study on steel bars embedded in the plain concrete. As mentioned previously, the rebar and concrete were not in full contact because of the micro-voids. After the specimen had been subjected to fatigue loading, some of the voids were closed, resulting in a larger contact area.

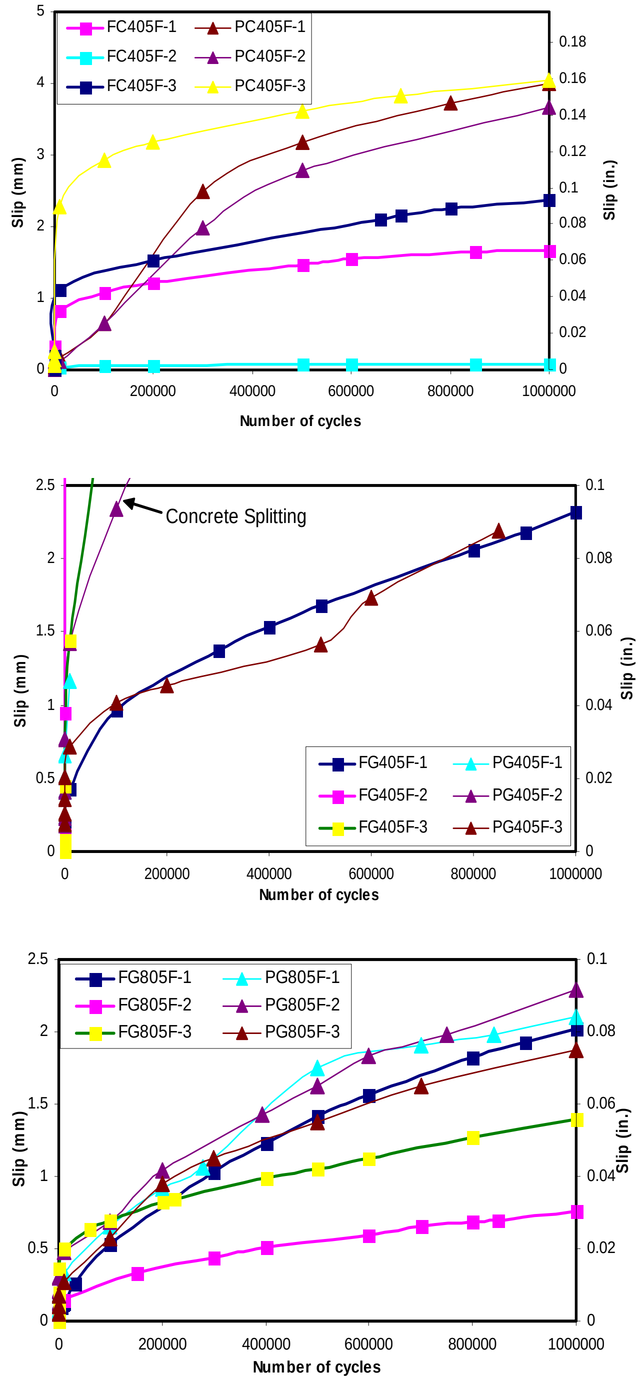

Figure 4.11 Residual slip versus numbers of fatigue cycles (a) Top - #4 CFRP, (b) Middle - #4 GFRP, and (c) Bottom - #8 GFRP

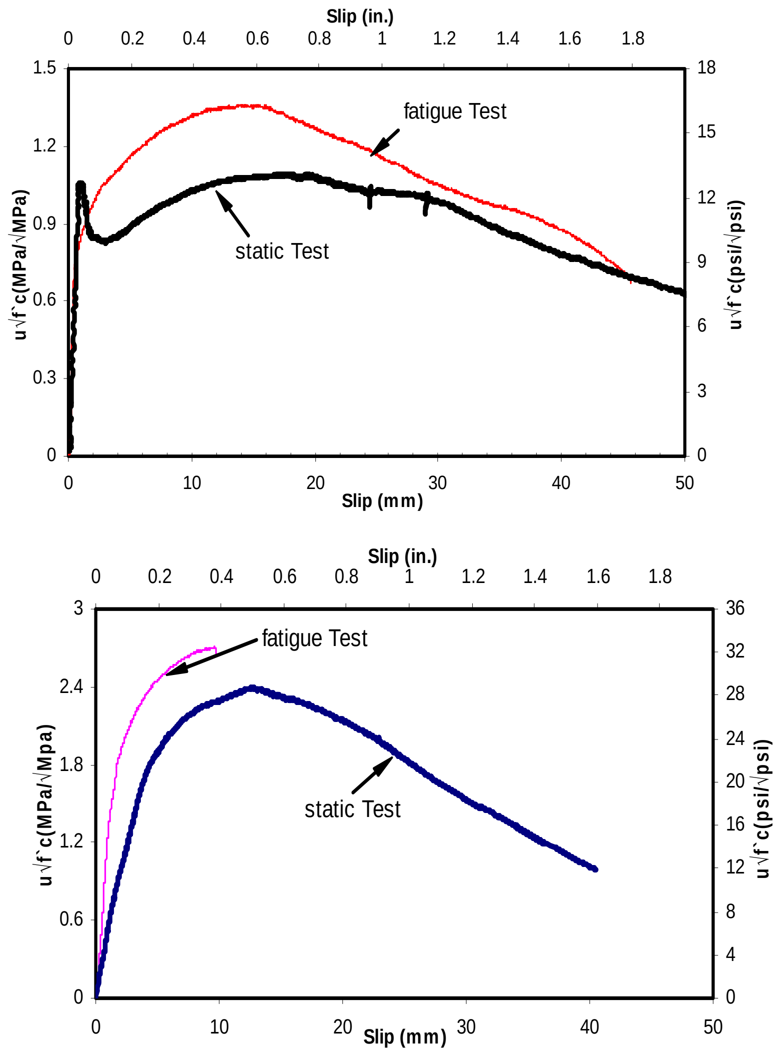

Figure 4.12. Bond-slip response before and after fatigue loading (a) Top #4 CFRP, and (b) Bottom - #8 GFRP

Another reason could be the fact that the rebar surface became rougher after being subjected to the fatigue loading, and the friction resistance increased consequently.

(b) **<u>Fatigue Loading Effect on Ultimate Bond Strength:</u>** The fatigue loading may increase the ultimate bond strength to some extent, as shown in Figure 4.12 and Table 4.2. The probable reasons are that fatigue loadings cause the micro-voids close up and result in more contact area.

(c) <u>Accumulated Slip's Effect on Load-Slip Behavior:</u> Specimens that did not fail during the fatigue tests were subjected to monotonic pullout tests. When compared to the specimens without fatigue loading, the slip, s_m, of the post-fatigue specimens decreased. Interestingly, when adding the slip, s_m, and residual slip, s_r, due to the fatigue loading (see Table 4.2), the sum of the slip would be very close to that of the specimen without fatigue loading, s_m. This may be due to the slip, that may have already occurred during the fatigue loading. Also, the total slip is an inherent property between the rebar and the concrete and has little relationship with the loading history. A similar phenomenon was observed for the steel rebar embedded in plain concrete (Rehm and Eligehausen, 1979; Clark and Johnston, 1983).

Table 4.2. Fatigue Bond Tests Results

I.D.	Post-fatigue Specimens						Specimens without fatigue loading	
	Bond strength $u/\sqrt{f_c'}$ ($psi/\sqrt{psi}$)		**Slip**[1] s_m **(in.)**	**Residual slip due to fatigue**[2] s_r **(in.)**	$s_m + s_r$ **(1)+(2)**		**Average Bond Strength** $u/\sqrt{f_c'}$ ($psi/\sqrt{psi}$)	**Average Slip** s_m **(in.)**
PC405F	15.12	15.6	0.50	0.16	0.66	0.64	15.24	0.69
	15.24		0.44	0.16	0.60			
	16.56		0.51	0.14	0.65			
PG805F	35.52	36	0.23	0.08	0.31	0.32	30.6	0.34
	35.4		0.16	0.09	0.26			
	36.96		0.30	0.08	0.38			
FC405F	13.8	14.4	0.60	0.07	0.67	0.67	13.2	0.67
	13.2		0.66	0.00	0.67			
	16.32		0.57	0.09	0.66			
FG805F	27.84	29.52	0.43	0.08	0.51	0.45	26.04	0.54
	32.28		0.38	0.03	0.41			
	35.52		0.36	0.06	0.42			

Note: (1) PG405F and FG405F specimens did not sustain 1 million cycles and are not listed
(2) Unlike the static tests, fatigue test results are more scattering. Thus, individual test results are also listed

(d) **<u>Fatigue Loading Effect on Failure Mode:</u>** The load-slip behavior became more brittle after being subjected to fatigue loading, and the fatigue loading could even change the failure mode. Two of the three FG805F specimens failed by the concrete splitting, while all the specimens FG805M failed in the rebar pullout. The fatigue loading did not change the failure mode of the CFRP specimens.

Effect of Polypropylene Fibers: Polypropylene fibers could effectively decrease the rate of microcracks propagation, which was manifested by the fatigue bond tests.

(a) Residual Slip: With the addition of polypropylene fibers, the residual slip due to fatigue loading decreased (see Figure 4.13). The test results were scattered, a characteristic well documented in fatigue tests. However, it was clear that the progressive rate of the residual slip was noticeably reduced with the addition of fibers.

(b) Degradation of Bond Stiffness: With the addition of polypropylene fibers, the degradation rate of bond stiffness due to the fatigue loading decreased (see Figure 4.13). For CFRP specimens without fibers, the bond stiffness reduction ranged from 0% to 35%. However, for CFRP specimens after adding fibers, no bond stiffness degradation was observed. For GFRP specimens without fibers, the bond stiffness reduction ranged from 20% to 30%. However, for GFRP specimens after adding fibers, the reduction range was reduced to 5% to15%. Similar observations were made by Gopalaratnam et al. (2004) based on their flexural bond tests.

4.2.2 Prediction of Ultimate Bond Strength

Bond of GFRP to concrete is controlled by the following internal mechanisms: chemical bond, friction resistance, and mechanical bearing of the GFRP rod against the concrete. When large slip exists, friction and mechanical bearing are considered to be the primary means of stress transfer.

Based on the test results, slippage between the FRP rebar and the concrete was very large at failure (more than 0.4 in. at the loaded end and 0.1 in. at the free end). Thus it is safe to conclude that all the chemical adhesion has already been destroyed; that is, the final bond strength consisted only of friction and mechanical bearing.

Through mechanical analysis (Figure 4.14), the summation of longitudinal component, u, is equal to the total pullout force. Thus, $\pi d_b l_d u = T$ will result in:

$$u = \frac{T}{\pi d_b l_d} \tag{4.1}$$

$$R_r = \frac{u}{\tan(\alpha + \arctan\mu)} = \frac{T}{\pi d_b l_d \tan(\alpha + \arctan\mu)} \tag{4.2}$$

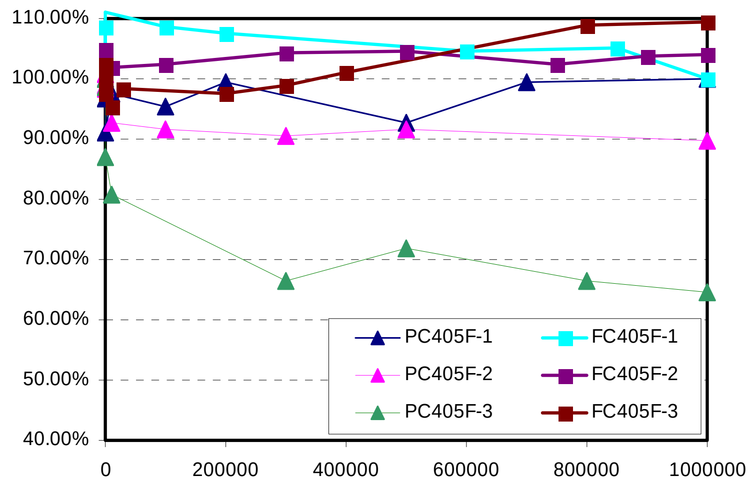

(a) #4 CFRP

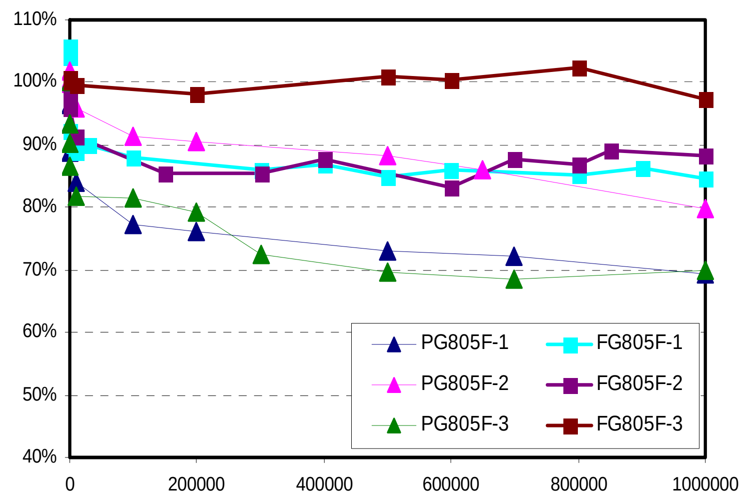

(b) #8 GFRP

Figure 4.13. Degradation of bond stiffness

The splitting force is caused by radial component, R_r. For simplification, it is assumed that the concrete is split into one half, and the force is evaluated as follows:

$$F_{split} = \int_{-\frac{\pi}{2}}^{\frac{\pi}{2}} R_r l_d \frac{d_b}{2} \cos\theta d\theta = \frac{T(1-\mu \tan\alpha)}{\pi(\mu + \tan\alpha)} \tag{4.3}$$

* where P is normal bearing force on deformation with unit area, F is friction force on deformation with unit area, R is resultant of P and F, R_r is radial component of R, u is

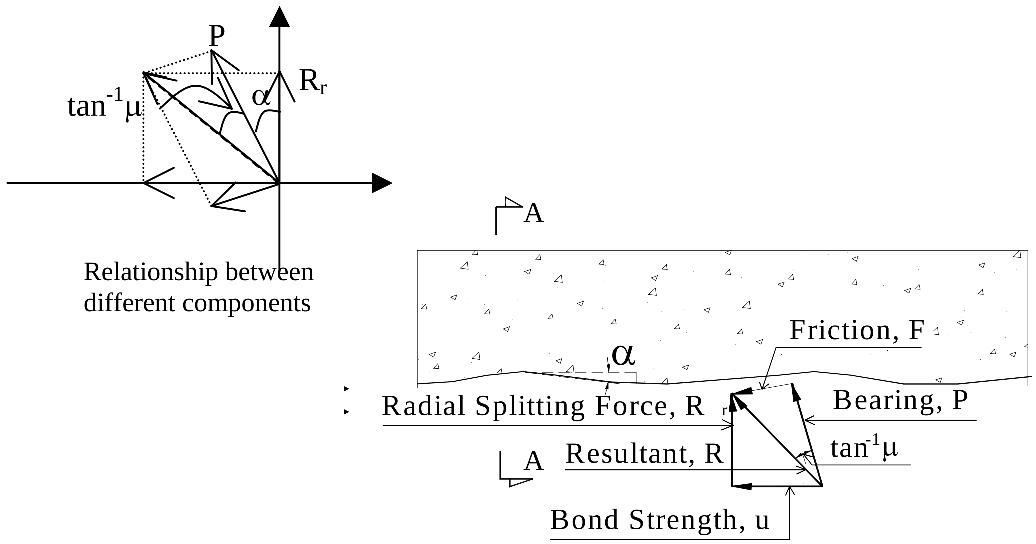

Figure 4.14. Relationship between Bond Strength and Splitting Force

longitudinal component of R=bond strength, T is pullout force, μ is friction coefficient, and α is rib angle.

The pullout force is then expressed by:

$$T = \frac{\pi(\mu + \tan\alpha)}{1 - \mu\tan\alpha} \times F_{split} \tag{4.4}$$

It is assumed that the splitting tensile strength is reached and uniformly distributed along the splitting plane at the ultimate stage because of the plasticity of the concrete. Therefore,

$$F_{split} = f_{ct} A_{split} \tag{4.5}$$

Substituting Equation 4.5 into Equation 4.4 results in

$$T = \frac{\pi(\mu + \tan\alpha)}{1 - \mu\tan\alpha} \times f_{ct} A_{split}$$

Finally, the bond strength, u, is expressed by:

$$u = \frac{T}{\pi d_b l_d} = f_{ct} \frac{\mu + \tan\alpha}{1 - \mu\tan\alpha} \frac{A_{split}}{d_b l_d} \tag{4.6}$$

where A_{split} is the concrete splitting area, and f_{ct} is the splitting tensile strength. f_{ct} has been related to $\sqrt{f_c^{'}}$ in many publications. According to Carrasquillo et al. (1981), f_{ct} is approximated by $f_{ct} = 6.8(f_c^{'})^{0.5}$ in psi and $f_{ct} = 0.56(f_c^{'})^{0.5}$ in MPa. It is assumed that the tensile strength will not be changed with the addition of a small amount of polypropylene fibers.

Based on results reported in Table 4.3, by assuming μ equals 0.45, predictions of the bond strength correlated well with the test results.

Table 4.3. Comparison of bond strength between prediction and experiment

$f_c^{'}$ (psi)	d_b (in.)	α degree	u_{test} (psi)	μ=0.4		μ=0.45		μ=0.5	
				U_{theo} (psi)	$\frac{u_{test}}{u_{theo}}$	$u_{pred.}$ (psi)	$\frac{u_{test}}{u_{theo}}$	$u_{theo.}$ (psi)	$\frac{u_{test}}{u_{theo}}$
7,400	0.5	2	2,850	2,263	1.25	2,524	1.12	2,785	1.02
7,400	1	5	2,644	2,553	1.04	2,814	0.94	3,075	0.86
5,360	0.5	2	2,352	1,929	1.22	2,146	1.09	2,379	0.99
5,360	0.5	2	2,070	1,929	1.07	2,146	0.96	2,379	0.87

Equation 4.6 shows good correlation for bond strength controlled by concrete splitting. In this study, it is assumed that deformation of the FRP bar is strong enough to prevent itself from being sheared off. This assumption is generally valid in normal strength concrete, especially for the rebar with deformations with small angles to the longitudinal direction, like the GFRP used in this study. The FRP rebar with steep deformations (as shown in Figure 4.6b) will produce larger shear stresses on the ribs, even when they have the same projected rib areas (i.e. the same h_r), and thus, the ribs are easier to be sheared off. When the bond behavior is governed by the rib shear strength other than concrete splitting, Equation.4.6 is no longer valid.

4.2.3 Basic Development Length

The application of the ultimate bond strength data to real design is not appropriate because of the excessive slip occurring in these specimens at large loads. Too much slip will result in intolerable crack widths. Although FRP rebars were relatively inert to environmental exposure, the slip may cause some other problems, e.g., aesthetics. For traditional steel reinforced structures, ACI 318-02 requires a maximum crack width of 0.016 in. for interior exposure and 0.013 in. for exterior exposure. ACI 440 recommends crack limitation for FRP structures to be 0.020 in. and 0.028 in. for exterior and interior exposure, respectively. From a designer's point of view, Mathey and Watstein (1961) suggested that bond stress corresponding to 0.01 in. slippage of loaded end or 0.002 in. of free end for steel reinforced structures can be defined as critical bond stress. The criterion of 0.01 in. slippage at loaded-end was decided based on half of the crack width limitation. In a study conducted by Ferguson et al. (1965), the researchers discovered that the loaded-end slip of the pullout specimens was larger than that of the beam specimens because flexural cracks in beam specimens tended to distribute the slip in several places along the beam. Also, since there is relatively low elastic modulus of FRP materials (GFRP is about 1/5 that of steel, CFRP is about 2/3 that of steel), greater elongation along the embedded rebar will be produced and lead to larger loaded-end slip. Thus, 0.01 in. slippage at the loaded-end of pullout specimens as design criterion is too conservative. To keep it comparable to limits imposed on steel rebar, bond strength corresponding to 0.002 in. slippage at the free-end is recommended as designing bond strength.

For an FRP rebar, the basic development length, l_{db}, is defined as the minimum embedment length required to develop fracture tensile strength, f_{fu}, of the FRP rebar.

Based on the equilibrium equation, $l_{db} \pi d_b u = A_f f_{fu}$ results in:

$$l_{db} = \frac{A_f f_{fu}}{\pi d_b u} \tag{4.7}$$

Referring to ACI 318-02, the development length of the rebar is expressed as follows:

$$l_d = \frac{f_{fu}}{K\sqrt{f_c^{'}}} d_b \tag{4.8}$$

Equating (4.7) to (4.8) gives an expression to the coefficient $K = \frac{4u}{\sqrt{f_c^{'}}}$

where A_f = area of the FRP bar in in.^{2}; f_{fu} = ultimate strength of FRP bar in psi, $f_c^{'}$=concrete strength, psi., d_b = diameter of FRP rebar in in., and u = bond strength in psi.

A statistical analysis was performed on the design bond strength. Assuming the test results were distributed as Student "t" distribution, the bond strength with 95% confidence was computed as $\bar{u} - t\frac{s}{\sqrt{n}}$, where t is t distribution quantity, and is equal to 2.353 for 95% confidence in the case of three specimens; $\bar{u}$ is the average bond strength; s is the standard derivation; n is the number of the test specimens, in this study n = 3. Thus, a coefficient K =

42 was obtained. As mentioned previously, specimens after fatigue loading have higher bond stiffness and capacity. Thus, this equation can also be safely used in the fatigue loading situations.

If adjusting the development length to the AASHTO format, the equation used for development length is:

$$l_{db} = 0.05\frac{A_f f_{fu}}{\sqrt{f_c'}} \text{ (in)} \tag{4.9}$$

where A_f= area of the FRP rebar, in^2.

A K value of 0.04 is adopted by AASHTO for the steel reinforcement. Based on this study, the development length for the FRP bars is recommended to be 25% larger than that of the steel bar.

4.3 SPLITTING BOND TESTS

4.3.1 Test Results and Discussions

In the following sections, the observations from the tests and several parameters that would influence the bond characteristics will be discussed. These parameters included the fiber effect by volume fraction (V_f), cover effect (C_b), and rebar diameter (d_b).

The average bond strength is calculated as the pullout force over the embedded area of the rebar. When comparing the bond strength of specimens with different concrete strengths, f_c', bond strength was normalized by dividing by the square root of f_c', which is adopted in the current AASHTO Code.

Cracks, if any, initiated from the loaded end and propagated to the free end. Following this, some cracks deviated from the longitudinal direction to the transverse direction. Crack patterns observed on the outside of the specimens are shown in Figure 4.15 and listed in Table 4.4.

After failure, concrete covers were removed from the specimens to allow inspection of the surface conditions of the rebars after testing. No major differences were observed between the FRC specimens and the plain concrete specimens. The following are some of the observations (see Figure 4.16):

(a) Crack patterns in #4 CFRP with 1 d_b cover in plain concrete and FRC

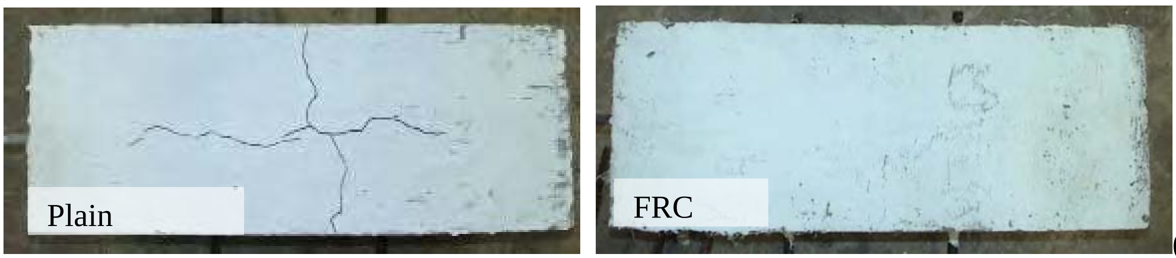

(b) Crack patterns in #4 CFRP with 3 d_b cover in plain concrete and FRC

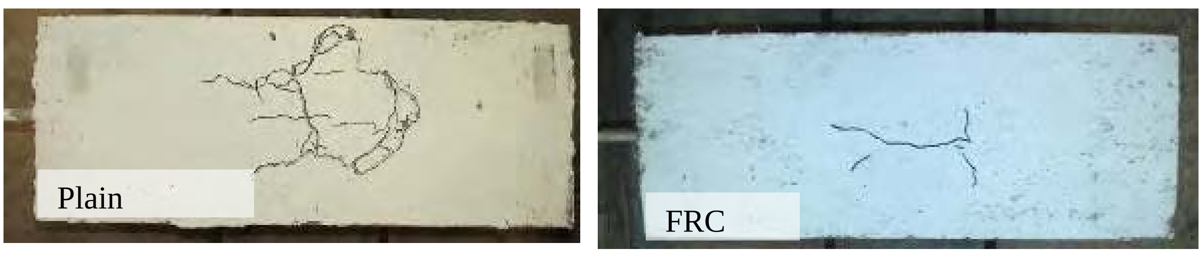

(c) Crack patterns in #4 GFRP with 1 d_b cover in plain concrete and FRC

Figure 4.15. Crack patterns in specimens showing effect of C_b and V_f (cont'd..)

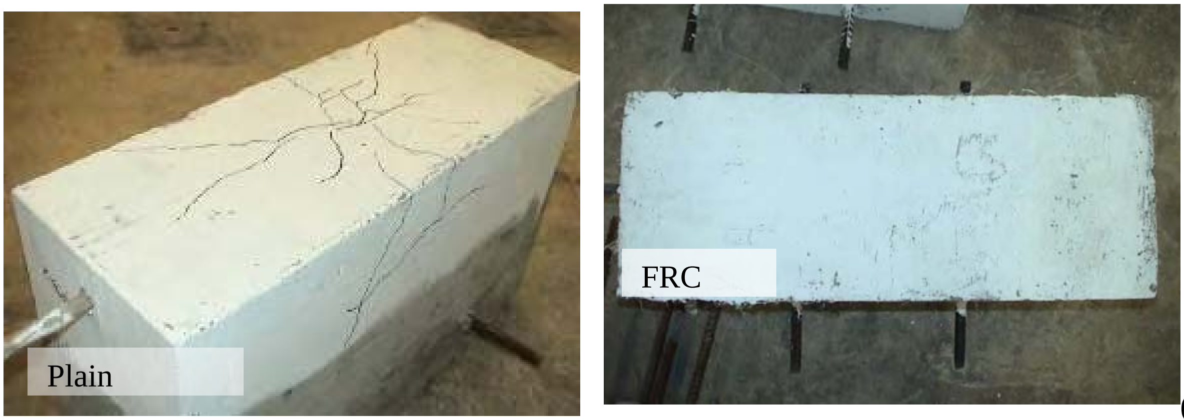

d) Crack patterns in #4 GFRP with 3 d_b cover in plain concrete and FRC

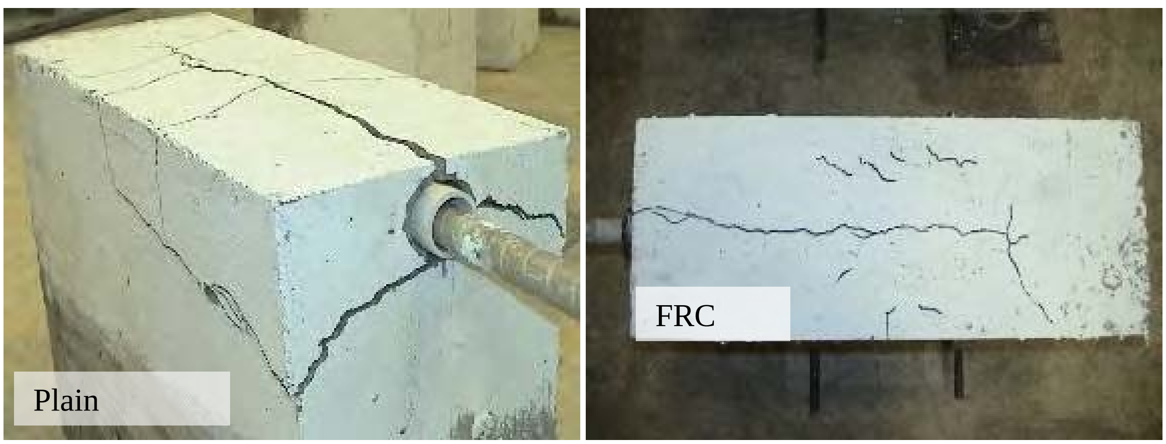

(e) Crack patterns in #8 GFRP with 1 d_b cover in plain concrete and FRC

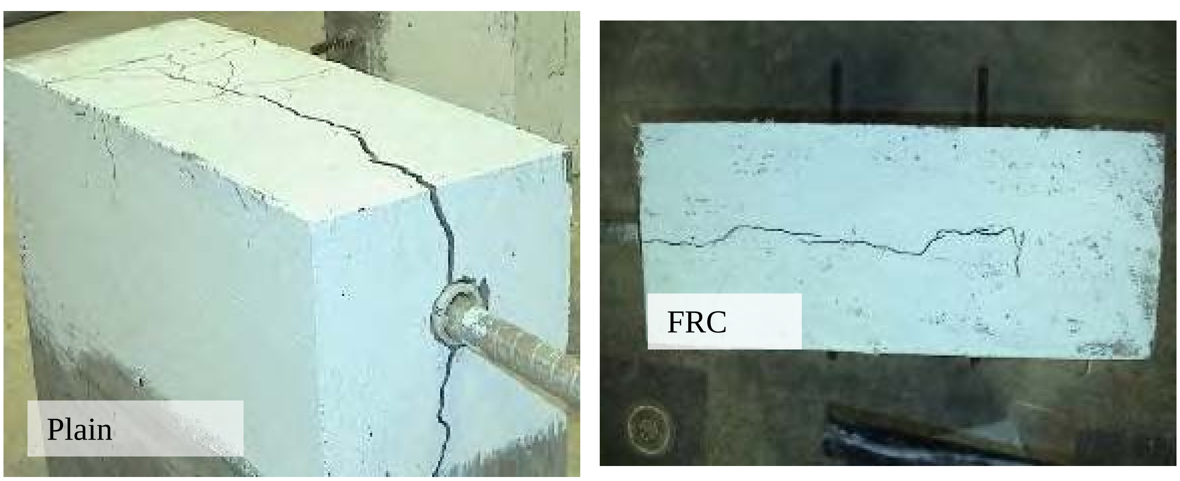

(f) Crack patterns in #8 GFRP with 3 d_b cover in plain concrete and FRC

Figure 4.15. Crack patterns in specimens showing effect of C_b and V_f

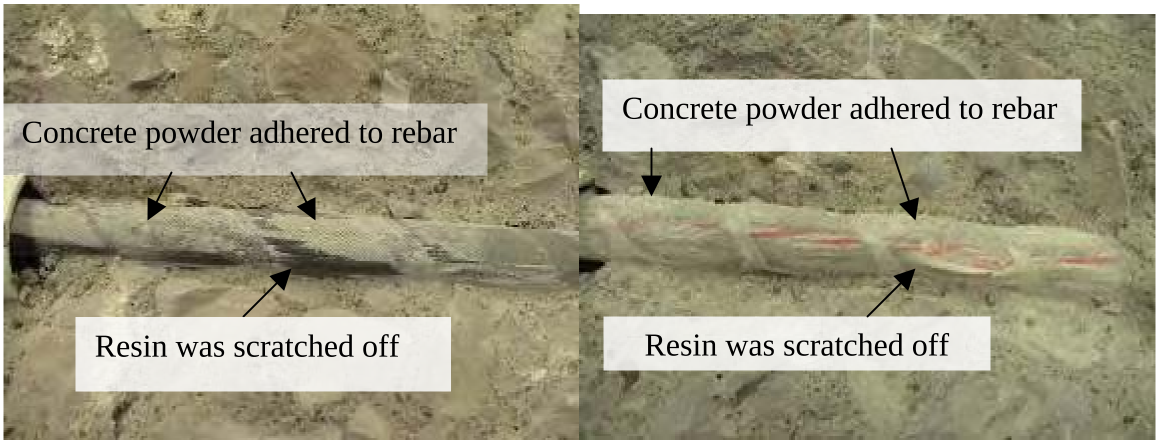

Figure 4.16. Surface condition of FRP rebars after testing

Table 4.4. Description of test results

I.D.	Failure Mode	Splitting Crack Width	Descriptions
4PC1	Splitting	0.001 in.	One longitudinal crack along the embedment portion developed first, and then the concrete cover at the embedment portion spalled.
4PC3	Splitting	0.007 in.	One longitudinal crack along the embedment portion developed and extended toward the front face but did not reach the front face. Transverse flexural cracks were also observed.
4PG1	Splitting	0.035 in.	Concrete cover spalled at the embedment portion. No cracks at side faces were observed.
4PG3	Splitting	0.011 in.	Longitudinal splitting crack developed and extended toward the front face but did not reach the front face. Transverse flexural cracks were observed. Cracks at side faces developed at the embedment portion. No cracks at the front face were observed.
8PG1	Splitting	0.2 in.	One big crack went through from front face to the free end, accompanied by several transverse cracks induced by bending. Two large cracks were also observed at the front face. They extended along the side faces and finally connected with the longitudinal crack at the surface, splitting the concrete into several pieces.
8PG3	Splitting	0.25 in.	One large crack crossed from front face to the free end and extended down to the bottom at the front face; it almost split the concrete into halves. Several transverse cracks also were observed.
4FC1	Splitting	0.001 in.	One crack developed and was limited to the embedment

			region.
4FC3	Pullout	N/A	
4FG1	Splitting	0.003 in.	One crack developed and was limited to the embedment region.
4FG3	Pullout	N/A	
8FG1	Splitting	0.015 in.	One longitudinal crack developed at the embedment portion, extended to the front face, and then went down to the rebar.
8FG3	Splitting	0.009 in.	One longitudinal crack developed at the embedment portion, extended to the front face, and then went down to the rebar.

Note: (1) See Figure 4.15 for crack patterns.
(2) Results and descriptions are based on two duplicate specimens.
(3) Splitting crack width was measured by microscope.

In the GFRP specimens, some resin of the rebar was scratched off the rebar surface and remained attached to the concrete. The indentation shape of the GFRP rebar was not changed, showing that the transverse direction of the rebar could sustain the bearing compression force. Traces of concrete were observed on the rebar surface, which revealed a good chemical bond between the rebar and the concrete.

In the CFRP specimens, some resin was scratched off the rebar surface and remained glued to the concrete surface. Traces of concrete were observed on the rebar surface, which revealed a good chemical bond between the rebar and the concrete.

4.3.1.1 Fiber Effect on Bond Characteristics

In the following sections, the fibers' effects on the bond characteristics, in terms of crack patterns and bond slip response, are discussed.

(a) Splitting Crack Patterns

The following are some of the different observations regarding the crack patterns between the plain concrete specimens and the FRC specimens.

All the plain concrete specimens failed by concrete splitting. Most of the FRC specimens failed also by concrete splitting, except for the #4 CFRP and #4 GFRP specimens with 3 d_b cover, which failed by rebar pullout. The width of the splitting cracks was smaller in the case of the FRC specimens, which revealed that the fibers could effectively restrict the development of cracks. Concrete spalling was observed in several plain concrete specimens, but it did not occur in the FRC specimens. Since concrete spalling is a sign of more severe damage of concrete cover, one could say that with the addition of fibers, the damage is less severe compared to the plain concrete specimen. When specimens failed by concrete splitting, the FRC specimens failed in a much more ductile fashion.

(b) Bond-Slip Response

The bond-slip curve could roughly be divided into two portions, the ascending portion and descending portion. The fibers showed some effects on the overall bond-slip curves. In the ascending portion (as shown in Figure 4.17), the plain concrete and FRC specimens did not show any significant difference. At the initial loading stage, the bond-slip curves increased linearly. Since no splitting cracks were developed, the bond stiffness was quite high. At about 50% to 80% of the ultimate capacity, the splitting micro-cracks developed. The stiffness of the bond-slip curve decreased accordingly.

In the descending portion, the confinement from the concrete to rebar decreased with the propagation of the splitting cracks. Consequently, the pullout loads dropped. In the descending portion (as shown in Figure 4.17), significant differences were observed between the plain concrete specimens and the FRC specimens. In the plain concrete, after reaching its capacity, the load dropped suddenly to zero. However, in the FRC, after reaching the peak, with the presence of fibers, which limited the propagation of splitting cracks, the confinement force from the concrete was still relatively significant. Therefore, the bond-slip curve dropped gently and maintained at more than 70% of its capacity, even at the slip of 0.4 in.

4.3.1.2 Cover Effect on Bond Characteristics

The bond strength increased with the increase of the clear cover depth. The increasing rates differed for the different specimens, as shown in Figure 4.17 and Table 4.5. Before the bond reached the peak, the bond-slip curves for specimens with 1 d_b and 3 d_b were almost identical. Specimens with 1 d_b cover failed always with less capacity and smaller slips.

4.3.1.3 Diameter Effect on Bond Characteristics

The smaller diameter rebar had higher bond capacity, similar to the behavior of the traditional steel rebar, as shown in Table 4.5.

Table 4.5. Test Results of Beam End Tests

I.D.	Ultimate Bond Strength u (psi)	Ultimate Bond Strength* $u/\sqrt{f_c'}$ ($psi/\sqrt{psi}$)	Loaded-End Slip at Peak (in.)	Free-End Slip at Peak (in.)	Design Bond Strength u_{design} (psi)	95% of Design Strength (psi)
4PC1	943	12.48	0.011	0.001	904	863
4PC3	1,318	17.52	0.018	0.002	1,025	962
4FC1	357	6.00	0.003	0.004	454	428
4FC3	880	14.88	0.009	0.001	1,107	995
4PG1	1,607	21.24	0.038	0.002	1,072	1,012
4PG3	2,055	27.24	0.052	0.010	1,089	982
4FG1	1,279	21.60	0.037	0.011	1,146	1,054
4FG3	1,388	23.40	0.215	0.202	1,398	1,387
8PG1	969	12.84	0.020	0.002	844	696
8PG3	1,436	19.08	0.026	0.001	957	848
8FG1	893	15.12	0.019	0.002	976	964
8FG3	1,179	19.92	0.162	0.132	975	954

(1) Numbers are the average values for two testing specimens.
(2) The asterisk indicates the bond strength normalized to square root of concrete strength.

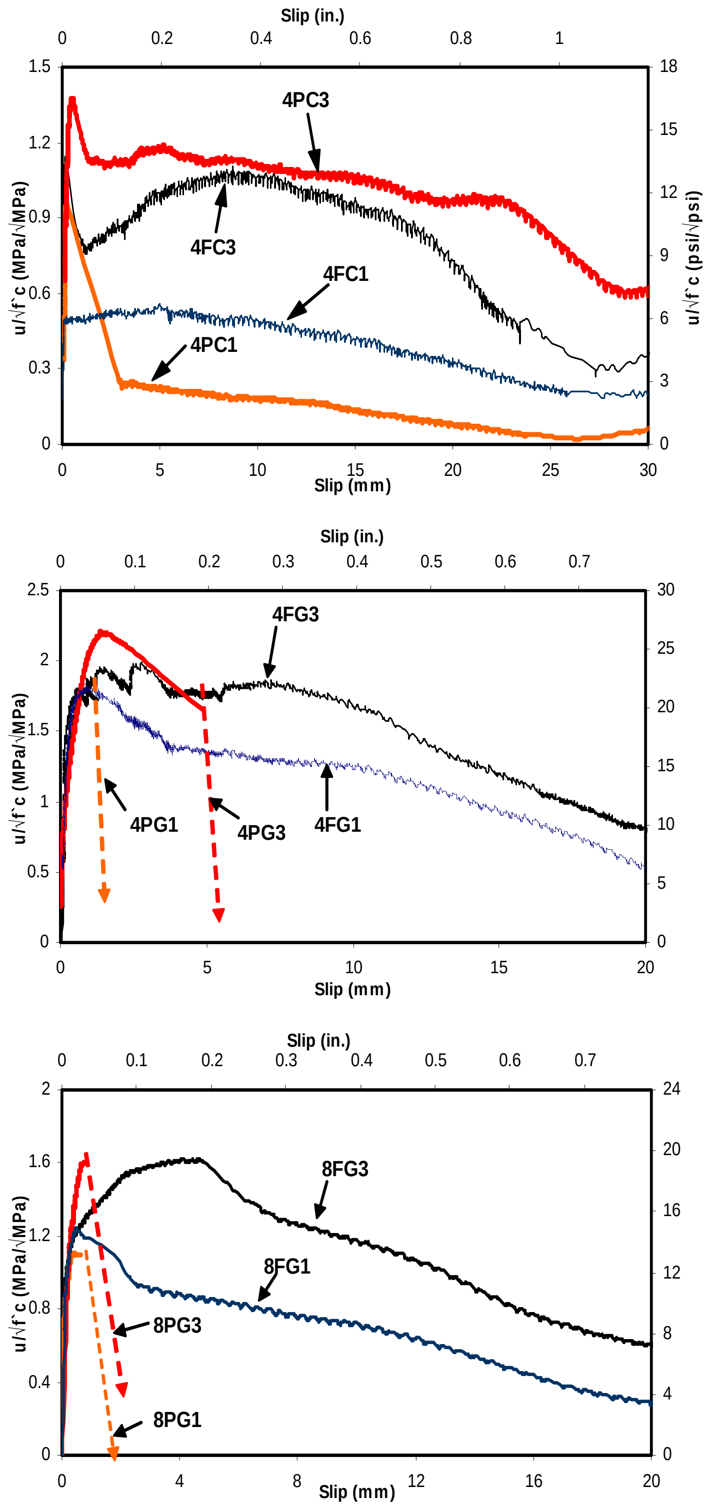

Figure 4.17 Bond-slip relationship of various rebars in plain concrete and FRC (a) Top - #4 CFRP, (b) Middle - #4 GFRP, and (c) Bottom - #8 GFRP

4.3.2 Theoretical Prediction of Bond Strength

The theory used and described in pullout specimens should also be valid in beam end specimens since the bond mechanism is similar. However, the definition of the effective splitting area, A_{split}, is necessary before the direct application of Equation 4.6.
Several models have been developed for the bond strength prediction of the traditional steel rebar. In these models, an assumption is commonly used: concrete within the cylinder or square (the largest square or circle that can be drawn within the beam section around the rebar, as shown in Figure 4.18) is regarded as the effective portion to prevent the beam from splitting. In other words, the contribution from the portion outside the cylinder or square is ignored (Kemp, 1986). This theory does not consider the beam-width effect on bond strength. Two beams, as shown in Figure 4.18, should have the same bond strength based on this theory, since they have the same area of concrete to resist the beam from splitting. However, research showed that the width of the beam could influence the bond strength and that wider beams resulted in higher bond strength (Chinn et al., 1955; Ferguson and Thompson, 1962). This phenomenon reveals that concrete outside the circle or square has a noticeable effect on bond strength and cannot be ignored. Wider beams have more concrete to prevent beams from splitting. In other words, the effective splitting area increases with the increasing of the beam width. Apparently, it is the effective beam width rather than the total beam width that influences the bond strength.

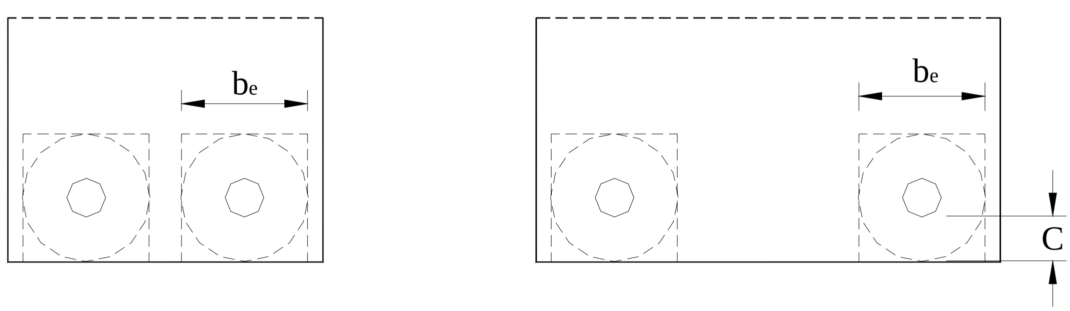

Figure 4.18. Previous definition of contribution from concrete

Based on the above explanation, schematic pullout specimens (rectangular concrete blocks surrounded by dash lines with an area of $b_e \times (l_e + d_b + C)$, as shown in Figure 4.19), are used to represent the beam to describe its bond mechanism. Thus, the approach used in the pullout specimens can be applied to the beam situation. The effective splitting area, as shown in Figure 4.19b, is taken as

$$A_{split} = (l_e + C)l_d \tag{4.10}$$

where l_e is the effective splitting length, and l_e is a function of effective beam width. In this analysis, l_e is assumed to be equal to $b_e/3$ in this study and b_e is the effective beam width, from center to center of the rebar spacing or from the edge of the beam to the center of the rebar spacing. Substituting Equation 4.9 into Equation 4.6 and taking $l_e=b_e/3$ results in the following:

$$u = \frac{(3C + b_e)}{3d_b} \times \frac{\mu + \tan\alpha}{1 - \mu\tan\alpha}\, f_{ct} \tag{4.11}$$

To test the correlation of Equation 4.11, a comparison was made between test results and predictions, as shown in Table 4.6. Since Equation 4.10 is based on the assumption that the specimen fails in concrete splitting, only specimens that failed in this mode were included. As shown in Table 4.6, the predictions of Equation 4.11 are close to the test results but are consistently lower by about 10% than those of the test results. Bond strength is highly dependent on the embedment length as well. Specimens with longer embedment length usually result in lower average bond strength. To account for this, an adjustment factor, γ, is added to reflect the embedment length. Thus, Equation 4.11 becomes

$$u = \frac{(3C + b_e)}{3d_b} \times \frac{\mu + \tan\alpha}{1 - \mu\tan\alpha}\, \gamma f_{ct} \text{ psi} \tag{4.12}$$

in which γ is a function of embedment length, based on the current test results, where $l_d=10d_b$, γ can be taken as 0.9. Further study is needed to look into various embedment lengths and other situations, such as the effect of different fiber volume fraction.

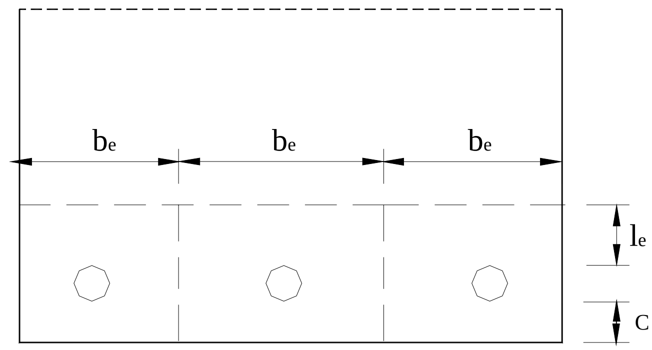

(a) Schematic pullout specimens in a beam

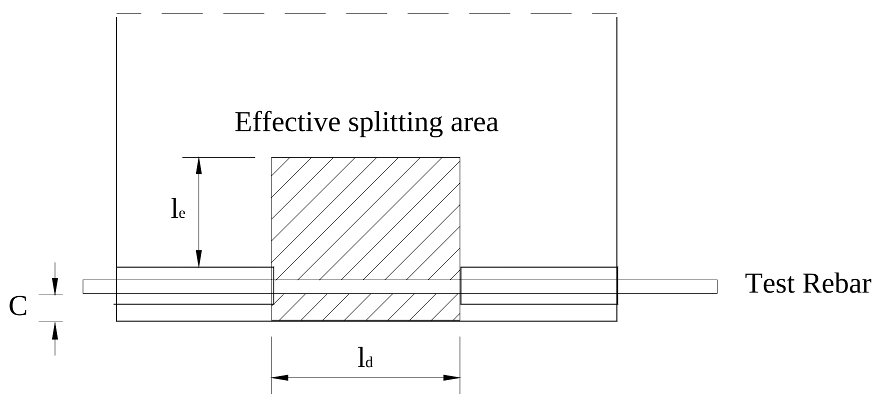

(b) The effective splitting area (hatched area)

Figure 4.19. Definition of splitting area for splitting-bond specimen

4.3.3 Basic Development Length

By adopting the same methodology used in the pullout tests, a similar expression based on the test data from splitting bond test was developed for the basic development length for the FRP rebars embedded in FRC. Based on the test data from a total of 24 specimens, (The #4 CFRP with 1 d_b cover was not considered, which had much lower bond strength value when compared to the other cases. This may be due to the ill vibration during fabrication of the specimen. A statistical analysis with 95% confidence was conducted (the method is the same as that conducted in pullout bond test). The following expression was obtained

$$l_{db} = \frac{f_{fu} d_b}{37\sqrt{f_c^{'}}} \text{ (in.)} \tag{4.13}$$

Also, by adjusting the format to the AASHTO, the development length can be computed as the following expression:

$$l_{db} = 0.056 \frac{A_f f_{fu}}{\sqrt{f_c^{'}}} \text{ (in.)} \tag{4.14}$$

As mentioned previously, a K value of 0.04 is adopted by AASHTO for the steel reinforcement. Based on this study, the development length for the FRP bars is recommended to be 40% larger than that of the steel bar.

Table 4.6. Comparison of Bond Strength between Prediction and Experiment

Specimen I.D.	f`c (psi)	C/d_b	d_b (in.)	b_e (in.)	α degree	u_{test} (psi)	u_{theo} (psi) Eq. (9)	$\frac{u_{test}}{u_{theo}}$
4PG1	5656	1	0.5	9	2	1588	1743	0.91
4PG3	5656	3	0.5	9	2	2055	2241	0.92
8PG1	5656	1	1	9	5	969	1131	0.86
8PG3	5656	3	1	9	5	1436	1697	0.85
4FG1	3480	1	0.5	9	2	1279	1368	0.94
8FG1	3480	1	1	9	5	893	888	1.01
8FG3	3480	3	1	9	5	1179	1331	0.89
Average								0.91
COV								0.05

The development length derived based on the beam tests are slightly larger (approximately 10%) than that obtained from the pullout bond test. As we discussed previously, the pullout bond specimen is under compression in the case of pullout bond tests, which will induce confinement effect on the bond and result in larger bond strength. Consequently, the development length computed by the pullout test method is smaller. Since the stress condition in beam end specimens are closer to the real conditions, Equation 4.13 or 4.14 is recommended as the equation to calculate the development length for FRP reinforcement.

ACI 440 recommendations for the development length is:

$$l_{db} = \frac{f_{fu} d_b}{2700} \text{ (in.)} \tag{4.15}$$

By assuming the concrete strength of 5000 psi, one can see that the development length computed by Equation 4.15 is very close to ACI 440 recommendations.

4.4 FLEXURAL BOND TESTS

Flexural bond tests were performed on concrete specimens reinforced with one of three types of bars including #4 CFRP, #4 GFRP and #8 GFRP reinforcing bars. Specimens were cast in four batches. Batches 1 and 3 used a plain concrete matrix and Batches 2 and 4 used a fiber-reinforced concrete (FRC) matrix. The flexural bond test program has been detailed earlier in Table 3.4 and described in Section 3.3.3.

4.4.1 Results from the Static Tests

4.4.1.1 Failure Modes

Figures 4.20 and 4.21 show two typical static load-deflection plots. Two types of failure modes can be observed in the flexural bond tests. Mode 1 is characterized by the failure of the frictional bond between the reinforcing bar and the surrounding concrete. A large amount of reinforcement slip is observed in this failure mode. Mode 1 failure was consistently observed in the failure of #4 CFRP reinforced specimens. Figure 4.20 shows the typical load-deflection response for such a specimen.

Mode 2 failure is characterized by shear failure of the concrete matrix precipitated by initiation of bond-splitting cracks. The shear failure results from the geometry of the specimen (shear span to effective depth ratio). Little end slip is observed in specimens that fail in this manner (classified as bond-splitting failure). All specimens reinforced with #4 and #8 GFRP bars failed due to bond splitting. A typical Mode 2 load-defection response curve is illustrated in Figure 4.21.

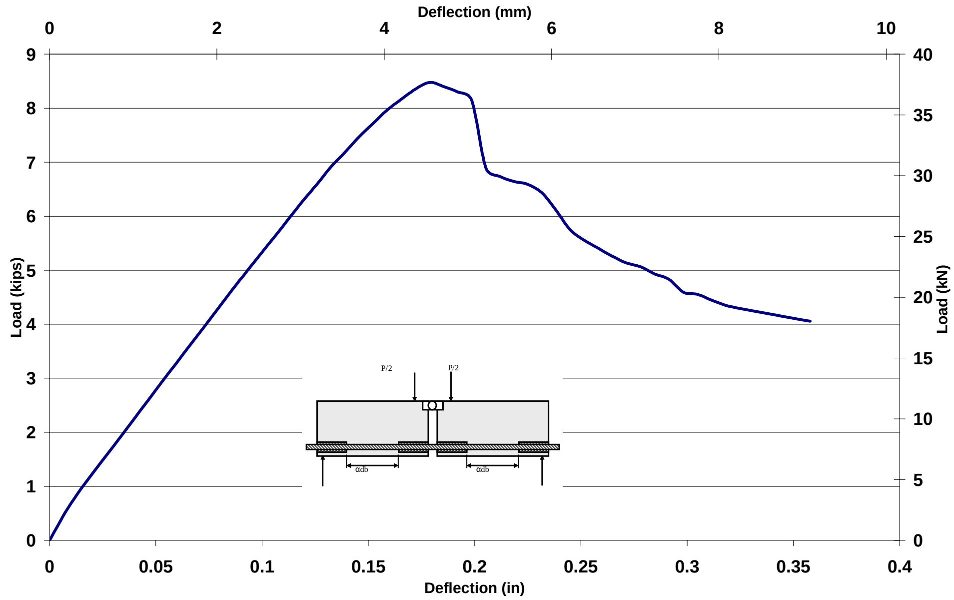

Figure 4.20 Static load-deflection response of specimens using #4 CFRP reinforcement bars showing bond failure due to slip (Mode 1 Failure)

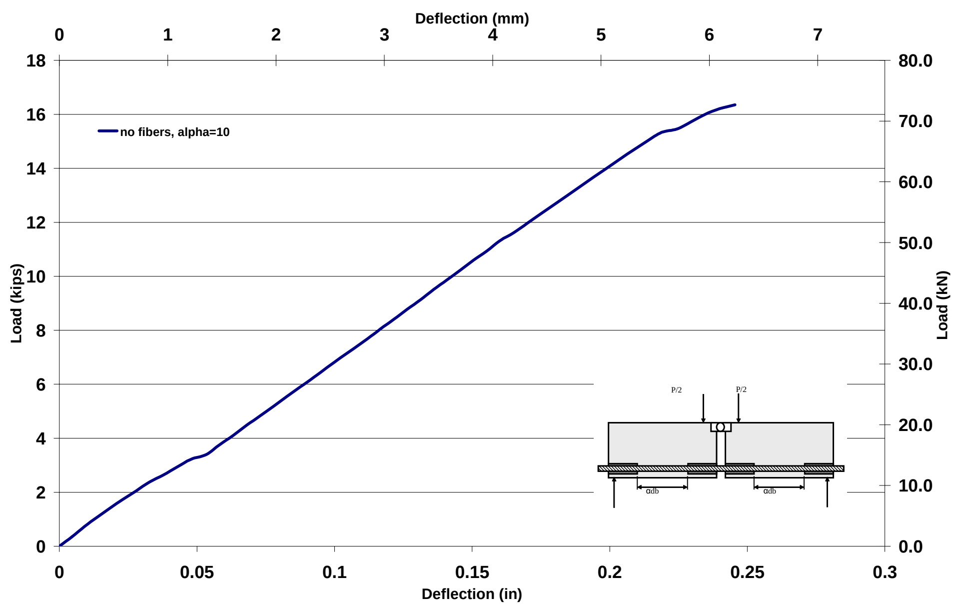

Figure 4.21 Static load-deflection response of specimens using #8 GFRP reinforcement bars showing bond splitting failure (Mode 2 Failure)

Mode 1 and Mode 2 failures are different in several ways. For one, Mode 1 failures are gradual with an early pullout initiation followed by a gradual degradation in stiffness due to progressive failure of the bond between the concrete and the reinforcement. Mode 2 failures are catastrophic in nature as the specimen exhibits a relatively elastic load-deflection response until failure is initiated. In most cases, catastrophic crack growth immediately follows crack initiation. The resultant strength loss is abrupt. Figure 4.22 includes schematic diagrams depicting the two modes of failure observed. In principle, Mode 2 failure is dominated by concrete strength and geometry effects of the test configuration and hence should not be considered as bond failures. Even so, one can assume that capacity from such failures can be used to provide a lower bound estimate of bond strength in such cases.

4.4.1.2 Load Capacity

Table 4.7 summarizes the maximum capacities of the statically loaded flexural bond test specimens.

Static test specimens reinforced with CFRP all exhibited Mode 1 failure. Failure in the #4 CFRP specimens was induced by slip and pullout of reinforcement. Increase in strength as the bonded length is increased from 10 to 20 times d_b can be observed. The bond strength of the specimen is related to the bonded area of the reinforcement. Therefore, as the bonded area increased, the overall strength of the specimen will increase as well until the length is sufficient enough to initiate another type of failure.

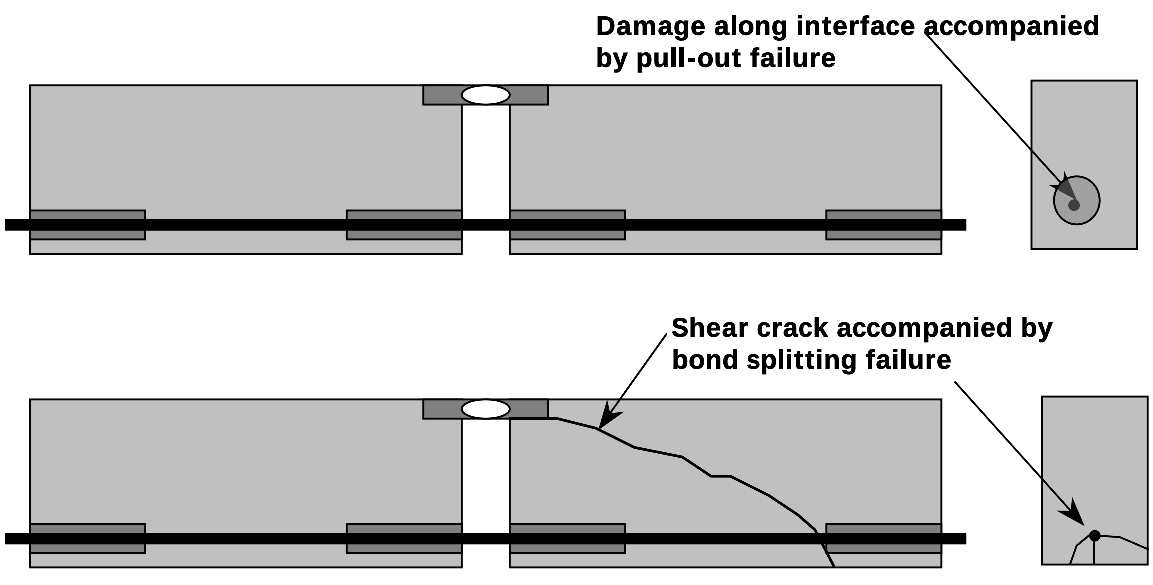

Figure 4.22 Schematic diagrams showing Mode 1 (top) and Mode 2 (bottom) failures

Table 4.7 Summary of static test results

Reinforcement	Matrix	Bonded Length α	αd_b (in)	Peak load (lbs)	Bar stress at peak load (ksi)
# 4 CFRP	Plain Concrete	10	5	8,400	67
		20	10	13,000	47
	FRC	10	5	6,000	104
		20	10	8,400	67
# 4 GFRP	Plain Concrete	10	5	14,100	84
		20	10	15,300	91
	FRC	10	5	8,300	49
		20	10	13,300	79
# 8 GFRP	Plain Concrete	10	10	14,000	21
		20	20	14,200	21
	FRC	10	10	13,900	21
		20	20	18,800	28

Values reported in the table are based an average of two specimens

The nature of the flexural bond test allows reliable determination of the stress in the reinforcing bar at any time during the test. This is because of the well-defined locations of the application of the compressive thrust (hinge center) and the tensile force in the reinforcement, and as a result the moment arm distance. The tensile stresses in the reinforcement bars at failure of the flexural bond specimens are listed in Table 4.7.

The CFRP bars have only limited surface deformations and as a result bond is primarily governed by bonding area between the reinforcing bar and the surrounding concrete. At short bonded lengths (α = 10), the normal stress in the reinforcing bar at failure of the flexural bond specimen is approximately 25% of the ultimate tensile capacity.

The bond developed between the reinforcing bar and the concrete is a function of the bonded length as well as the compressive strength of the concrete. As mentioned earlier, the two fiber reinforced concrete (FRC) mixes had significantly lower compressive strengths than the plain concrete mixes. This is most likely the reason for the lower failure loads observed in the FRC flexural bond specimens. This reduced strength of the FRC matrices makes analysis of the results more complicated. Since interface failure is associated with shear strength of the concrete matrix, if one were to normalize the maximum load capacity of the bond specimens with respect to $\sqrt{f_c'}$, it would mitigate most of the influence of the differences in matrix strengths (between plain concrete and FRC, where f_c' is the compressive strength of the matrix).

Specimens reinforced with GFRP rebars (both #4 and #8) exhibited Mode 2 failure. Due to the more pronounced surface deformations of the GFRP bars (ribbed bars with a “sand” coating), even the smaller bonded length of $10d_b$ used in this study generated adequate bond capacity to initiate splitting failure that eventually progressed into shear failure in the concrete matrix. Table 4.7 includes the ultimate load capacities of bond specimens made using GFRP reinforcing bars.

Given the excellent bond between the concrete and the GFRP reinforcing bars, two types of failures are possible. If adequate cover is available, the bars can develop high tensile stresses resulting in rupture of the bars. If the cover available is limited as is the case of bridge deck slabs, the good bond will lead to a bond-splitting failure in the concrete matrix. Both types of failures are relatively brittle compared to a pull-out failure described earlier for the CFRP reinforced flexural bond specimen.

Due to differences in the ratio of the bonded area to the cross-sectional area of the reinforcements used, the flexural bond specimens reinforced with #4 GFRP bars were able to attain stresses approaching their ultimate tensile strength, while the specimens reinforced with #8 GFRP bars were stressed to less than a third of their ultimate tensile strength.

Since the GFRP bar reinforced bond specimens develop adequate bond even at a bonded length of $10d_b$, one would expect no significant increases in the maximum capacity of the flexural specimens with larger bonded lengths. This was what was generally observed (Table 4.7). Small differences can be attributed to the differences in concrete compressive strength variations between different batches of concrete cast and also some differences in the age that the flexural-bond specimens were tested.

4.4.1.3 <u>Reinforcement Slip</u>

In Mode 1 failure (reinforcement pullout), the major contributor to bond strength between the reinforcement and the concrete is frictional resistance from shear transfer at the interface. In the case of Mode 2 failure (bond splitting), the dominant bond strength mechanism can be attributed to mechanical interlock resulting in local bearing stresses and resultant radial cracking in the matrix.

Mode 1 failures were observed in static tests of the #4 CFRP reinforced specimens and are characterized by large amount of end slip prior to failure. End slips were measured using two 0.1-inch LVDT fixed to the protruding ends of the reinforcing bar as described earlier in Chapter 3.

End slip in the #4 CFRP specimens begins almost instantaneously once load is applied to the specimen (Fig. 4.23). At low load levels elastic bond ensures small magnitude of slip linearly related to the applied load. Once elastic bond is broken, and progressive debonding occurs near the peak load, further load transfer and pull-out at the interface is largely due to frictional bond. At large slip magnitudes, the specimen stiffness (defined as the instantaneous slope of the load-deflection curve) decreases gradually. Since bond strength in a frictional pullout type of failure mode is directly related to the bonded area, smaller magnitude of bonded area results in smaller pull-out load capacities.

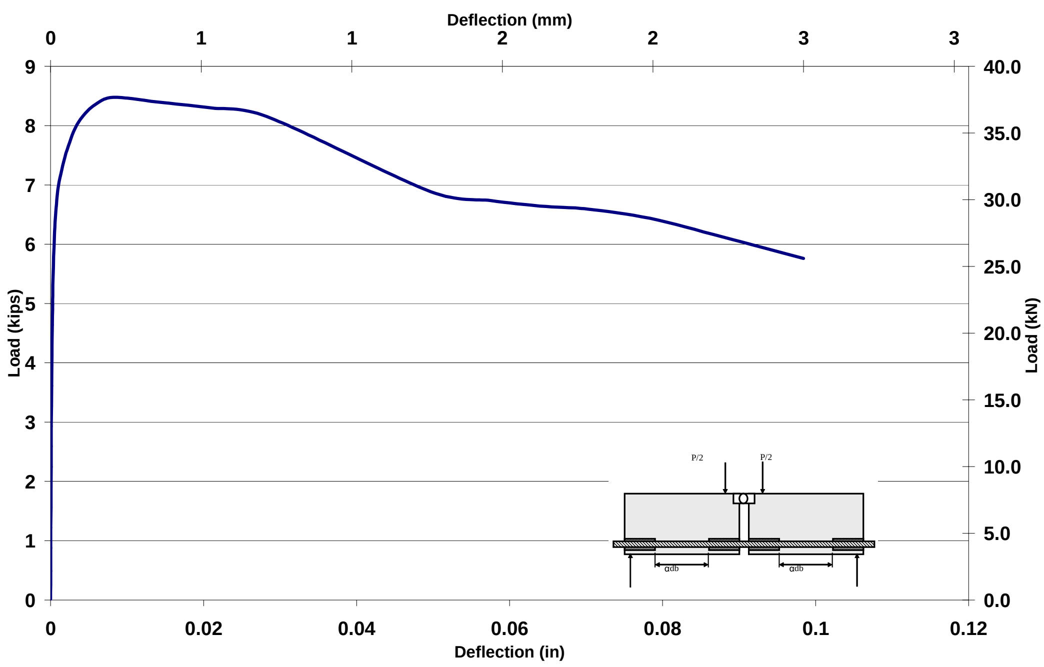

Figure 4.23 Load-End-slip response of specimen reinforced with #4 CFRP reinforcement

For both the #4 and #8 GFRP bar reinforced specimens bond-splitting failures were observed (Mode 2 Failures). With this type of failure, mechanical interlock (local bearing) serves as the main contributor to the bond strength of the specimen. Figure 4.24 shows a typical load - end slip response for a bond splitting failure. Slip values prior to initiation of failure are very small, on the order of 0.0005 inch. Since only a small amount of slip takes place until catastrophic failure, there is no gradual degradation of stiffness prior to specimen failure. It is noted that in Figure 4.21, the load-deflection response is relatively linear until catastrophic failure of the specimen.

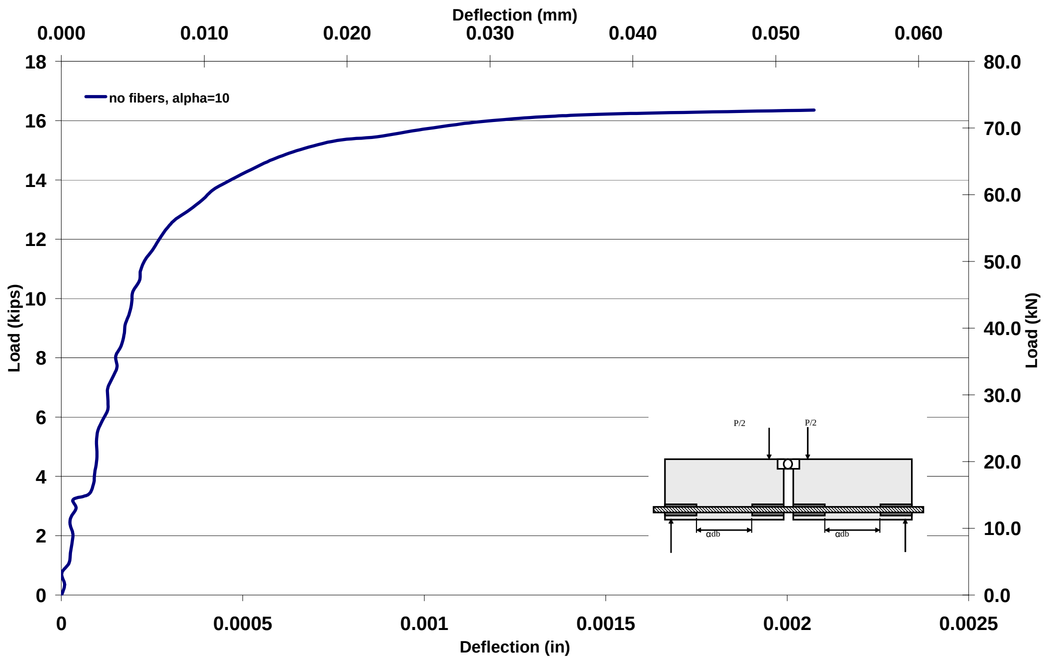

Figure 4.24 Load – End-slip response of specimen reinforced with #8 GFRP reinforcement

4.4.1.4 <u>Effects of Fiber Reinforced Concrete</u>

Figures 4.25, 4.26 and 4.27 show the load-deflection responses of #4 CFRP, #4 GFRP and #8 GFRP reinforced specimens, respectively, (at a bonded length of $10d_b$) for specimens that use plain concrete and FRC matrix. It can be observed that fibers in the matrix do not improve the ultimate capacity of the flexural bond specimens under static loading conditions. Their effects however become quite significant under fatigue loading

4.4.1.5 <u>Effects of Bonded Length</u>

Bond strength of the reinforcing system is directly related to the bonded length of the reinforcing bar. In the case of #4 CFRP reinforced specimens, bonded lengths of $10d_b$ and

$20d_b$ were insufficient to prevent pullout type failure. Figure 4.28 shows the load-deflection response for plain concrete specimens reinforced with #4 CFRP at both $10d_b$ and $20d_b$. Because the smooth surface of the CFRP bar creates difficulty in developing bond with the concrete, doubling the surface area of the reinforcing bar improves the developed bond strength and therefore the overall specimen strength.

Figure 4.29 and 4.30 show similar load-deflection response curves for #4 and #8 GFRP reinforced specimens. In these cases, a bonded length of $10d_b$ is sufficient to develop the reinforcing bar to the point that bond splitting dominates the failure. Therefore, the maximum bond strength is never seen at a bonded length of $10d_b$, so the increase of bond length to $20d_b$, although providing more bond strength capacity, does not add to the overall strength capacity of the beam specimen.

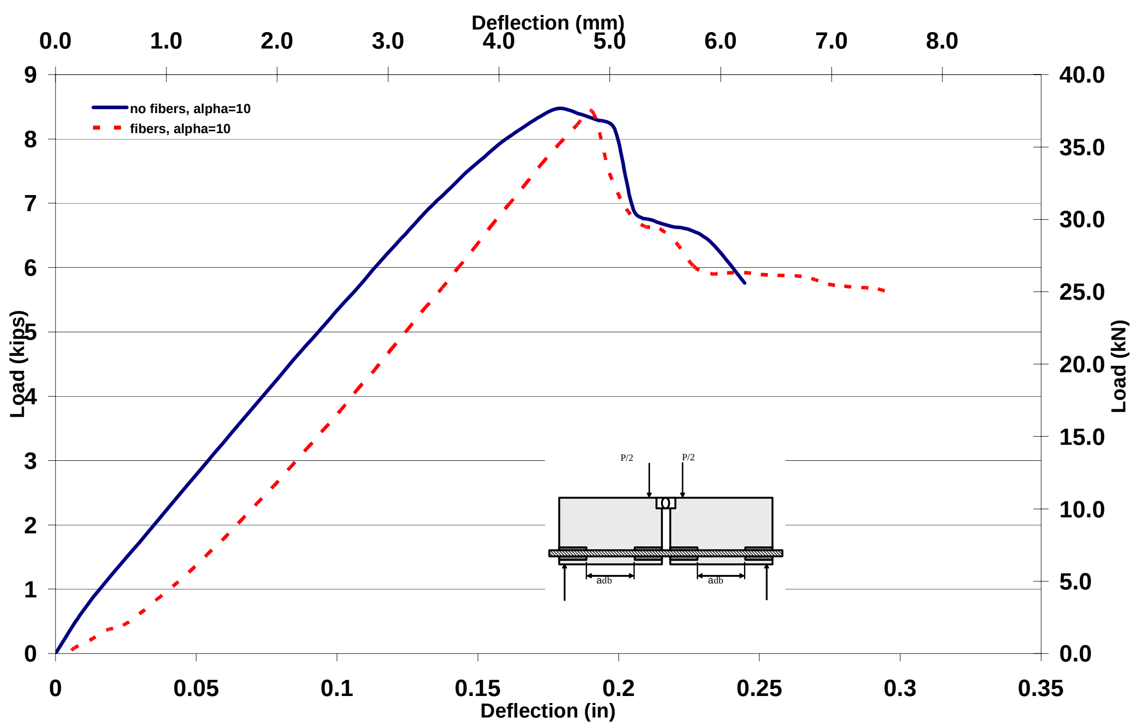

Figure 4.25 Load-deflection response of specimen reinforced with #4 CFRP reinforcement in a plain concrete (solid) and FRC (dashed) matrix

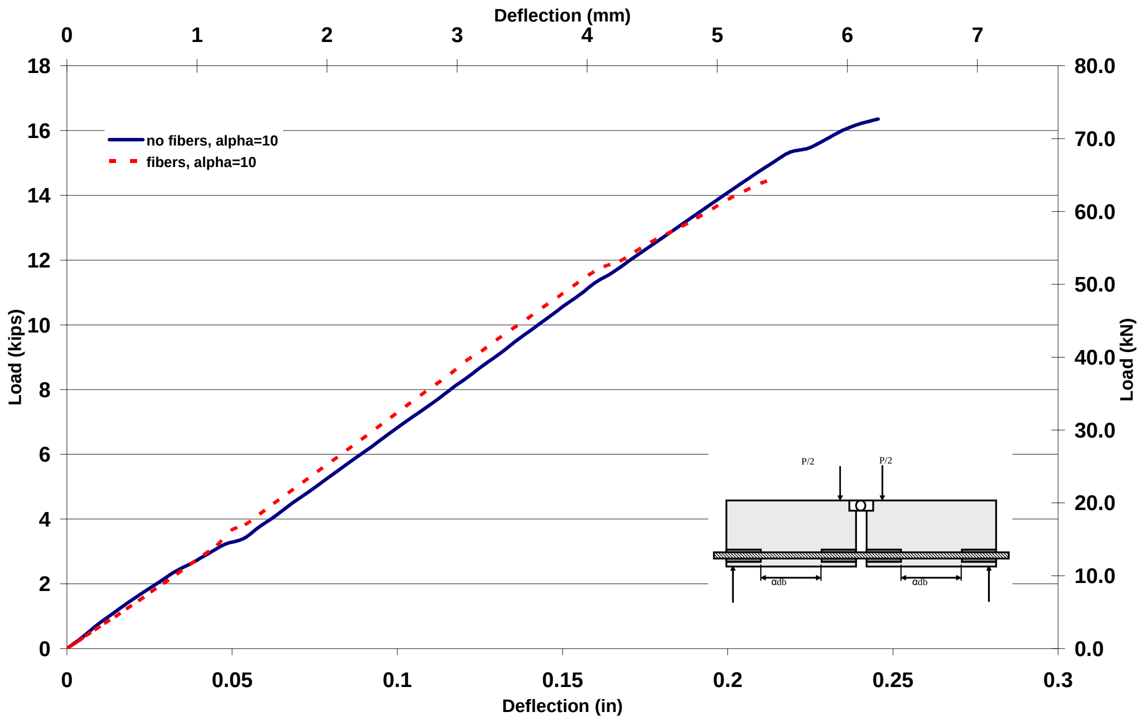

Figure 4.26 Load-deflection response of specimen reinforced with #4GFRP reinforcement in a plain concrete (solid) and FRC (dashed) matrix

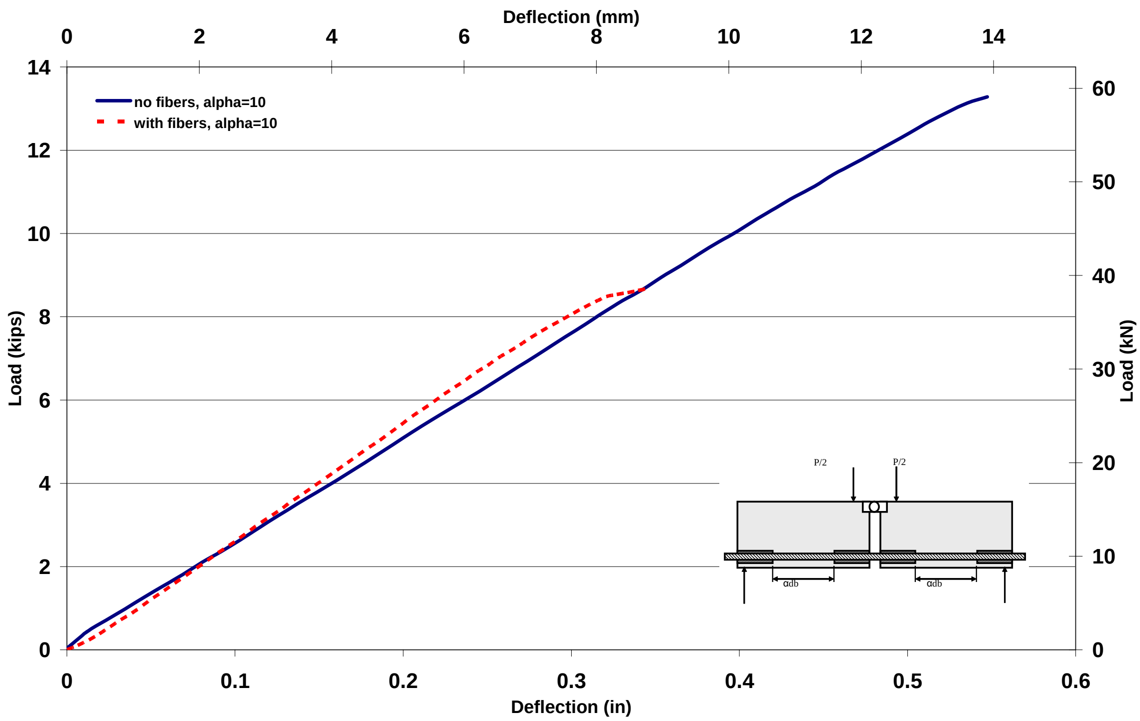

Figure 4.27 Load-deflection response of specimen reinforced with #8 GFRP reinforcement in a plain concrete (solid) and FRC (dashed) matrix

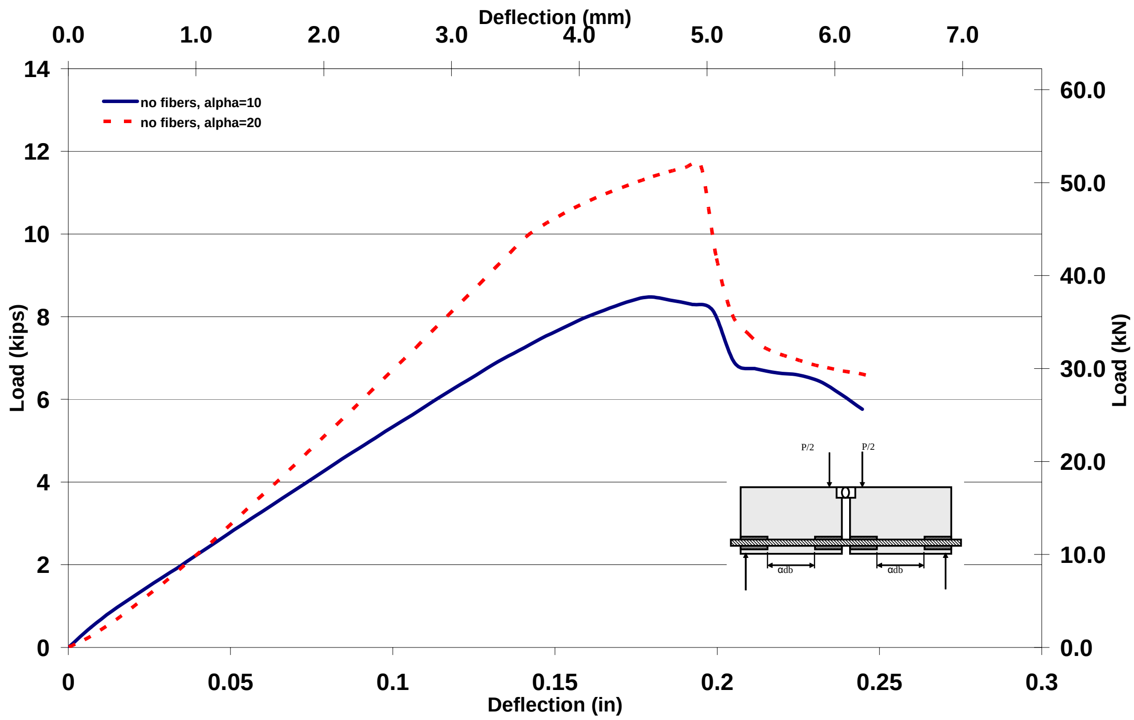

Figure 4.28 **Load-deflection response of specimen reinforced with #4 CFRP reinforcement in a plain concrete (bonded length = 10 d_b solid, bonded length = 20 d_b dashed)**

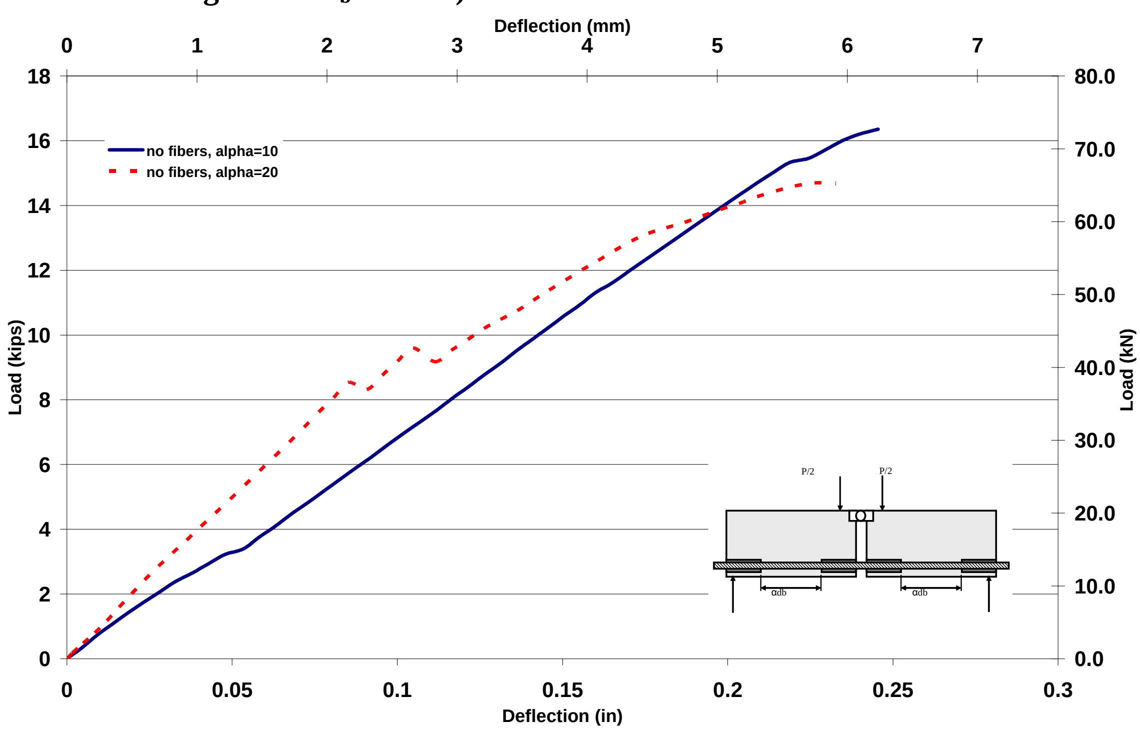

Figure 4.29 **Load-deflection response of specimen reinforced with #4 GFRP reinforcement in a plain concrete (bonded length = 10 d_b solid, bonded length = 20 d_b dashed)**

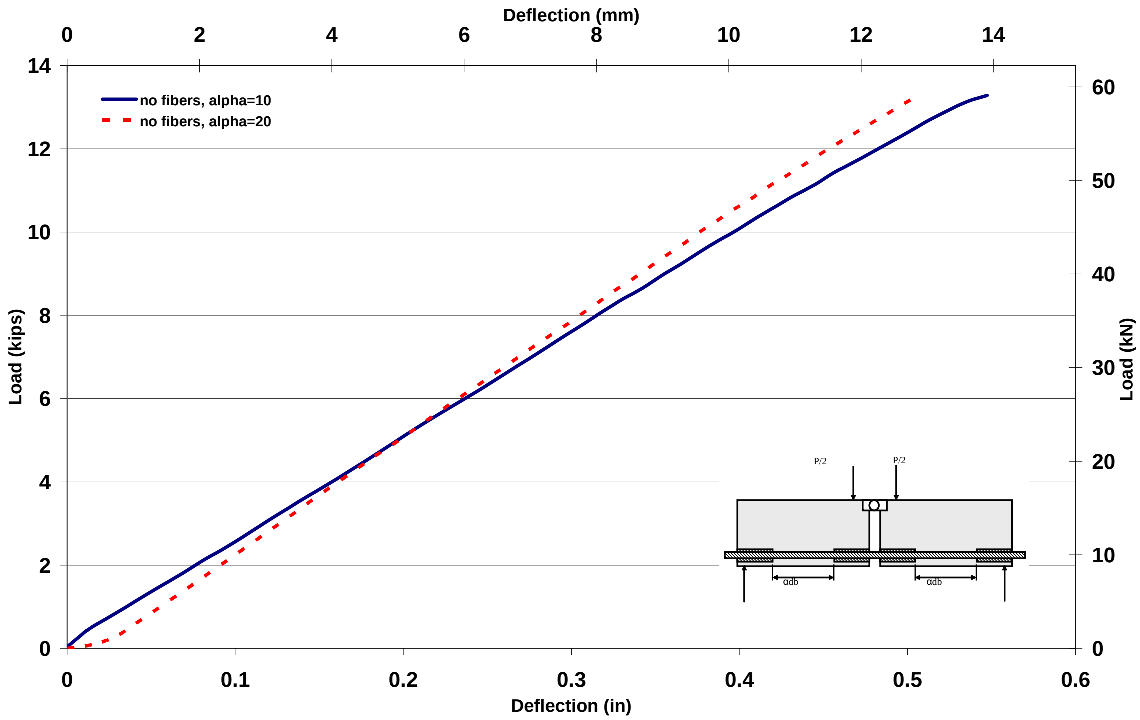

Figure 4.30 Load-deflection response of specimen reinforced with #8 GFRP reinforcement in a plain concrete (bonded length = 10 d_b solid, bonded length = 20 d_b dashed)

4.4.2 Results from the Fatigue Tests

Results from fatigue tests performed on concrete beams reinforced with #4 CFRP and #8 GFRP reinforcing bars are discussed in this section (#4 GFRP specimens were not tested under fatigue loading conditions). Other variables prescribed included the presence of fibers in the concrete mix (0.0% and 0.5% by volume) and bonded length of the reinforcing bar ($10d_b$ and $20d_b$).

4.4.2.1 <u>Failure Modes</u>

Failure modes observed in the fatigue tests were similar to those observed in the static tests. As in the static tests, #4 CFRP specimens exhibited Mode 1 failure while #8 GFRP specimen failures were dominated by Mode 2 failures.

4.4.2.2 <u>Fatigue Performance</u>

Fatigue specimens underwent 1,000,000 cycles under fast loading conditions (with periodic slow cycle fatigue to establish degradation in stiffness with fatigue cycles). Upper limits for the fatigue cycling were set to either 80% or 60% of ultimate static load capacity (high-level and low-level, respectively). Specimens that survived the fatigue loading program were then loaded quasi-statically to failure and compared to the virgin static test specimens.

While all #8 GFRP specimens tested at low-level loads survived 1,000,000 fatigue cycles, there were two specimen failures at the high-level loading. Both specimens from Concrete Batch 4 (FRC, $20d_b$) failed before 500,000 cycles of high-level fatigue loading. Virgin static test ultimate strength for these specimens was 18,800 lbs; therefore, the high-level fatigue tests were run at an upper load limit of 14,000 lbs. However, during the virgin static tests, the first (visible) crack in the concrete matrix appeared at 10,000 lbs. This suggests that from the initial cycle of high-level fatigue loading, significant cracking had already occurred. Because of the small stiffness values of GFRP (compared to steel), damage accumulation continued until the premature failure of the specimen.

This suggests that minimizing cracks at service loads is imperative when designing FRC-FRP hybrid reinforcing systems. Specimens that were tested at load levels less than those required to produce the first macro-crack in the concrete matrix performed very well under fatigue loading conditions.

Fatigue performance in the CFRP specimens was also related to the mode in which they failed. High-end level tests for specimens in Concrete Batches 2 and 3 failed prior to 1,000,000 cycles of loading. The high-end level loads for these tests are larger than those needed to induce considerable reinforcement slip in the virgin static specimens (on the order of two-one hundredths (0.02) of an inch – approximately 25% of the total reinforcement slip observed in the #4 CFRP specimens). Once the internal reinforcement slips to such large levels, the effective bonded area is smaller and therefore specimen stiffness is dramatically reduced.

The other #4 CFRP fatigue specimens were tested at load levels such that large end slips are not introduced into the reinforcing system. These specimens performed well, surviving the 1,000,000 cycles of fatigue loading.

4.4.2.3 <u>Stiffness Degradation</u>

Specimen stiffness during the fatigue test was computed in two ways. During the fast-cycle loading (5 Hz) stiffness was computed by the LabVIEW custom-built data acquisition program. Stiffness in the program was computed as the difference between the maximum and minimum loads divided by the difference between the maximum and minimum deflections.

During the slow cycle loading (0.2 Hz), specimen stiffness is computed post-test. Figure 4.31 shows the slow cycle load deflection response (for a #8 GFRP specimen) after the number fast cycle loading cycles shown in the inset table. Specimen stiffness is computed by taking the slope of this load-deflection curve.

Figure 4.32 shows a plot of stiffness degradation versus the number of fast cycles for a #8 GFRP specimen. While there were typically no failures prior to 1,000,000 cycles, a gradual decrease in specimen stiffness can be readily observed. The same trend can be seen in #4 CFRP specimens as well (Figure 4.33). After 1,000,000 cycles, a drop in specimen stiffness of 10-15% is noted for both #8 GFRP and #4 CFRP plain concrete specimens.

Fast cycle stiffness values are typically larger than stiffness values calculated during slow cycle iterations. This can be attributed to the effect that the loading rate has on flexural bond. Initial slow cycle stiffness values are comparable to those acquired during the virgin static tests. Similar observations were made of stiffness values computed using CMOD deflection.

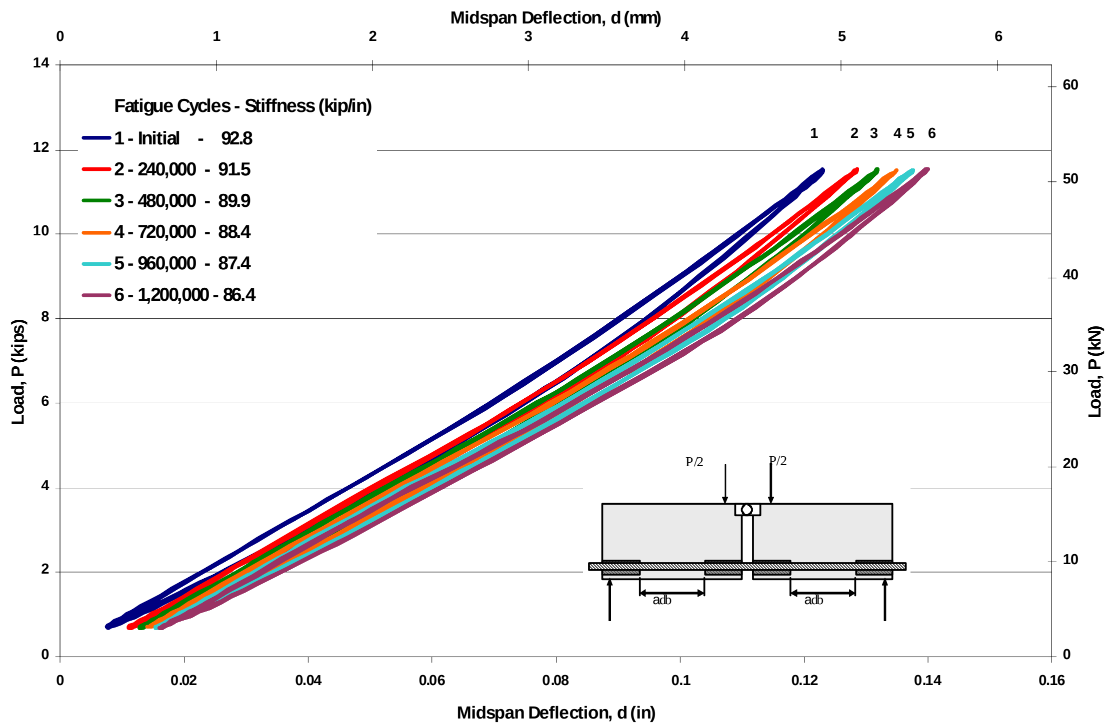

Figure 4.31 **Slow-cycle load-deflection response after prescribed number of fast fatigue cycles (see inset legend) for the No. 8 GFRP reinforced specimens (plain concrete matrix).**

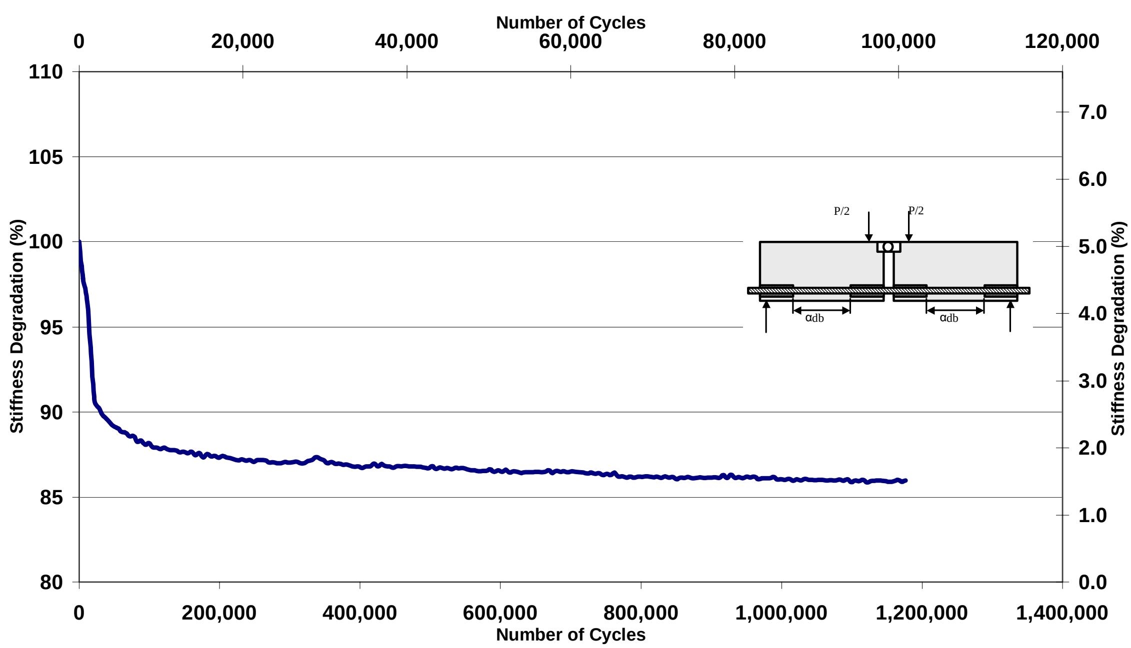

Figure 4.32 **Stiffness degradation computed from fast cycle fatigue test versus number of fatigue cycles for a No. 8 GFRP reinforced specimen (plain concrete matrix).**

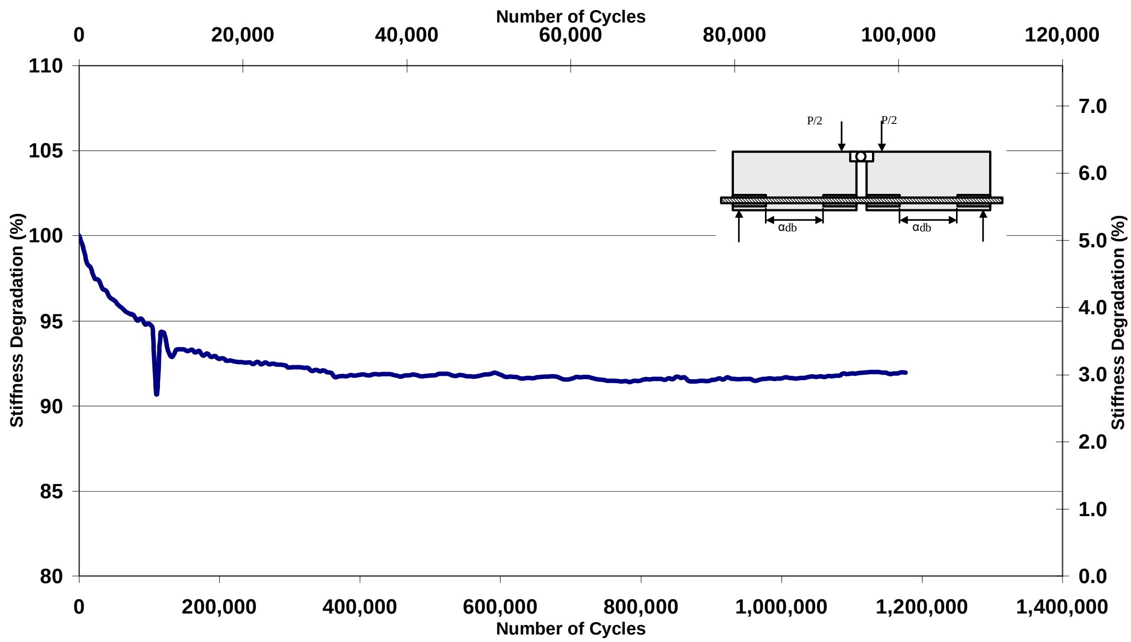

Figure 4.33 Stiffness degradation computed from fast cycle fatigue test versus number of fatigue cycles for a No. 4 CFRP reinforced specimen (plain concrete matrix).

4.4.2.4 <u>Effect of Fibers</u>

While the incorporation of fibers into the concrete mix design showed to have little effect on the quasi-static load response of the flexural bond specimens, the impact is readily witnessed during the fatigue loading test program. Fibers improved stiffness degradation response for both #4 CFRP and #8 GFRP specimens.

Figure 4.34 compares both fast and slow cycle relative stiffness values for a #8 GFRP plain concrete specimen to those of a #8 GFRP FRC specimen. Stiffness degradation response is vastly improved in the FRC specimen. The addition of fibers to the concrete matrix aides in mitigating damage caused to the specimen during fatigue cycle loading. The result is a slower damage accumulation rate than that seen in the specimens with a plain concrete matrix.

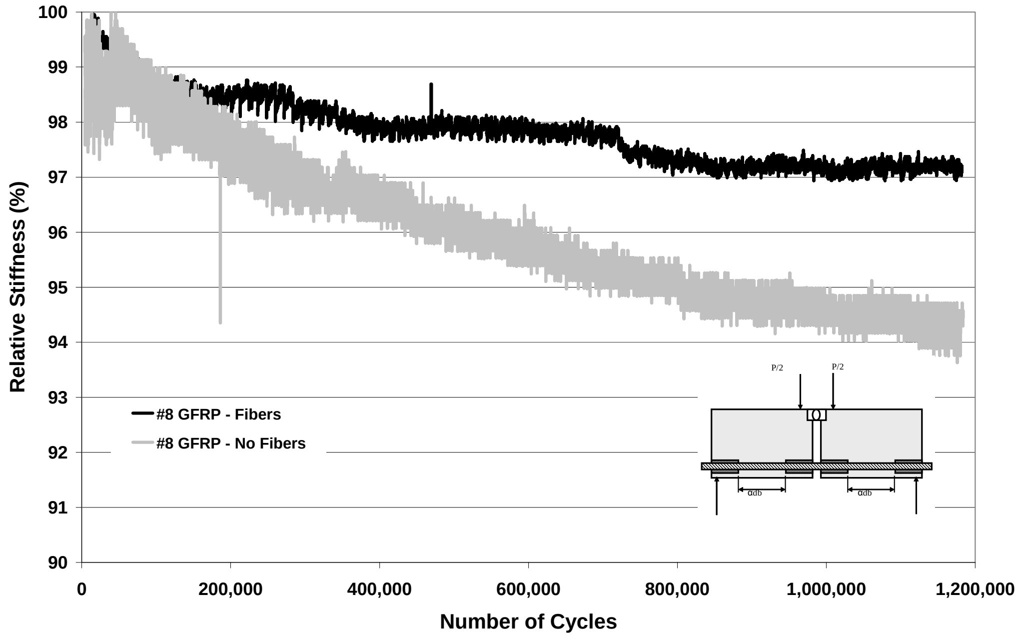

Figure 4.34 Influence of fibers in the fatigue performance of the No. 8 GFRP reinforced specimens. Substantial reduction in stiffness degradation with fatigue cycles is observed.

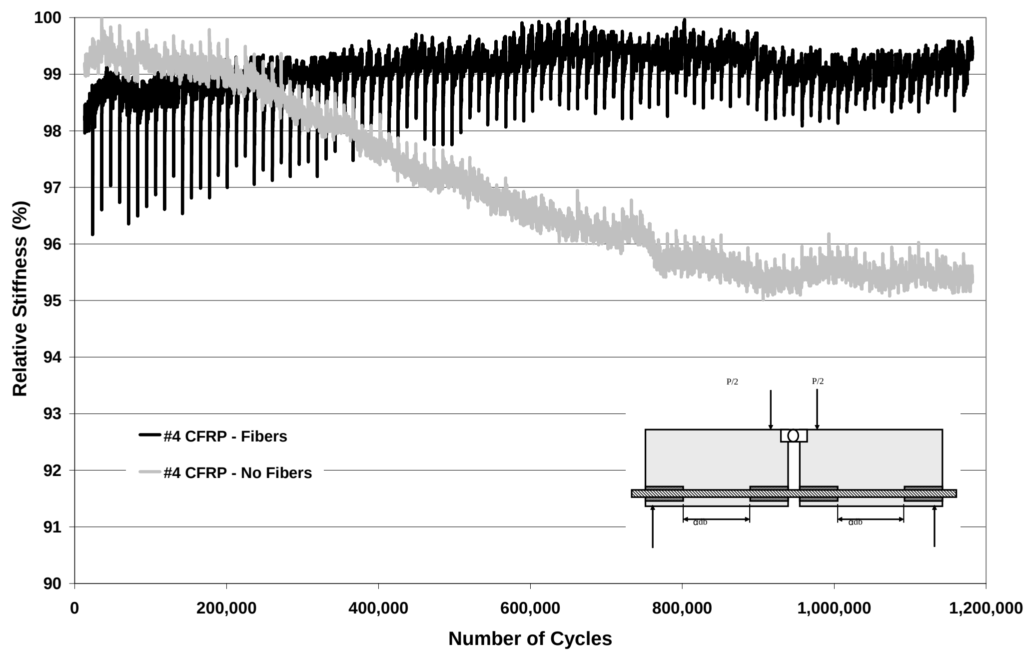

Figure 4.35 Influence of fibers in the fatigue performance of the No. 4 CFRP reinforced specimens. Significant improvement in relative stiffness over specimens with plain concrete matrices is observed. No loss in relative stiffness with fatigue cycles was observed for the specimens reinforced with No. 4 CFRP in a fiber concrete matrix.

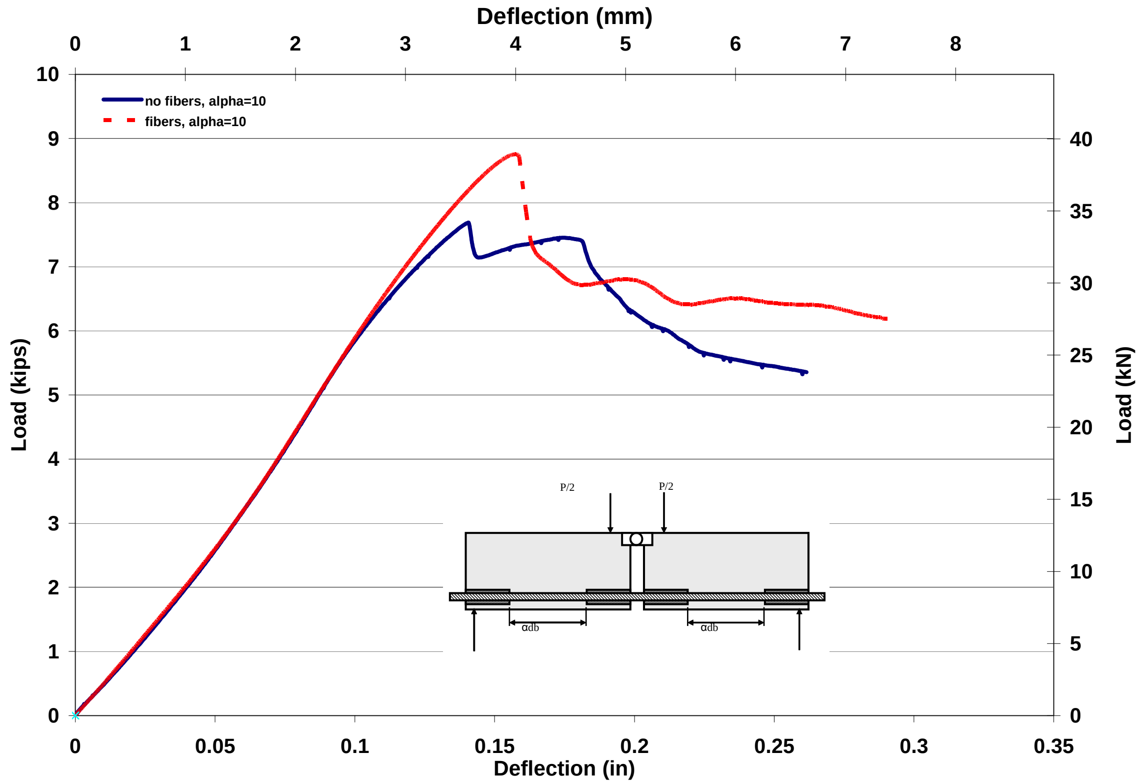

Figure 4.36 **Load-deflection responses for No. 4 CFRP specimens in the post-fatigue static tests showing the influence of fibers.**

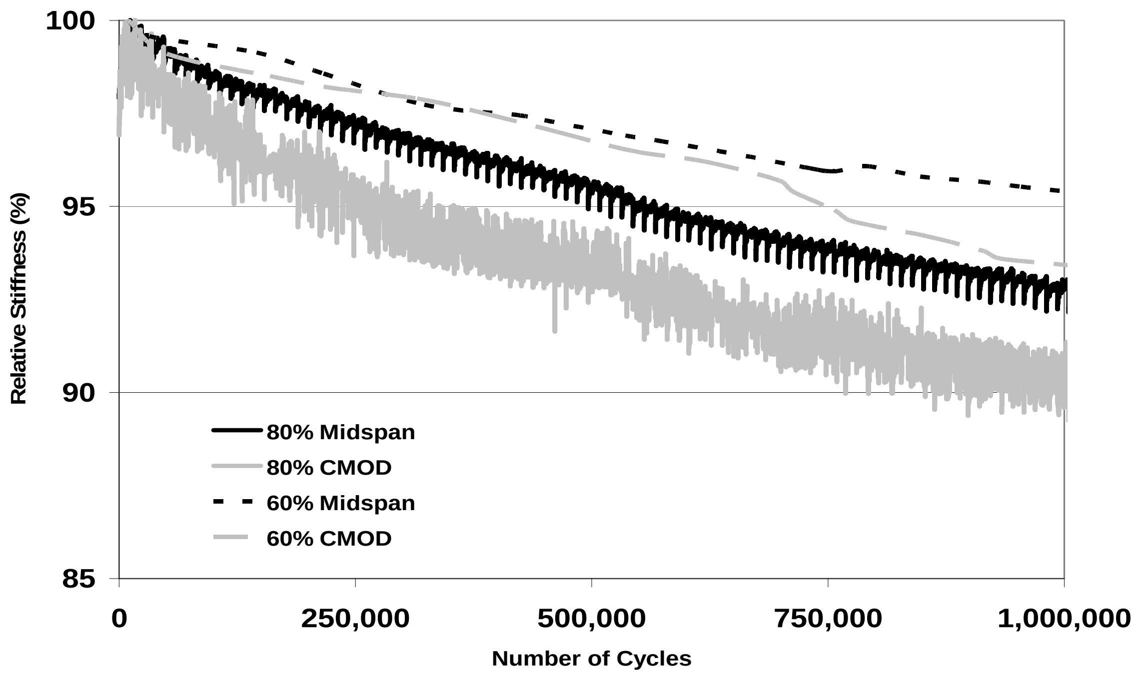

Figure 4.37 **Stiffness degradation measured using CMOD and midspan deflection at two different upper limit fatigue load levels showing increased damage accumulation at the higher upper limit fatigue load**

Figure 4.35 shows relative stiffness response for plain concrete and FRC specimens reinforced with #4 CFRP. As in the case with #8 GFRP specimens, stiffness degradation response is improved with the FRC mix design. In this case of #4 CFRP specimens, however, there is a slight increase in the specimen stiffness during fatigue loading. This increase is observed in both fast and slow cycle loading iterations.

The presence of fibers in this case provides confinement to the reinforcing system and improves the slip resistance response of the beam. This is manifested as a minimal decrease (or slight increase) in specimen stiffness as the beam undergoes fatigue loading.

The increase in specimen stiffness is also evident in the post fatigue static test results, shown in Figure 4.36.

Figure 4.37 shows the degradation in stiffness measured using CMOD and midspan deflection for two different upper limit fatigue load levels. The relatively small differences in relative stiffness measurements using two different parameters is to be expected. CMOD is a local cross-section dominated property, while the midspan deflection represents the cumulative influence of curvature changes along entire specimen length. What is more significant however, is the fact that higher upper limit fatigue loads are observed to cause more fatigue damage than a lower upper limit fatigue load level. This is again to be expected.

4.5 CONCLUDING REMARKS

Bond characteristics were investigated by two different methods; i.e., the pullout bond test and the splitting bond test. Fibers, bar surface, diameter, embedment length, cover depth, and fatigue loading’s effect on bond characteristics were investigated. The following concluding remarks could be made:

- With the addition of fibers, the bond-slip relationship significantly improved in the post-peak region, while little change was observed for the pre-peak behavior. The FRC specimens failed in a more ductile fashion with a smooth descending portion. A large portion of the load could be held, even at large slip. The plain concrete specimens failed in a very brittle fashion. Once it reached the peak value, the load dropped suddenly to zero.

- Different bond mechanisms were observed for the CFRP and the GFRP specimens due to their different surface treatments. Bond strength of the GFRP specimen was about twice as much as that of the CFRP. The GFRP specimen failed by concrete splitting; while the bond failure of the CFRP specimen initiated by the rebar pullout, providing more ductile behavior;
- Fatigue loading, within a working stress range, was shown to increase the bond stiffness and the bond strength, while causing the bond behavior to be more brittle and often change the failure mode from rebar pullout to concrete splitting.
- The large amount of slip between the rebar and concrete has occurred during the fatigue loading. Therefore, the total slip, including the residual slip due to fatigue loading, could be regarded as an inherent property for bond behavior between the rebar and the concrete, and it has little relationship with the loading history.
- Polypropylene fibers can effectively decrease the rate of bond degradation due to the fatigue loading.
- Based on analytical derivation and experimental calibration, an equation was proposed to predict the bond strength for the FRP bars embedded in FRC failed by concrete splitting.
- Bond value corresponding to 0.002 in. at the free-end slip or 0.01 in. at the loaded end was recommended as the designing bond strength in previous studies (Mathey and Watstein, 1961). Based on this criterion, an equation for the basic development length of the FRP rebar in the FRC was proposed.

5. FLEXURAL DUCTILITY

5.1 INTRODUCTION

Ductility is a structural design requirement in most design codes. In steel RC structures, ductility is defined as the ratio of ultimate (post-yield) deformation to yield deformation which usually comes from steel. Ductile structural members offer many benefits for the structures. The most important aspect is that for the ductile structures, there will be a warning before failure; while little or no warning can be observed before failure for the brittle structures. Due to the linear-strain-stress relationship of the FRP bars, the traditional definition of ductility cannot be applied to structures reinforced with FRP reinforcement. Several methods, such as energy based method and deformation based method have been proposed to calculate the ductility index for FRP reinforced structures (Naaman and Jeong, 1995, and Jaeger et al., 1995).

Due to the linear elastic behavior of the FRP bars, the flexural behavior of FRP reinforced beams exhibits no ductility as defined in the steel reinforced structures. A great deal of effort has been made to improve and define the ductility of beams reinforced with FRP rebars. To date, there are three approaches; one approach is to use the hybrid FRP rebars; that is, pseudo-ductile character is achieved by combining two or more different FRP reinforcing materials to simulate the elastic-plastic behavior of the steel rebars. Harris, Somboonsong, and Ko (1998) tested beams reinforced with the hybrid FRP reinforcing bars and they found that the ductility index of those beams can be close to that of beams reinforced with steel. This method has shown some success in the research studies but has resulted in limited practical applications because of the complicated and costly manufacturing process of the hybrid rebars. Another approach to realize the ductility of the FRP reinforced members is through the progressive failure of bond and the combination of rebars with different mechanical properties (Gopalaratnam, 2005). The third approach is to improve the property of concrete. ACI 440 recommends that FRP reinforced structure be over-reinforced and designed so that the beams fail by concrete failure rather than by rebar rupture. Thus, the ductility of the system is strongly dependent on the concrete properties. Alsayed and Alhozaimy (1999) found that with the addition of 1% steel fibers, the ductility index could be increased by as much as 100%. Li and Wang (2002) reported that the GFRP rebars reinforced with engineered cementitious composite material showed much better flexural behaviors. The ductility was also found to be significantly improved.

This chapter presents research results on the flexural behavior of concrete beams reinforced with FRP rebars and concrete containing polypropylene fibers. The different behaviors of plain concrete beams and FRC beams are also discussed.

5.2 TEST RESULTS AND DISCUSSIONS

This Chapter provides a summary of the overall flexural behavior of the FRP/FRC hybrid system in terms of crack distribution, load-deflection response, relative slip between the rebar and concrete, cyclic loading effect on flexural behavior, and strain distribution in concrete and reinforcement. Comparison between FRP/Plain concrete system and FRP/FRC system is also discussed.

5.2.1 Crack Distribution

Figures 5.1 to 5.3 show the typical crack patterns for the FRP reinforced beams at moderate (40% M_u) and high (80% M_u) load levels to investigate the crack distribution at different load level. Like traditional steel rebar reinforced beams, vertical flexural cracks developed first at the pure bending regions. Then, the inclined shear cracks were induced with the increase of load.

- **Cracking Moment.** Theoretical and experimental values for cracking moments are given in Table 5.1. As shown in Table 5.1, the experimental values were close to the theoretical values but were consistently lower by about 20% than those of the theoretical predictions. Also, as expected, the cracking moment was not affected by the addition of 0.5% of polypropylene fibers. This was due to the elongation at rupture of the polypropylene fiber that was three orders of magnitude greater than the cracking tensile strain of the concrete due to the low elastic modulus (500 to 700 ksi). Hence, the concrete would crack long before the fiber strength was approached. So concrete cracking controlled the M_{cr}.

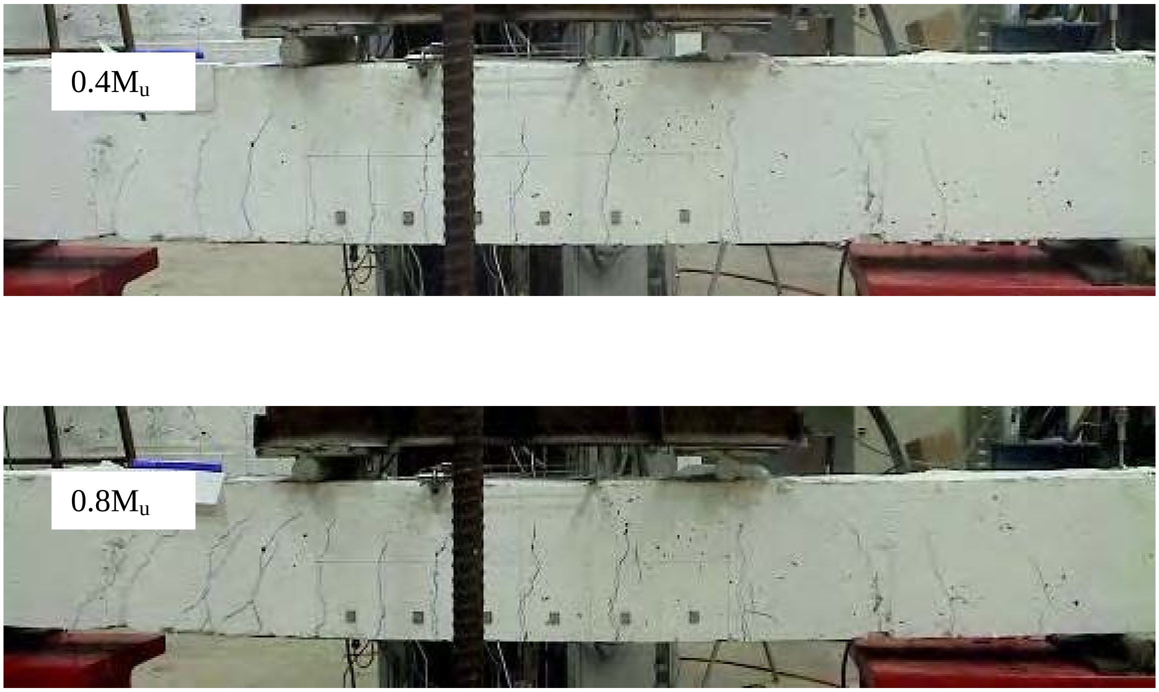

(a) VF4C (FRC beams)

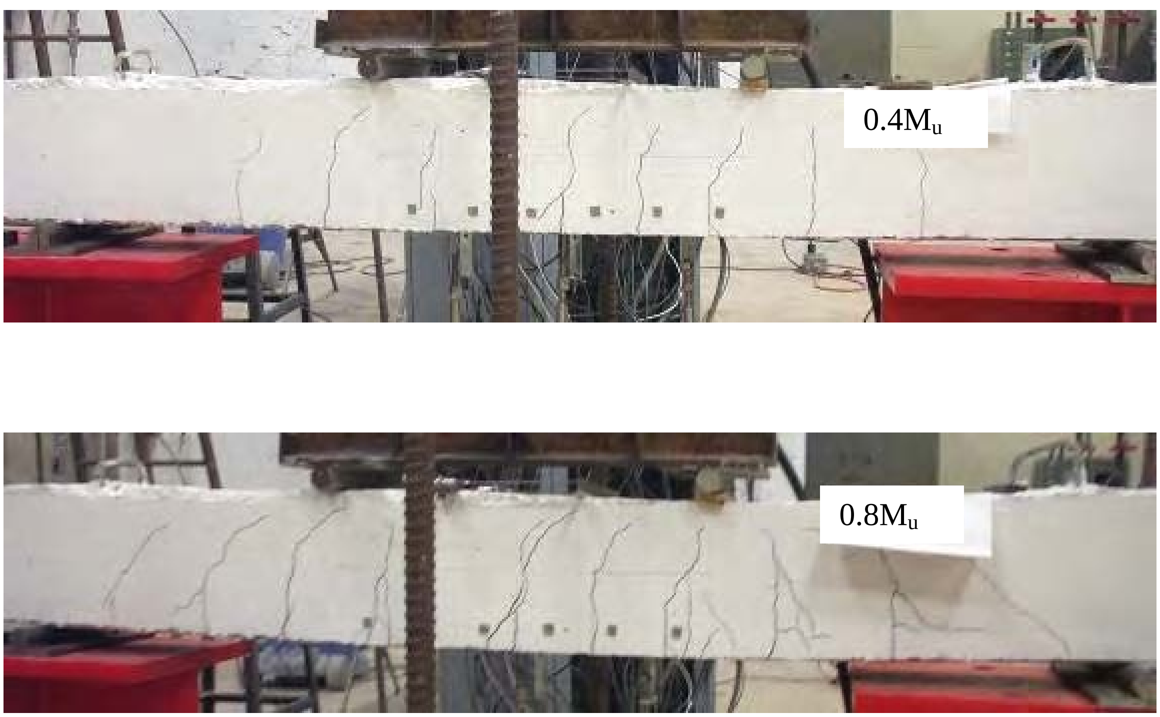

(b) VP4C (Plain concrete beams)

Figure 5.1. Crack patterns for #4 CFRP beams at moderate and high level loading

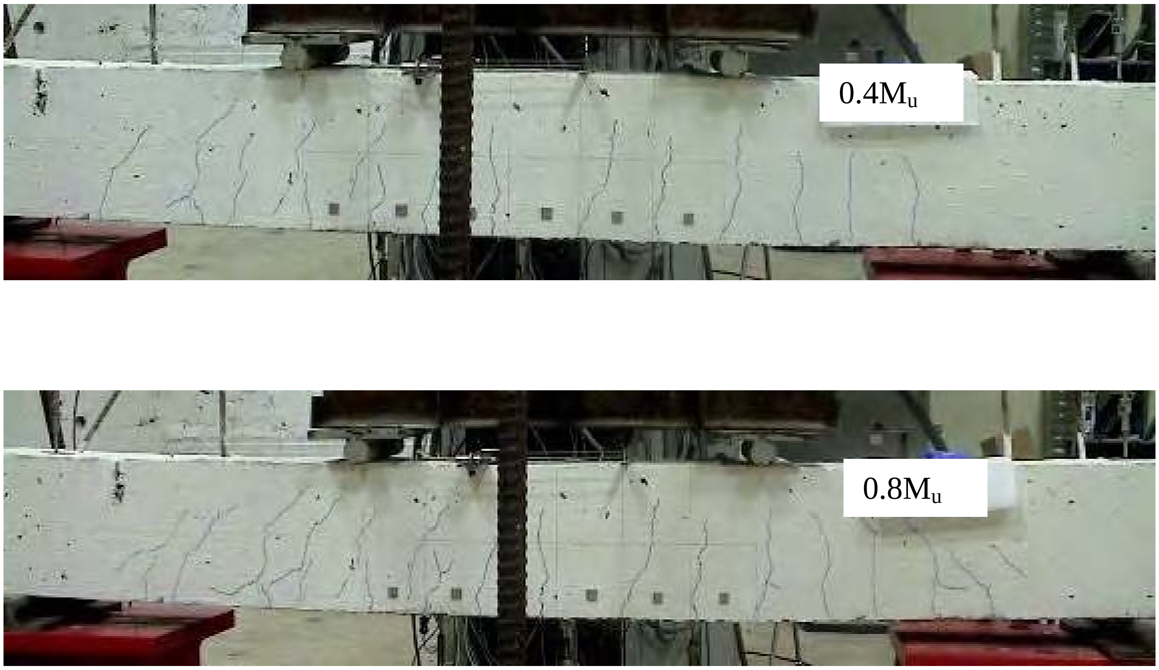

(a) VF4G (FRC beams)

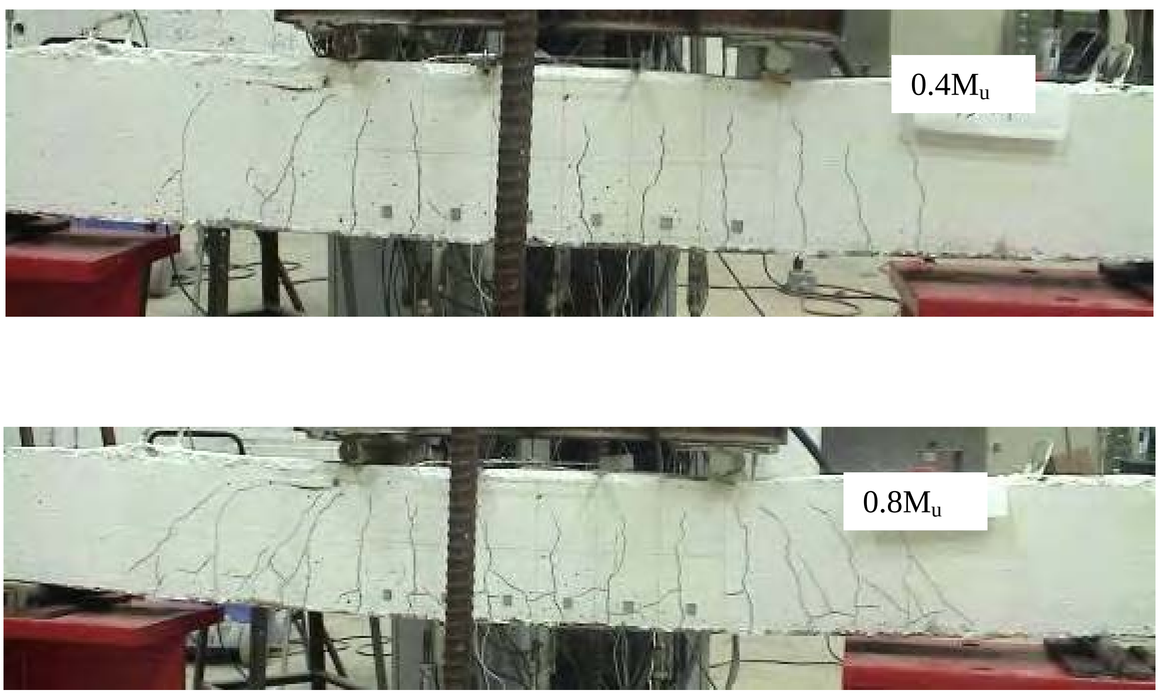

(b) VP4G (Plain concrete beams)

Figure 5.2. Crack patterns for #4 GFRP beams at moderate and high level loading

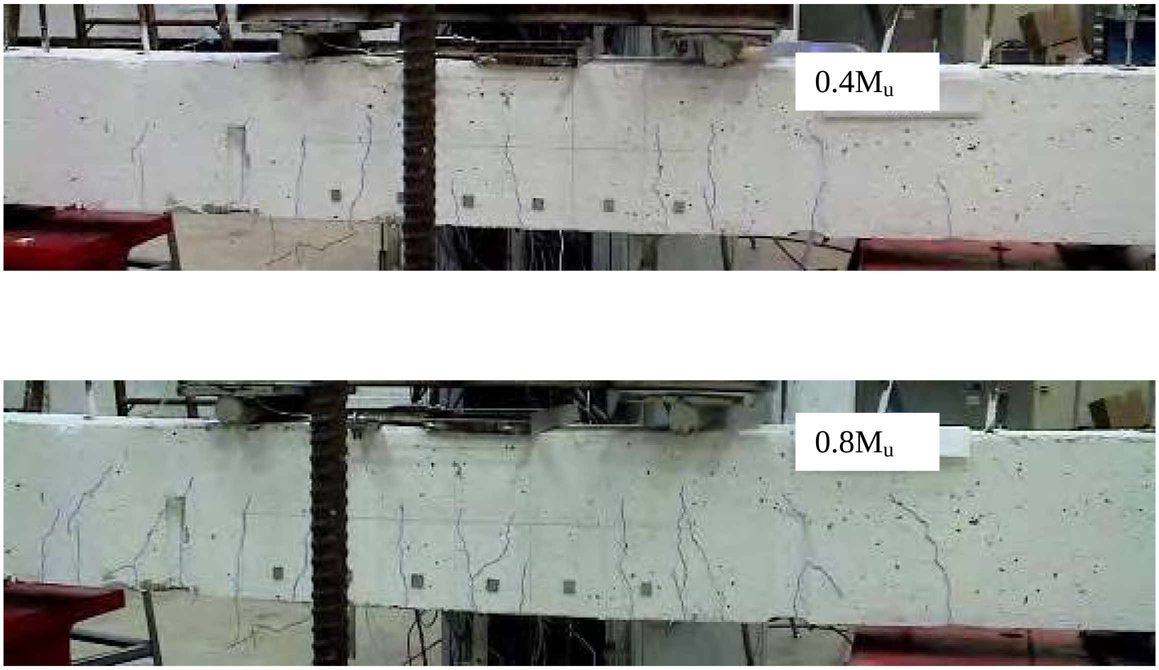

(a) VF8G (FRC beams)

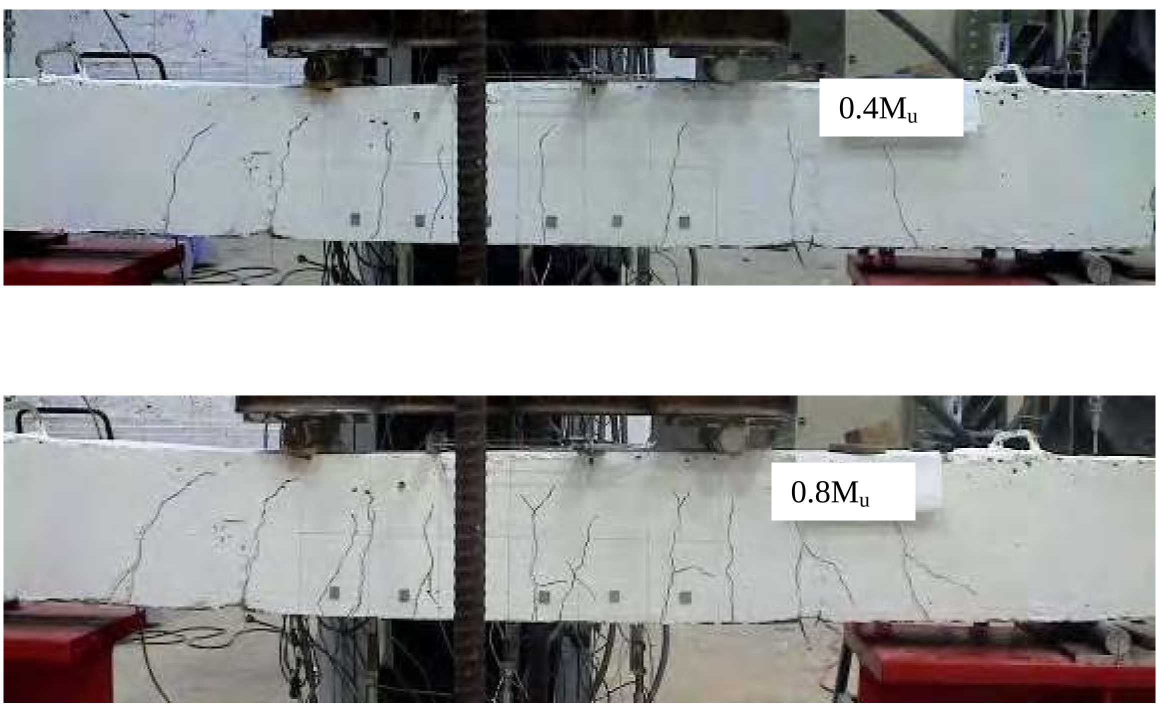

(b) VP8G (Plain concrete beams)

Figure 5.3. Crack patterns for #8 GFRP beams at moderate and high level loading

Table 5.1. Cracking moment and average crack spacing

Specimen I.D.	$M_{cr\text{-}theo}$ (kips-in.)	$M_{cr\text{-}exp}$ (kips-in.)	$\frac{M_{cr-theo}}{M_{cr-\exp}}$
VP4C-1	60.0	53.1	1.13
VP4C-2		48.3	1.24
VP4G-1	60.0	54.3	1.10
VP4G-2		48.3	1.24
VP8G-1	60.4	48.1	1.26
VP8G-2		48.3	1.25
Average		50.1	1.20
VF4C-1	47.7	42.3	1.13
VF4C-2		42.3	1.13
VF4G-1	47.7	40.3	1.18
VF4G-2		44.0	1.08
VF8G-1	48.1	36.3	1.33
VF8G-2		36.7	1.31
Average		40.3	1.19

The self weight of beams has been included while calculating the experimental cracking moments.

- **Crack Spacing.** Table 5.2 shows the average crack spacing at 40% and 80% of the flexural capacity. With the increase of load, crack spacing slightly decreased. Interestingly, by comparing the crack spacing between the plain concrete beams and the FRC beams, the crack spacing was virtually the same at 80% of ultimate load, while the crack spacing of the FRC beams was about 20% smaller than that of plain concrete at a moderate service load (about 40% of ultimate load).

Studies suggest that the flexural cracking can be closely approximated by the behavior of a concrete prism surrounding the main reinforcement and having the same centroid. Cracks initiate when the tensile stress in the concrete exceeds the tensile strength of concrete, f_t'. When this occurs, the force in the prism is transferred to the rebar. Away from the crack, the concrete stress is gradually built up through the bond stress between the rebar and the concrete. When the stresses in the concrete are large enough and exceed the tensile strength of concrete f_t', a new crack forms. The above mechanism is demonstrated in Figure 5.4.

Table 5.2. Average crack spacing

Specimen I.D.	Crack Spacing, S_m, at 40%M_u (in.)	Crack Spacing, S_m, at 80%M_u (in.)	$\frac{S_{FRC}}{S_{plain}}$ at 40%M_u	$\frac{S_{FRC}}{S_{plain}}$ at 80%M_u	ACI-440 (in.) at service	CEB-FIP Code (in.) at service
VP4C	6.00	4.55	N/A	N/A	7.30	4.50
VP4G	5.28	3.58	N/A	N/A	5.40	3.75
VP8G	6.00	4.23	N/A	N/A	8.02	4.24
VF4C	4.60	4.20	0.77	0.93	7.30	4.50
VF4G	4.00	3.43	0.76	0.96	5.40	3.75
VF8G	4.80	4.40	0.8	1.04	8.02	4.24

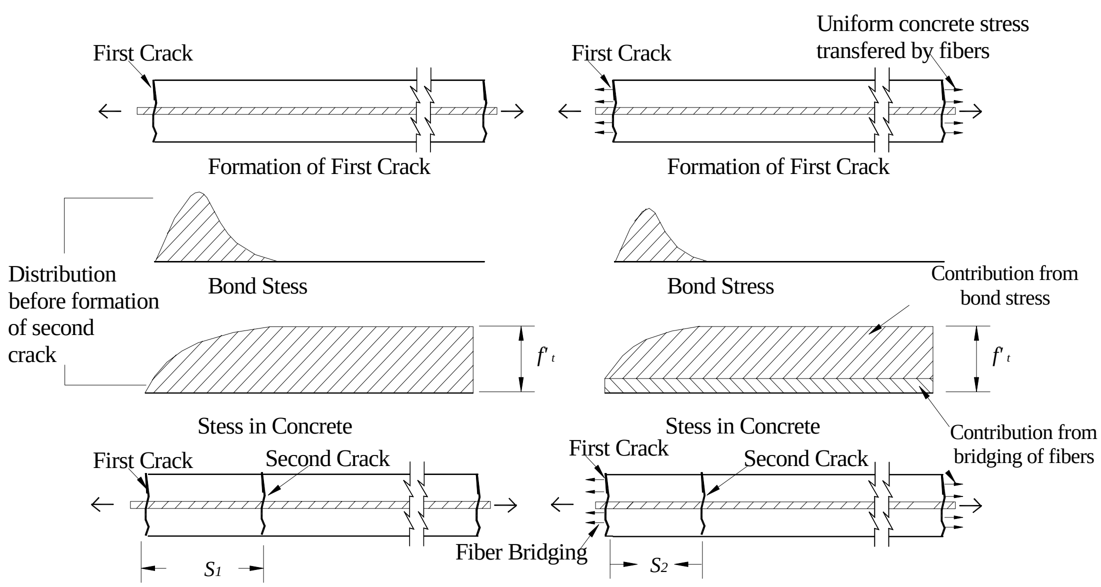

(a) Plain concrete beam **(b) FRC beam**

Figure 5.4. Mechanism of crack formation in plain concrete and FRC beams

With the addition of fibers, the mechanism of crack formation is changed slightly, as shown in Figure 5.4. Some tensile loads can be transferred across the cracks by the bridging of fibers. Thereby, the stress in the concrete comes from not only the bond stress, but the bridging of fibers as well. With the contribution from the fibers, less bond stress is needed to reach the same cracking stress. Consequently, the spacing of crack is smaller in the FRC beams than in the plain concrete beams ($S_2 < S_1$ as shown in Figure 5.4). At a high load level, due to inadequate bond between the fibers and concrete, fibers are pulled out and the contribution from the bridging of fibers is diminished.

- **Predictions using CEB-FIP Code.** The CEB-FIP Code expression for the average crack width, S_m, for the steel reinforced concrete is in the following manner:

$$S_m = 2(c + \frac{s}{10}) + k_1 k_2 \frac{d_b}{\rho_{ef}} \text{ in.} \tag{5.1}$$

where c = clear concrete cover

s = maximum spacing between longitudinal reinforcing bars but shall not be taken greater than 15 d_b

d_b = bar diameter

$\rho_{ef} = A_s / A_{cef}$

A_s = area of steel considered to be effectively bonded to the concrete

A_{cef} = area of effective embedment zone of the concrete

k_1 = 0.4 for deformed bars; and 0.8 for plain bars

k_2 = coefficient to account for stain gradient

In this study, the same method is adopted for the FRP reinforced beams and compared to the test data. As shown in Table 5.2, the prediction values underestimate the crack spacing at the service load (40% of the ultimate), especially in the case of the plain concrete beams.

- **Prediction using ACI 440.** Based on the current ACI 440 recommends for the crack width of the FRP reinforced member, the following equations can be derived to calculate the crack spacing:

$$w = 2200 k_b \sqrt[3]{d_c A} \frac{f_f}{E_f} \text{ in.} \tag{5.2}$$

where w = the crack width at tensile face of the beam,

A = the effective tension area per bar,

d_c = the thickness of concrete cover measured from extreme tension fiber to the center of the closest layer of longitudinal bars, and

k_b = the coefficient that accounts for the degree of bond between the FRP bar and the surrounding concrete. ACI suggests 1.2 for deformed FRP bars if k_b is not experimentally known.

As shown in Table 5.2, the ACI-440 predictions overestimate the crack spacing for both plain concrete beams and FRC beams when k_b is taken equal to 1.2.

- **Crack Width.** During the tests, crack widths were measured by the distance changes between the Demec gages. Figures 5.5 to 5.7 show the relationships between the crack width and the applied moment. In the following section, several currently available models to predict the crack width are discussed and compared with test results.

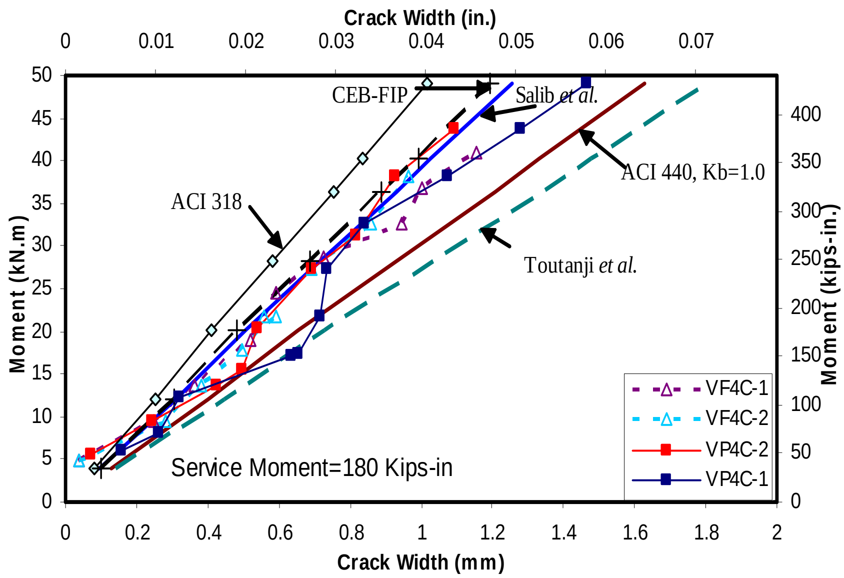

Figure 5.5. Crack width versus applied moment of #4 CFRP beams

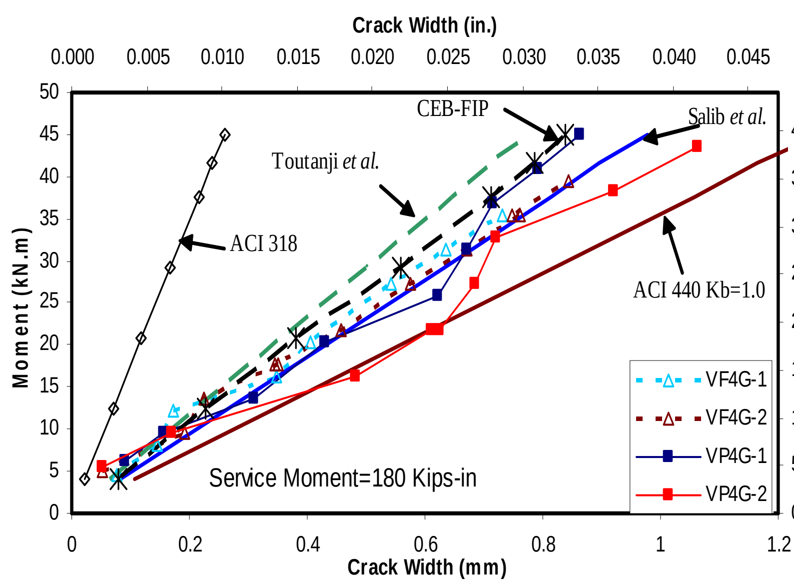

Figure 5.6. Crack width versus applied moment of #4 GFRP beams

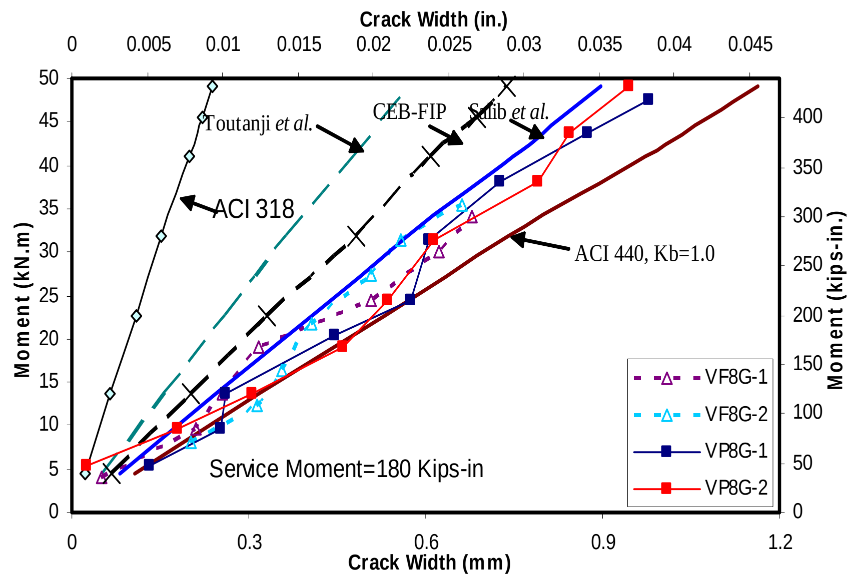

Figure 5.7. Crack width versus applied moment of #8 GFRP beams

Based on the well-known Gergely-Lutz (1973) equation, ACI 440 recommends the equation to calculate the crack width of FRP reinforced member as follows:

$$w = \frac{2200}{E_f} k_b \beta f_f \sqrt[3]{d_c A} \text{ in.} \qquad (5.3)$$

where w = the crack width at tensile face of the beam,

A = the effective tension area per bar,

d_c = the thickness of concrete cover measured from extreme tension fiber to the center of the closest layer of longitudinal bars,

f_f = the stress in the FRP reinforcement,

β = the coefficient to converse crack width corresponding to the level of reinforcement to the tensile face of beam, and

k_b = the coefficient that accounts for the degree of bond between the FRP bar and the surrounding concrete. It was reported that k_b ranges from 0.71 to 1.83 for different types of GFRP bars (Gao et al., 1998). ACI 440 does not give a mathematical relationship between k_b and the bond strength. And it suggests 1.2 for deformed FRP bars if k_b is not experimentally known.

Toutanji and Saafi (2000) reported that the crack width is a function of the reinforcement ratio. They proposed the following equation to predict the crack width:

$$w = \frac{200}{E_f \sqrt{\rho_f}} \beta f_f \sqrt[3]{d_c A} \text{ in.} \tag{5.4}$$

where ρ_f is the reinforcing ratio.

Based on the equivalent beam concept, Salib and Abdel-Sayed (2004) proposed the following equation:

$$w = 0.076 \times 10^{-3} \times \{(E_s / E_f)(u_{b,s} / u_{b,f})^{2/3}\} \times \beta f_f \sqrt[3]{d_c A} \text{ in.} \tag{5.5}$$

By substitute E_s=29000 ksi; thus

$$w = \left(\frac{2200}{E_f} \times \sqrt[(2/3)]{\frac{u_{b,s}}{u_{b,f}}} \right) \times \beta f_f \sqrt[3]{d_c A} \text{ in.} \tag{5.6}$$

where $u_{b,s}$ and $u_{b,f}$ are the bond strengths of steel rebar and FRP rebar, respectively. In Equation 5.6, the values of $u_{b,f}$ and $u_{b,f}$ need to be evaluated and decided upon. For traditional steel rebar, according to ACI 318-02, $l_d = \frac{f_y d_b}{25\sqrt{f_c'}}$ (neglecting the adjusting coefficients) and based on the definition of the development length,

$$\pi d_b l_d u_{b,s} = f_y A_s \tag{5.7}$$

One gets: $u_{b,s} = 6.25\sqrt{f_c'}$ psi.

For FRP rebar used in this study, based on the previous study (Belarbi and Wang, 2005), $u_{b,f} = 9.25\sqrt{f_c'}$. Based on these approximate values, Equation 5.6 become

$$w = \frac{1700}{E_f} \beta f_f \sqrt[3]{d_c A} \text{ in.} \tag{5.8}$$

The crack width can also be derived based on the crack spacing. Concrete can sustain very small tensile stain due to stress before it cracks. After cracking, the tensile side of the beam elongates by widening of the cracks and by formation of new cracks. Ignoring the small elastic stain in the concrete between the cracks, the crack width can also be expressed as follows:

$$w = \varepsilon_f S_m \text{ in.} \tag{5.9}$$

Substituting Equation 5.1 into 5.9, results in

$$w = \varepsilon_f \left\{ 2(c + \frac{s}{10}) + k_1 k_2 \frac{d_b}{\rho_{ef}} \right\} \text{ in.} \tag{5.10}$$

As shown in Figures 5.5 through 5.7, the Salib et al. model gives reasonable predictions of the crack width for both plain concrete beams and FRC beams. For the Toutanji et al. model, the prediction values show poor correlation with the experimental results. For low reinforcing ratios, (for the CFRP beams, ρ=0.67%), the model overestimates the crack width. Vice versa, for high reinforcing ratios (#4 GFRP beams, ρ=2.2%, and #8 GFRP beams, ρ=3.3%), the model underestimates the crack width. Therefore, it may be concluded that it is the bond characteristics rather than the reinforcing ratio that affect the crack width.

The predictions based on the current ACI 440 equations were also compared with the test results. The accuracy of the equations largely depends on the value of k_b. Even when selecting k_b =1.0, one can see that the predictions are still conservative. Similar observations were made by El-Salakawy and Benmokrane (2004).

Compared to the test results, the predictions based on the CEB-FIP Code underestimated the crack width, especially in the case of #8 GFRP. As shown in Table 5.2, the prediction by Equation 5.1 underestimate the crack spacing at the service load, thus, the predicted crack width will be underestimated.

- **Fiber Effect on Crack Width.** With the addition of fibers, the crack widths were slightly decreased at the same load level, especially at the service load, as shown in Figures 5.5 through 5.7. As shown in Table 5.3, the crack widths were smaller in the case of FRC beams as compared to plain concrete beams, at the service load. As discussed earlier, the crack spacing was decreased at the service load due to the contribution from the fibers. Since the crack width is proportionally related to the crack spacing, the crack width is expected to be smaller in the FRC beams at the service load.

Table 5.3. Comparison of crack width between plain concrete beams and FRC beams at service load

Specimen I.D.	VP4C	VP4G	VP8G	VF4C	VF4G	VF8G
Crack Width (in.)	0.024	0.019	0.018	0.021	0.016	0.014
% decrease relative to respective plain concrete	N/A	N/A	N/A	10%	16%	20%

Note: the values are average of two beams.

5.2.2 Load-Deflection Response

Figures 5.8 and 5.9 show the typical experimental moment-deflection curves for the plain concrete beams and the FRC beams reinforced with different types of FRP rebars. With the increasing of moment, cracks developed in the testing region when the moment exceeded the cracking moment, M_{cr}. Consequently, the flexural stiffness of the beams was significantly reduced and the curves were greatly softened. As expected, due to the linear-elastic behavior of FRP rebars, the FRP reinforced beams showed no yielding. The curves show linear behavior until the crushing of concrete.

Fiber Effect on Moment-Deflection Curves. In order to compare the flexural behaviors between plain concrete beams and FRC beams, all the load-deflection curves of the plain concrete beams were normalized, based on the following rules: 1) moment was divided by a coefficient C_M, defined as $C_M = \frac{M_{ACI-plain}}{M_{ACI-FRC}}$, where $M_{ACI\text{-}plain}$ and $M_{ACI\text{-}FRC}$ are theoretical ultimate capacities computed based on ACI 440 for beams with concrete strengths equal to the plain concrete beams and the FRC beams using the same approach, respectively; 2) deflection was divided by a coefficient C_D, defined as $C_D = \frac{\Delta_{ACI-plain}}{\Delta_{ACI-FRC}}$, where $\Delta_{ACI\text{-}plain}$ and $\Delta_{ACI\text{-}FRC}$ are theoretical deflection based on ACI 440 for beam with concrete strengths equal to the plain concrete beams and FRC beams at the service load (40% of the ultimate load), respectively.

As shown in Table 5.4 and Figures 5.10 through 5.12, with the addition of fibers, the ultimate moments and deflections were increased. The plain concrete beams failed in a more brittle manner. Once it reached the capacity, the concrete was crushed and the load dropped suddenly and violently. FRC beams failed in a more ductile way as the load dropped more gently and smoothly.

Table 5.4. Comparison of flexural strength and deflection between FRC beams and plain concrete beams

Specimen I.D. (1)	Ultimate Moment (kips-in.) (2)		Ultimate Deflection (in.) (3)		Ultimate Moment (kips-in.) (4)		Ultimate Deflection (in.) (5)		$\frac{M_{FRC}}{M_{Plain}}$ (6)	$\frac{\Delta_{FRC}}{\Delta_{Plain}}$ (7)
VP4C-1	457	450	1.19	1.18	375	369	1.03	1.02	N/A	N/A
VP4C-2	442		1.17		362		1.00			
VP4G-1	405	413	1.03	1.03	330	336	0.94	0.94	N/A	N/A
VP4G-2	420		1.02		342		0.93			
VP8G-1	448	449	0.96	0.96	360	360	0.87	0.87	N/A	N/A
VP8G-2	449		0.95		360		0.86			
VF4C-1	415	402	1.20	1.15	415	402	1.20	1.15	1.09	1.13
VF4C-2	388		1.10		388		1.10			
VF4G-1	350	356	1.19	1.19	350	356	1.19	1.19	1.06	1.27
VF4G-2	362		1.19		362		1.19			
VF8G-1	371	366	0.95	0.91	371	366	0.95	0.91	1.02	1.05
VF8G-2	361		0.87		361		0.87			

Note: Columns (4) and (5) are the normalized values of Column (3) and (4); Columns (6) and (7) are the ratios of moment or deflection between the FRC beams to those of the plain concrete beams after normalizations.

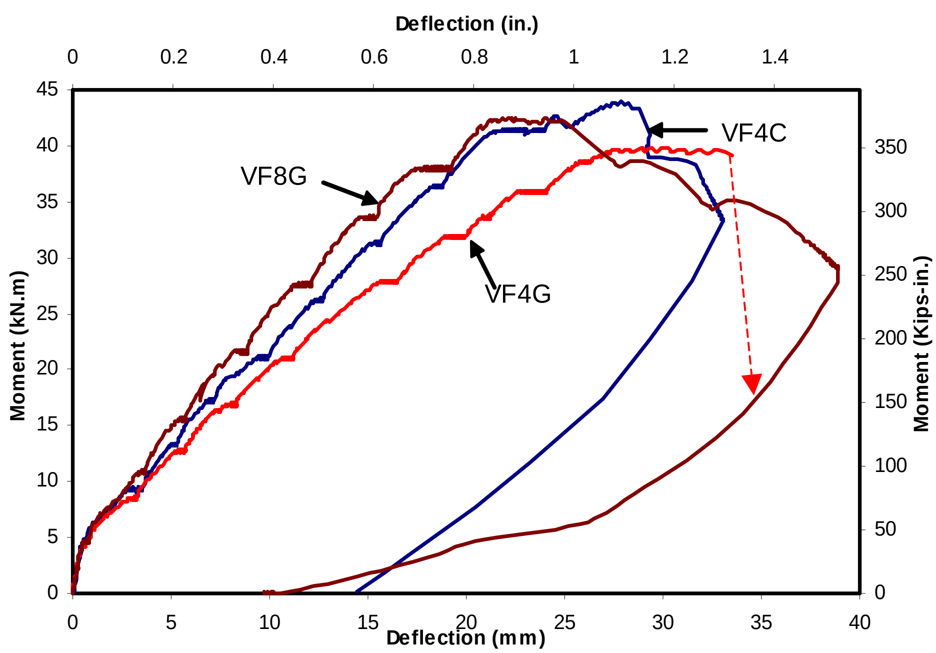

Figure 5.8. Moment-deflection response for FRC beams

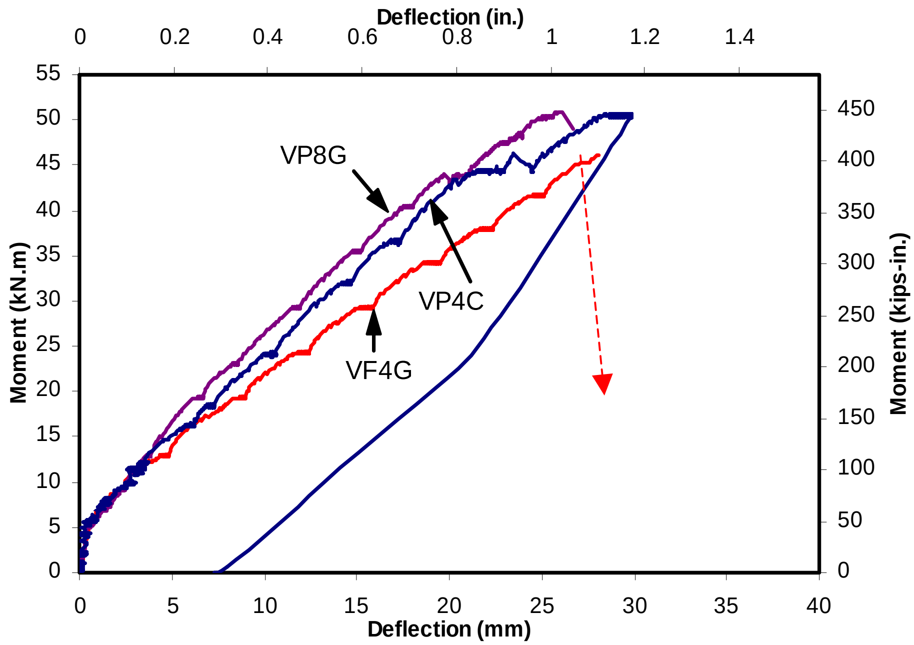

Figure 5.9. Moment-deflection response for plain concrete beams

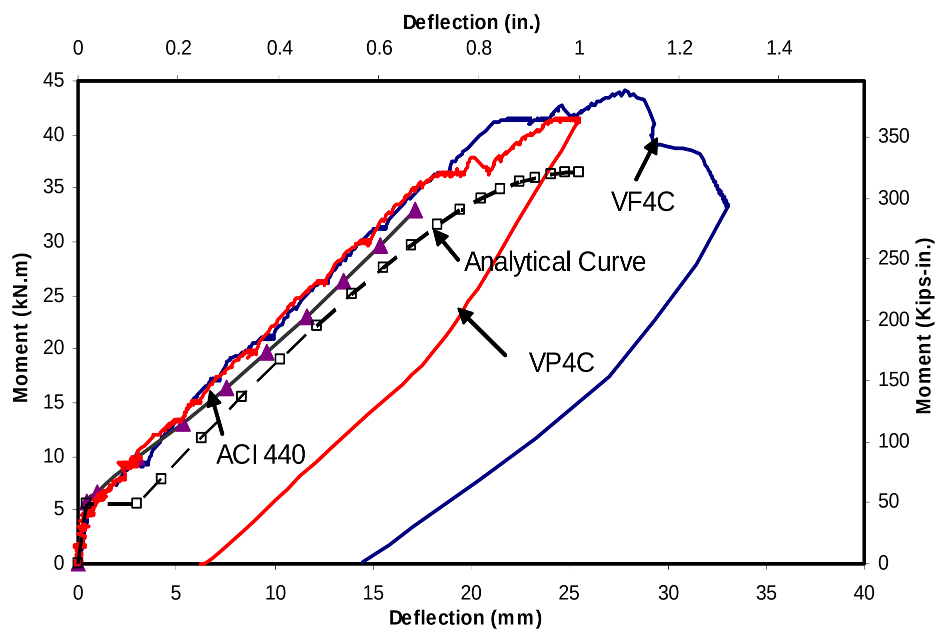

Figure 5.10. Moment-deflection response for #4 CFRP with/without fibers

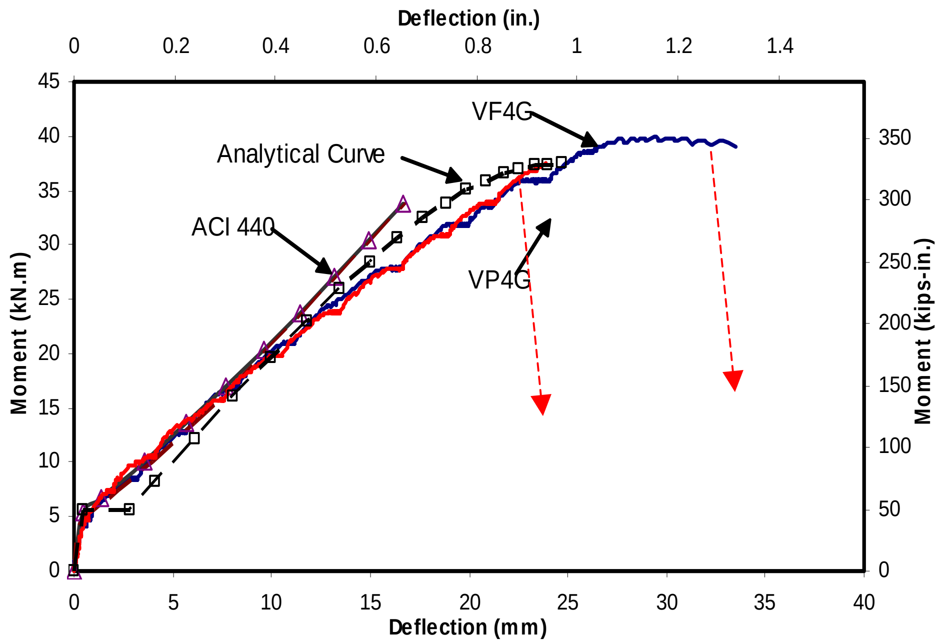

Figure 5.11. Moment-deflection response for #4 GFRP with/without fibers

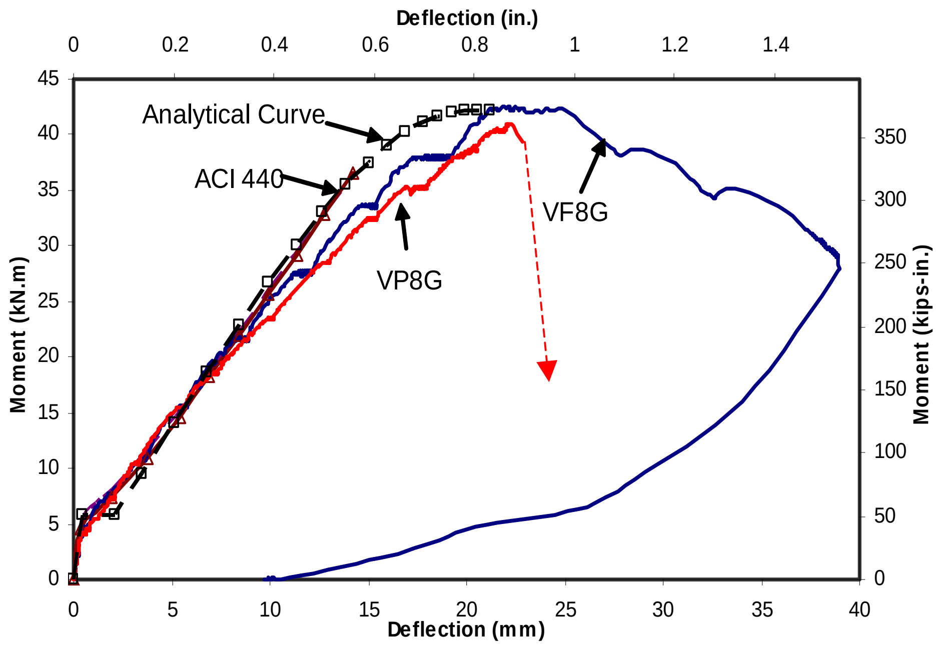

Figure 5.12. Moment-deflection response for #8 GFRP with/without fibers

Theoretical Correlation. Deflection at mid-span for a simply supported beam of total span L and subjected to a four-point flexural test is given as

$$\Delta_{mid} = \frac{Pa}{24E_cI_e}(3L^2 - 4a^2) + \frac{Ph^2a}{10GI_e} \tag{5.11}$$

The first term on the right is from the flexural component, and the second term is from the shear component. In this study, testing beams had a span-depth ratio of 2.67. Based on calculation, it was found that the shear component was about 3% of the flexural component. It was, therefore, neglected for simplicity. Thus, Equation 5.11 becomes

$$\Delta_{mid} = \frac{Pa}{24E_cI_e}(3L^2 - 4a^2) \tag{5.12}$$

ACI 440 recommends the following expressions to calculate the effective moment of inertia I_e:

$I_e = I_g$ when $M_a \le M_{cr}$;

$$I_e = \left(\frac{M_{cr}}{M_a}\right)^3 \beta_d I_g + \left[1 - \left(\frac{M_{cr}}{M_a}\right)^3\right] I_{cr} \le I_g \text{ when } M_a > M_{cr} \tag{5.13}$$

where $\beta_d = \alpha_b\left[\frac{E_f}{E_s} + 1\right]$, (5.14)

ACI 440 recommends taking the value of $\alpha_b = 0.5$ for all the FRP rebar type.

As shown in Figures 5.10 to 5.12, ACI 440 equations predict the moment-deflection response fairly well, especially at the service stage. Thus, the equations recommended by the current ACI 440 would be used for the design purpose for both plain concrete beams and FRC beams.

A more refined analysis was also conducted to compare the theoretical and experimental results. The theoretical moment-deflection curves were obtained based on the double integration of a theoretical moment-curvature relationship, in which the Thorenfeldt model was used to represent the stress-strain relationship of the concrete, as shown in the following equation:

$$f_c = \frac{n(\varepsilon_c / \varepsilon_c^{'}) f_c^{'}}{n - 1 + (\varepsilon_c / \varepsilon_c^{'})^{nk}} \tag{5.15}$$

Based on the information provided by Collins and Mitchell (1991) for the parameters of Eq. 5.15, n = 2.6, k = 1.16, $\varepsilon_c' = 0.00198$ were adopted in this study when the concrete strength of 4,400 psi. The above coefficients were derived based on experimental study on normal-weight concrete. Because the concrete in this study was also normal-weight concrete, it is assumed that the above predictions could reasonably predict the stress-strain relationship of the concrete used in this study. The implementation of the double integration of the theoretical moment-curvature relationship was based on the conjugate beam method. The analytical curve was interrupted at ε_c = 0.0045. As shown in Figure 5.10 to 5.12, the theoretical curves show good correlation with the experimental results.

5.2.3 Relative Slip between Longitudinal Rebar and Concrete at Ends.

No relative slip was observed for any test specimens during the test program. That means that the development lengths as designed based on the previous bond study (Belarbi and Wang, 2005) were adequate for the FRP bars to develop the required forces.

5.2.4 Loading/Unloading Effect on the Flexural Behaviors.

No significant differences were observed before and after loading and unloading cycles in the crack width, crack distribution, and deflection. Also, the flexural stiffness did not change after cyclic loading, as shown in Figures 5.13 to 5.14.

5.2.5 Strains in Reinforcement and Concrete.

Figures 5.15 to 5.17 present the measured mid-span strains in reinforcement and in concrete versus the applied moment. It can be seen that after cracking, the strains in the reinforcement increased almost linearly up to failure. Because all test beams failed in concrete crushing rather than FRP reinforcement rupture, the maximum measured strains in the reinforcement were less than the ultimate tensile strains. In beams reinforced with #4 CFRP, #4 GFRP, and #8 GFRP, the maximum measured strains were 12,000; 12,000; and 8,000 microstrains, respectively; while the ultimate strains were 16,700; 16,900; and 13,500 microstrains, respectively.

The differences of the moment-strain curves between the plain concrete beams and the FRC beams were significant. In the plain concrete beams, once reaching the ultimate, concrete failed by crushing, and strains in the reinforcement dropped suddenly. However, in the FRC beams, when beams reached the ultimate, concrete was held together and the strains in the concrete and strains in the reinforcement kept increasing gradually. Furthermore, with the addition of fibers, the ultimate strain for the concrete was increased. In plain concrete beams, the measured ultimate concrete strains ranged from 2,700 microstrains to 3,300 microstrains with an average of 2,950 microstrains. In the FRC beams, the measured ultimate concrete strains ranged from 4,000 microstrains to 5,000 microstrains with an average of 4,500 microstrains.

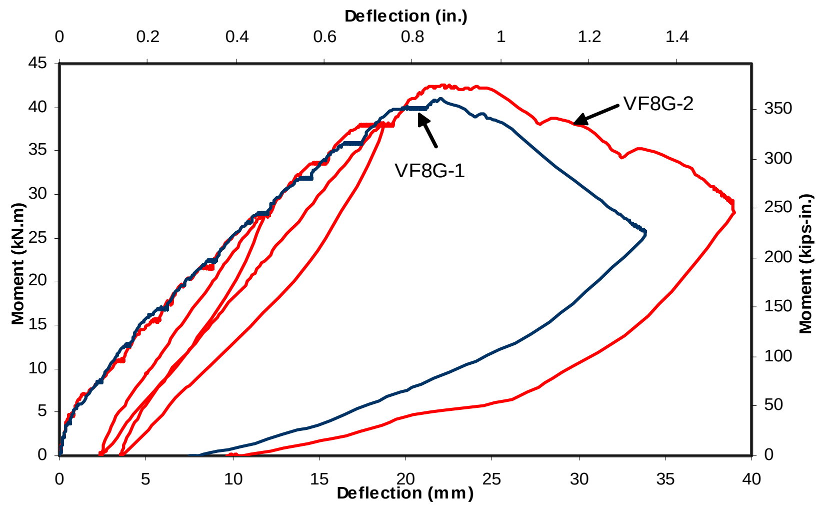

Figure 5.13. Typical Loading/unloading Cycle's Effect on FRC Beams

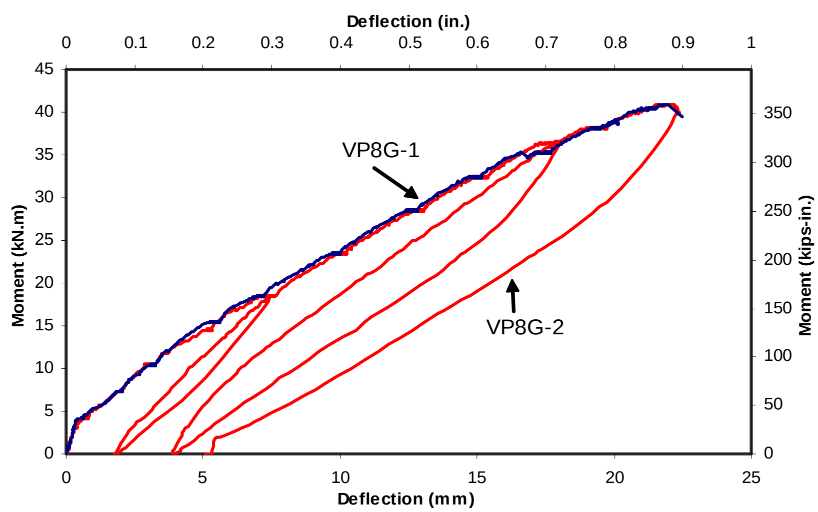

Figure 5.14. Typical loading/unloading response of plain concrete beams

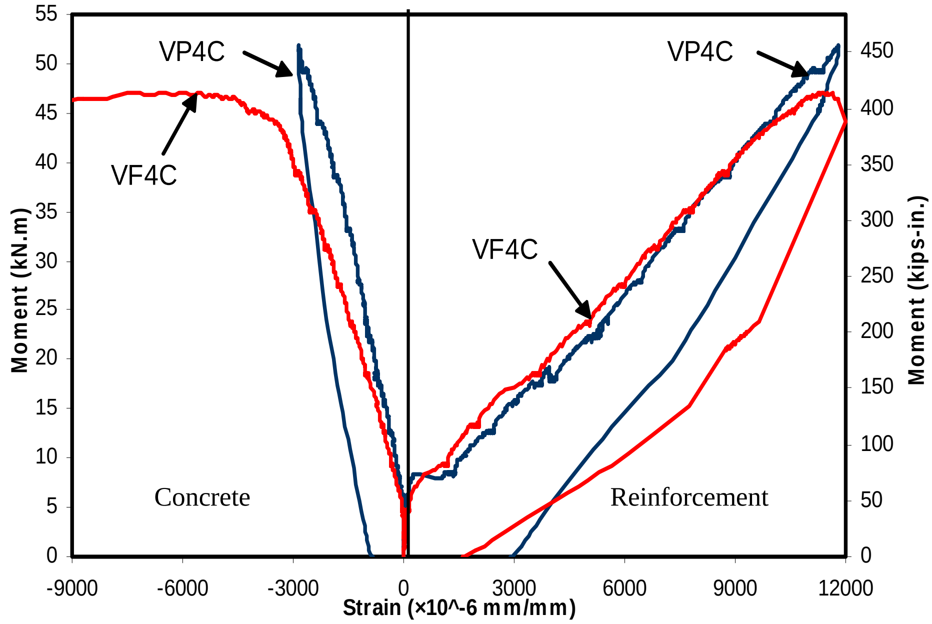

Figure 5.15. Typical strain distributions of #4 CFRP beams

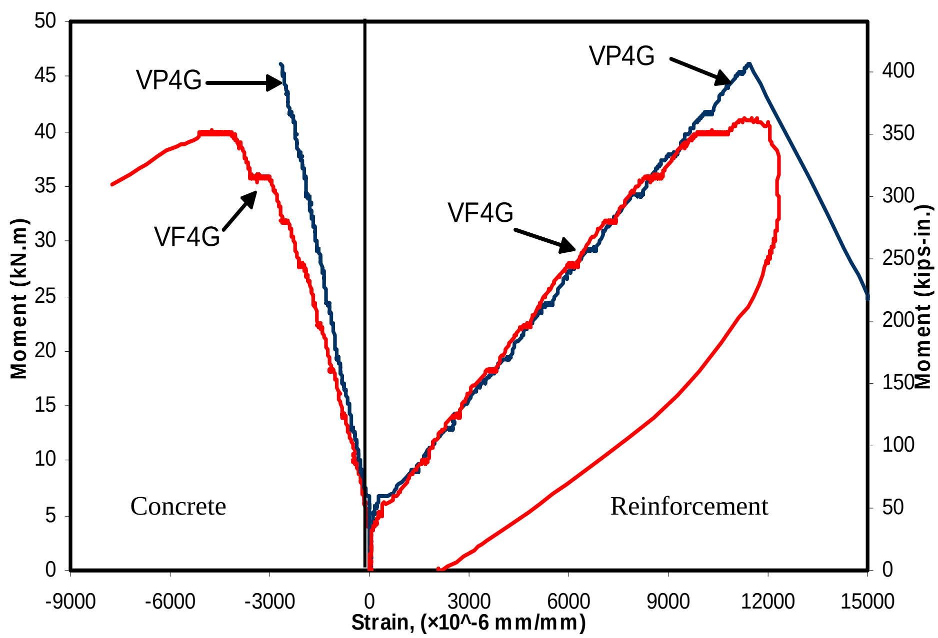

Figure 5.16. Typical strain distributions of #4 GFRP beams

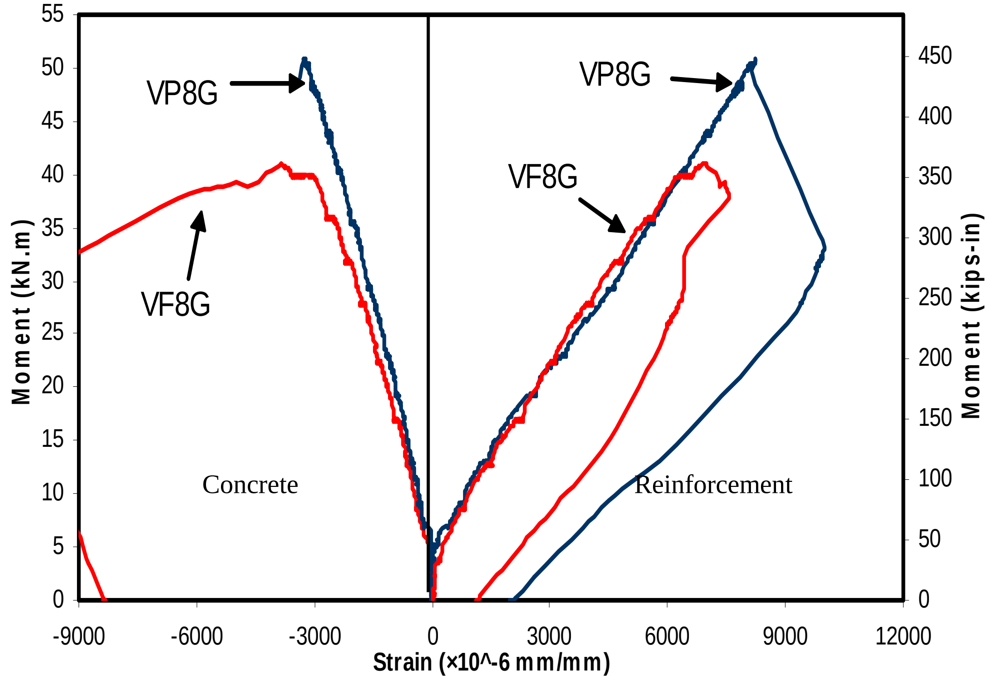

Figure 5.17. Typical strain distributions of #8 GFRP beams

5.3 PREDICTIONS OF THE ULTIMATE FLEXURAL CAPACITY

As shown in Table 3.5, the reinforcing ratio, ρ_f, for all the beams were greater than the balanced ratio, ρ_{bf}, which is defined by:

$$\rho_{bf} = \alpha_1 \beta_1 \left(\frac{f_c'}{f_{fu}} \right) \left(\frac{\varepsilon_{cu}}{\varepsilon_{cu} + \varepsilon_{fu}} \right) \tag{5.16}$$

where ε_{cu}=0.003 as defined by ACI 318-02.

As expected, all the beams failed by concrete crushing. Figure 5.18 shows the typical failure mode.

Figure 5.18. Typical failure mode

Predictions by the ACI 440 equations were based on the following assumptions:

(1) Plane section remain plane; that is, the concrete and the reinforcement strain values are proportional to their distance from the neutral axis.

(2) The tensile strength of the concrete is ignored.

(3) A parabolic stress distribution in the concrete was utilized, and the stress block factors, α_1 and β_1, as defined in ACI 318-02, were adopted.

(4) The ultimate concrete compressive strain ε_{cu} is 0.003. ε_{cu} =0.0035 were also computed for comparison in this study.

(5) There is perfect bond between the reinforcement and the concrete.

ACI 440 recommends the following equations to predict the flexural strength:

$$M_n = \rho_f f_f \left(1 - 0.59 \frac{\rho_f f_f}{f_c^{'}}\right) bd^2 \text{ kips-in.} \tag{5.17}$$

$$f_f = \left(\sqrt{\frac{\left(E_f \varepsilon_{cu}\right)^2}{4} + \frac{0.85\beta_1 f_c^{'}}{\rho_f} E_f \varepsilon_{cu}} - 0.5 E_f \varepsilon_{cu}\right) \leq f_{fu} \text{ psi} \tag{5.18}$$

There are two possible ways by which fibers can increase the flexural strength: one is that the fibers function as auxiliary reinforcement to carry some tensile stresses; the other way is that the fibers can improve the concrete properties. In this study, contribution of fibers in tensile strength was neglected since

(1) Compared to the steel fibers, the tensile strength of polypropylene fibers is low: less than 1/3 of the tensile strength of the steel fibers.

(2) Due to the low elastic modulus of polypropylene fiber (500 to 700 ksi), the elongation at break is three orders of magnitude greater than the tensile strain at failure of the concrete. Hence, the concrete will crack long before the fiber strength is approached.

Thus, the most likely contribution from the fibers to increase the flexural strength is to improve the concrete properties. As shown in Figure 5.19, ultimate concrete strain measured for FRC beams in this study is larger than the value recommended by ACI. In this study, a value of 0.0035 is used. As shown in Table 5.5, the theoretical predictions agreed well with the test results. As discussed earlier, the concrete strains of the FRC beams at failure were greater than 0.0035. For the design of the FRC beams, it is suggested that ε_{cu} to be equal to 0.0035, with a comparable safety factor of ε_{cu} = 0.003 for the plain concrete beams.

5.4 DUCTILITY EVALUATION

As mentioned earlier, since the traditional definition of ductility can not be applied to the structures reinforced with FRP reinforcement, there is a need for developing a new approach and a set of ductility indices to both quantitatively and qualitatively evaluate the FRP reinforced members. The calculations of ductility index related to the FRP reinforced members have been widely studied. Two approaches have been proposed in the literature to address this problem.

Table 5.5. Predictions of ultimate capacities

Specimen I.D.	$M_{exp.}$ (kips-in.)	M_{ACI} (kips-in) ε_{cu} =0.003	$\frac{M_{ACI}}{M_{exp.}}$	M^*_{ACI} (kips-in.) ε_{cu} =0.0035	$\frac{M^*_{ACI}}{M_{exp.}}$
VP4C	450	355	0.79	377	0.84
VP4G	413	367	0.89	388	0.94
VP8G	449	401	0.89	423	0.94
Average			**0.86**		**0.91**
VF4C	402	290	0.72	306	0.76
VF4G	356	298	0.84	314	0.88
VF8G	366	322	0.88	338	0.92
Average			**0.81**		**0.86**

Note: M_{ACI} and M^*_{ACI} is the prediction of moment capacity based on ACI equations. And the ultimate strain assumed to be 0.003 for M_{ACI} and 0.0035 for M^*_{ACI}, respectively;

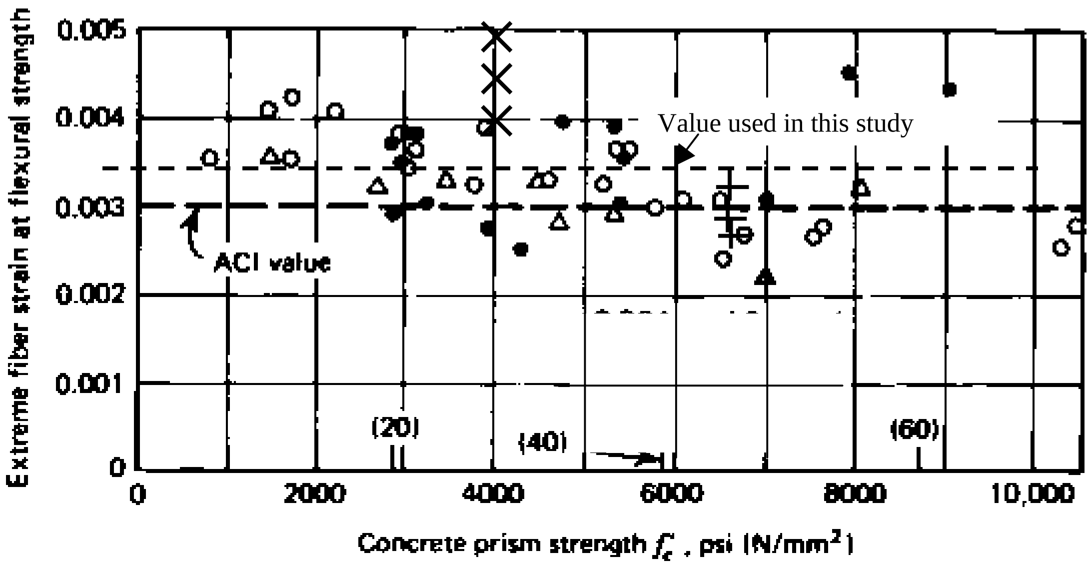

Figure 5.19. Comparison of ultimate strain values of concrete (Courtesy of Park and Paulay). Note: × is the values of FRC measured in this study; + is the values of plain concrete measured in this study.

5.4.1 Energy Based Approach.

Based on the definition of the energy based approach, ductility can be defined ability to absorb the energy and can be expressed as the ratio between the total energy and the elastic energy, as shown in Figure 5.20. Naaman and Jeong (1995) proposed the following equation to compute the ductility index, μ_E:

$$\mu_E = \frac{1}{2}\left(\frac{E_t}{E_e} + 1\right) \text{ kips-in.} \tag{5.19}$$

where E_t is the total energy computed as the area under the load deflection curve; and E_e is the elastic energy. The elastic energy can be computed as the area of the triangle formed at failure load by the line having the weighted average slope of the two initial straight lines of the load deflection curve, as shown in Figure 5.20.

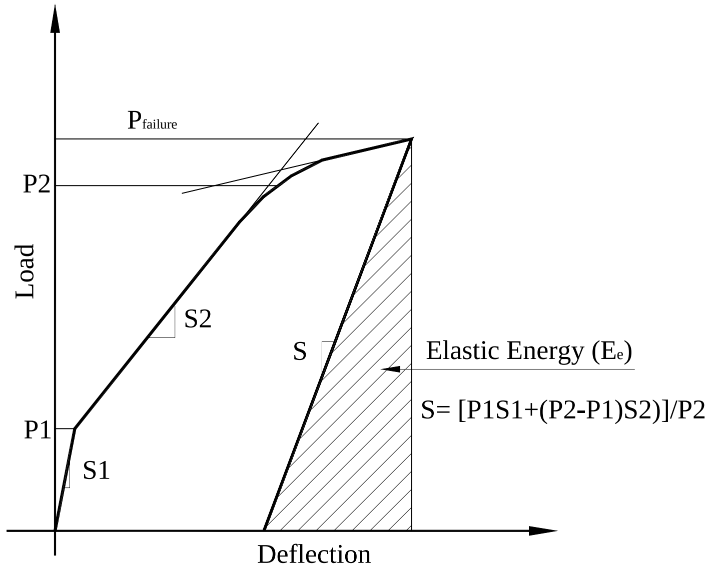

Figure 5.20. Energy-based ductility index (Naaman and Jeong, 1995)

5.4.2 Deformation Based Approach

The deformation based approach was first introduced by Jaeger et al. (1995). It takes into account the strength effect as well as the deflection (or curvature) effect on the ductility. Both the strength factor C_s and the deflection factor C_d (or curvature factor C_c) are defined as the ratio of moment or deflection (or curvature) values at ultimate to the values corresponding to the concrete compressive strain of 0.001. The strain of 0.001 is considered the beginning of inelastic deformation of concrete.

$$\mu_E = C_s \times C_d \text{ or } \mu_E = C_s \times C_c \tag{5.20}$$

$$C_s = \frac{M_u}{M_{\varepsilon=0.001}} \tag{5.21}$$

$$C_d = \frac{\Delta_u}{\Delta_{\varepsilon=0.001}} \tag{5.22}$$

$$C_c = \frac{\psi_u}{\psi_{\varepsilon=0.001}} \tag{5.23}$$

Thus, the ductility is reflected by its deformability margin between the ultimate stage and the service stage.

In the following sections, ductility indices based on both approaches, that is deformation based approach and energy based approach, are computed and compared.

5.4.3 Ductility Index Computed by the Energy Based Method

As shown in Figure 5.20, the definition of elastic slope is dependent on the selections of P1, P2, S1, and S2. Also, the experimental moment-deflection curves, as shown in Figures 5.8 and 5.9, were hard to be idealized into three portions with three distinct slopes and it could induce some subjective errors if the curves are artificially divided. In this study, the elastic slopes were decided by the slopes of loading/unloading cycles during the tests rather than using the theoretical predictions proposed by Naaman and Jerong (1994). The ductility indices computed are shown in Table 5.6.

5.4.4 Ductility Index Computed by the Deformation Based Method

Theriault and Benmokrane (1998) found that the ductility indices computed by the curvature factor demonstrated more consistent in comparison to those computed by deflection factor. Therefore, the curvature factor is adopted in this study. Figures 5.21 through 5.23 show the typical moment-curvature relationship of the testing beams. The ductility indices are computed and shown in Table 5.7.

5.4.5 Ductility Index

As shown in Tables 5.6 and 5.7, the ductility indices computed by the two methods are quite different. The effect from the addition of fibers on the ductility indices is much more pronounced when calculated based on the Jaeger method.

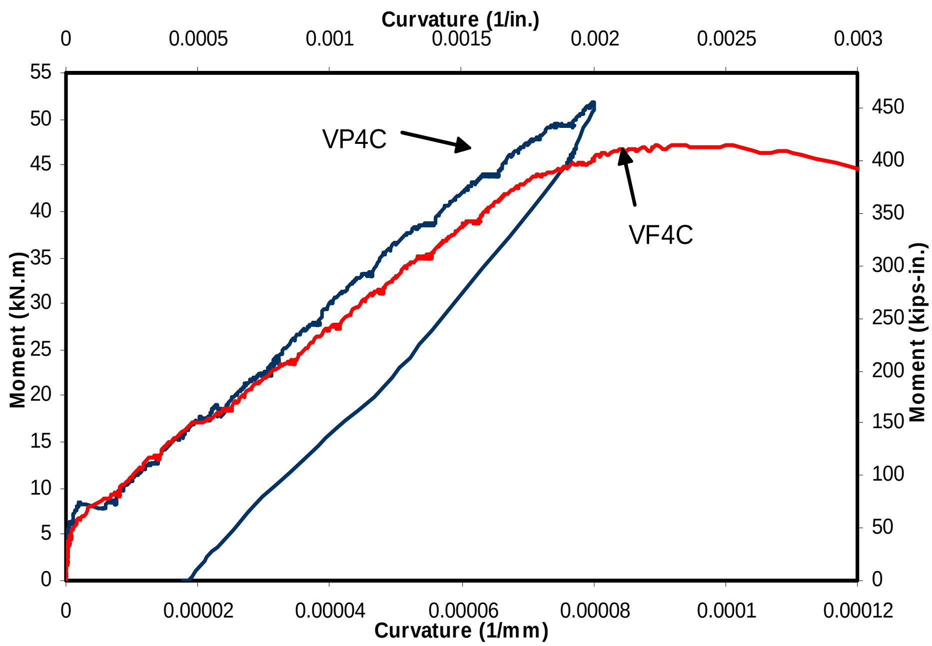

Figure 5.21. Typical moment curvature response for #4 CFRP beams

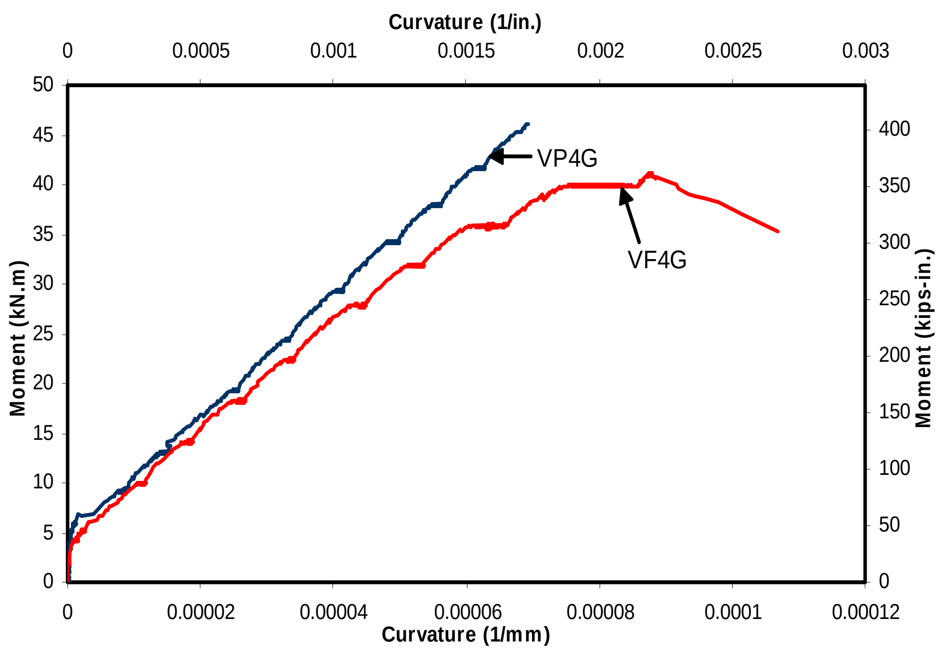

Figure 5.22. Typical moment curvature response for #4 GFRP beams

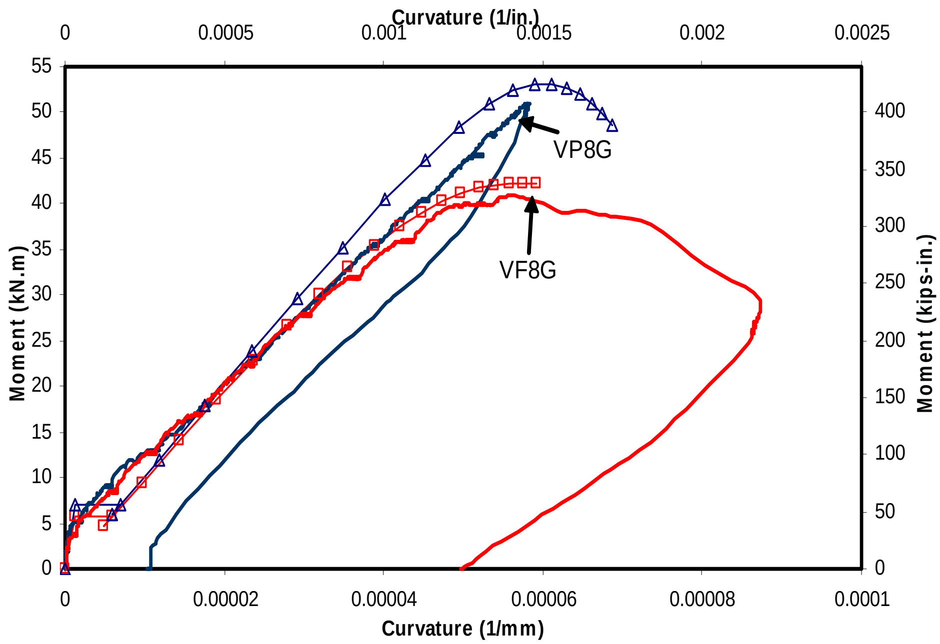

Figure 5.23. Typical moment curvature response for #8 GFRP beams

Table 5.6. Ductility index by energy based method (Naaman and Jeong, 1995)

Specimen I.D.	E_t (kips-in.)	E_e (kips-in)	μ_E	$\frac{\mu_{E-FRC}}{\mu_{E-Plain}}$
VP4C	27.83	14.58	1.45	---
VP4G	22.17	13.92	1.30	---
VP8G	23.00	12.00	1.46	---
VF4C	24.33	11.50	1.56	1.07
VF4G	22.08	11.33	1.48	1.14
VF8G	18.25	9.08	1.50	1.03
Average				1.08

Table 5.7. Ductility index by deformation based method (Jaeger, 1995)

Specimen I.D.	$M_{\varepsilon=0.001}$ (kips-in.)	$\psi_{\varepsilon=0.001}$ (1/in.)	M_u (kips-in.)	ψ_u (1/in.)	μ_E	$\frac{\mu_{E-FRC}}{\mu_{E-Plain}}$
VP4C	202	7.82×10^{-4}	450	19.46×10^{-4}	5.50	---
VP4G	177	6.66×10^{-4}	405	17.63×10^{-4}	6.05	---
VP8G	190	4.96×10^{-4}	449	14.73×10^{-4}	7.04	---
VF4C	163	6.15×10^{-4}	402	20.78×10^{-4}	8.35	1.52
VF4G	153	5.74×10^{-4}	356	22.10×10^{-4}	8.94	1.48
VF8G	157	4.45×10^{-4}	366	14.40×10^{-4}	7.56	1.08
Average						1.36

6. ACCELERATED DURABILITY TEST RESULTS

6.1 INTRODUCTION

Many studies have been carried out on the durability of individual FRP components, but literature concerning durability of the FRP and the concrete as a system, in terms of durability of bond and durability of flexural behavior, is sparse. The durability mechanism depends more on the inter-relation between the materials than on an individual component's property. In addition, the mechanical properties of a hybrid material system may deteriorate much faster than that suggested by the property degradation rates of the individual components making up the hybrid system (Schutte, 1994). The FRP/FRC hybrid system is a novel approach, and research on the durability characteristics of this hybrid system is paucity with limited information in open literature. Thus, accelerated durability tests on the FRP/FRC system are necessary as part of this study.

Limited research has been conducted on the durability characteristics of the FRP and the plain concrete system, in terms of the bond and the flexural behavior after being subjected to long-term environmental conditioning. Katz et al. (1999) observed a reduction of 80 to 90% in the bond strength as the temperature increased from 68°F to 482°F. In addition, a reduction of the bond stiffness was observed as the temperature increased. Mashima and Iwamoto (1993) noted that the bond strengths for both glass and carbon FRP seemed not to be reduced up to 300 cycles of freezing-and-thawing. Bank et al. (1998) studied the bond degradation by submerging the specimens that were made of different types of FRP rebars in tap water at 176°F for up to 84 days. They found a good relation between material degradation and the bond degradation. Al-Dulaijan et al. (2001) investigated the effect of the environmental pre-conditioning on the bond of the FRP reinforcement to concrete. The FRP rebars were exposed to three types of solution, ammonia, acetic acid, and water at 176°F for 28 days, before the rebars were embedded into concrete. They reported that the lugged rods had significantly reduced bond strength due to the degradation of the resin or the fiber/resin interface. On the other hand, little difference was observed for the smooth rods.

As for the durability of beam tests as a system, very limited information was found in the published literature. Laoubi et al. (2002) observed that the change in the overall behavior, in terms of deflection, ultimate capacity, and mode of failure, for the tested beams (both under-reinforced and over-reinforced) after 200 freezing-and-thawing cycles was insignificant. Approximately 10% reduction in the ultimate strength was observed by Tannous and Saadatmanesh (1998) in their tests of under-reinforced beams submerged in de-icing solutions for two years. Sen et al. (1993, 1999) investigated FRP pretensioned beams under tidal/thermal cycles. They found that fiberglass strands were unsuitable for pretensioning application in a marine environment. The CFRP beams showed good durability, although degradation in both bond and flexural strength was observed.

Based on the limited information discussed above, it is still not clear whether the bond or flexural behavior degrades, and if so, to what extent, after being subjected to various environmental agents. Furthermore, most of the studies mentioned previously on the FRP and concrete system concentrate on certain specific applications and do not reflect the environmental conditions to which bridge decks would be subjected in the US Mid-West region, where bridge decks are oftentimes subjected to freezing-and-thawing cycles while exposed to de-icing salts. Therefore, further study is needed to investigate the durability characteristics of the whole system.

6.2 PROBLEM STATEMENT

Composite materials, as well as the entire reinforcing system, will degrade by the attack from various environmental agents. The environmental agents that have potential effects on the long-term structural behaviors of this FRP/FRC hybrid system are discussed as follows:

- **Thermal Effect**

The thermal parameters of steel reinforcement and concrete are very close, as shown in Table 6.1. Thus, there is little or no interaction between the steel rebar and concrete due to the thermal effect on RC structure. Unlike the traditional RC structures, the coefficient of thermal expansion (CTE) between fibers and concrete is different. Furthermore, the resin materials used to bind the fibers have very large CTE in comparison to that of concrete. A significant interaction can occur with the temperature variation, which may affect the interactive properties between the two materials. To study the thermal effect on the FRP/FRC system, temperatures were varied from -4 ^{o}F to 140 ^{o}F in this study to investigate the thermal effect on the system.

- **Freezing-and-Thawing Effect**

A serious environmental threat to bridge structures with a poor quality of concrete is the freezing-and-thawing cycles. Research shows that cycles of freezing-and-thawing will damage the concrete (ACI 201.2R-92) and the damage is greatly accelerated by the use of deicing salts. Concrete is a permeable material. In addition, cracks usually exist throughout the service life of RC structures. Water or de-icing salt water could potentially reach the interface between the rebars and concrete. Therefore, accumulated damages may occur to the concrete and the FRP rebars as well as the interface by the repeated freezing-and-thawing cycles. The structural behaviors will thus be adversely affected. The effect of the freezing-and-thawing cycle on the hybrid system was examined in this study.

Table 6.1 Coefficient of thermal expansion of various materials (Balazs and Borosnyoi, 2001)

Material	Coefficient of thermal expansion $*10^{-6}$ 1/K	
	Longitudinal	transverse
Carbon fiber	-0.9 to +0.7	8 to 18
Aramid fiber	-6.0 to -2.0	55 to 60
Glass fiber	5 to 15	5 to 15
Resin	60 to 140	
CFRP	-0.5 to 1.0	20 to 40
AFRP	-2.0 to -1.0	60 to 80
GFRP	7 to 12	9 to 20
Steel	12	
Concrete	6 to13	

- **Ultraviolet Radiation**

Polymeric materials can absorb the ultraviolet and, therefore, are susceptible to reactions initiated by the absorption of ultraviolet (UV) energy. Generally, the effects of UV exposure are confined to the top few microns of the surface. Thus, the degradation from UV exposure may be a concern for the external application of FRP materials. However, test results indicated that the mechanical properties of the FRP rebars were not significantly affected even by direct exposure to the UV radiation (Tannous and Saadatmanesh, 1998). For the application of FRP material in this project, FRP rebars were protected by concrete cover. Therefore, the degradation caused by UV radiation was expected to be negligible and was not investigated in this study.

- **De-icing Salt Solution**

De-icing salt used in cold climates, and associated chloride penetration, is a major cause of corrosion in steel reinforced highway structures. It may also affect the strength of the FRP materials. More than 20% tensile strength reduction was observed for E-glass/ vinylester immersed in de-icing salt solution for 180 days (Tannous and Saadatmanesh, 1998). As discussed previously, damage caused by the freezing-and-thawing cycles will be aggravated by the use of salt solution. The effect of de-icing solution on this new hybrid system was simulated and investigated in this study.

- **Humidity Effect**

FRP rods are not waterproof. Moisture can diffuse into resin, leading to changes in mechanical characteristics as well as in physical appearance (increase of volume). As a result, the overall performance of the FRP/FRC hybrid system may be altered. Since the specimens in this study were in contact with salt water, the humidity effect on the FRP/FRC system was not investigated separately.

- **Alkaline Effect**

When in contact with alkaline media, FRP material will degrade due to the chemical reaction with an alkaline solution. For the proposed hybrid FRP/FRC system, FRP rods were embedded in concrete, which is known to have a pH level as high as 13.5. This alkaline environment can damage glass fibers through the loss of toughness and strength. Several studies have been conducted out on the effect of alkaline on the FRP material. However, in most of these studies, FRP rods were directly immersed into an alkaline solution to simulate the FRP rods in concrete, and significant degradation for GFRP rebars was reported (Uomoto and Nishimura, 1999). Direct immersion into an alkaline solution was thought to be much more severe than real conditions. Some researchers (Sekijima et al., 1999) conducted durability test in which prestressed concrete beams reinforced with GFRP grids were exposed outdoors for 7 years, where the annual average temperature was 60^{o}F, and the annual precipitation amounted to 58 in.; an extremely small effect was observed. A similar observation was made by Tannous and Saadatmanesh (1998). Most likely, it is the mobility of the alkaline ions that greatly affects the test results. To accelerate the possible degradation effect from alkaline while not exaggerating it, FRP rods were embedded in concrete and the specimens were kept moist in this study.

In this study, a total of 36 bond specimens and 24 beam specimens were fabricated to study the effect of various environmental agents on the durability of the FRP/FRC system. To simulate the seasonal weather changes in the mid-west region of the US, specimens were subjected to combined environmental cycles, consisting of the freezing-and-thawing cycles and the high temperature cycles, while in contact with a salt solution. Then, bond behaviors as well as flexural beam behaviors were compared with unweathered specimens to investigate the durability of this new hybrid system.

6.3 TEST RESULTS AND DISCUSSIONS

6.3.1 Influence of Durability on Bond Performance

In the following sections, the environmental conditioning's effect on the specimen conditions and the bond behaviors are discussed. Differences of the bond performance between the plain concrete specimens and the FRC specimens after being subjected to the environmental conditioning are also presented.

6.3.1.1 Specimen appearance after environmental conditioning

After the environmental conditioning, the specimen conditions were changed and are explained in details below.

- **Plain Concrete Specimens**

In addition to concrete scaling on the surface, most specimens also showed some damage on the concrete, especially at the corner areas. One specimen (DP4C) and one specimen (DP4G) were severely damaged and large portions of concrete were broken apart, as shown in Figure 6.1.

- **FRC Specimens**

Damages were limited to the surfaces of the specimens. With the scaling of concrete at the surfaces, fibers could clearly be observed. However, all FRC specimens remained integrated, as shown in Figure 6.1. In comparison to plain concrete specimens, the FRC specimens were more immune to the attack of the environmental conditioning.

(a) #4 GFRP

(b) #4 CFRP

Figure 6.1 Different in appearance of plain concrete specimen and FRC specimen after environmental conditioning

6.3.1.2 <u>Effect of environmental conditioning on bond behavior</u>

The test results are summarized in Table 6.2. The bond-slip responses at the loaded end and the free end are shown in Figures 6.2 through 6.13. Herein, the average bond strength was calculated as the pullout force over the embedded area of the rebar. The slip on the side of loading was calculated as the value of LVDT2 minus the elastic deformation of the FRP rebar between the bond zone and the location of LVDT2 (see test setup of bond test). Again, the deformation of the steel frame is ignored due to the fact that the steel frame was very rigid.

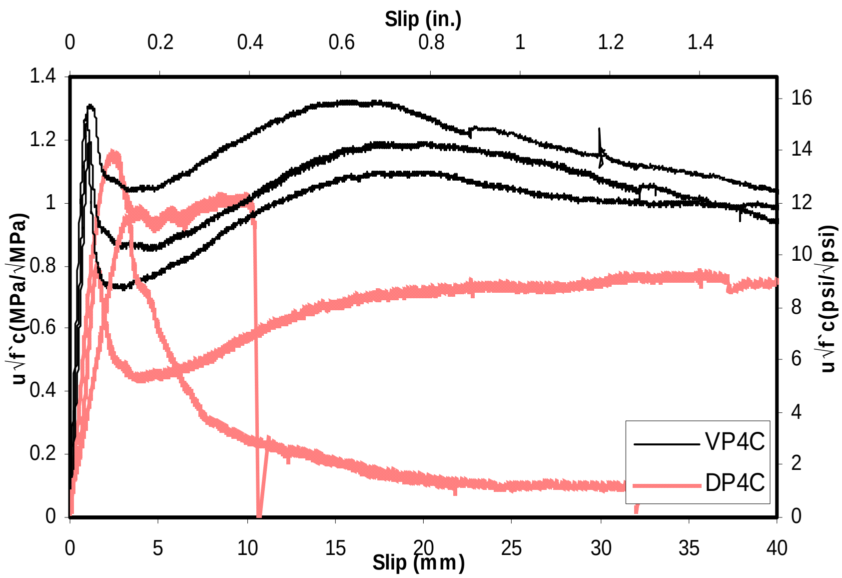

Figure 6.2 Loaded-end bond-slip response for #4 CFRP plain concrete specimens

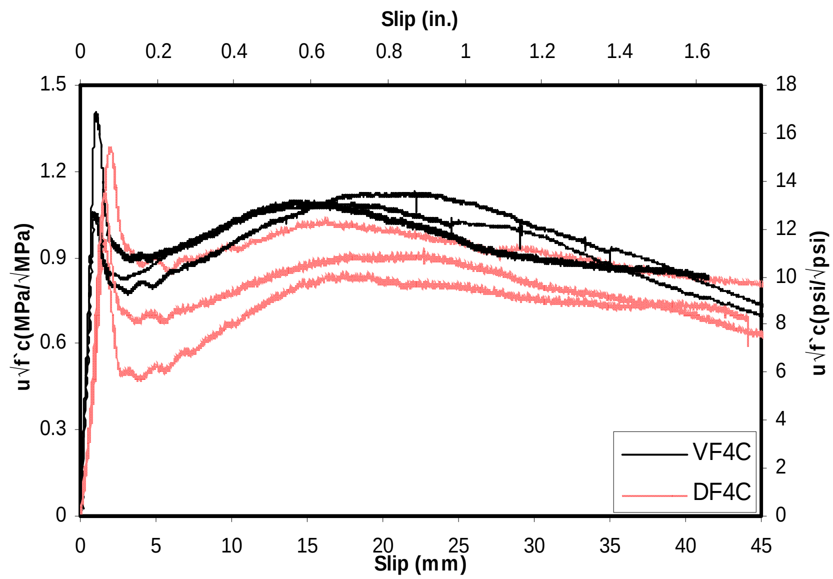

Figure 6.3 Loaded-end bond-slip response for #4 CFRP FRC specimens

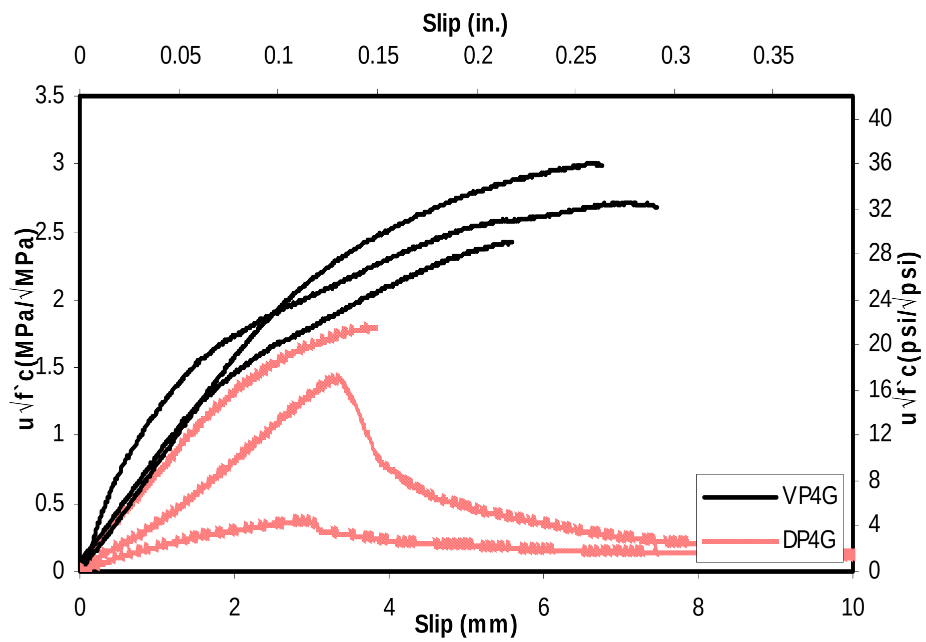

Figure 6.4 Loaded-end bond-slip response for #4 GFRP plain concrete specimens

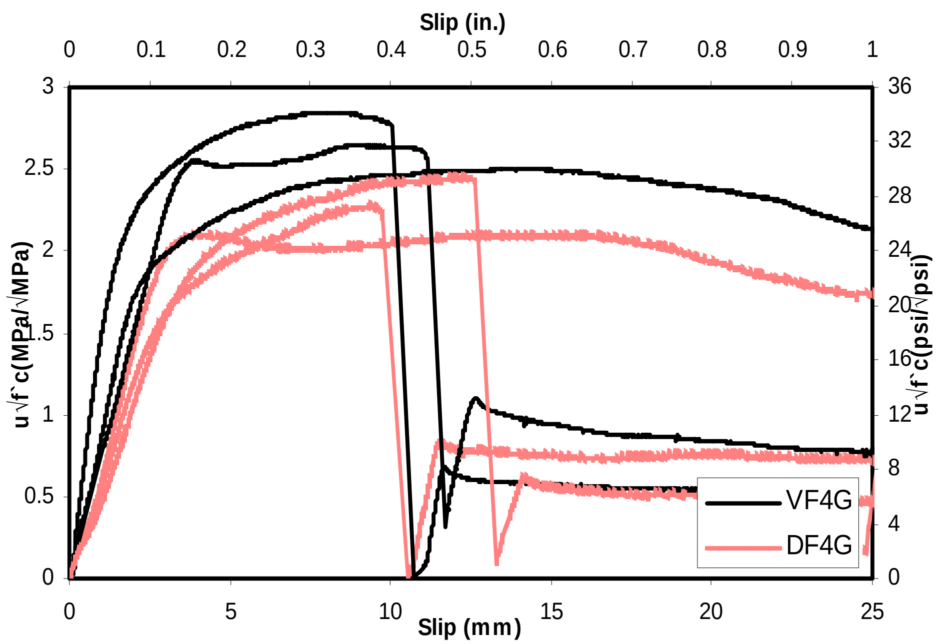

Figure 6.5 Loaded-end bond-slip response for #4 GFRP FRC specimens

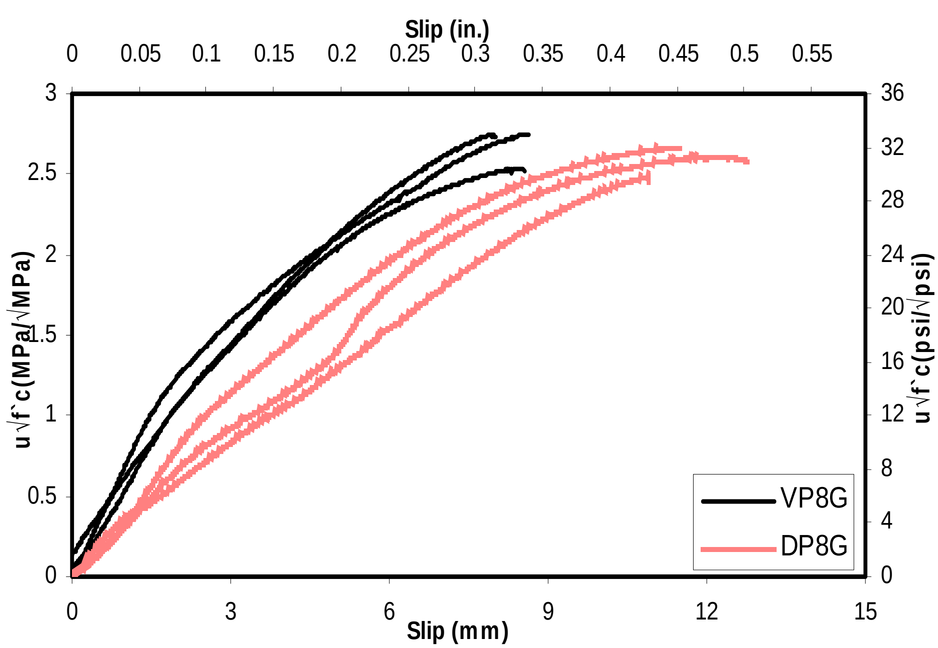

Figure 6.6 Loaded-end bond-slip response for #8 GFRP plain concrete specimens

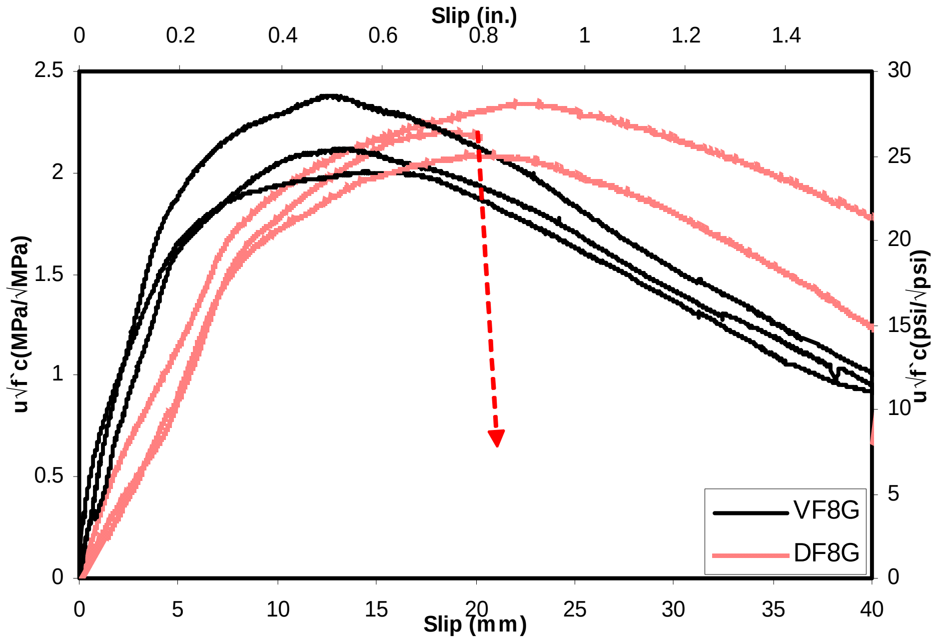

Figure 6.7 Loaded-end bond-slip response for #8 GFRP FRC specimens

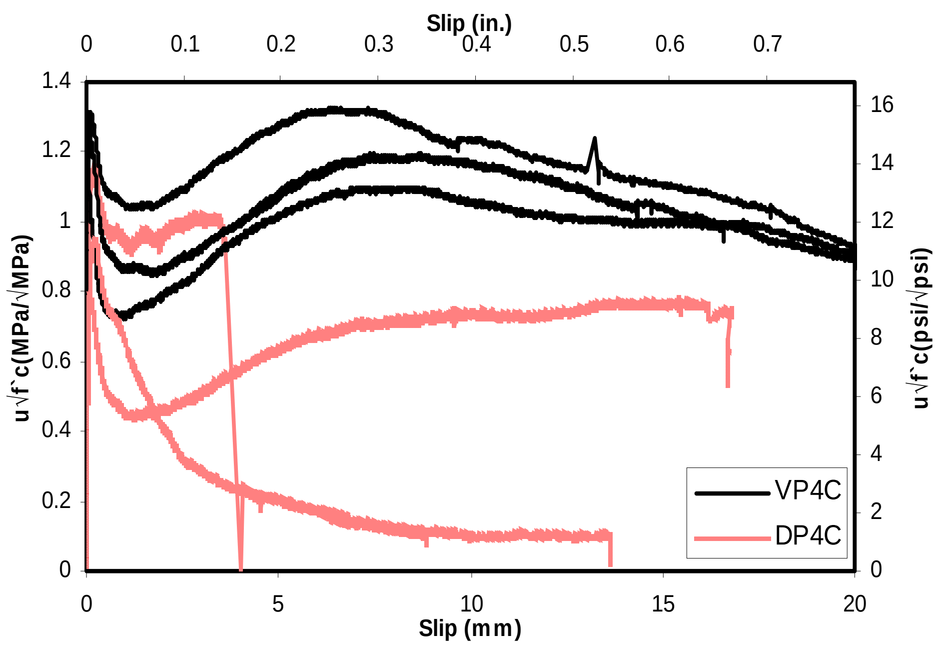

Figure 6.8 Free-end bond-slip response for #4 CFRP plain concrete specimens

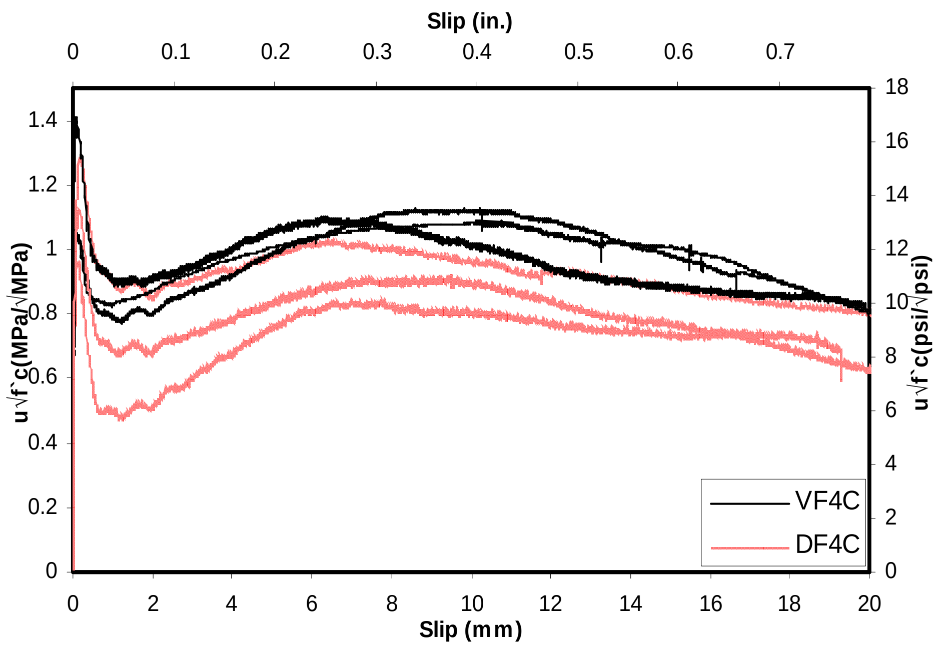

Figure 6.9 Free-end bond-slip response for #4 CFRP FRC specimens

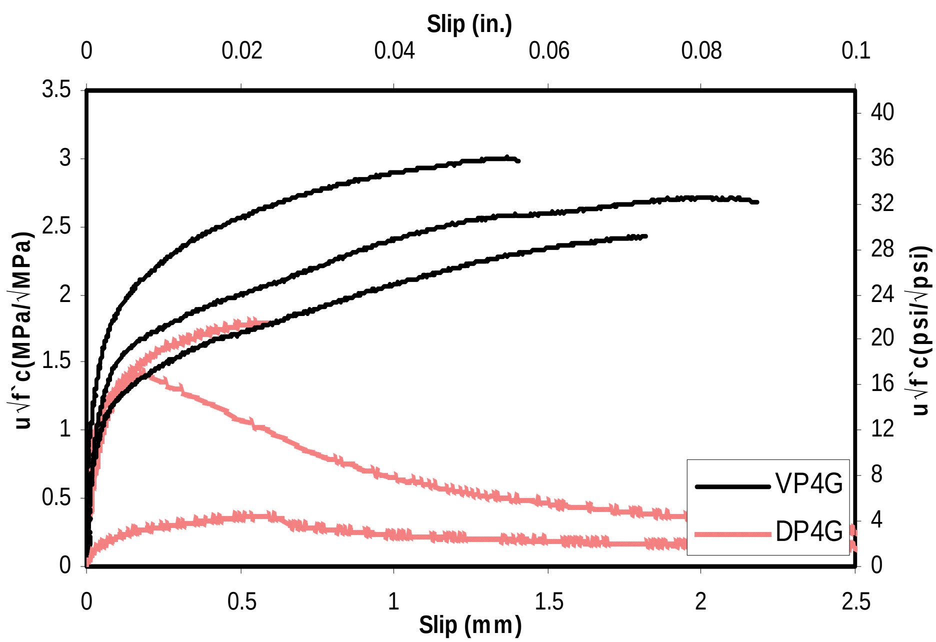

Figure 6.10 Free-end bond-slip response for #4 GFRP plain concrete specimens

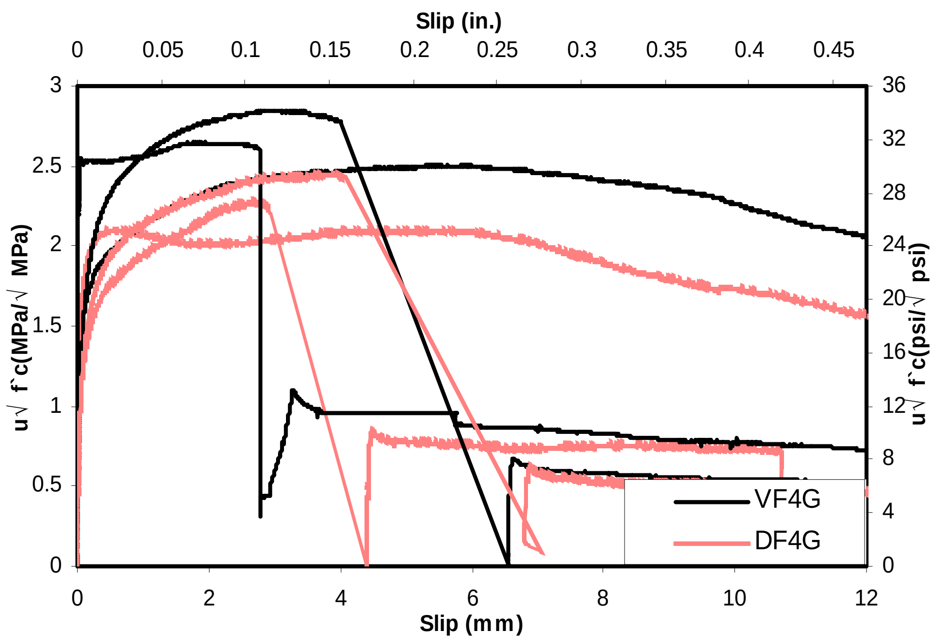

Figure 6.11 Free-end bond-slip response for #4 GFRP FRC specimens

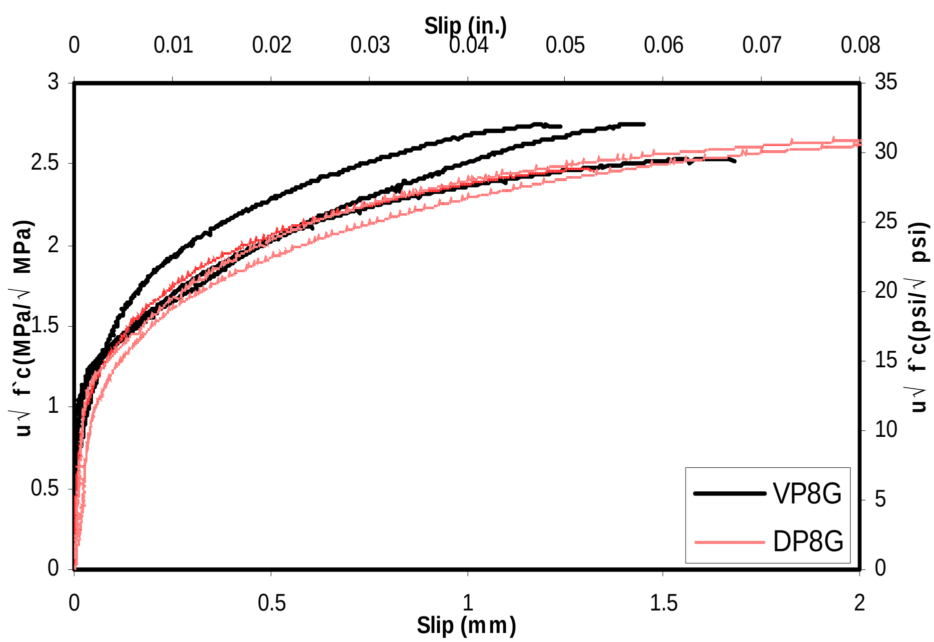

Figure 6.12 Free-end bond-slip response for #8 GFRP plain concrete specimens

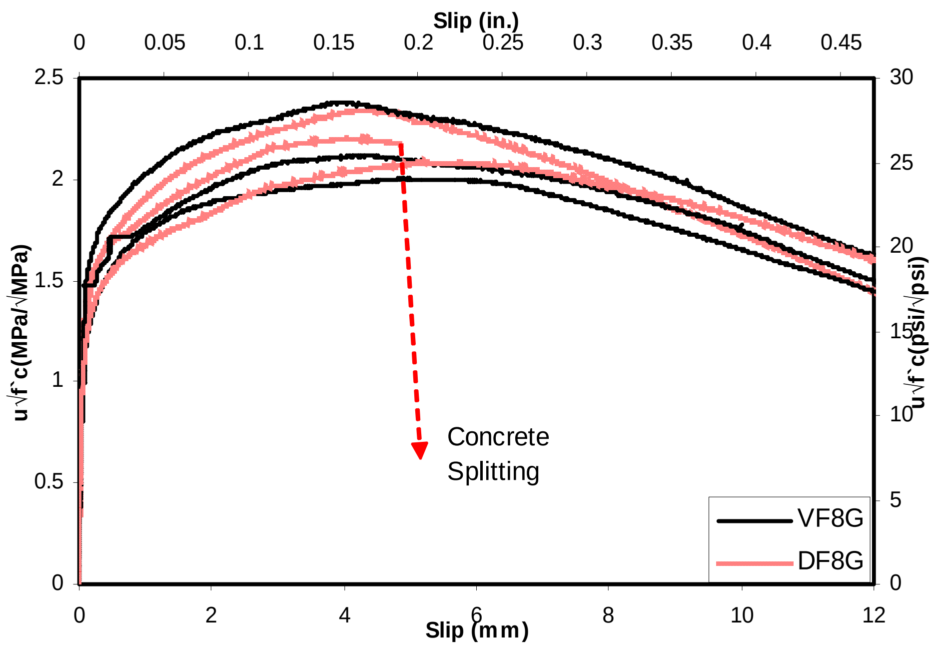

Figure 6.13 Free-end bond-slip response for #4 GFRP FRC specimens

Table 6.2 Results from the bond durability tests

I.D.	Bond Strength (psi)		Loaded –End Slip (in.)		Design Bond Strength (psi)		Bond Stiffness (ksi/in.)		Failure Mode+
VP4C	1,269	1,255	0.03	0.04	1,273	1,080	637	540	P
	1,299		0.04		843		421		P
	1,198		0.04		1123		561		P
VP4G	2,437	2,712	0.22	0.26	1034	1,322	517	661	S
	3,001		0.27		1706		853		S
	2,699		0.29		1226		613		S
VP8G	2,759	2,682	0.34	0.33	1252	1,232	626	616	S
	2,538		0.34		1288		644		S
	2,748		0.32		1156		578		S
DP4C	947	970	0.13	0.08	692	813	346	406	S
	805		0.06		782		391		P
	1,157		0.05		964		482		S
DP4G	342	1,185	0.12	0.13	154	748	77	374	S
	1,803		0.15		1124		562		S
	1,400		0.13		967		484		S
DP8G	2,598	2,585	0.50	0.46	935	1,101	468	551	S
	2,467		0.43		1162		581		S
	2,689		0.45		1207		603		S

VF4C	1,243	1,035	0.04	0.04	1223	1,026	611	513	P
	930		0.04		922		461		P
	933		0.03		933		466		P
VF4G	2,335	2,352	0.36	0.40	1716	1,293	858	647	S
	2,212		0.53		1139		569		P
	2,508		0.32		1025		513		S
VF8G	1,768	1,916	0.57	0.53	795	959	397	480	P
	1,869		0.52		1036		518		P
	2,103		0.49		1047		524		P
DF4C	979	985	0.06	0.06	888	906	444	453	P
	847		0.06		728		364		P
	1,130		0.07		1101		550		P
DF4G	2,161	2,005	0.49	0.47	901	1,081	450	540	S
	2,012		0.37		967		484		S
	1,843		0.54		1375		687		P
DF8G	1,835	1,938	0.85	0.85	876	946	438	473	P
	1,914		0.80		998		499		S
	2,064		0.90		963		482		P

Note:$^{+}$ P=Pullout failure; S=Splitting failure;

Plain concrete specimens

As shown in Figures 6.2 through 6.13, in comparison to the unweathered specimens, the bond-slip response was significantly altered after being subjected to the environmental conditioning.

- **Bond-Slip Response**

Unweathered specimens showed fairly consistent test results given the same testing parameters. However, test results for specimens, after being subjected to environmental conditioning, were inconsistent. The inconsistent behavior may be due to the random nature of the development of the degradation (Bank et al., 1998). Different levels of damage on the specimens were observed visually. In general, specimens with more severely damaged concrete showed lower bond strength. In other words, the bond strength was strongly dependent on the condition of the concrete. Figure 6.1 showed the most severely damaged specimens (DP4C and DP4G). These specimens had large amounts of concrete broken apart and thus showed very low bond strengths.

After specimens had been subjected to the environmental conditions, have their bond-slip curves softened. The slopes of the pre-peak curves were decreased and the shapes of the curves were even changed in some specimens. As discussed in Chapter 4, bond between the CFRP rebar and the concrete initially consisted of chemical adhesion and friction. With the increase of the relative slip between the rebar and the concrete, chemical adhesion was broken and the pullout load was then resisted by friction force only. Therefore, two peak bond strengths have been observed. This occurred when the chemical bond reached its ultimate; the other occurred when the friction force reached its maximum. As shown in Figure 6.3, only one peak was observed in specimen (DP4C) after environmental conditioning, which may be due to the serious damage to the chemical bond.

- **Failure Modes**

Most of the specimens had the same failure modes as the unweathered specimens. However, the failure modes were changed in the DP4C specimens. All three unweathered specimens, VP4C, failed by the rebar pullout. However, two of the three DP4C specimens failed in concrete splitting; the other one failed in rebar pullout. This was caused by the damage of concrete. Some portions of the concrete were broken apart; thus a smaller amount of concrete could resist the splitting force caused by the rebar.

- **Ultimate Bond Strength**

Ultimate bond strengths of all the specimens were reduced and this effect was more significant in specimens with smaller size (#4 rebar specimens). As shown in Figure 6.14, 23%, 56 %, and 4% reductions were observed in ultimate bond strength for DP4C, DP4G, and DP8G specimens, respectively.

- **Bond Stiffness**

Because the bond stiffness gives a relationship between load and deformation, this value has an important effect on the width of flexural cracks in reinforced concrete and on the deflection of beams and slab (Katz, et al., 1999). Its value can be computed by the slope of the bond-slip curve at the loaded end or at the free end. As mentioned previously, after being subjected to environmental conditioning, the surfaces of most of the specimens were severely damaged. Thus, the measured loaded end slip was affected and increased somehow. However, the slip measured from the free-end slip did not have this influence. As shown in Figures 6.2 to 6.13, the slopes of the curves, at the free end, did not show as much reduction as those at the loaded end. Thus, the bond stiffness in this research was computed by the slope of the bond-slip curve at the free end. On the other hand, bond behavior at the service stage is of more significance since bond failure rarely controls the design of the structural members. It is more related to the serviceability. In this study, bond stiffness is defined as the slope of the secant modulus corresponding to the slip of 0.002 in. at the free end. The value of 0.002 in. was used because this value is often selected as the criteria for the design strength of bond. Some more explanation can be found in the later paragraphs.

As shown in Figure 6.15, 25%, 43%, and 11% reductions were observed in the bond stiffness for DP4C, DP4G, and DP8G specimens, respectively.

- **Design Bond Strength**

The application of the ultimate bond strength data to real design is not appropriate because of the excessive slip occurring in these specimens at large loads. Too much slip will result in intolerable crack width. From a designer's point of view, Mathey and Watstein (1961) suggested that bond stress corresponding to 0.01 in. slippage of loaded end or 0.002 in. of free end for steel reinforced structures can be defined as the critical bond stress. The criterion of 0.01 in. slippage at the loaded-end was decided based on half of the crack width limitation (Mathey and Watstein, 1961).

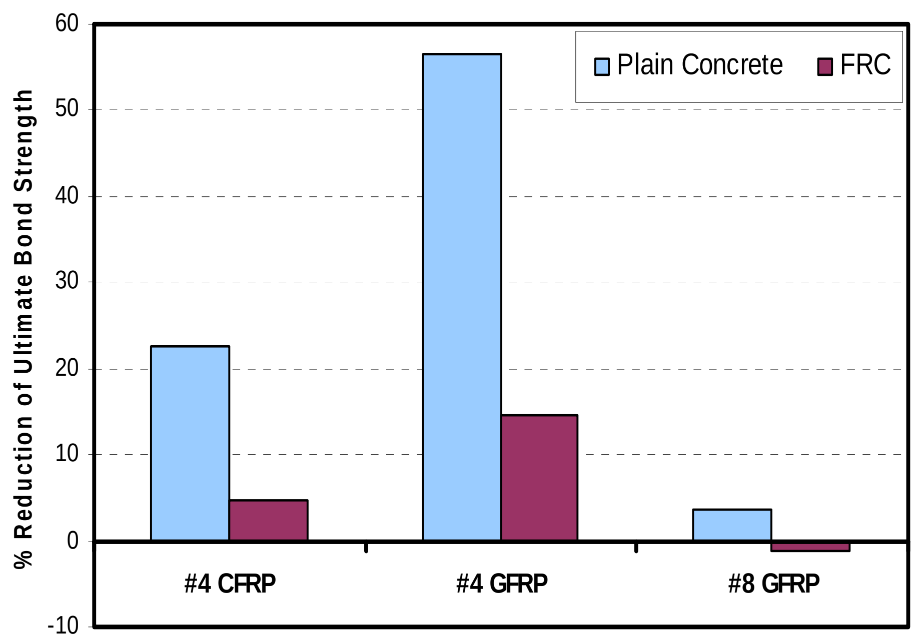

Figure 6.14. Reductions in ultimate bond strength

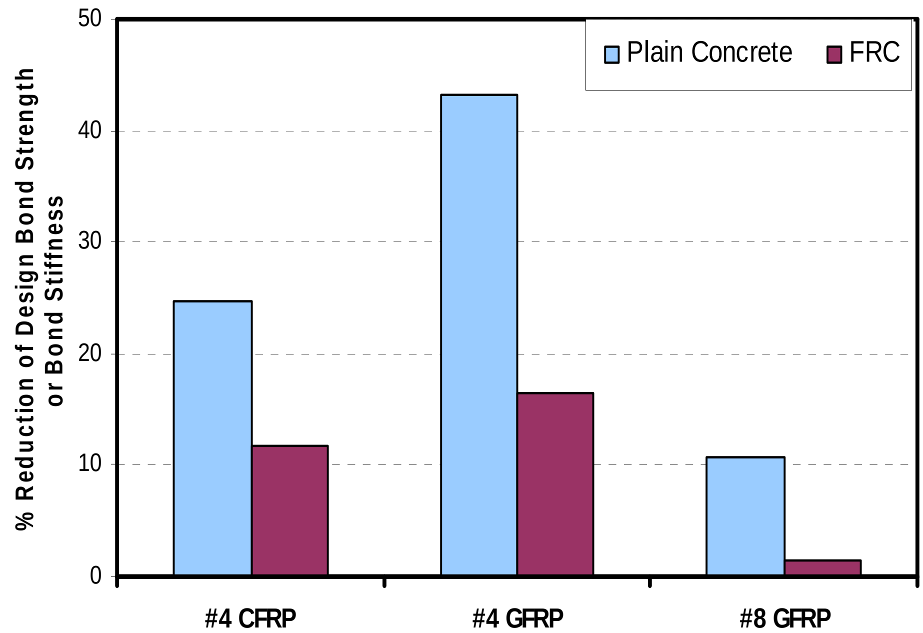

Figure 6.15. Reductions in design bond strength or bond stiffness

Ferguson et al. (1966) pointed out that the loaded-end slip of the pullout specimens was larger than that of the beam specimens because flexural cracks in beam specimens tended to distribute the slip in several places along the beam. Also, since there is relatively low elastic modulus of FRP materials (GFRP is about 1/5 that of steel, CFRP is about 2/3 that of steel), greater elongation along the embedded rebar will be produced and will lead to a larger loaded-end slip. Thus, 0.01 in. slippage at the loaded-end of the pullout specimens as design criterion is not appropriate. To keep it comparable to limits imposed on the steel rebar, bond strength corresponding to 0.002 in. slippage at the free-end was adopted as the designing bond strength. Based on the definition of the bond stiffness and the design bond strength in this study, the reduction rates of the design bond strengths were the same as those of the bond stiffness.

FRC specimens

In the following sections, test results regarding the FRC specimens are presented.

- **Bond-Slip Response**

In general, the test results of the FRC specimens showed good consistency. The behavior of the specimens in the same testing group was similar. Similar to the plain concrete specimens, all the bond-slip curves were softened after being subjected to the environmental cycles.

- **Failure Modes**

Similar to the plain concrete specimens, most of the FRC specimens had the same failure modes as the unweathered specimens. However, the failure mode of one of the three DF8G specimens changed from rebar pullout to concrete splitting.

- **Ultimate Bond Strength**

Reductions of the bond strength in the FRC specimens were observed as in the plain concrete specimens. As shown in Figure 6.14, 5%, 15%, and -1% (basically 0%) reductions were observed in the ultimate bond strength for DF4C, DF4G, and DF8G specimens, respectively.

- **Bond Stiffness**

Similar to the plain concrete specimens, reductions of the bond stiffness were observed in the FRC specimens. As shown in Figure 6.15, 12%, 16%, and 1% reductions were observed in the bond stiffness for DF4C, DF4G, and DF8G specimens, respectively.

- **Design Bond Strength**

The reduction rates of design bond strength were the same as the rates of the bond stiffness, which are 12%, 16%, and 1% for DF4C, DF4G, and DF8G specimens, respectively.

6.3.1.3 <u>Discussions on the influence of durability on bond</u>

After being subjected to the environmental conditioning, both the plain concrete specimens and the FRC specimens showed bond degradations. Bond is determined by the properties of its constituents (concrete and rebar) and the interaction between the constituents. Three possible reasons are provided to explain the bond degradation as follows:

1. Microvoids between the rebar and the concrete exist at the time of the specimen fabrication; i.e., rebar is not totally in contact with the concrete (Gylltoft, et al., 1982). When specimens are submerged in the solution, the solution will permeate into the interface between the rebar and concrete. Later, the microvoids will be filled with solutions. The volume of water will expand about 10% when frozen. Microcracks will thus be induced if the stresses, f_c, are larger than the tensile strength of the concrete, f'_t. With the subsequent

freezing-and-thawing cycles, damage will build up and more and bigger microcracks would develop.

2. As shown in Table 6.1, the FRP rebar has a higher CTE than that of concrete. When the temperature increases, the expansion rate of the FRP rebar is larger than that of the concrete. Radial busting force will be imposed on the concrete surface at the interface, and the structure at the interface will be disrupted. When the stress in the concrete, f_c, is larger than the tensile strength, f'_t, cracks would develop. When the temperature reduces, the contraction rate of the FRP rebar is bigger than that of the concrete, micro-gaps will form along the interface.

The above two mechanisms function together and degrade the bond mainly by disturbing the structures at the interface. Bond degradation may also come from the degradation of the rebar itself.

3. FRP rods are not waterproof. Moisture may diffuse into the polymer resin to a certain degree (Micelli and Nanni, 2004). Studies also show that some deterioration of the polymer resins may occur since water molecules can act as resin plasticizers, thereby disputing van der Waals bonds in polymer chains (Bank and Gentry, 1995). Furthermore, during the freezing-and-thawing cycles, water will expand and lead to the cracking of the resin. Resin damage will speed up the process by which moisture is transported inside the composite, thereby allowing the deteriorations to be accelerated. The surface area is most vulnerable to be attacked; thus, the surface is expected to be the most seriously deteriorated. Consequently, the rebar and concrete will not be bonded as tightly as before. Bond thus is degraded.

All these three mechanisms play a certain role in the bond degradation and the combined effects are likely to be even more detrimental to the bond. As mentioned previously, all specimens showed bond degradation to some extent after environmental conditioning. However, the degradation magnitude differed among the different specimens.

(a) Influence of specimen dimension on bond degradation

Compared to the large (#8) specimens, the small specimens (#4) showed greater degradation effect. This was so in both the plain concrete specimens and the FRC specimens. As shown in Figure 6.14, the ultimate bond strengths reduced 56% for DP4G specimens, while only 4% reduction was observed in DP8G specimens. Similarly, the ultimate bond strengths reduced 15% for DF4G specimens; while DF8G specimens showed 1% increase. In design bond strength or bond stiffness, the small specimens also showed a much more serious reduction, as shown in Figure 6.15. Specimen dimensions effect on the bond durability can be explained by ways that the salt solution attacks the bond behavior. There are two ways in which the salt solution can reach the interface between the rebar and concrete, as shown in Figure 6.16. One is through the loaded-end of the specimens, since the free-end was coated with water-proof epoxy, and it was assumed that no solution can permeate the epoxy, as shown in Figure 6.16. The other way is through the concrete cover, as shown in Figure 6.16. In the large specimens, there were relatively smaller portions of the bonded area that could be immediately attacked by the solution. In this study, the loaded end of the specimen was directly exposed to the solutions, and the solutions could easily access the interface near the loaded end. Since the depth of the specimen that was immediately accessible to the solution was independent of the size of the specimens, the absolute depths that were affected were the same. On the other hand, the larger specimens had a larger embedment length; thus, the ratio of affected area to the whole bonded area was smaller in the case of large specimens. Another reason may be due to the larger cover depth of the large specimens. The #4 specimens had 2.5 in. embedment length and dimensions of 5 in. × 5 in. × 5 in., which meant a 2.25 in. concrete clear cover. The #8 specimens had 5 in. embedment length and dimensions of 10 in. × 10 in. × 10 in., which meant a 4.5 in. concrete clear cover. The concrete cover played a significant role in decreasing the rate of the ingress of the solution. Potter and Ho (1987) found that the depth of water penetration was a function of square root of time, which meant it would take three times longer for water to reach the rebar if double the cover depth. Since the cover of the large specimens was twice as thick as the small specimens, the interface between the rebar and concrete was better protected.

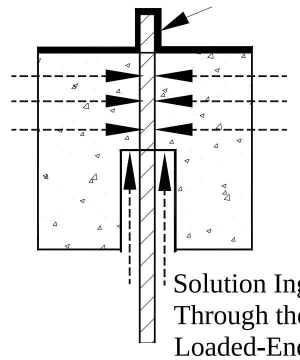

Figure 6.16 Two ways of solution ingress

Influence of fibers on bond degradation

With the addition of fibers, the degradation rate of bond was significantly reduced. As shown in Figure 6.14, an average reduction of 28% of bond strength was observed in the plain concrete specimens, while only 6% reduction was observed in the FRC specimens. In the design bond strength, an average reduction of 26% was observed in the plain concrete specimens, while only 10% reduction was observed in the FRC specimens, as shown in Figure 6.15. It could be concluded that fibers can effectively alleviate the bond deteriorations caused by environmental conditioning. As discussed earlier, cracks or voids were created during the environmental conditioning. Although the addition of fibers would not increase the first cracking load, the fibers would restrict further development of the cracks due to the expansion of the water or the rebar. Hence, the deteriorations would not be accumulated, or this would happen at a much more moderate rate.

It should also be noted that the fact that there was less bond degradation for the FRC specimens could also be partly attributed to the fact that there was less damage of the concrete after the environmental conditioning. It was clear from the difference in appearance between the plain concrete specimens and the FRC specimens, after being subjected to environmental conditioning, the fibers could effectively alleviate the damage to the concrete caused by the freezing-and-thawing cycles. During the freezing cycles, the water entrained in the concrete microvoids would have expanded and induce microcracks. Microcracks were increased by the subsequent freezing-and-thawing cycles. In the worse cases, this cumulative effect resulted in the damage of the concrete, as shown in the Figure 6.1. With the addition of fibers, the progress of the microcracks was restricted and the concrete was held together by the fibers. Also, the air content of the plain concrete used in this study was lower than of FRC, which may also be responsible for the more severe damage of the plain concrete specimens.

Difference between bond behavior of GFRP and CFRP specimens

The bond degradation rate of the GFRP specimens was more severe than that of the CFRP specimens. As shown in Figure 6.14, the bond reduced by 23% in the DP4C specimens and 56% in the DP4G specimens. Similarly, the bond was reduced by 5% in the DF4C specimens and 15% in the DF4G specimens. In the design bond strength or bond stiffness, the reductions were also observed to be larger in the GFRP specimens, as shown in Figure 6.15.

As discussed previously, the degradation of the rebar may partly be attributed to the bond degradation. Due to the attack by the salt water, the rebar, especially the outer surface, was damaged. Thus, less contact area may result. Research has shown that the CFRP rebar has superior durability characteristics compared to the GFRP rebar. Thus, less damage was expected in the case of the CFRP rebar, and hence, the CFRP specimens showed better durability of bond.

6.3.2 Influence of Durability on Flexural Performance

In the following sections, the effect of the environmental conditioning on the beam, in terms of specimen condition, flexural behaviors, and ductility is discussed. Differences in the flexural performances between the plain concrete specimens and the FRC specimens after being subjected to environmental conditioning are also reported.

6.3.2.1 Specimen Appearance after Environmental Conditioning

After the environmental cycles were completed, the appearance of the specimens was examined. Some observations were made as follows:

1. Concrete scaling on the surface of the beams was observed, as shown in Figure 6.17. Concrete scaling was limited to the top surface, and no concrete was broken apart. It can be concluded that the deterioration to the beam’s flexural behavior due to the concrete scaling is negligible, if any. The most obvious concrete scaling occurred in locations where

rebar chairs were placed. This is expected since the CTE of the plastic rebar chairs is different from that of the concrete. Overall, the damage was much less severe as compared to the damage in bond specimens. In bridge decks, the exposure condition is expected to be similar to that of beam specimens in this study, thus, the concrete damage due to the environmental conditioning for bridge decks is expected to be minimal.

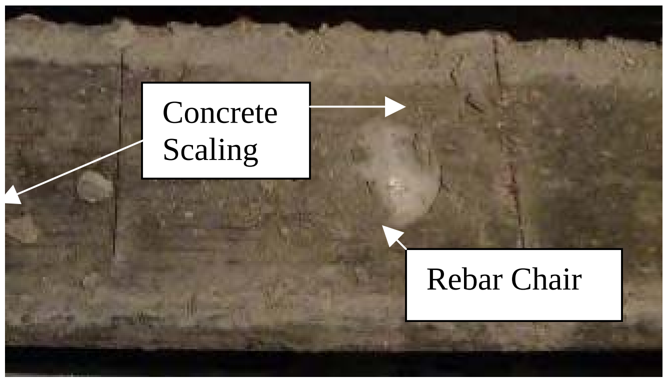

Figure 6.17 Concrete scaling on the beam surface

2. Traces of steel rust can be found on the beam surface, as shown in Figure 6.18, indicating steel stirrups have already corroded to a certain degree. On the other hand, the corrosion of steel stirrups revealed that the environmental conditionings of this study were very critical for the steel reinforced structures.

6.3.2.2 Effect of Environmental Conditioning on Flexural Performance

In this section, the effect of the environmental conditioning on the overall flexural behavior, in terms of failure modes, flexural stiffness, and flexural strength is presented.

- **Failure Mode**

After being subjected to the environmental conditioning, the failure modes for the beams did not change. That is, all the beams failed by concrete crushing. No slips between the rebar and concrete were observed during the tests, which meant that the development length was properly provided for the required stresses in the rebars to develop.

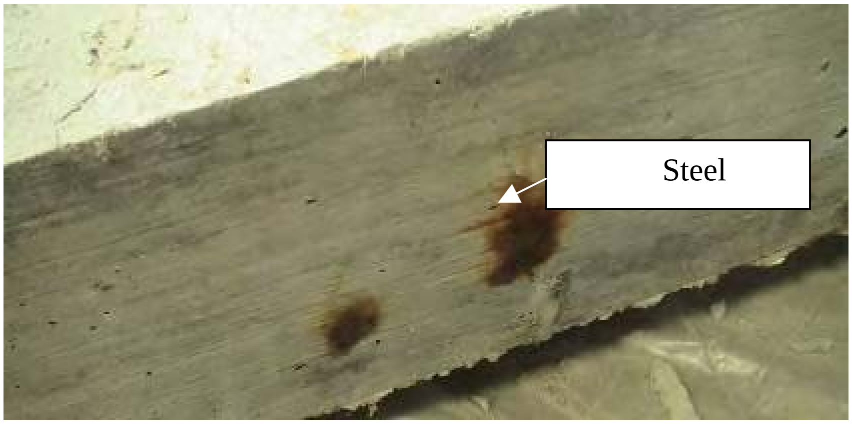

Figure 6.18 Photo showing corroded steel stirrups

- **Flexural Stiffness**

Figures 6.19 to 6.24 show the moment-deflection responses of the beams before and after the environmental conditioning. The post cracking flexural stiffness remained approximately the same for beams before and after the environmental conditioning. Flexural stiffness is determined as a function of E_cI_m, and it is assumed that E_c has not changed after the environmental conditioning. Thereby, I_m is expected to remain the same before and after environmental conditioning. According to current ACI code, I_m is determined by M_{cr}, I_g, and I_{cr} and the load level. M_{cr} remained constant, which was verified by the moment-deflection curves. I_g was not expected to have any change, since concrete scaling induced by the environmental conditioning was limited to the top surface and no concrete disintegration occurred. Thus, it was indicated that the I_{cr} did not change. The value of I_{cr} is strongly dependent on the rebar properties, including its elastic modulus and rebar area. Therefore, it can be concluded that the rebar properties, including elastic modulus, E_f, and rebar effective area, A_f, did not significantly change after being subjected to environmental conditioning. Similar findings were made by Giernacky et al. (2002).

- **Flexural Strength**

Tables 6.3 and 6.4 summarize the flexural strengths and ultimate deflections for all the plain concrete beams and the FRC beams before and after the environmental conditioning. Generally, the beams showed insignificant changes in both the flexural strength and the ultimate deflection. In the flexural strength, reductions ranged from 4% to 16% for the plain concrete beams and from 4% to 8% for the FRC beams. For the ultimate deflection, reduction ranged from -6% to 17% (basically no change) for the plain concrete beams and from 3% to 18% for the FRC beams.

According to the current design theory, the flexural strength controlled by the concrete crushing is determined by the rebar and the concrete. As discussed previously, the mechanical properties of the rebars were not significantly changed. Thus, the most plausible reason for the reduction of flexural strength was the degradation of concrete. The strains in the concrete at the ultimate were decreased slightly after the environmental conditioning. In the plain concrete beams, the average ultimate concrete strains decreased from an average 2,950 microstrains to 2,660 microstrains. In the FRC beams, the average ultimate concrete strains decreased from 4,500 microstrains to 3,800 microstrains, as shown in Figures 6.25 to 6.30.

In the previous study, it was found that the flexural strengths predicted by assuming ε_{cu} equal to 0.0035 for the FRC beams have a comparable safety factor as ε_{cu} = 0.003 for the plain concrete beams. After the concrete beams were subjected to environmental conditioning, the concrete ultimate strain decreased as shown in Figure 6.31. To reflect this change in the design, 0.0025 and 0.003 were selected as the ultimate concrete strains for the plain concrete beams and FRC beams after the environmental conditioning. By using the new values of ultimate concrete strains, the beams after environmental conditioning have a comparable safety level of design as the unweathered beams, as shown in Tables 6.5 and 6.6.

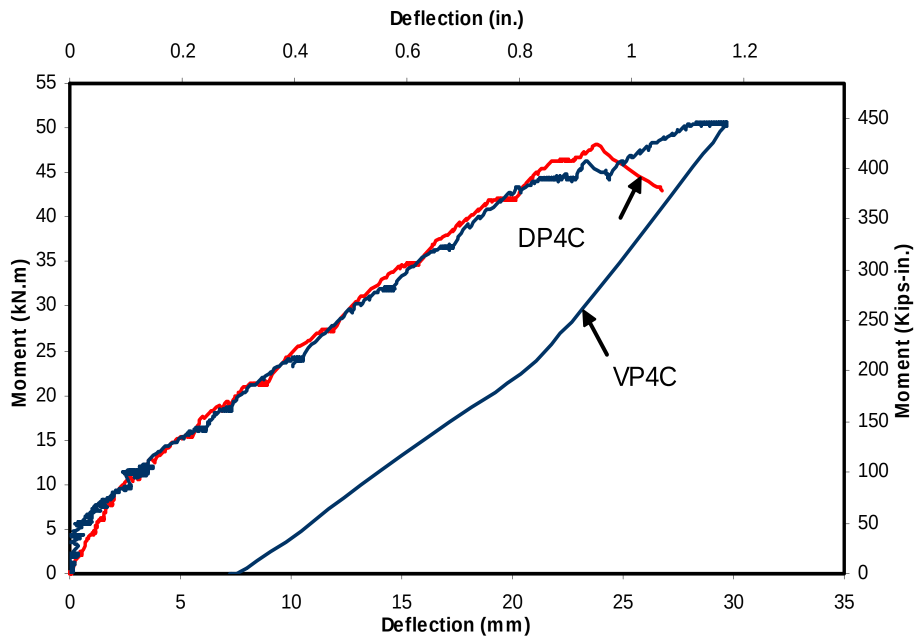

Figure 6.19 Moment-deflection response for #4 CFRP plain concrete specimens

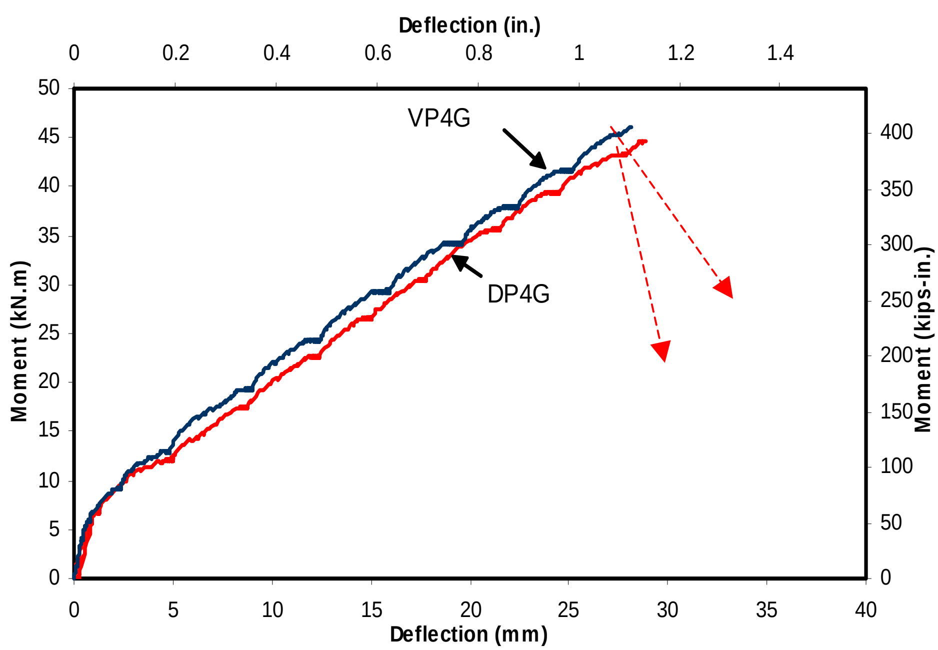

Figure 6.20 Moment-deflection response for #4 GFRP plain concrete specimens

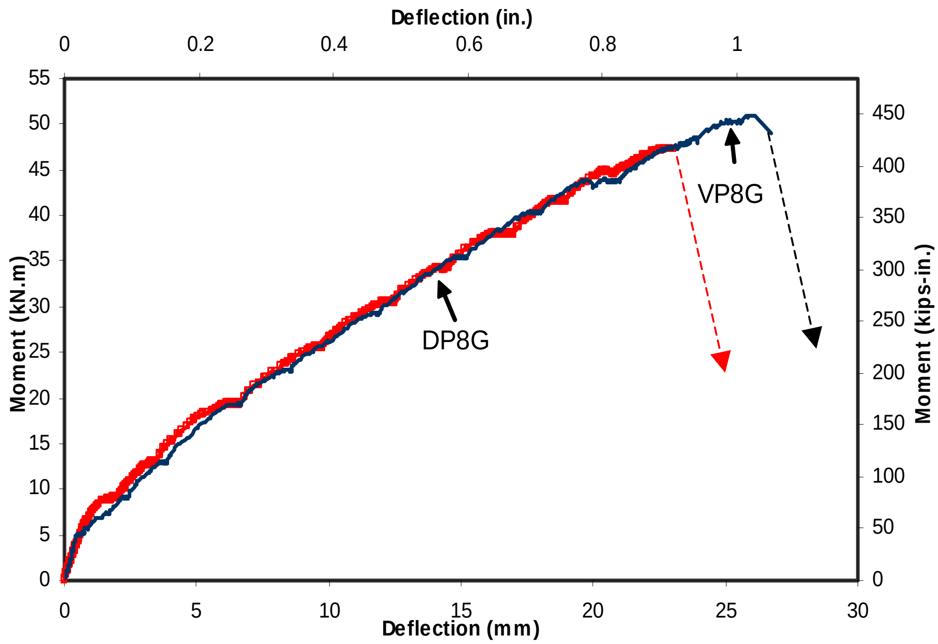

Figure 6.21 Moment-deflection response for #8 GFRP plain concrete specimens

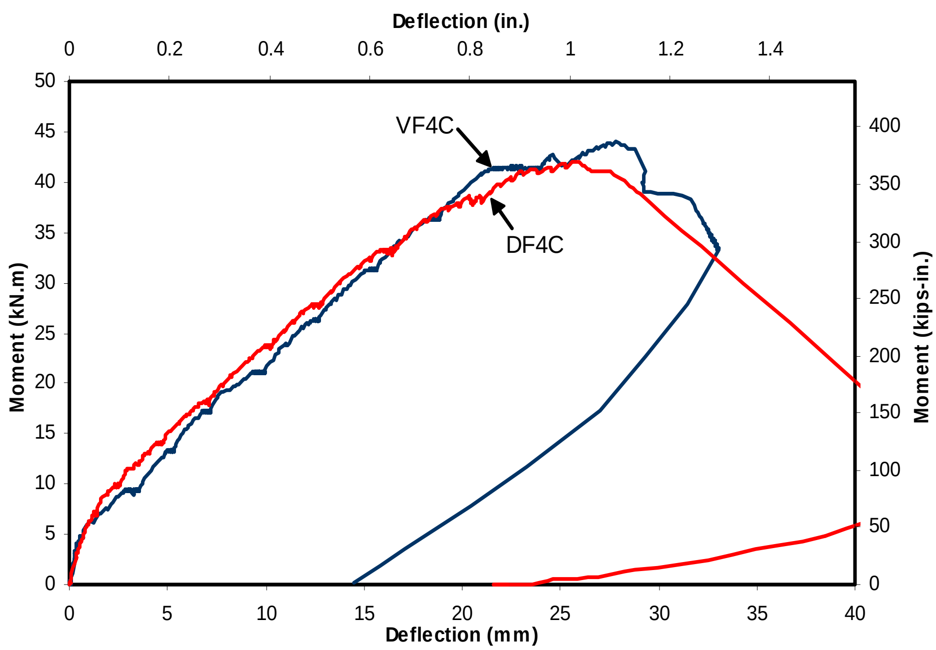

Figure 6.22 Moment-deflection response for #4 CFRP FRC specimens

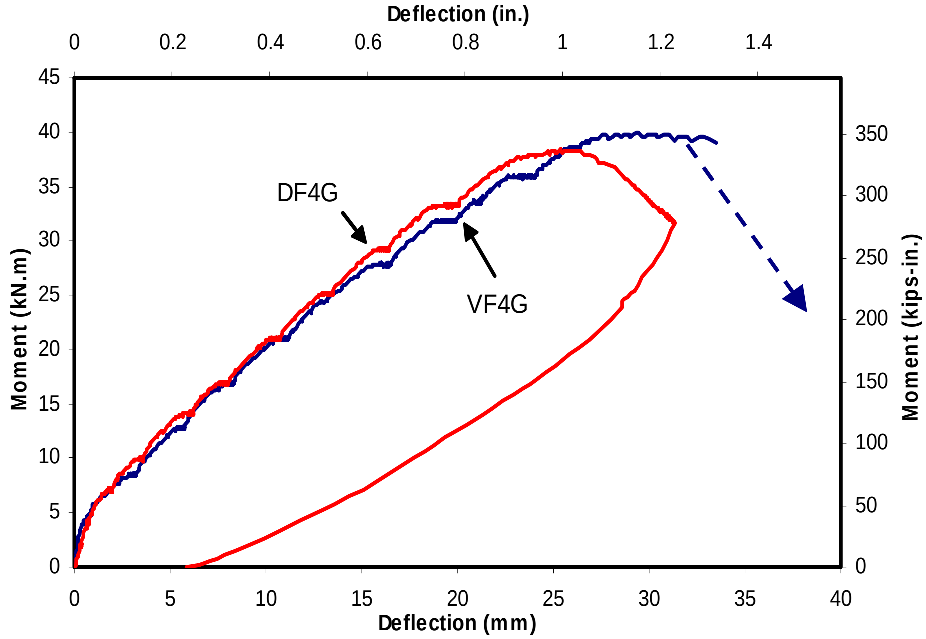

Figure 6.23 Moment-deflection response for #4 GFRP FRC specimens

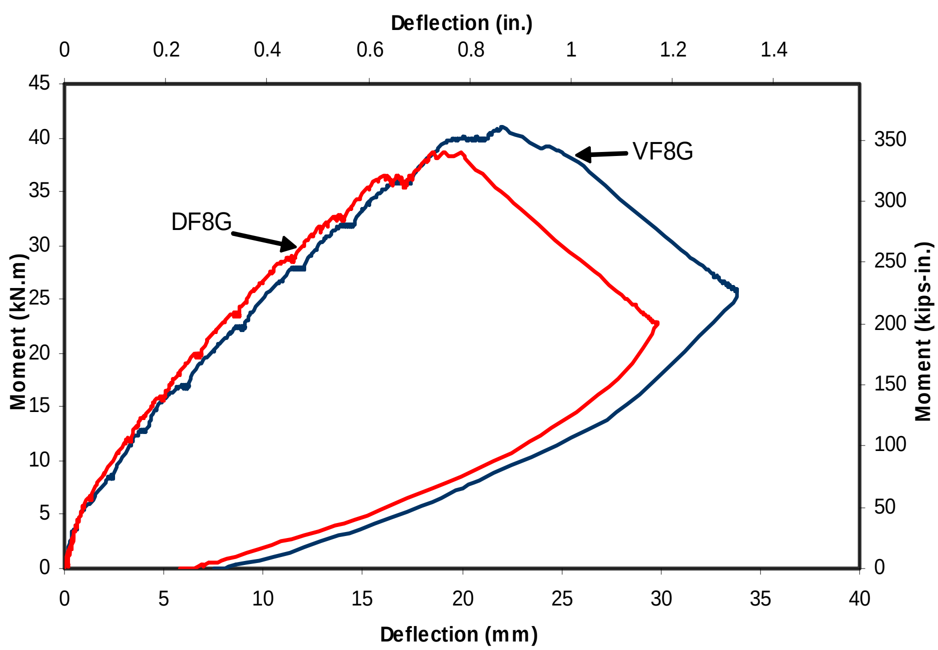

Figure 6.24 Moment-deflection response for #8 GFRP FRC specimens

Table 6.3 Beam durability results for plain concrete beams

Specimen I.D.	Ultimate Moment M_V (kips-in.)		Specimen I.D.	Ultimate Moment M_D (kips-in.)		$\frac{M_D}{M_V}$
VP4C-1	457	450	DP4C-1	423	420	0.93
VP4C-2	442		DP4C-2	417		
VP4G-1	405	413	DP4G-1	393	397	0.96
VP4G-2	420		DP4G-2	401		
VP8G-1	448	449	DP8G-1	339	378	0.84
VP8G-2	449		DP8G-2	416		
Specimen I.D.	**Ultimate Deflection Δ_V (in.)**		**Specimen I.D.**	**Ultimate Deflection Δ_D (in.)**		$\frac{\Delta_D}{\Delta_V}$
VP4C-1	1.19	1.18	DP4C-1	0.84	0.98	0.83
VP4C-2	1.17		DP4C-2	1.12		
VP4G-1	1.03	1.03	DP4G-1	1.14	1.09	1.06
VP4G-2	1.02		DP4G-2	1.04		
VP8G-1	0.96	0.96	DP8G-1	0.83	0.87	0.91
VP8G-2	0.95		DP8G-2	0.91		

Table 6.4 Beam durability results for FRC beams

Specimen I.D.	Ultimate Moment M_V (kips-in.)		I.D.	Ultimate Moment M_D (kips-in.)		$\frac{M_D}{M_V}$
VF4C-1	415	402	DF4C-1	370	388	0.96
VF4C-2	388		DF4C-2	405		
VF4G-1	350	356	DF4G-1	326	332	0.93
VF4G-2	362		DF4G-2	338		
VF8G-1	371	366	DF8G-1	341	335	0.92
VF8G-2	361		DF8G-2	328		
Specimen I.D.	**Ultimate Deflection Δ_V (in.)**		**I.D.**	**Ultimate Deflection Δ_D (in.)**		$\frac{\Delta_D}{\Delta_V}$
VF4C-1	1.20	1.15	DF4C-1	1.01	1.11	0.97
VF4C-2	1.10		DF4C-2	1.21		
VF4G-1	1.19	1.19	DF4G-1	0.98	1.00	0.82
VF4G-2	1.19		DF4G-2	1.01		
VF8G-1	0.95	0.91	DF8G-1	0.78	0.77	0.84
VF8G-2	0.87		DF8G-2	0.76		

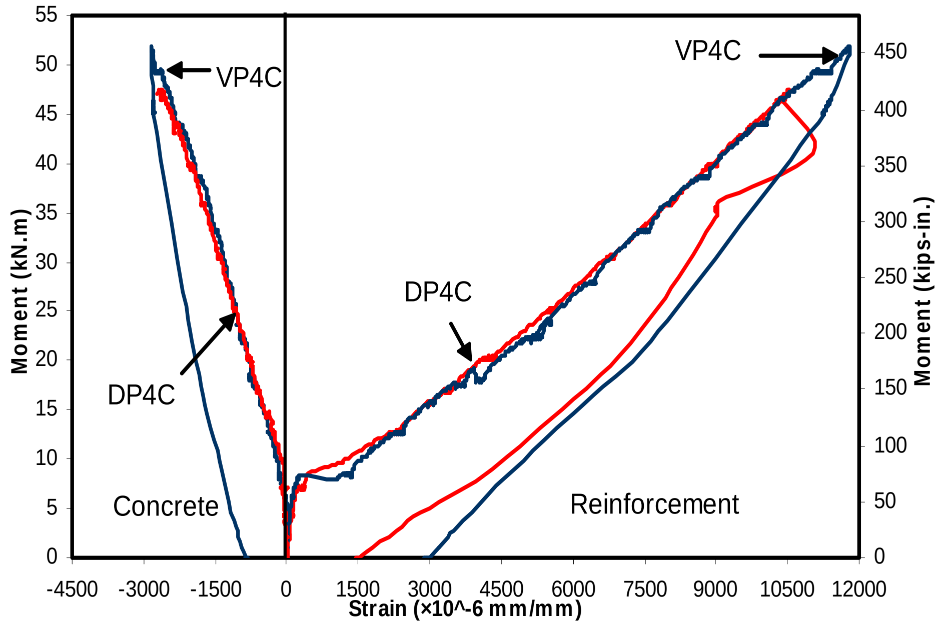

Figure 6.25 Strain distribution in #4 CFRP plain concrete specimens

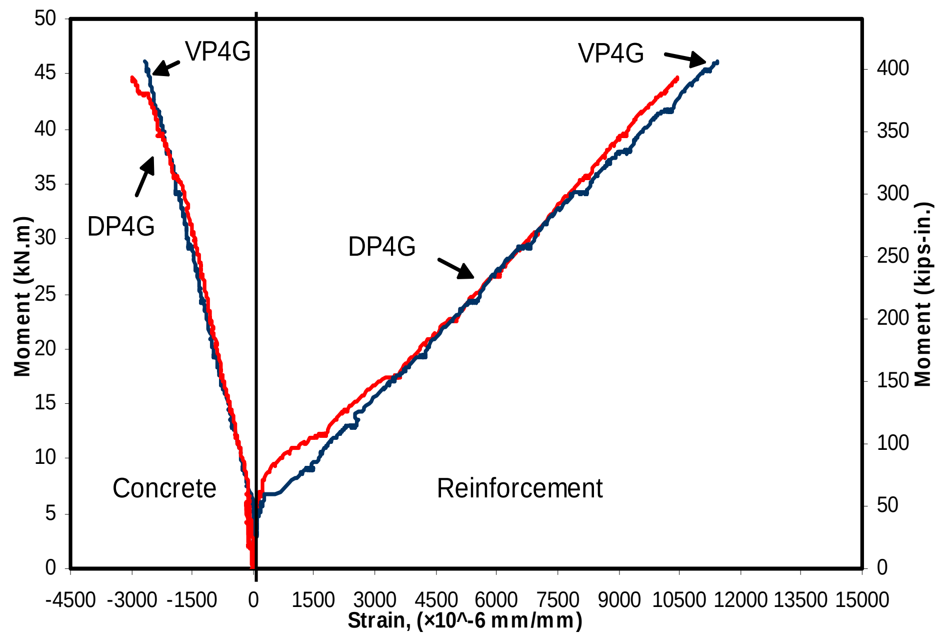

Figure 6.26 Strain distribution in #4 GFRP plain concrete specimens

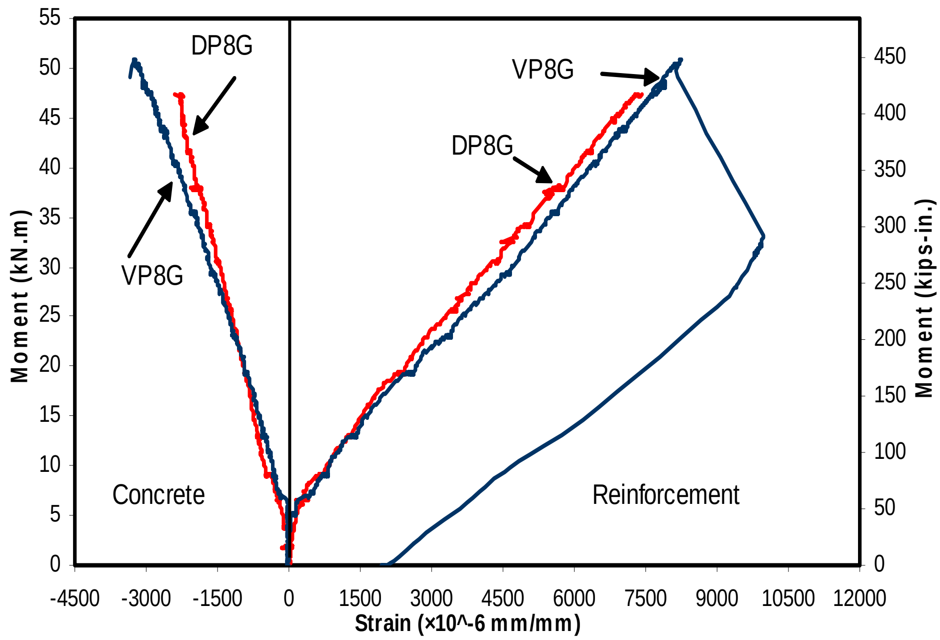

Figure 6.27 Strain distribution in #8 CFRP plain concrete specimens

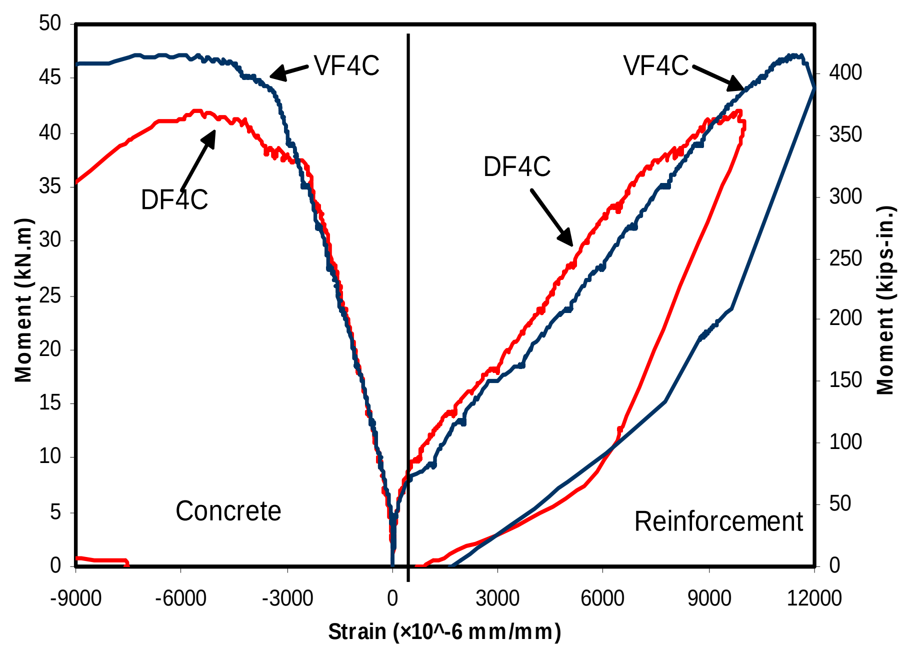

Figure 6.28 Strain distribution in #4 CFRP FRC specimens

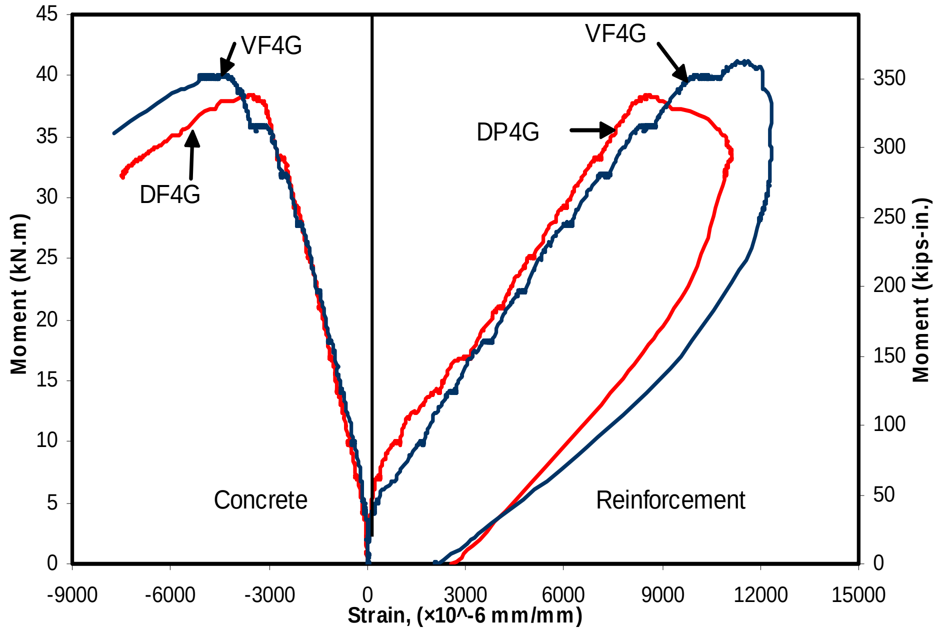

Figure 6.29 Strain distribution in #4 GFRP FRC specimens

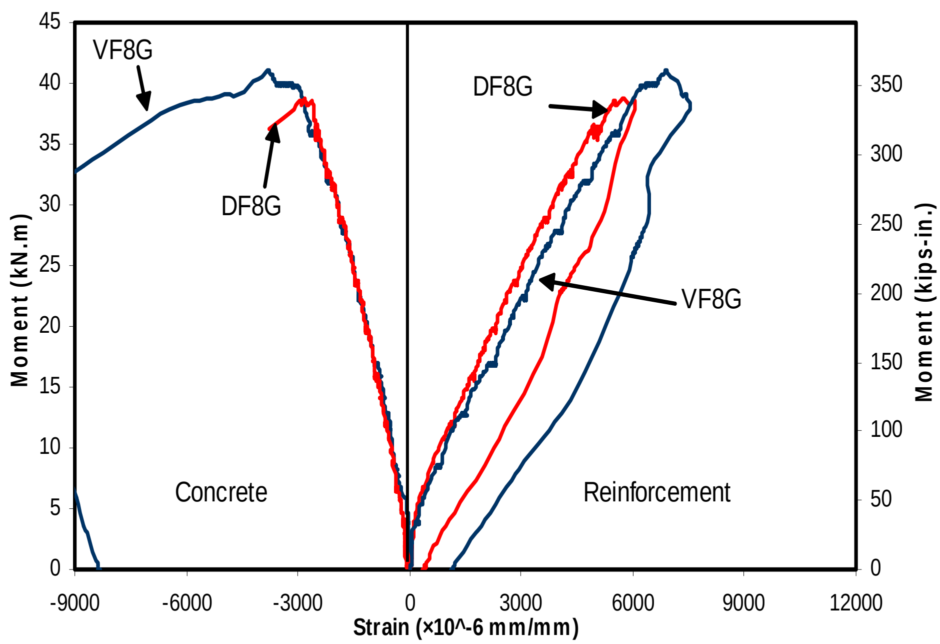

Figure 6.30 Strain distribution in #8 CFRP FRC specimens

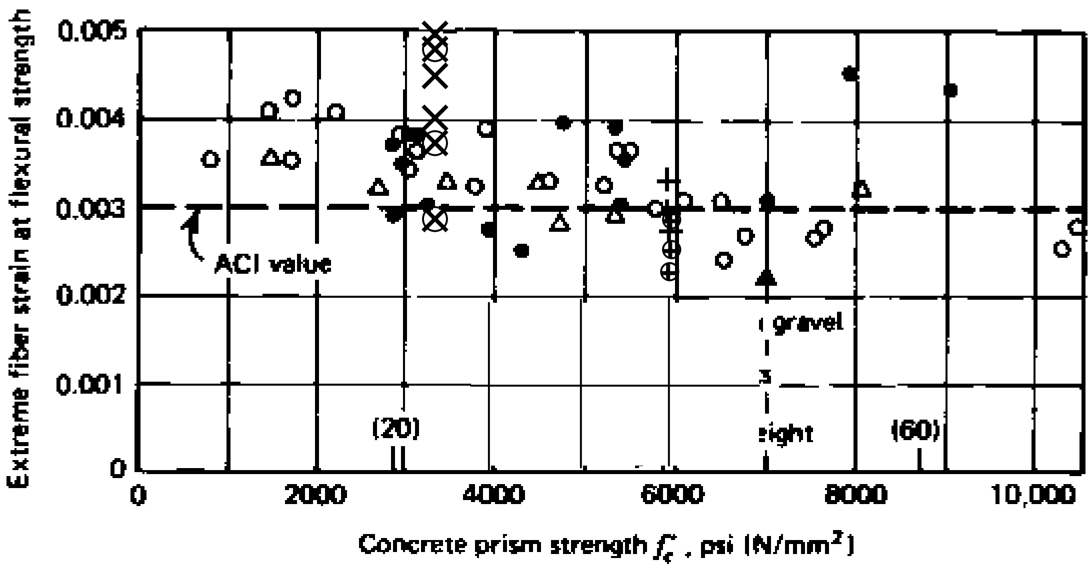

Figure 6.31 Comparison of Ultimate Strain of Concrete of ACI Value and Test Results in this Study (Courtesy of Park and Paulay). Note: × represents the values of FRC measured in this study; + represents the value of plain concrete measured in this study. ⊗ is the FRC measured after environmental conditioning; and ⊕ is the plain concrete measured after environmental conditioning

6.3.2.3 <u>Flexural Ductility</u>

Since ductility is an important parameter in the design of civil engineering structures, it is of interest to study the effect of the environmental conditioning on the ductility of beams. As discussed in Chapter 4, Jaeger's deformation based approach seems to be most appropriate to evaluate the ductility characteristics for FRP reinforced concrete structures. This approach is adopted in this environmental study.

After being subjected to the environmental conditioning, the ductility indices of the beams showed small reductions, as shown in Table 6.7. The reduction of the ductility index was mainly due to the degradation of concrete, which lead to the reduction of the ultimate strength and the associated curvature, as shown in Figures 6.32 to 6.37. The reduction rate between the plain concrete beams and the FRC beams was similar. However, after environmental conditioning, the FRC beams showed higher ductility compared to the plain concrete beams.

Table 6.5 Predictions of ultimate capacity for plain concrete beams

I.D.	$M_{exp.}$ (kips-in.)		M_{ACI} (kips-in.)	$\frac{M_{ACI}}{M_{exp.}}$
VP4C-1	457	450	355	0.79
VP4C-2	442			
VP4G-1	405	413	367	0.89
VP4G-2	420			
VP8G-1	448	449	401	0.89
VP8G-2	449			
Average				**0.86**
DP4C-1	423	420	331	0.79
DP4C-2	417			
DP4G-1	393	397	341	0.86
DP4G-2	401			
DP8G-1	339	378	375	0.99
DP8G-2	416			
Average				**0.88**

Note: For the unweathered plain concrete beams, the above calculations were based on ε_{cu} =0.003; for the plain concrete beams after environmental conditioning, the above calculations were based on ε_{cu} =0.0025.

Table 6.6. Predictions of ultimate capacity for FRC beams

I.D.	$M_{exp.}$ (kips-in.)		M_{ACI} (kips-in.)	$\frac{M_{ACI}}{M_{exp.}}$
VF4C-1	415	402	306	0.76
VF4C-2	388			
VF4G-1	350	356	314	0.88
VF4G-2	362			
VF8G-1	371	366	338	0.92
VF8G-2	361			
Average				**0.86**
DF4C-1	370	388	290	0.75
DF4C-2	405			
DF4G-1	326	332	298	0.90
DF4G-2	338			
DF8G-1	341	335	322	0.96
DF8G-2	328			
Average				**0.87**

Note: For the unweathered FRC beams, the above calculations were based on ε_{cu} =0.0035; for the FRC beams after environmental conditioning, the above calculations were based on ε_{cu} =0.003.

Table 6.7. Ductility index using deformation based method

I.D.	$M_{\varepsilon=0.001}$ (kips-in.)	$\psi_{\varepsilon=0.001}$ (1/in.)	M_{ult} (kips-in.)	ψ_{ult} (1/in.)	μ_E	$\frac{\mu_{ED}}{\mu_{EV}}$
VP4C	202	7.82×10^{-4}	450	19.46×10^{-4}	5.50	1
VP4G	177	6.66×10^{-4}	405	17.63×10^{-4}	6.05	1
VP8G	190	4.96×10^{-4}	449	14.73×10^{-4}	7.04	1
VF4C	163	6.15×10^{-4}	402	20.78×10^{-4}	8.35	1
VF4G	153	5.74×10^{-4}	356	22.10×10^{-4}	8.94	1
VF8G	157	4.45×10^{-4}	366	14.40×10^{-4}	7.56	1
DP4C	191	7.09×10^{-4}	420	17.07×10^{-4}	5.29	0.96
DP4G	180	6.53×10^{-4}	397	17.20×10^{-4}	5.80	0.96
DP8G	183	4.47×10^{-4}	378	12.88×10^{-4}	5.95	0.85
DF4C	166	5.44×10^{-4}	388	20.09×10^{-4}	8.62	1.03
DF4G	139	4.62×10^{-4}	332	16.13×10^{-4}	8.33	0.93
DF8G	158	4.14×10^{-4}	335	13.49×10^{-4}	6.89	0.91

Note: μ_{ED} is the ductility index after environmental conditioning; μ_{EV} i

Based on the criterion proposed by Jaeger et al. (1995) and the Canadian Highway Bridge Design Code, both plain concrete beams and FRC beams exceeded the ductility index limit of 4. Therefore, all beams in this study can be considered acceptable for design in terms of ductility requirement.

6.4 CONCLUDING REMARKS

Durability performance, in terms of bond and flexural behavior, for FRC reinforced with FRP rebars was investigated and compared to the performance of plain concrete reinforced FRP rebars. The accelerated aging test was accomplished by placing specimens in contact with salt solutions and subjecting them to 10 combined environmental cycles, each of which consisted of 20 freezing-and-thawing cycles and 20 high temperature cycles. The following conclusions can be drawn from this study:

- Three reasons mainly contributed to the bond degradation: (1) expansion of solutions in the microvoids at the interface of concrete and FRP rebar; (2) variation in CTE between the rebar and concrete; (3) damage of the rebar, especially on the surface. The first two mechanisms function together and degrade the bond mainly at the interface. The third reason is through damage of the rebar surface, resulting in separation between the rebar and concrete.

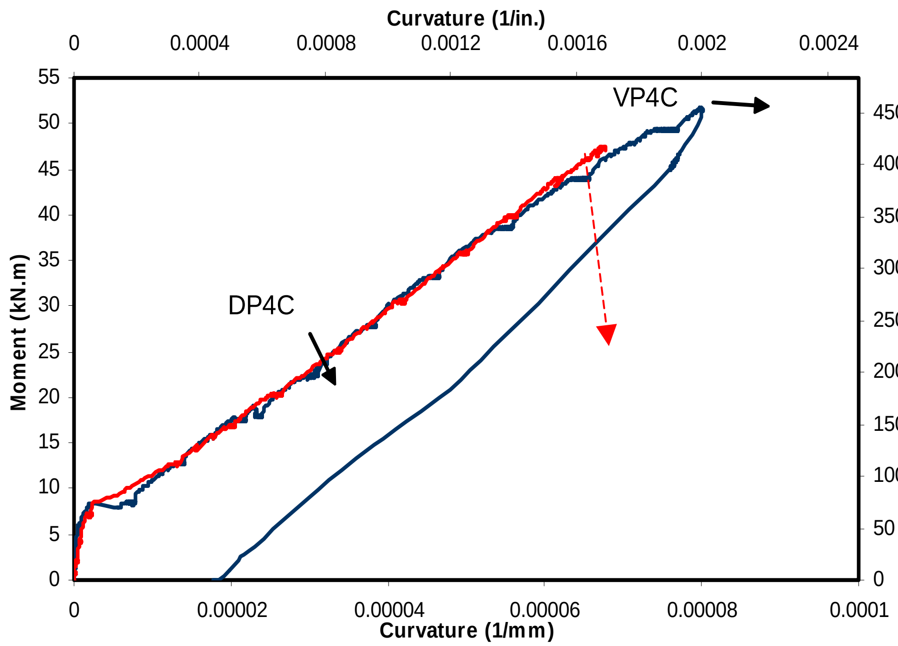

Figure 6.32 Typical moment curvature response for #4 CFRP plain concrete beams

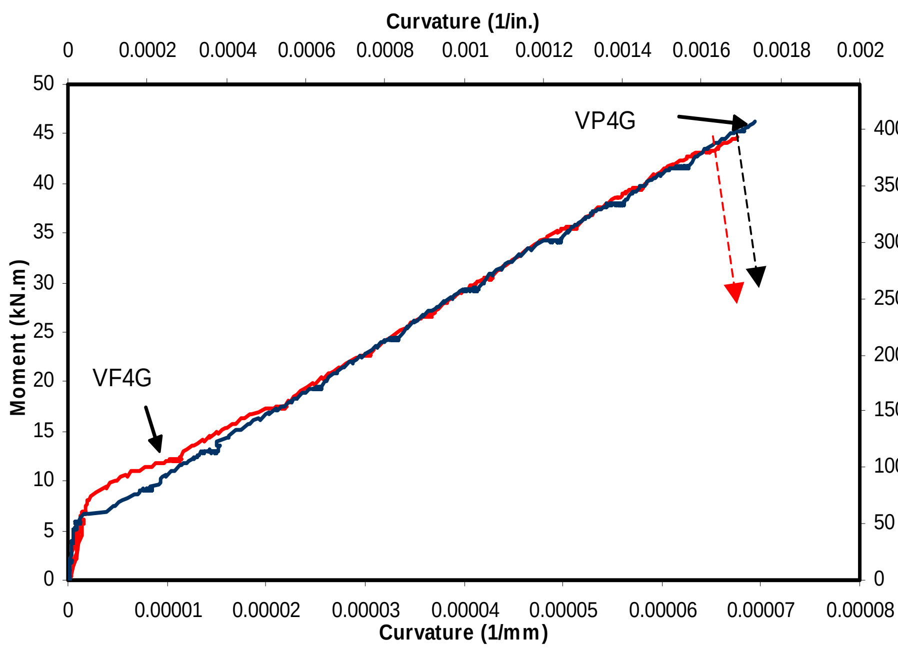

Figure 6.33 Typical moment curvature response for #4 GFRP plain concrete beams

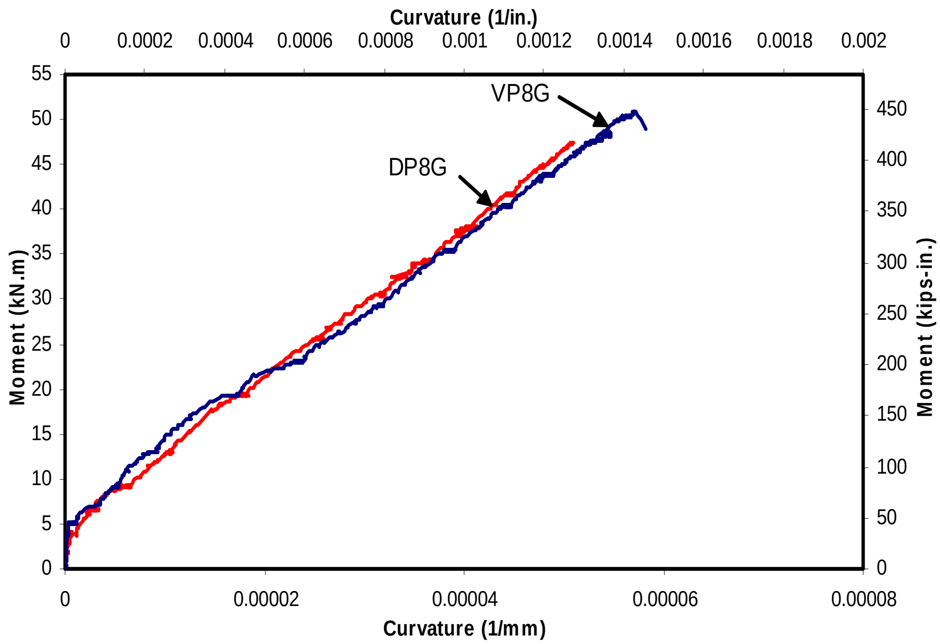

Figure 6.34 Typical moment curvature response for #8 GFRP plain concrete beams

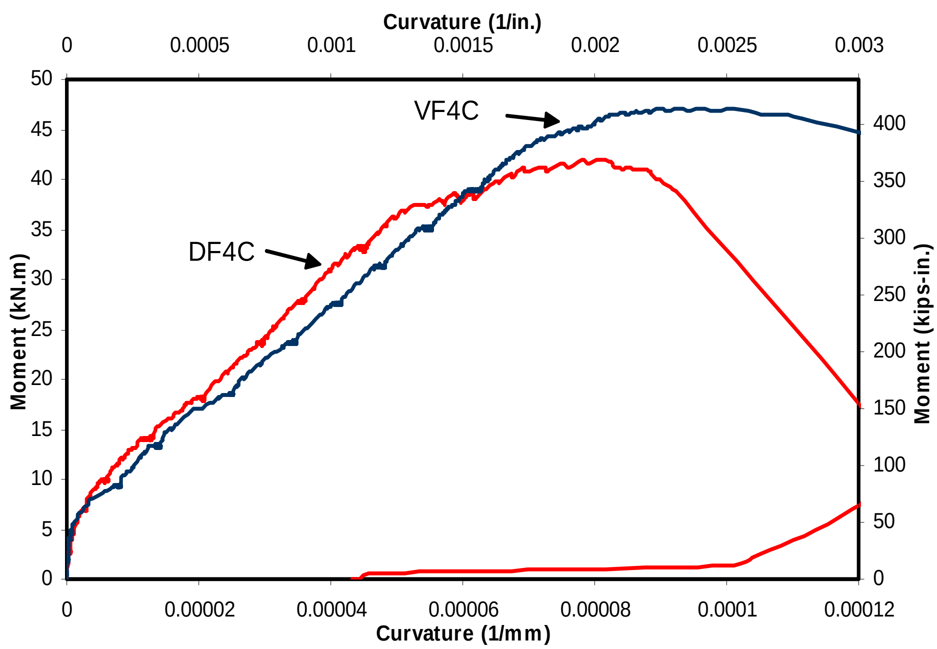

Figure 6.35 Typical moment curvature response for #4 CFRP FRC beams

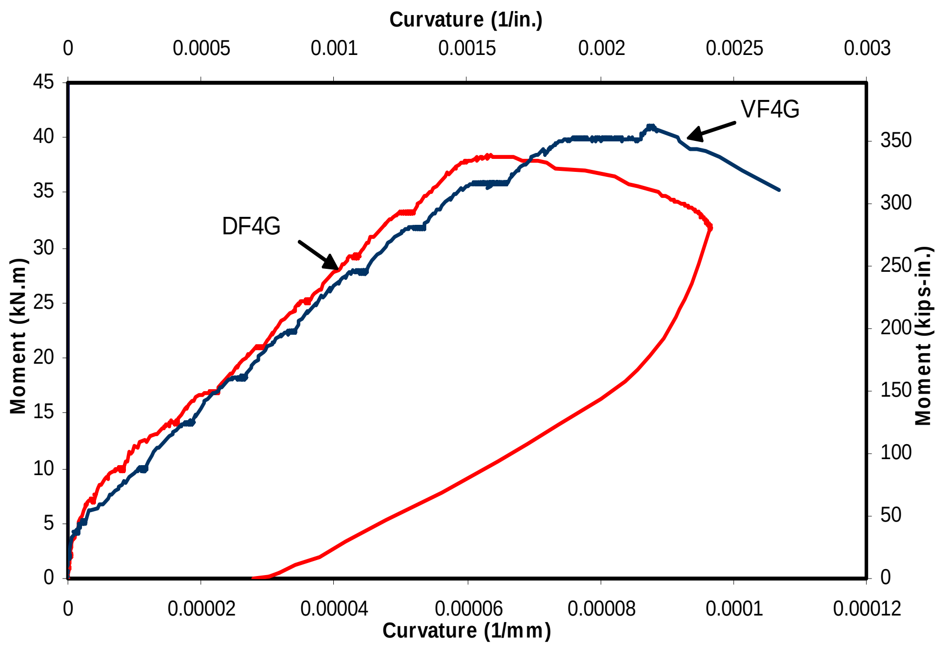

Figure 6.36 Typical moment curvature response for #4 GFRP FRC beams

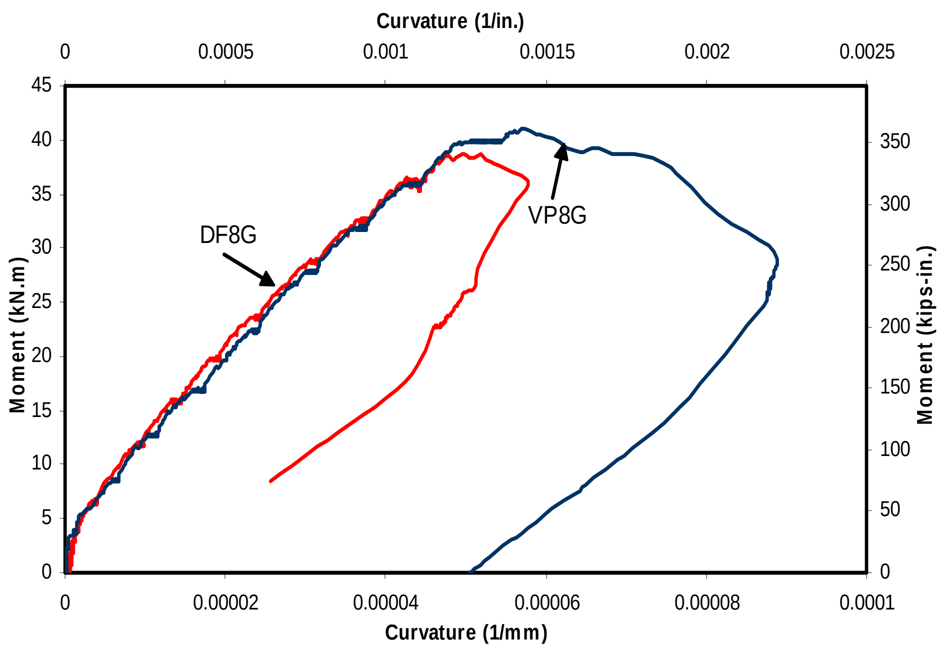

Figure 6.37 Typical moment curvature response for #8 GFRP FRC beams

- With the addition of polypropylene fibers, the bond of environmentally exposed (weathered) specimens significantly improved due to restriction of the development of cracks. The reduction of the ultimate bond strength of the FRP rebars in the plain concrete due to weathering effects was found to be 28% on average, while only 6% reduction was observed in the FRC specimens. Similarly, bond stiffness exhibited a 26% average reduction in plain concrete specimens, while only 10% reduction was observed in the FRC specimens.
- The larger specimens with longer embedment length and relatively smaller exposed area to the solution of sodium chloride (NaCl) showed better performance.
- Under durability effect, the CFRP specimens exhibited superior bond performance as compared to the GFRP specimens. This may be attributed to the more durable characteristics of the CFRP rebar.
- Both plain concrete beams and FRC beams exhibited a small reduction in ultimate flexural strength and ductility in the durability test. The degradation of concrete was the main reason for the flexural degradation.
- Under environmental conditioning and weathering, all beams included in this study showed similar performance in terms of ductility requirement. Compared to the plain concrete beams, FRC beams showed approximately 40% increase in ductility index based on deformation based approach, both, before and after the environmental conditioning.

It should be noted that the above conclusions are drawn based on the tests conducted in this study, where bond specimens and beam specimens are unstressed. In the real world conditions, the structures are under loading conditions, thus, the above conclusions may not be suitable for such. Also, different environmental conditionings may have different results; cautions should be used when applying the results into different situations.

7. FULL-SCALE SLAB TESTS

7.1 Test Program and Associated Testing Protocols

Three full-scale slabs were tested under static (slow cycling of virgin and fatigue tested slabs), fatigue (fast cycling), and static tests to failure as described earlier in Chapter 3. The three types of slabs tested included a conventionally designed epoxy-coated steel reinforced plain concrete slab, a GFRP reinforcing bar reinforced slab in a fiber reinforced concrete matrix, and a hybrid system of reinforcement comprising alternate GFRP and CFRP bars reinforced slab in a fiber reinforced matrix. Details of the reinforcing mats for the three test slabs were included in Table 3.9 and will not be duplicated here. The test configuration used for the slab tests was designed to simulate transverse bending effects observed in bridge deck slabs. This is unlike longitudinal bending in bridges, where the deck slab largely experiences compressive stresses except where it is continuous over support piers. The slabs tested represented the full-scale depth of actual bridge deck slab, and had girder spacing of 9 ft. similar to that in an actual bridge, Figure 7.1. The scaled W 16 x 57 girders chosen had spans restricted to 6.5 ft. (with concrete slab width of 5 ft. acting as a composite with the two W 16 x 57 supporting girders) so that the composite bending stiffness of the test set up was comparable to that of the actual bridge spanning 80 ft. The girders used were W16 x 57 girders and 8' long. Each girder contained 14 shear studs placed in two rows at 8" spacing. The shear studs were ¾" in diameter and 4" tall.

Static loading/unloading tests were conducted where a ramp loading function was used to obtain the load deflection response of the slab before beginning any fatigue testing. The ramp was simulated with triangular waveform operated at a frequency of 0.03 Hz so as to produce 3 loading/unloading cycles of load-deflection and thereby providing adequate data points for stiffness computations. Such displacement controlled static tests were also repeated several times during the fatigue test protocol so as to facilitate monitoring of progressive stiffness degradation after desired numbers of fatigue cycles were completed. Static tests were carried up to a midpoint load of approximately 20 kips which ensured tensile cracking of the deck slab in the positive moment region. Complete load deflection characteristics were recorded for the static tests. Figure 7.2

shows the electronic test control facility used for the slab test program. Automated data acquisition programs were customized for each type of test using LabView software and associated hardware. The front panel of the program for the static (slow cycle fatigue) test is shown in Figure 7.3.

Figure 7.1 Two views of the full-scale slab test set up showing test specimen, loading frame and support mechanism

Figure 7.2 Electronic controls and data acquisition system used for test control as well as monitoring of the full-scale slab tests

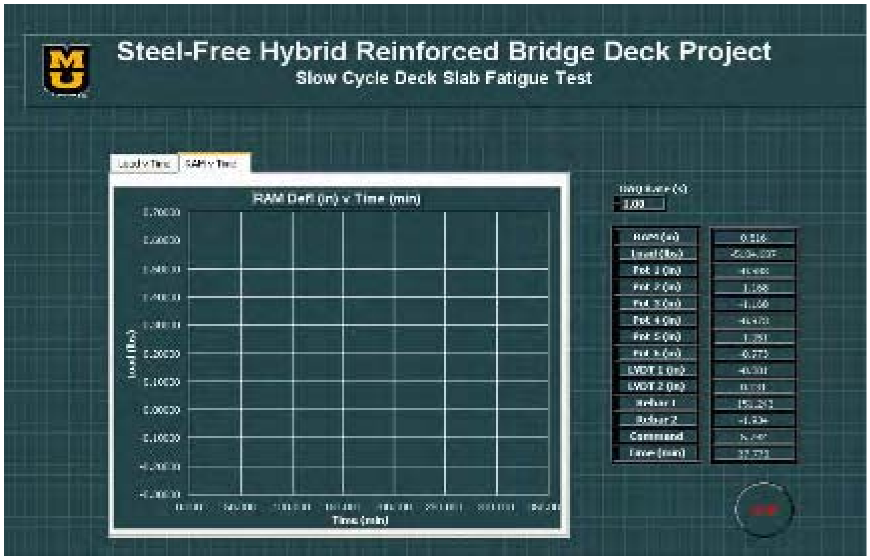

Figure 7.3 LabView front panel for the slow cycle fatigue tests

A 3-Hz sinusoidal loading was used for the fatigue tests. The lower limit load was approximately 10 kips and the upper limit load was approximately 20 kips. Fatigue tests were conducted under ram-displacement controlled mode. To avoid collecting a lot of data of little practical significance, only maximum and minimum load and maximum and minimum deflection/strain responses were recorded during the fatigue tests. This facilitated monitoring of stiffness degradation versus number of fatigue cycles during the application of fatigue loading. Fatigue tests were stopped after 1 million fatigue cycles were completed.

Following fatigue testing, all the slabs were tested to failure under static loading rate using a ramp loading function. Complete load deflection histories were recorded during these tests.

In addition to automated digital data acquisition, visual observations of the cracking patterns and crack widths were completed at regular intervals. Following the failure test, cracking in the slab along the underside as well as at the top surface were recorded using a template of the deck slab.

As noted earlier in Chapter 3, parameters monitored during the full-scale slab tests included 9 displacements, 2 strains and the applied load. Displacements (Figures 7.4 and 7.5) were measured using LVDTs (LVDT 1 and LVDT 2 in the Figure 7.4 and the displacement of the hydraulic actuator) and potentiometers (Pots 1-6, Figure 7.4).

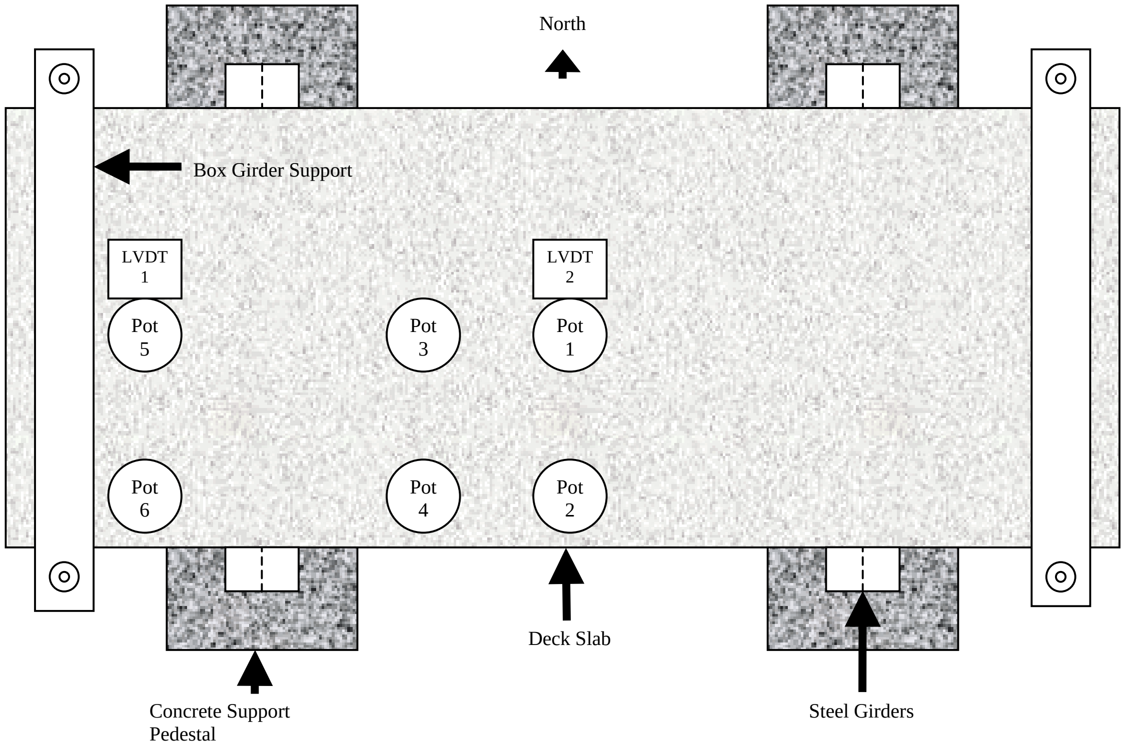

Figure 7.4 Plan view schematic showing location of external instrumentation

Figure 7.5 Close-up showing typical LVDT and potentiometer configuration to monitor slab deflections

7.2 Loading Used for Static and Fatigue Tests

AASHTO LRFD and MoDOT Draft LRFD manuals were used to compute the shear and moment envelopes for a typical steel girder bridge, geometrical and computational details of which are included in Chapter 8. A complete set of design calculations is included there and will not be duplicated here. The design moment magnitude for positive moment region is 12.9 k-ft for a 1 ft. strip of the deck as reported in Chapter 8. To generate the same moment magnitude in the three span test set-up (Figures 3.19 and 7.1) loaded with one concentrated load at the center of the middle span (using a 6 in. x 6 in. steel platen), a 20-kip force is required. It was decided early on in the testing program that this load level be used to establish the virgin static load-displacement response. The same load limit was also used for static tests conducted after regular prescribed numbers of fatigue tests. Also, due to the concentrated load used in the slab test for convenience of dynamic test control (as opposed to some mechanism of applying more realistic distributed loads), the local stresses exceeded the cracking capacity of the concrete slab. As a result, the post-cracking fatigue response which was of interest in this investigation could be readily studied. The upper limit fatigue load of 20 kips was used to simulate maximum service moment of interest. Since the slab deflections were such that at the desired 3 Hz fatigue test frequency only limited ram travel was possible (limited only by the oil flow capacity of the hydraulic pump). Hence the lower limit of the fatigue cycling was kept at approximately 10 kips (instead of setting this closer to 0 kips). As the slabs exhibited stiffness reduction during the 1,000,000 fatigue cycles applied using a displacement controlled test-set-up, the upper and lower limit loads had to be adjusted so as to maintain the desired lower and upper limit fatigue loads. Figure 7.6 and 7.7 show the stress contours obtained at the bottom of the concrete slab for the full-scale slab test configuration using a numerical model of the three-span bridge deck slab. The slab is loaded with a 20 kip concentrated force at the center of the slab distributed through the 6 in. x 6 in. steel loading platen. Tensile stresses are shown as negative numbers in the legend and the stress units are in lb./in^2.

The maximum tensile stresses on the underside of the deck slab right under the loading platen are of the 700-750 psi range (larger than the tensile strength of the concrete used).

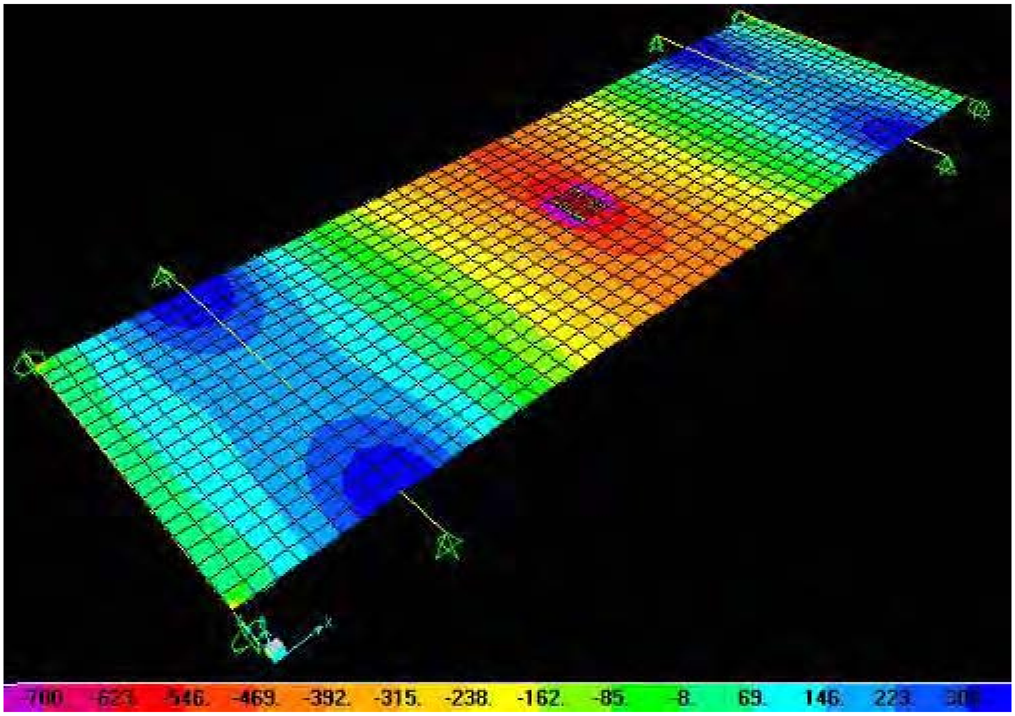

Figure 7.6 Stress contours on the underside of the concrete deck slab obtained using SAP-2000 analysis of the full-scale slab test configuration. Tensile stresses are negative.

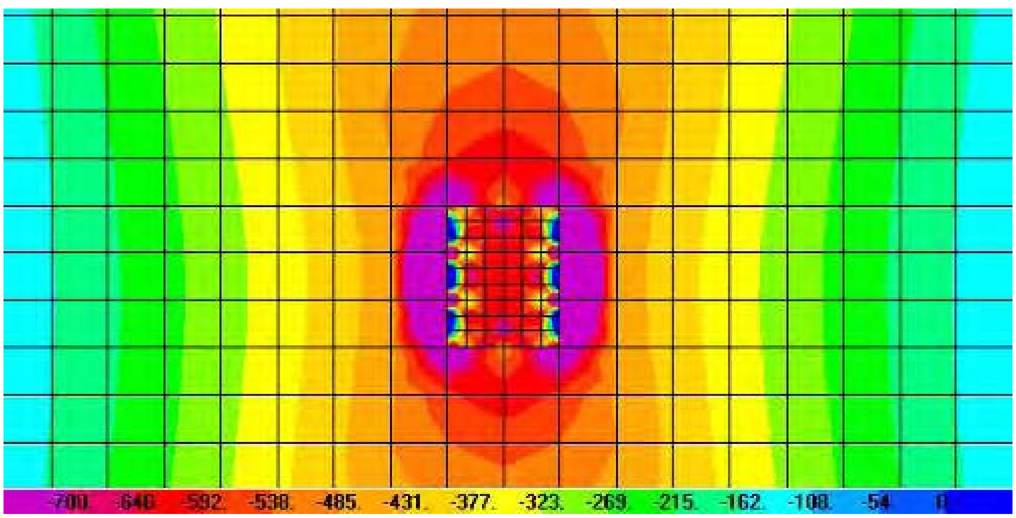

Figure 7.7 Close-up of the stress contours highlighting the fact that tensile stresses on the bottom face of the concrete slab immediately under the 6 in. x 6 in. steel loading plate is in the 700 – 750 psi range

7.3 Test Results and Discussions

7.3.1 Concrete Slab Properties

In addition to the results from the three full-scale slab tests reported in this chapter, results from tests on wet concrete and compression tests on concrete cylinders made from the deck slab concrete mixes are also reported. Mixture proportion details of the mixes were discussed in Chapter 3. Despite the air content being on the higher side of the desired range, the target design strength of 5,000 – 6,000 psi was achieved for each of the three deck slabs. These values reported in Table 7.1. The modulus values determined from these tests are lower than values computed using standard empirical formulae and the associated compressive strength.

Table 7.1 Properties of wet and hardened concrete used for the deck slabs

Properties	Steel Reinforced Slab (Plain Concrete Matrix)	GFRP Reinforced Slab (FRC Matrix)	GFRP/CFRP Hybrid Reinforced Slab (FRC Matrix)
Unit Wt. (lb/ft^3)	143.2	145.6	142.0
Air Content (%)	4.5	4.25	5.0
Slump (in.)	4.50	4	4.25
Compressive strength (psi)	5,835	5,745	6,078
Elastic Modulus (psi)	3.338×10^6	3.795×10^6	2.964×10^6
Strain at Peak (in./in.)	0.0021	0.0021	0.0027

7.3.2 Reinforcing Bar Properties

Static tensile tests were conducted on the GFRP and CFRP reinforcing bars as described in Chapter 3. Results from these tests are summarized in Appendix I.

7.3.3 Virgin Static and Slow Cycle Fatigue Tests

Virgin static (slow cycle fatigue) response prior to fast cycle loading are shown in Figures 7.8 -7.10. Figure 7.8 shows plots of load versus displacement, where the displacements are measured using LVDTs under the deck slab. In addition to slab displacement, these LVDTs also measure elastic deformations of the support mechanism as well as small rigid body movements of the slab and supports. In full-scale tests such as these, it is not possible to eliminate these spurious displacements altogether. They can be mitigated by using wet plaster and shims to minimize skewness in support during initial set up, and also use preloads to avoid walking of the specimen during fatigue tests. In any case, one should avoid relying on absolute displacement magnitudes and use relative measurements (e.g. stiffness degradation during fatigue loading) and trends that are more robust to evaluate overall performance of the slab systems. The direction of displacement and the relative magnitudes of the displacements measured using LVDT 1 and LVDT 2 is consistent with analytical predictions of the same. The inset in Figure 7.8 shows schematic of the locations where the load was applied and the locations of where the displacements were measured (shown using gray arrows). The four line supports (across entire slab width) are shown as black arrows in the inset.

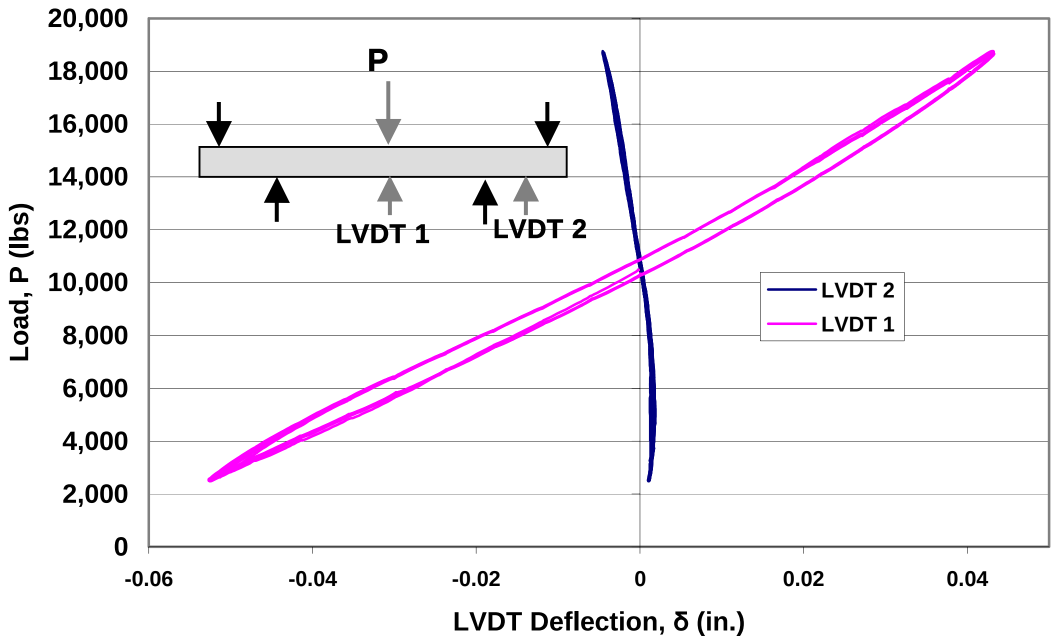

Figure 7.8 Load LVDT displacement plots from slow cycle virgin static tests on steel reinforced slab

Figure 7.9 shows load displacement plots recorded using 6 potentiometers under the deck slab. Even while the resolution of the potentiometers are not as high as those from the LVDTs, the information from the potentiometers validate the ranges of displacements measured from the LVDTs and also provide a more comprehensive displacement profile for the plate. Potentiometer (Pot) 1 was located at the same location as LVDT 1.

Potentiometer 2 was located at the same location along the span as Pot 1 but was placed at the edge of the slab instead of the centerline as Pot 1. Pot 3 and Pot 4 were placed at the quarter-points of the central span, along the slab centerline, and edge, respectively (see Figure 7.4). It can be seen from Figure 7.9 that Pots 1-4 all exhibit the same direction of displacement. Pots 1 and 2 measure larger displacements compared to Pots 3 and 4. Pots 5 and 6 which are located in outer span exhibit negative displacements (upward displacement or camber). The magnitudes and directions of all potentiometer displacements are consistent with those expected from elastic theory. The hysteresis in all the displacement plots (Figures 8-10) are due to slow cycle fatigue tests of a cracked slab.

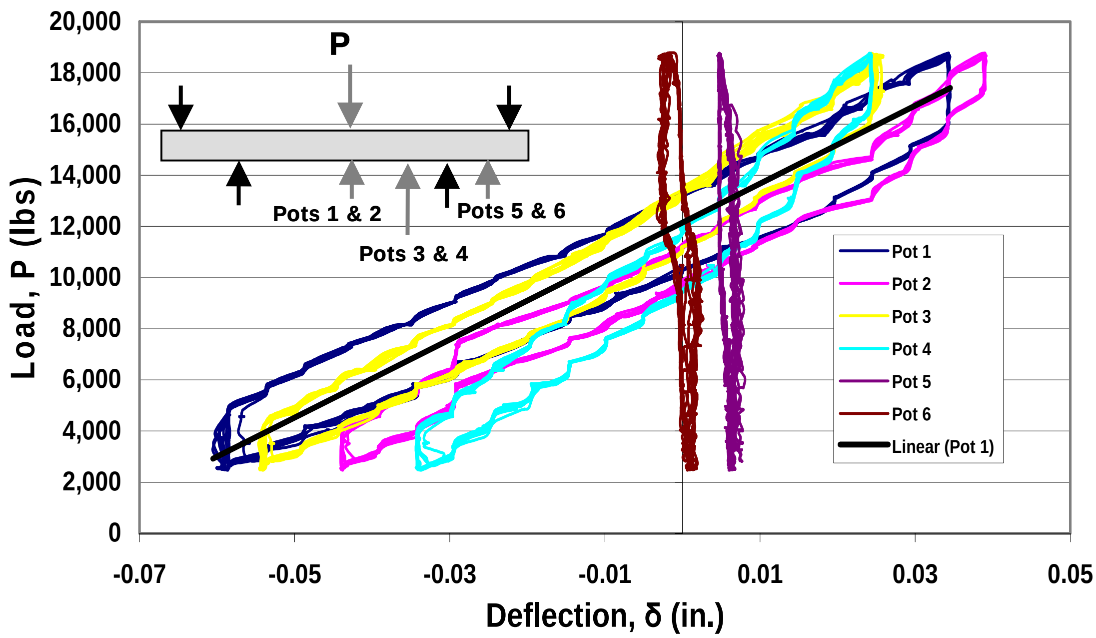

Figure 7.9 Load potentiometer displacement plots from slow cycle virgin static tests on steel reinforced slab

Figure 7.10 shows plots of load versus strains recorded from instrumented rebars that were embedded in the concrete slab. These measure slab flexural strains and are unaffected by spurious displacements (elastic deformations of the supports, rigid body movements of the support pedestals, rocking of the test specimens due to support skewness etc.) associated with external displacement transducers (LVDTs and potentiometers). The inset shows location of the two instrumented rebars. Since both are designed to read tensile strains, they are placed at the level of the top and bottom mat of transverse reinforcement. Unlike LVDTs and potentiometers which exhibit directional displacement response depending upon if they are placed in the positive or negative moment regions (Figures 7.8 – 7.9) instrumented Rebars 1 and 2 both exhibit tensile strains. Rebar 2 shows maximum strain values of 380 μstrains which is in excess of the tensile cracking strain of concrete (approximately 150-250 μstrains depending upon concrete mixture). The magnitude of strains measured by Rebar 1 is relatively small due to the small outer span used for the test configuration. Both instrumented rebars were 2 ft. long and hence measure strains averaged over their length. Local maximum strains within this gage length could be significantly higher than the 380 μstrains registered by the data acquisition system.

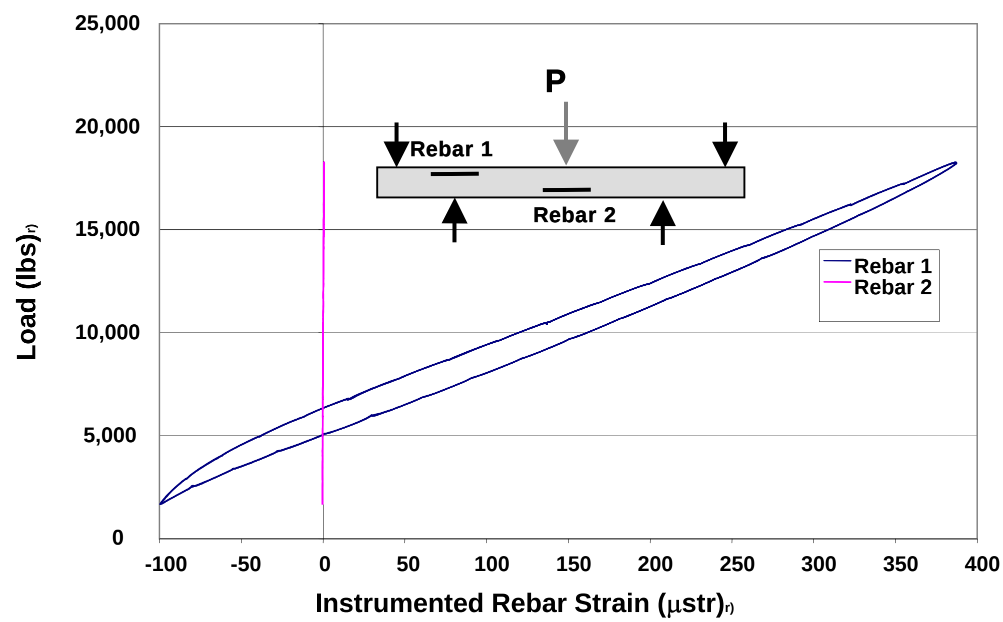

Figure 7.10 Load versus instrumented rebar strain plots from slow cycle virgin static tests on steel reinforced slab

The fatigue response of relatively brittle reinforcement (like GFRP and CFRP) in a relatively brittle matrix (concrete/fiber reinforced concrete) is not well understood, particularly when the matrix is cracked. It is with this intent that both the study of progressive stiffness degradation with fatigue loading due to damage in bond characteristics and cracking of the concrete slab documented using regularly interspersed static (actually slow cycle fatigue), and direct stiffness computations from fast cycle fatigue was undertaken.

Figure 7.11 shows the load deflection response as recorded using LVDT 1 which is the central deflection measured on the underside of the slab directly beneath the point of application of the load on the top surface of the slab.

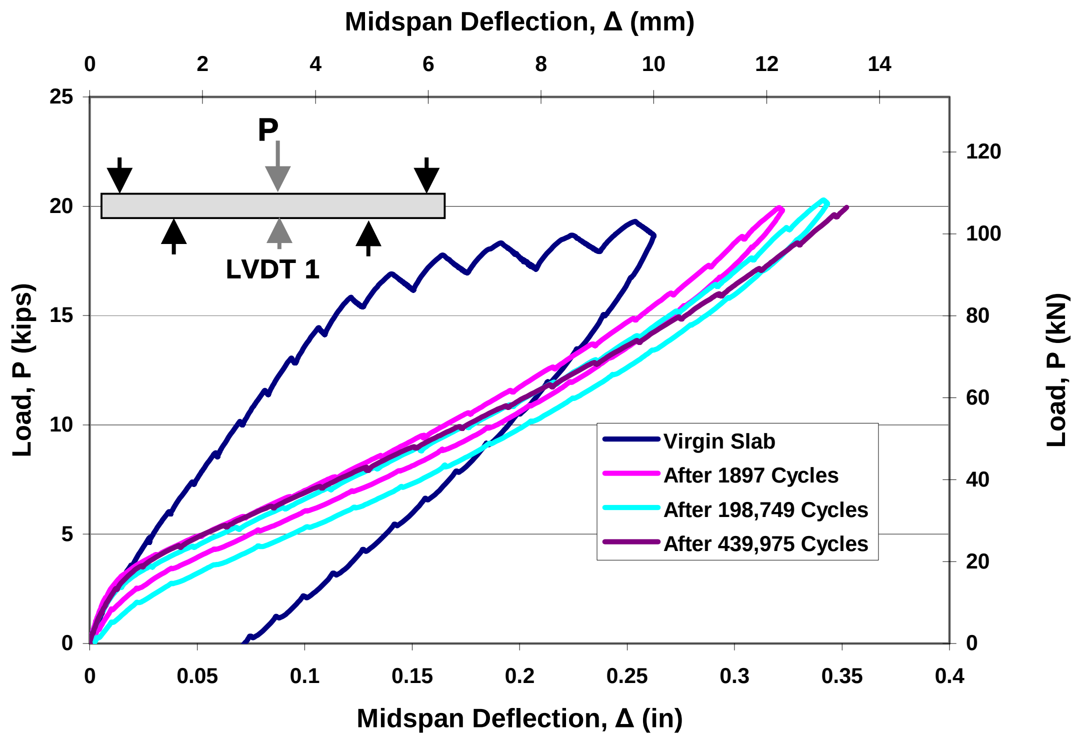

Figure 7.11 Load mid-span deflection from virgin and slow cycle fatigue tests on GFRP reinforced slab

The blue line denotes the static response of the virgin specimen. Significant nonlinear behavior attributed to cracking and associated bond failures begin when the load is approximately 15 kips. Multiple cracking contributes to significantly larger deflection at 20 kips when the specimen was unloaded. Subsequent load-deflection responses are from slow cycle (0.03 Hz triangular waveform) fatigue tests conducted after prescribed intervals of fast cycle fatigue (3 Hz). The legend shows the numbers of fast fatigue cycles completed prior to the slow cycle fatigue test. Slow but gradual degradation in specimen stiffness can be observed. The pinching effect of the hysteresis loops observed near zero load is typical for concrete composites subjected to fatigue loading. This effect has been attributed to increased apparent stiffness on unloading due to inability of cracks to close completely as a result of fatigue debris accumulation at cracks. Even though fatigue tests were conducted up to 1,000,000 cycles for each slab, the data from LVDT1 was unusable for the GFRP slab due to slip of LVDT1 in the test fixture after approximately 500,000 cycles.

Figure 7.12 shows similar data from the static and slow-cycle fatigue tests after prescribed number of fast fatigue cycles.

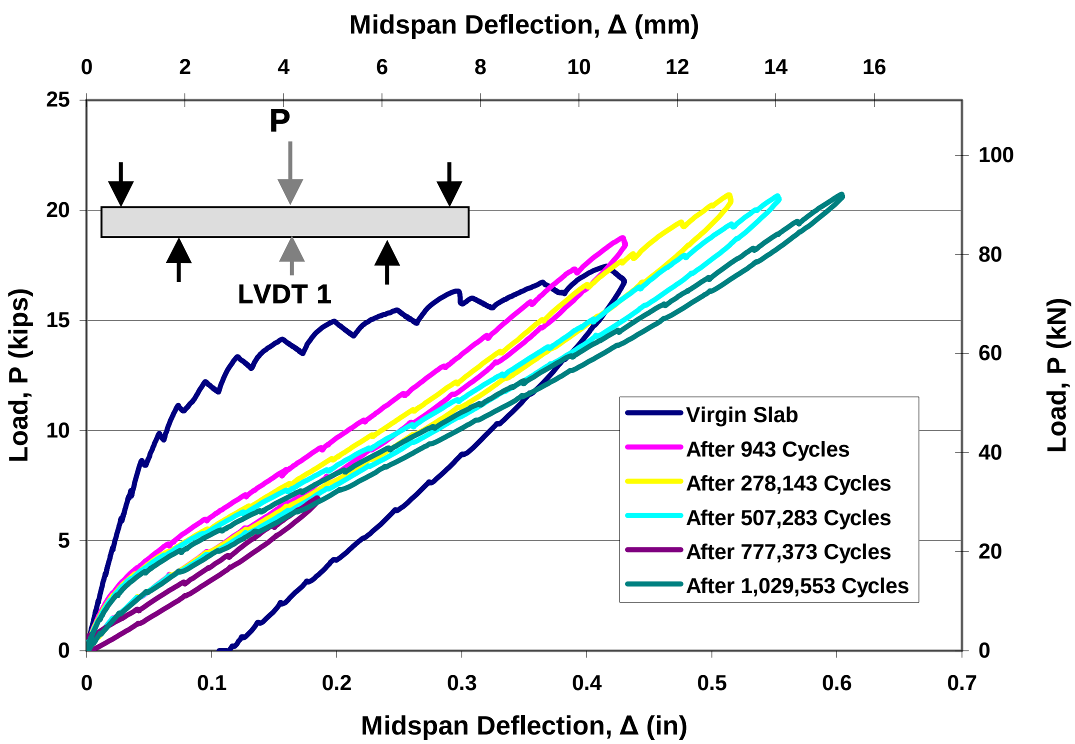

Figure 7.12 Load mid-span deflection from virgin and slow cycle fatigue tests on GFRP/CFRP hybrid reinforced slab

The lower elastic modulus of the fiber concrete matrix (Table 7.1) observed for the hybrid GFRP/CFRP reinforced slab exhibits slightly larger deflections and somewhat premature nonlinear behavior compared to the GRFP slab. This may also be attributed to the increased air content measured in the wet concrete for this deck slab concrete. Gradual degradation in specimen stiffness as determined by the average slope of the load deflection response can be readily observed. Even after 1,000,000 fatigue cycles, the slab still possesses 80% of the stiffness of a slab cracked due to virgin static loading. The stiffness degradation behavior of GFRP reinforced slabs and hybrid GFRP/CFRP reinforced slabs under fatigue loading is gradual and very similar to that observed for conventionally reinforced bridge deck slab (ductile steel reinforcing a brittle plain concrete matrix).

7.3.4 Fatigue Tests

To avoid collecting a lot of data during the four-day long fatigue test program for each slab (1,000,000 fatigue cycles at 3 Hz), only the magnitude range (upper limit minus lower limit) for each parameter were recorded. This was adequate to monitor progressive stiffness degradation, particularly since slow-cycle fatigue tests where complete load deflection response were recorded at regular intervals interspersed between fast cycle fatigue tests. In any case, if there is only slow progressive damage accumulation and not any catastrophic local or global failure, much of the acquired data is of a duplicate nature. Also as discussed earlier, since external deflection measurements are prone to several spurious (other than flexural behavior of the slab) effects such as elastic deformation of the support fixtures, rocking and walking of the test specimen at the high frequency fatigue test, and inertial effects of larger displacement transducers at the high frequency tests, more reliable information can be ascertained from embedded sensors that are typically not prone to many of the effects listed.

A very good way to compare the fatigue performance of the FRP reinforced slabs is to compare post-cracking stiffness degradation during fast cycle fatigue with the performance of conventional steel reinforced slabs. A robust method of obtaining this stiffness is through measurements of applied load as a ratio with the strains measured using instrumented rebars embedded at the level of the transverse slab reinforcement. Figure 7.13 includes a comparison of normalized stiffness computed from the instrumented rebar strains for each of the three slabs. Stiffness values are normalized with respect to the initial post-cracking stiffness of the same slab measured after flexural cracking of the slab due to the virgin static loading of 20 kips (treated as 100% in each of the three slabs tested under fatigue loading). It can be readily observed that the hybrid

GFRP/CFRP reinforced slab does as well as the conventionally reinforced slab all during the 1,000,000 fatigue cycles. Overall response of the GFRP reinforced slab is also comparable after 1,000,000 fatigue cycles. It can however be observed that the GFRP reinforced slab shows higher early degradation, even if it stabilizes to steady state after about 200,000 fatigue cycles. Given the limited number of fatigue tests conclusive analysis of the specific magnitudes of degradation and their timeline may be less relevant than the fact that the overall fatigue performance of the GFRP and hybrid GFRP/CFRP reinforced slabs are nearly identical to that of the conventionally reinforced slab.

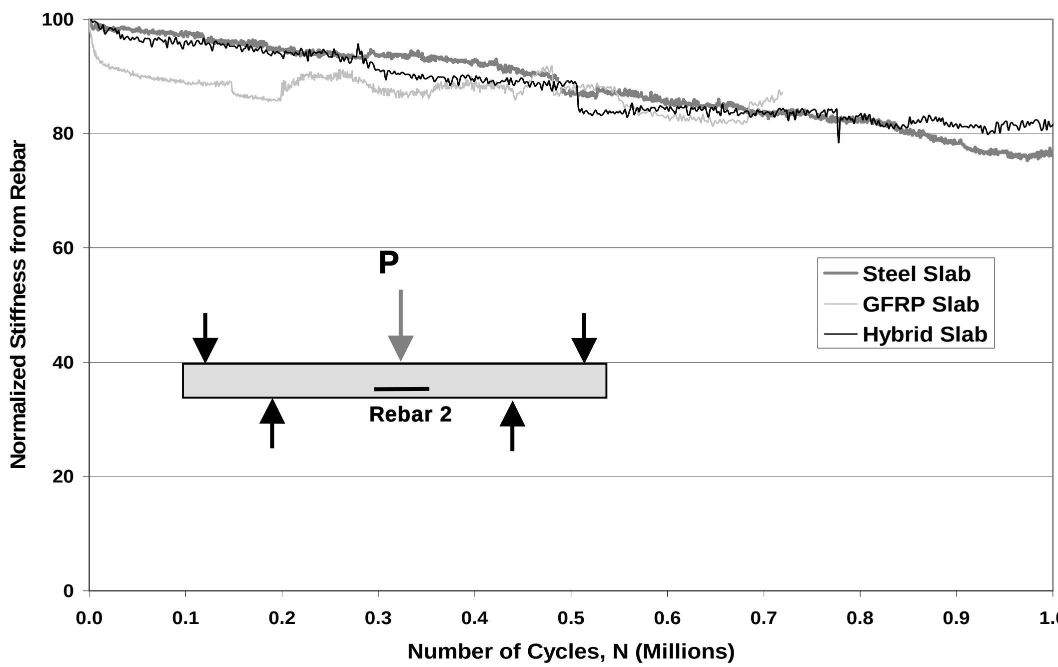

Figure 7.13 Normalized degradation in stiffness during fatigue loading for the three slabs tested

During the 1,000,000 cycle fatigue tests, the tests were interrupted at regular intervals of at least once a day to conduct slow-cycle fatigue tests to obtain complete load-deflection response and to study crack growth patterns at all the critical locations of the positive and negative moment regions. Discussions of growth of cracks during fatigue loading and associated crack patterns from the static failure tests are presented later in Section 7.3.6.

7.3.5 Post-Fatigue Static Tests

After the fatigue test program involving a 3 Hz sinusoidal loading for 1,000,000 cycles with upper and lower limit loads of approximately 20 kips and 10 kips respectively, no catastrophic failures either local or global were observed in any of the three test slabs. Cracks while visible to the naked eye on the underside of the slab, and over the negative moments along two girder supports, were smaller than $1/16^{th}$ in. in width when the slab was unloaded and supported only its self weight.

Static ramp test to failure (or limiting load capacity of the test set-up) were carried out upon completion of the fatigue test program. Each test lasted approximately 1-1.5 hours depending upon the failure mode and associated displacement ram displacement required.

Figure 7.14 presents the load ram deflection plots for the three slabs tested. The steel reinforced slab essentially exhibited a linear response characterized by the post-cracking (and post fatigue) stiffness measured earlier. Failure at approximately 98 kips was clearly due to punching shear. There were substantial damage to the underside of the slab including spalling of cover concrete and exposure of reinforcement mat (Figure 7.15).

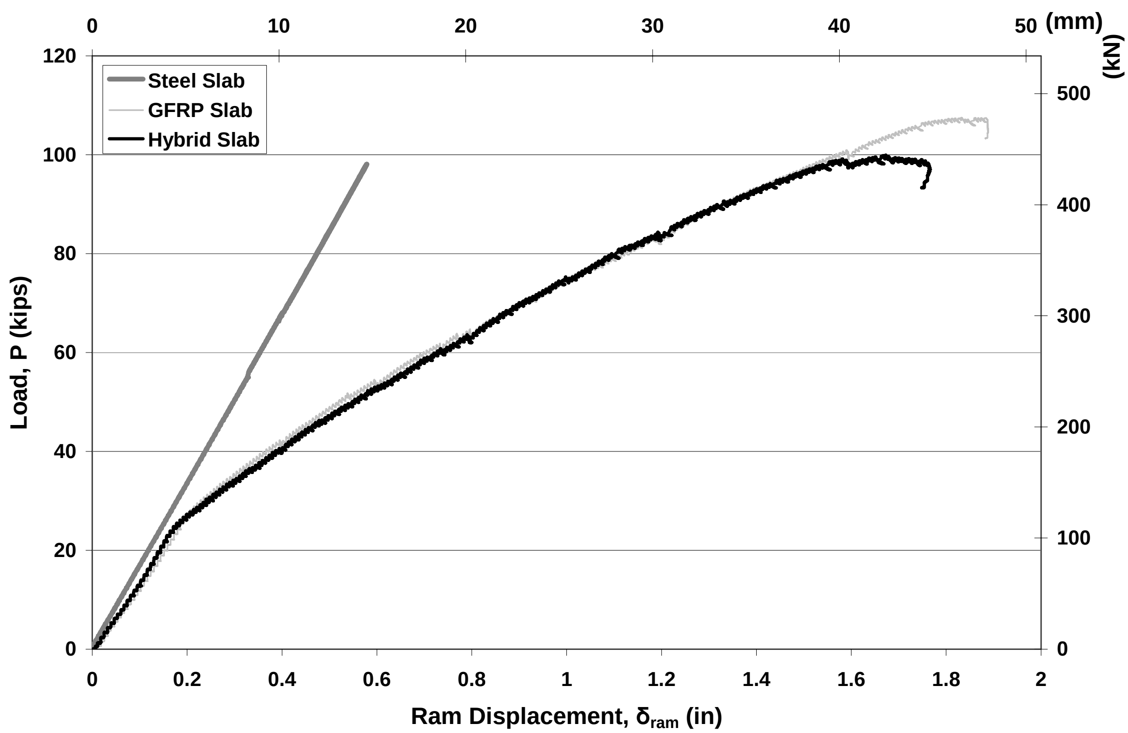

Figure 7.14 Load mid-span deflection from post-fatigue static tests to failure of the three slab systems

More than a characteristic of the conventionally reinforced slab, this mode of failure was perhaps largely due to the concentrated force test configuration used in this study (applied via a 6in. x 6 in. steel platen which punched through at the top surface during failure - Figure 7.15 left).

The slabs with FRP reinforcement and fibrous concrete both deflected much more than the steel reinforced slab. Extensive cracking and bond failures due to splitting and reinforcement slip contributed to the large deflections observed. All the slabs had nearly comparable stiffness up to approximately 20 kips of concentrated mid-point loading.

The FRP reinforced slabs did not exhibit catastrophic failure even when the limit loads of 100-110 kip (limited for the test set-up) were reached. The tests were stopped due to the large deflections and permanent deflections (bowing) of the large box girder supports along the other spans. It appeared that these slabs were very near their flexural capacities when the tests were stopped. Audible cracking and incipient bond failures were observed when the tests were stopped.

7.3.6 Cracking Patterns and Failure

Since the steel reinforced concrete slab failed due to punching shear very characteristic crack patterns can be observed at failure (Figure 7.15).

Figure 7.15 Punching shear failure of the steel reinforced slab showing the top of the slab (left) and the bottom of the slab (right). Notice spalling, loss of cover and exposure of epoxy reinforcement.

Prior to this catastrophic failure, cracking was largely transverse to the direction of principal tension. Multiple cracking as is typical in reinforced concrete were observed. Very little longitudinal or bond splitting type cracks were observed on completion of the fatigue test program.

Figures 7.16 and 7.17 show schematic crack patterns recorded post test on the underside and the top of the GFRP reinforced slab. The shaded grids were sketched on the slab to facilitate recording of crack patterns at locations of anticipated tensile cracking. The GFRP slab clearly had significant bond splitting failures at the limiting load exceeding 100 kips. These are evident in Figure 7.16 where the crack pattern to the right of the shaded grid represents cracking in the pattern of the reinforcing mat (good bond between the FRC matrix and the GFRP reinforcing but inadequate cover to prevent bond splitting). Similar observations were made for GFRP reinforced composite systems while reporting results from all of the pull-out and flexural ductility tests.

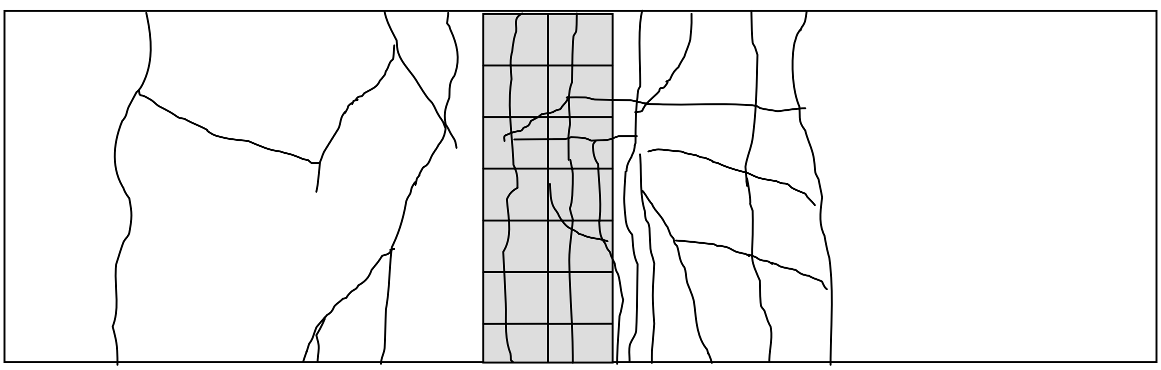

Figure 7.16 Schematic cracking patterns on the bottom of the GFRP slab.

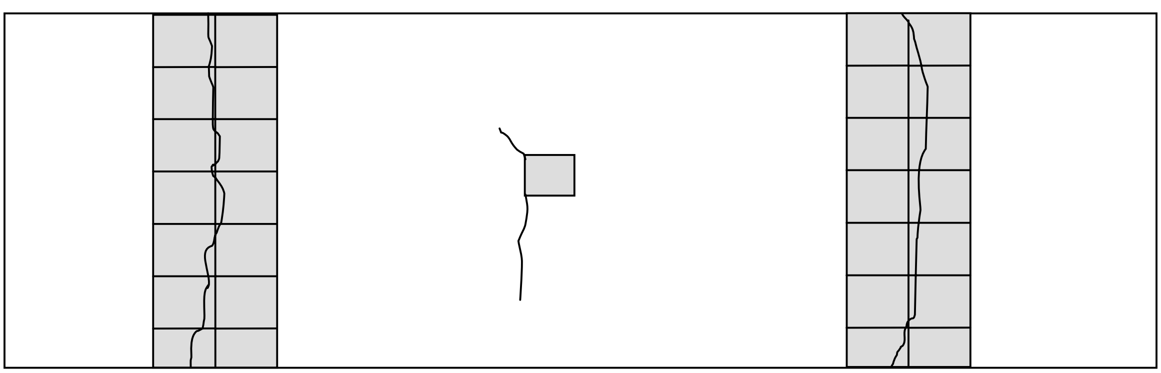

Figure 7.17 Schematic cracking patterns on the top of the GFRP slab. Square shading at the center represents location of the loading platen.

Figures 7.18 and 7.19 show schematic crack patterns recorded post test on the underside and the top of the hybrid GFRP/CFRP reinforced slab. The shaded grids were sketched on the slab to facilitate recording of crack patterns at locations of anticipated tensile cracking. The square shading at the center of Figure 7.19 represents the location of the steel loading platen. The cracks in the hybrid GFRP/CFRP reinforced slab had widths that were noticeably smaller than that in the GFRP slab most likely due to the higher reinforcement stiffness in this hybrid system. The number of cracks was more and the cracks were more uniformly distributed in the hybrid reinforced slab. This explains why the global stiffness were still comparable (GFRP versus hybrid GFRP/CFRP reinforcement system), even while locally the cracks were visibly finer.

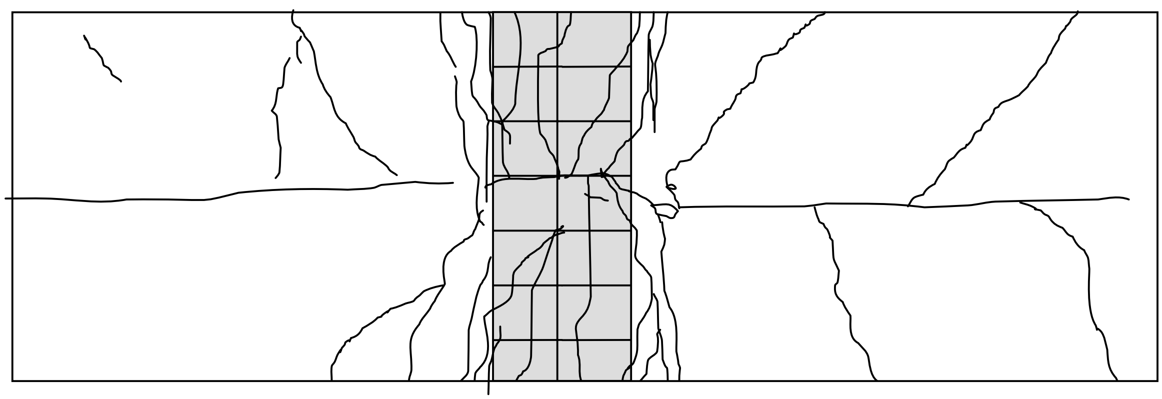

Figure 7.18 Schematic cracking patterns on the bottom of the GFRP/CFRP hybrid slab.

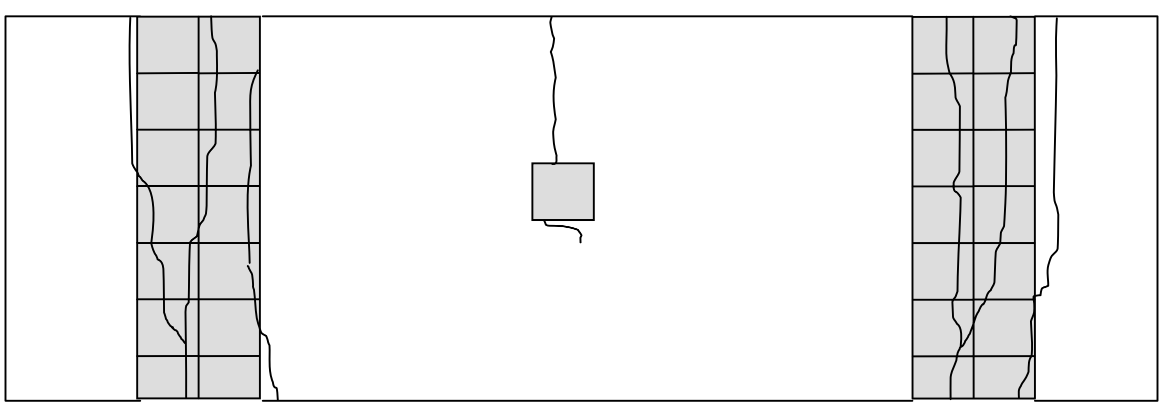

Figure 7.19 Schematic cracking patterns on the top of the GFRP slab highlighting tensile cracking observed at the negative moment region over support.

The hybrid reinforced slab had very little bond-splitting type of cracking mimicking the reinforcement mat pattern (again unlike the GFRP reinforced slab). The presence of one long but fine longitudinal crack (Figure 7.18) cannot be reasoned based on mechanics of failures typical in such systems. The multiple fine cracking is also observed in Figure 7.19 over the girder supports on the top of the slab.

7.4 Summary Observations

- Rigid body movement of support system during fatigue loading and skewness of original slab significant
- Elastic deformations of support and loading frame not insignificant. Exterior displacement measurements as a result can be used to predict relative trends but absolute magnitudes may be less meaningful due to the additional deformations.
- Embedded instrumentation gave more accurate magnitudes as these were unaffected by rigid body movement and elastic deformations as readily.
- Precracking stiffness of all three slabs were nearly identical
- Post-cracking stiffness of the GFRP and hybrid slabs significantly lower than that of the conventionally reinforced slab.
- Post-cracking fatigue performance almost identical for all three slabs.
- Crack widths were smaller for hybrid slab than for GFRP slab. Crack widths for hybrid slabs were more readily comparable to that for steel reinforced slab, even while the global stiffness of the hybrid slab was more comparable to the GRFP slab. This anomaly can be explained by the presence of many more finer cracks in the hybrid reinforced slab.
- FRP reinforced slabs used 0.5% by volume of polypropylene fibers unlike the steel reinforced slab which used plain concrete matrix. Fibers affect the near surface crack widths while being insignificant as far as global properties are concerned.
- Steel slab failed by punching shear failure. GFRP and hybrid slabs did not fail due to punching shear. Tests on these slabs had to be stopped due at the limiting load capacity of the hydraulic actuator and due to excessive displacements of the slab and the outer span support mechanism. At the time these tests were stopped, the GFRP slab exhibited extensive bond splitting type cracking (cracking patterns reflecting

profile of lower reinforcement mat) indicating that the incipient failure would have likely been in the flexural mode. The difference in the types of failure can be attributed to a strong influence on concentrated loading configuration used and concrete slab strength used. Had the loading configuration involved uniformly distributed loading, punching shear failure observed in the steel reinforced slab may not have preceded a flexural failure.

8. DESIGN EXAMPLE OF HYBRID FRP REINFORCED BRIDGE DECK SLAB

8.1 INTRODUCTION

Conventional steel reinforced concrete bridge decks comprise a brittle matrix – ductile reinforcement system. Such decks are typically designed for factored loads using conventional ultimate strength design procedures assuming steel yields at the ultimate state and prior to concrete crushing in compression. ACI 440.1 R03 recommends that flexural members reinforced with FRP rebars be designed using the ultimate strength design approach to ensure concrete crushing This is only because the failure at ultimate due to concrete crushing in such brittle reinforcement – brittle matrix composite systems is claimed to be marginally more ductile than failure due to rupture of the FRP reinforcing bar. While there may be some justification based on this logic, it should also be noted that there are fundamental problems with this approach.

The balanced reinforcement ratio defined for FRP systems based on a concept directly borrowed from conventional steel reinforced concrete is given by:

$$\rho_{fb} = 0.85\beta_1 \frac{f_c^{'}}{f_{fu}} \frac{E_f \varepsilon_{cu}}{E_f \varepsilon_{cu} + f_{fu}} \tag{8.1}$$

One is instructed in ACI 440.1 R03 to design for ρ_f = 1.4 ρ_{fb} (~1/0.75ρ_{fb} similar to limits on ρ_{max} in steel-reinforced concrete) to ensure concrete crushing failure at ultimate. Concrete is an aging material whose compressive strength increases as a function of time (even if marginally after the initial few months). Also, due to environmental degradation, the tensile strength of FRP rebars is known to deteriorate with time. As a result ρ_{fb} exhibits time dependent response which works contrary to the basic design intent of ensuring an over-reinforced design in FRP reinforced concrete composites (i.e as time goes by, the design will get less and less over-reinforced). This is unlike conventional steel reinforced concrete, where the increase in compressive strength in time only adds to ensuring that the designed section remains under-reinforced. In addition to this fundamental issue with the design guidelines proposed in ACI 440.1R03, when dealing with hybrid brittle reinforcement systems comprising two FRP reinforcements with different failure strains, such as the one proposed here, the definition of ρ_{fb} becomes even more nebulous. In the opinion of the PIs, while a check of ultimate capacity and knowledge of the anticipated failure mode at ultimate are useful, they are less relevant in brittle matrix –brittle reinforcement systems than for brittle matrix – ductile reinforcement systems. What is proposed here is hence a primary design based on working stresses analysis, with a mandatory follow-up check for ultimate capacity. Also, some of the allowable stress limits proposed in ACI 440.1R03 are relaxed based on (1) results from accelerated durability tests in this investigation, (2) the fact that matrix ductility is enhanced with fiber incorporation (shown earlier in results from this study and also from Gopalaratnam, El_Shakra and Mihashi, 2005), (3) bond performance is enhanced with the confining effects of fibers, and (4) crack-widths are smaller in hybrid FRP reinforced systems (where GFRP and CFRP rebars are used simultaneously) unlike in "GFRP only" reinforced composites. It should also be noted that the stringent limits on allowable stresses in ACI 4401R-03 do not appear to have systematic empirical or other theoretical basis (at least based on the references cited in the Guidelines). The primary design based on working stress approach makes more practical sense in such brittle matrix-brittle reinforcement systems.

8.2 STATEMENT OF THE DESIGN PROBLEM

A typical MoDOT steel-girder bridge with reinforced concrete deck slab is taken up to illustrate the design procedures. The latest AASHTO LRFD Bridge Design Manual and Draft (at the time this design was executed) MoDOT LRFD Bridge Manual were used to establish loading considerations.

8.3 LOADINGS AND DESIGN MOMENTS

8.3.1 Loading Considerations

The focus of the design problem is to address transverse bending of the reinforced concrete bridge deck. A typical interior bay is analyzed for positive and negative moments under both service loadings and factored loadings. Overhang of the slabs beyond the last girder line is considered under service and ultimate conditions. A 40 ft. roadway is considered (two 12 ft. lanes with an 8 ft. shoulder on each side). Barrier curb width of 16 in. is assumed. Five girder lines at 9 ft. spacing are assumed. Overhangs of 40 in. are assumed as is common in MoDOT steel-girder bridge designs. All calculations are computed initially based on a 1” width longitudinally (and later design moments and shear are converted one foot width along the longitudinal direction).

Strength I Condition is analyzed to obtain positive and negative moments for the interior bay.

Dead Loads:

Safety Barrier Curb (SBC) : 28.5 lb (Acting 5.5” from the outside edge)

Dead load from the slab: 9” x 1” x (1’/12”)^3 x150 pcf = 0.78 lb/in

(assuming a 9” deep deck slab, uniformly distributed load outside edge to outside edge)

Future Wearing Surface (FWS): 1” x 12” x (1’/12”)^2 x 35 psf = 0.24 lb/in

(uniformly distributed inside SBC to inside SBC)

Live Loads:

Using the HL-93 Live Loading

Design Lane Load

- is equivalent to 64 psf which translates to a transverse distributed load of 0.444 lb/in over a 1” longitudinal strip

Truck Load

- use the 32 kip axle and 16 kip per wheel load over the width of strip value (below) to distribute the load properly and to obtain the equivalent point load for transverse
- for the positive moment this is 16,000/85.4 = 187.35 lb
- for the negative moment this is 16,000/75 = 213.33 lb

Impact Load

33% of the Design Truck load [AASHTO Table 3.6.2.1-1]

- applied only to Design Truck not Design Lane load.

  Width of Strip [AASHTO Table 4.6.2.1.3-1]

  Positive Moment: 26 + 6.6 (S) {for this case S=9’} = 85.4”

  Negative Moment: 48 + 3.0 (S) {for this case S=9’} = 75”

  In both cases the single truck loading produced the largest loads so, the multiple presence factor, m = 1.2

Factored Loads [AASHTO 3.4.1]

$Q = \eta \Sigma \gamma_i q_i$, where, Q = total factored load, η = load modifier, q = loads, γ = load factors

Load Modifier

The structure is ductile, redundant, and important, hence,

η = 0.95 x 0.95 x 1.05 = 0.95

However to follow the MoDOT recommendations, use η = 1.0

Factored Moment

$$M = \eta\left[1.25M_{DC} + 1.5M_{DW} + 1.75M_{LL+IM}\right] \tag{8.2}$$

Interior positive and negative moments were obtained by placing the previously explained loads into RISA 3D (an appropriate structural analysis program) with the appropriate load factors (not shown in the loading diagrams but included in envelope calculations).

8.3.2 Design Moment Envelope

From the structural analysis:

M_{pos} = 11,795 in-lb (for a 1" strip along the longitudinal direction)

M_{neg} = -13,496 in-lb (for a 1" strip along the longitudinal direction

Some modifications are still in order as the negative moment is allowed to be taken at an offset from the centerline of the girder. In this case a 3" offset was used and the negative moment was reduced to: M_{neg} = -11,569 in-lb

Per MoDOT practice, the maximum dead load moment is used for both positive and negative interior moments. For the positive moment this is a difference of +1021 in-lb and for the negative moment this is a difference of -335 in-lb. The final factored moments hence become M_{pos} = 12,816 in-lb, and M_{neg} = -11,904 in-lb

When these moments are changed to correspond to a one foot width of strip the moments are: M_{pos} = 12.82 kip-ft, and M_{neg} = -11.90 kip-ft

Details of the loading cases analyzed are illustrated in Figures 8.1 and 8.2 for the interior bay positive and negative moments respectively. Similar analysis was also carried out on the overhang for negative moment. A summary of the calculations is presented in Table 8.1

Table 8.1 Summary of Design Moments

Loading class	Interior Bay		Overhang
	Positive Moment (kip-ft/ft)	Negative Moment (kip-ft/ft)	Negative Moment (kip-ft/ft)
Service Loads	6.91	-7.88	-7.38
Factored Loads	12.82	-11.90	-12.09

(a) Truck Loads (multiple presence factor - m=1.2)

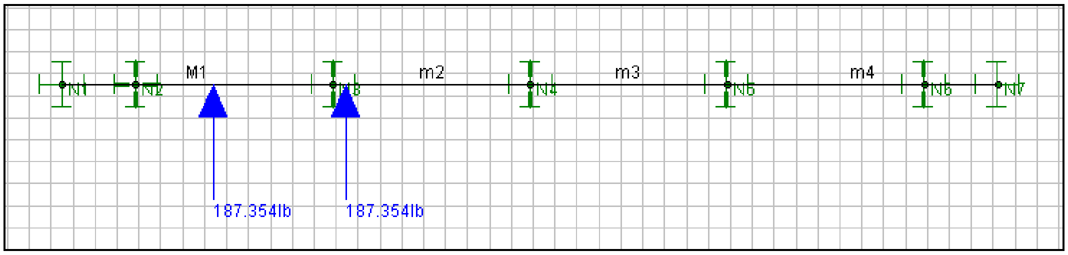

(b) Design Lane Load

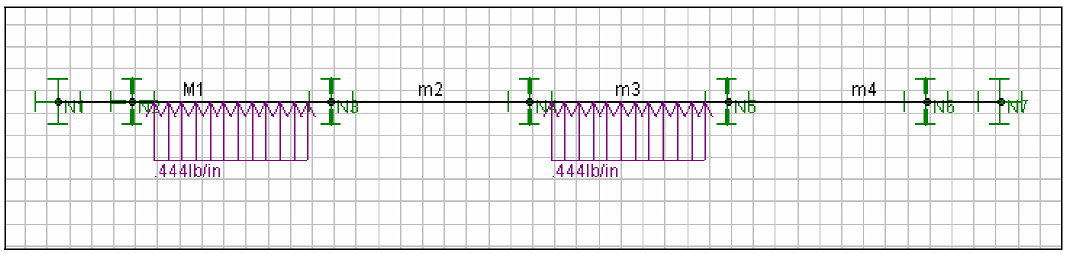

(c) Slab and SBC Loads

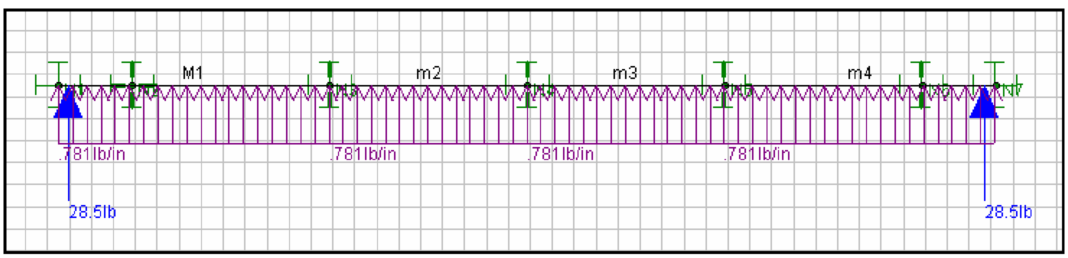

(d) FWS Loads

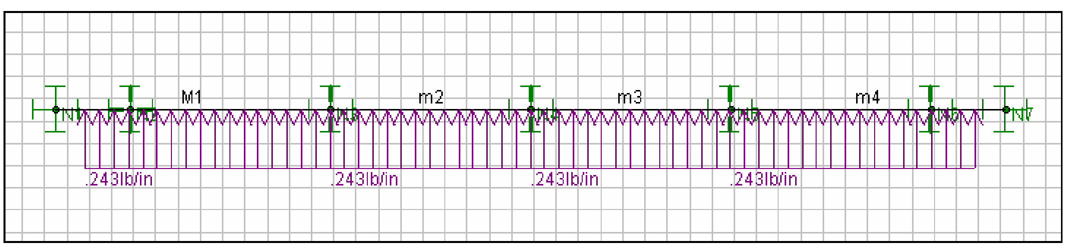

Figure 8.1 Interior bay loading considerations for positive moment

(a) Truck Loads (multiple presence factor - m=1.2)

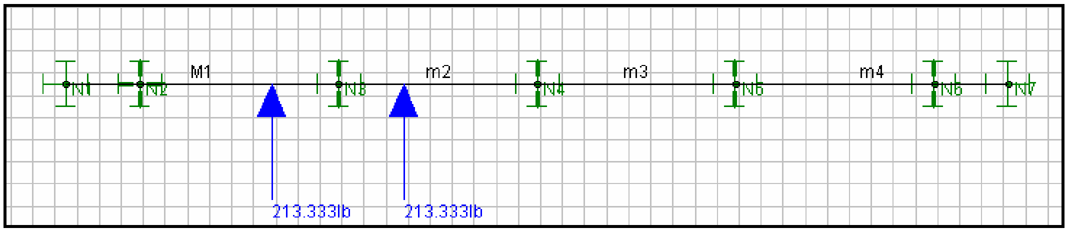

(b) Design Lane Load

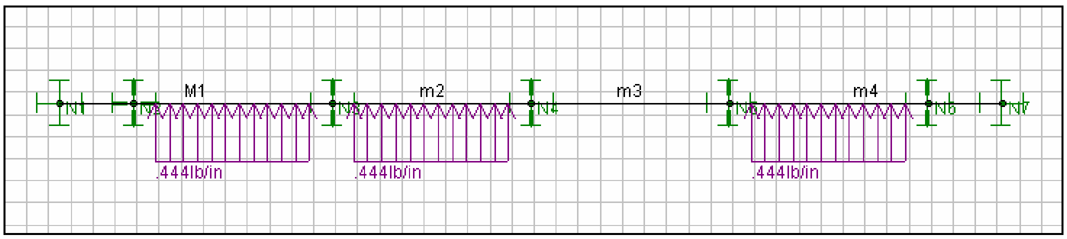

(c) Slab and SBC Loads

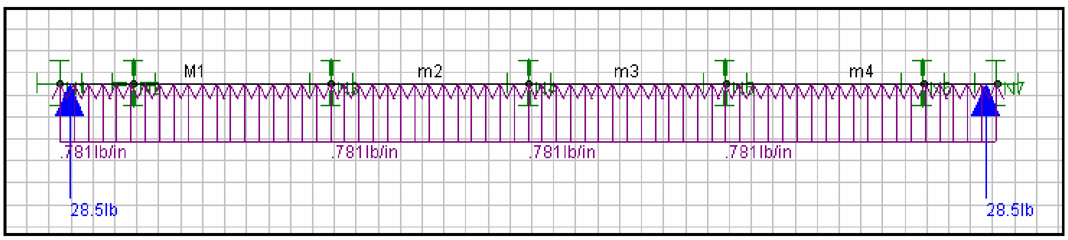

(d) FWS Loads

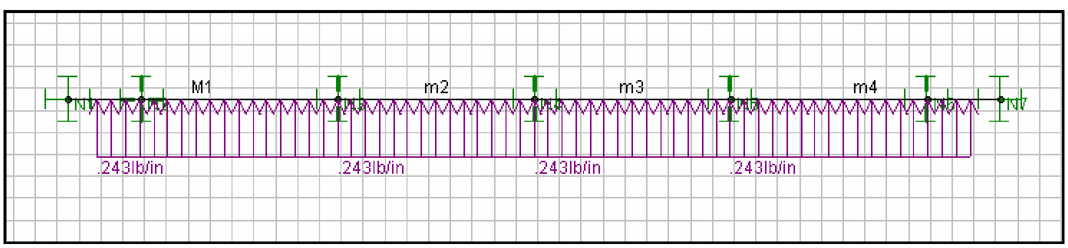

Figure 8.2 Interior bay loading considerations for negative moment

8.4 WORKING STRESS DESIGN

The hybrid reinforcement system consists of alternate bars of No. 6 GFRP and No. 4 CFRP used in all four layers of reinforcement (top and bottom mats comprising longitudinal and transverse reinforcement). A total deck slab depth of 9 in. is used, including a 1 in. sacrificial layer at the top of the deck. Once the diameter of the two types of rebars are chosen (based on commercial availability and considerations of practicality), the working stress design is an iterative process where the rebar spacing to carry flexural tensile stresses due to transverse bending in the bridge deck slab is adjusted so as to ensure that the magnitudes of rebar stress due to service loads are within allowable stress limits. It is preferable that smaller diameter GFRP bars be used for structural components such as deck slabs where it may be important to minimize slab dead loads by restricting the overall depth of the slab. In these cases, the restriction on concrete cover may result in premature bond splitting failures when larger diameter GFRP rebars are used. Similar arguments may be less valid for CFRP bars whose bond characteristics in a concrete matrix are inferior to that of GFRP bars. In any case, congestion of reinforcement and the need to be able to place and consolidate concrete with ease may also dictate bar sizes.

Figure 8.3 shows a cross-section of the deck slab designed in this study. Placement of transverse and longitudinal rebars follows the patterns used by MoDOT in conventionally reinforced bridge deck slabs.

The spacing of the longitudinal bars (parallel to the traffic direction) is primarily based on temperature and shrinkage considerations.

For analysis of stresses at service due to transverse bending, a cracked elastic analysis is used. The strain and stress distribution diagrams are shown in Figure 8.4, which also includes details of the notations, used the analysis of service performance

Assuming that concrete in compression, and the GFRP and CFRP rebars in tension behave in an elastic manner under service loads, the following equilibrium equation is valid:

$$C = \frac{1}{2} bcE_c\varepsilon_c = A_{GFRP}E_{GFRP}\varepsilon_{GFRP} + A_{CFRP}E_{CFRP}\varepsilon_{CFRP} = T_{GFRP} + T_{CFRP} \tag{8.3}$$

The strains in the two types of rebars can be computed from compatibility of strains and are given by:

$$\varepsilon_{GFRP} = \frac{(d_{GFRP} - c)}{c} \varepsilon_c \text{, and} \tag{8.4a}$$

$$\varepsilon_{CFRP} = \frac{(d_{CFRP} - c)}{c} \varepsilon_c \tag{8.4b}$$

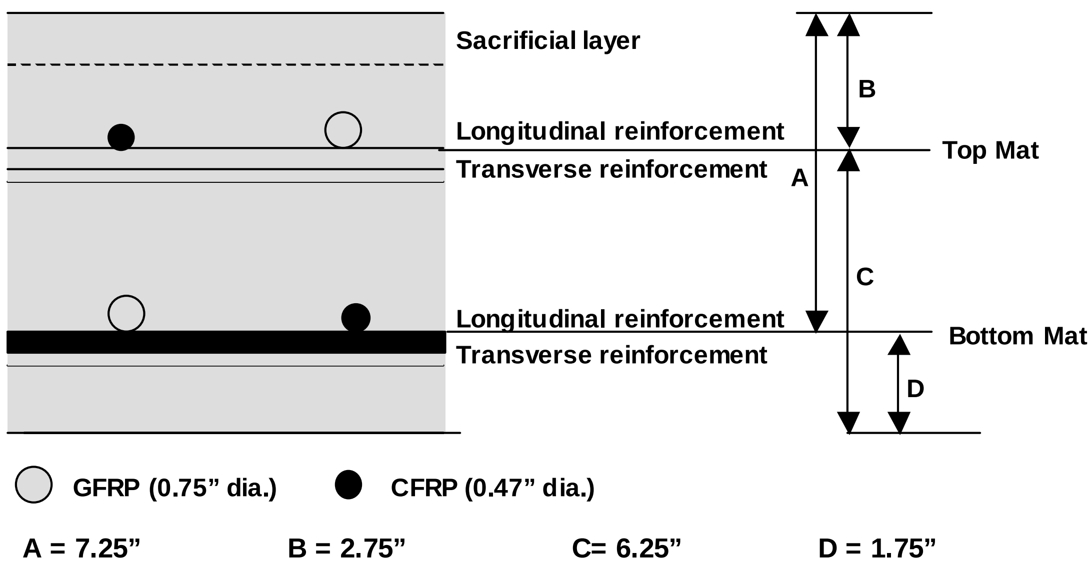

Figure 8.3 Cross-section of bridge deck slab being analyzed

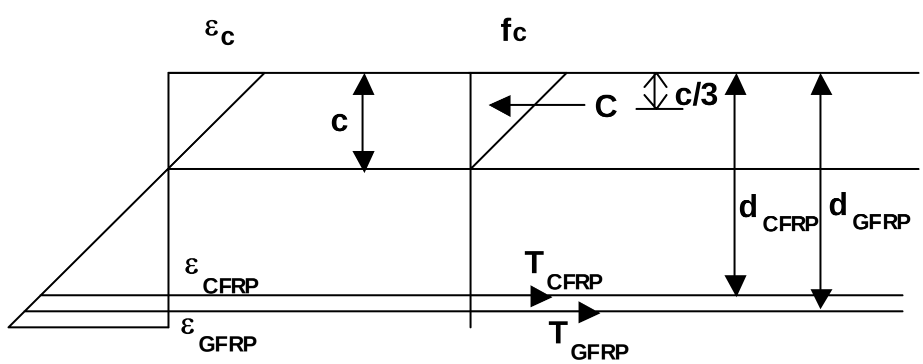

Figure 8.4 Strain and stress distributions in the cracked elastic deck section

The depth of the neutral axis can be solved using Eqns. 8.3 and 8.4. The cracked moment of inertia can then be computed as:

$$I_{cr} = \frac{bc^3}{3} + \frac{A_{GFRP} E_{GFRP} (d_{GFRP} - c)^2}{E_c} + \frac{A_{CFRP} E_{CFRP} (d_{CFRP} - c)^2}{E_c} \tag{8.5}$$

The stress in the GFRP and CFRP rebars can then be obtained using:

$$f_{GFRP} = \frac{M_{service}(d_{GFRP} - c)}{I_{cr}} \frac{E_{GFRP}}{E_c} \text{, and} \tag{8.6a}$$

$$f_{CFRP} = \frac{M_{service}(d_{CFRP} - c)}{I_{cr}} \frac{E_{CFRP}}{E_c} \tag{8.6b}$$

Check to verify $f_c < f_c^{'}/2$ (for linear elastic behavior) and check to ensure that $f_{GFRP} \leq \overline{f}_{GFRP}$, and $f_{CFRP} \leq \overline{f}_{CFRP}$, where $\overline{f}_{GFRP}$, and $\overline{f}_{CFRP}$ represent the allowable strengths under short duration service loads (unlike sustained loads) and can be assumed as prescribed fractions (40% is a reasonable value based on results from this and other investigations and also based on earlier conventions of service load design of steel and concrete structures) of the design tensile strength that account for reductions in strength due to the service environment, $f_{fu(GFRP)}$ and $f_{fu\ (CFRP)}$), respectively *(i.e* $\overline{f}_{GFRP} = 0.4\ f_{fu(GFRP)}$, *and* $\overline{f}_{CFRP} = 0.4\ f_{fu\ (CFRP)}$*).*

Interior Bay Positive Moments due to Service Loads

Consider the working stress design for the interior bay for the positive service moment, Table 8.1. Assume the slab is designed for a fatigue regime. Based on the design used for the hybrid slab tested (Table 3.9), consider No. 6 GFRP bars and No. 4 CFRP bars placed in the bottom mat alternately at a spacing of 6 in.: The following information is relevant for the design example:

Slab width considered in the longitudinal direction = b = 12 in. (to include one GFRP and one CFRP bar in the section considered), A_{GFRP} = 0.458 in.^{2}, A_{CFRP} = 0.1679 in.^{2}, E_{GFRP} = 5.92 x 10^6 psi, E_{CFRP} = 18 x 10^6 psi, $f_c^{'}$ = 6,000 psi, E_c = 2.96 x 10^6 psi (concrete properties based on actual tests, GFRP and CFRP properties based on manufacturer's test results supplied along with the rebars). For the case of positive moment, d_{GFRP} = 6.625 in. and d_{CFRP} = 6.485 in. (Fig. 8.3 – d_{GFRP} = A-1 + d_{bGFRP}/2, and d_{CFRP} = A-1 + d_{bCFRP}/2). Note that these depths do not include the 1" sacrificial layer at the top of the slab.

Based on these input parameters, the location of the neutral axis is computed from Eqs. 8.3-4 as c= 1.3 in. The corresponding value of I_{cr} is 62.16 in.^{4}. The stress in the transverse GFRP reinforcement of the bottom mat is f_{GFRP} = 14,255 psi (this is 22.6% of $f_{fu(GFRP)}$), and the transverse CFRP reinforcement of the bottom matt is f_{CFRP} = 42,205 psi (this is 15.63% of $f_{fu(CFRP)}$),. The stress at the top fiber in concrete f_c = 1,742 psi (which is 29% of $f_c^{'}$ and hence well with the linear portion of the concrete stress-strain response, as assumed in the analysis).

Alternately, if the sacrificial layer of 1 in. at the top of the slab is included, then d_{GFRP} = 7.625 in. and d_{CFRP} = 7.485 in. (Fig. 8.3 – d_{GFRP} = A + d_{bGFRP}/2, and d_{CFRP} = A + d_{bCFRP}/2).

Based on these input parameters, the location of the neutral axis is computed from Eqs. 8.3-4 as c= 1.41 in. The corresponding value of I_{cr} is 84.40 in.^{4}. The stress in the transverse GFRP reinforcement of the bottom mat is f_{GFRP} = 12,262 psi (this is 19.5% of $f_{fu(GFRP)}$), and the transverse CFRP reinforcement of the bottom matt is f_{CFRP} = 36,445 psi (this is 13.5% of $f_{fu(CFRP)}$),. The stress at the top fiber in concrete f_c = 1,388 psi (which is 23% of $f_c^{'}$ and hence well with the linear portion of the concrete stress-strain response, as assumed in the analysis). These numbers are marginally smaller than if the sacrificial layer is excluded from the analysis. There is no strong mechanics-based justification for selecting one of the two assumptions, however in the spirit of the layer being sacrificial (may not exist at some time during the future), it is recommended that calculations be made using the assumption that the sacrificial layer does not exist.

Interior Bay Negative Moments due to Service Loads

Next consider the working stress design for the interior bay for the negative service moment, Table 8.1. Based on the design used for the hybrid slab tested (Table 3.9), consider No. 6 GFRP bars and No. 4 CFRP bars placed in the top mat alternately at a spacing of 5 in.: The following information is relevant for the design example:

Slab width considered in the longitudinal direction = b = 10 in. (to include one GFRP and one CFRP bar in the section considered), A_{GFRP} = 0.458 in.^{2}, A_{CFRP} = 0.1679 in.^{2}, E_{GFRP} = 5.92 x 10^6 psi, E_{CFRP} = 18 x 10^6 psi, $f_c^{'}$ = 6,000 psi, E_c = 2.96 x 10^6 psi (concrete properties based on actual tests, GFRP and CFRP properties based on manufacturer's test results supplied along with the rebars). For the case of negative moment, d_{GFRP} = 5.875 in. and d_{CFRP} = 6.015 in. (Fig. 8.3 – d_{GFRP} = C - d_{bGFRP}/2, and d_{CFRP} = C - d_{bCFRP}/2). Note that since the sacrificial layer of concrete is in the tensile zone in a cracked section, it does not affect computations for the negative moment region in any manner.

Based on these input parameters, the location of the neutral axis is computed from Eqs. 8.3-4 as c= 1.34 in. The corresponding value of I_{cr} is 49.12 in.^{4}. The stress in the transverse GFRP reinforcement of the bottom mat is f_{GFRP} = 14,608 psi (this is 23.2% of $f_{fu(GFRP)}$), and the transverse CFRP reinforcement of the bottom matt is f_{CFRP} = 45,787 psi (this is 17.0% of $f_{fu(CFRP)}$),. The stress at the top fiber in concrete f_c = 2,152 psi (which is 35.9% of $f_c^{'}$ and hence well with the linear portion of the concrete stress-strain response, as assumed in the analysis).

All the stress values are well within respective allowable values. If this were a design problem, one would have to iterate for with spacing of reinforcement as the primary unknown variable (assuming b, the width of the slab section along the longitudinal direction, where b = 2s. and s is the spacing between the alternating GFRP and CFRP rebars)

The above analyses for both the bottom and top mats have been carried out assuming the slab behavior essentially as a one way singly reinforced flexural member. ACI 440 1R-03 recommends that the compression contribution of FRP bars be neglected. While this may be more appropriate recommendation for analysis at ultimate, the validity under service conditions where reliable compressive capacity can be anticipated (no loss in cover concrete), this assumption may be overly conservative and may need additional research. In this design example, assuming one way action and neglecting the contribution of compression reinforcement, only makes the design more conservative.

A check for the negative moment at the overhang due to service loads is not warranted as the applied service moment is marginally smaller than the negative moment in the interior bay.

8.5 FAILURE MODE AT ULTIMATE CAPACITY

Instead of designing based on factored load at ultimate, it is recommended that mandatory follow-up analysis be conducted to verify that the nominal capacity of the section exceeds the factored ultimate moment required. This check also facilitates determination of the most likely failure mode (concrete crushing in compression versus rupture of FRP in tension)

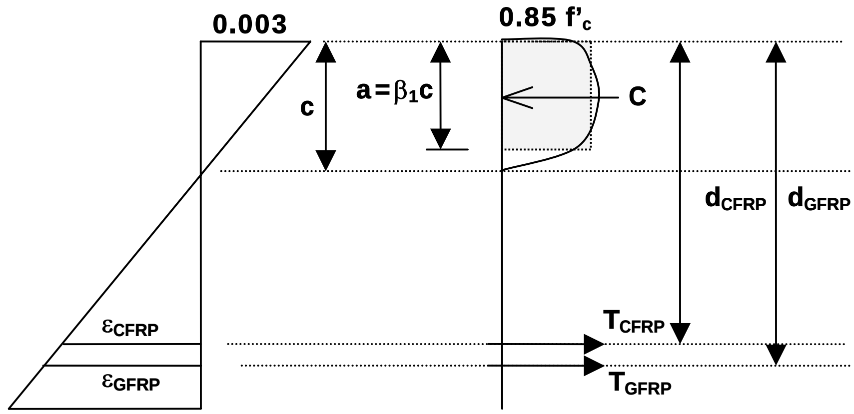

Figure 8.5 Strain and stress distributions at ultimate condition

ACI 440.1R-03 recommends that one assume that for a rectangular cross-section, the equivalent rectangular stress block at ultimate in flexure be defined by depth parameter, β_1, and stress magnitude 0.85 f'_c , with concrete strain in compression at ultimate of ε_{cu} = 0.003. These empirical assumptions have not been specifically validated using fundamental tests as done by Portland Cement Association for conventional steel-reinforced concrete systems, and are clearly questionable as demonstrated later in this section, where the neutral axis spuriously moves down at ultimate capacity compared to the value obtained from cracked elastic analysis (which is based purely on mechanics and does not involve unrealistic and unproven assumptions as recommended for ultimate analysis in ACI 440.1R-03). It is assumed that the GFRP and CFRP rebars behave elastically at ultimate. Due to this assumption, stresses in the rebars can be computed from compatibility. The equilibrium requires that:

$$C = T_{GFRP} + T_{CFRP} \tag{8.7}$$

$$0.85 f'_c\, b\beta_1 c = 0.003E_{GFRP}A_{GFRP}\frac{(d_{GFRP}-c)}{c} + 0.003E_{CFRP}A_{CFRP}\frac{(d_{CFRP}-c)}{c} \tag{8.8}$$

The depth of the neutral axis at ultimate, c, can be computed from Eq. 8.8. Once c is known, strains in the GFRP and CFRP rebars can be computed using:

$$\varepsilon_{GFRP} = 0.003\frac{(d_{GFRP}-c)}{c}, \text{ and } \varepsilon_{CFRP} = 0.003\frac{(d_{CFRP}-c)}{c} \tag{8.9}$$

These values will allow some judgment on the type of failure likely at ultimate. For hybrid reinforcement systems such as the one considered here, the failure mode may not be conclusive, as it is possible that one of the two types of rebar may be close to rupture and the other remain elastic, if perfect bond assumptions at ultimate are used. The validity of assumption of perfect bond at ultimate conditions in FRP reinforced concrete may not be as strong as for steel reinforced concrete. This is one additional reason why primary design based on analysis of section at ultimate may not be the best option for hybrid FRP reinforced concrete systems. Analysis of the section at ultimate is still recommended as a mandatory follow-up check to ensure adequate capacity and to provide some information on potential failure mechanisms at ultimate.

The nominal moment capacity may be computed from:

$$M_n = A_{GFRP} E_{GFRP} \varepsilon_{GFRP} (d_{GFRP} - \frac{\beta_1 c}{2}) + A_{CFRP} E_{CFRP} \varepsilon_{CFRP} (d_{CFRP} - \frac{\beta_1 c}{2}) \tag{8.10}$$

Nominal moment capacity reduced by the ϕ factor should be greater than the factored ultimate moment requirements at the cross-section. The capacity reduction factor, ϕ, suggested for FRP reinforced systems ranges from 0.5 for ultimate failure due to rupture of the reinforcement to 0.7 for failure due to compressive crushing in concrete. This factor should be revisited to reflect a reduction factor chosen based on tensile strain levels in the outermost reinforcement (as in the latest versions of the ACI 318 Code)

Interior Bay Positive Moments due to Factored Loads

Like in the positive moment region for service loads, computations are affected depending upon the assumption with regard to the top 1 in. deep sacrificial layer. If the sacrificial layer is neglected in the depth and stress calculations as was recommended earlier, then: d_{GFRP} = 6.625 in. and d_{CFRP} = 6.485 in. Slab width considered in the longitudinal direction = b = 12 in. (to include one GFRP and one CFRP bar in the section considered), A_{GFRP} = 0.458 in.^{2}, A_{CFRP} = 0.1679 in.^{2}, E_{GFRP} = 5.92 x 10^6 psi, E_{CFRP} = 18 x 10^6 psi, $f_c^{'}$ = 6,000 psi, E_c = 2.96 x 10^6 psi (concrete properties based on actual tests, GFRP and CFRP properties based on manufacturer's test results supplied along with the rebars).

Based on these input parameters, the location of the neutral axis is computed from Eq. 8.8 as c= 1.39 in. (this location of neutral axis is based on ACI440.1R-03 recommendations which do not originate from a rigorous calibration from fundamental tests unlike for steel-reinforced concrete sections at ultimate. Clearly the value of c at ultimate capacity is unrealistic based on results of service load cracked elastic analysis based purely on mechanics) The corresponding value of ε_{GFRP} = 0.0113 ($\varepsilon_{fu\ (GFRP)}$=0.01064 after an environmental reduction factor of 0.7 is applied, $\varepsilon_{fu\ (GFRP)}$=0.01216 if the environmental reduction factor of 0.8 is applied), and ε_{CFRP} = 0.0108 ($\varepsilon_{fu\ (CFRP)}$=0.0167 after an environmental reduction factor of 0.9 is applied). There are judgment calls to be made here with regard to limiting strains, particularly given the fact that when fibers are incorporated, these limiting strains recommended based on exposure conditions can be relaxed. Given these observations, the failure at ultimate can be considered to be due to concrete crushing. The nominal moment capacity computed is 31.81 kip-ft. Even using a capacity reduction factor of ϕ of 0.5, as recommended for failure by rupture of reinforcement, ϕM_n is 15.9 kip-ft., which is larger than the factored moment, M_u, requirements at the section of 12.86 kip-ft.

Overhang Negative Moment due to Factored Loads

Since the negative moment at the overhang marginally exceeds the negative moment in the interior bay (Table 8.1), the critical section to be considered for negative moments is at the overhang. Like earlier for the working stress analysis, the sacrificial layer does not in any way affect the nominal capacity of the cross-section as it is in the tensile region.

For the overhang section, d_{GFRP} = 5.875 in. and d_{CFRP} = 6.015 in. Slab width considered in the longitudinal direction = b = 10 in. (to include one GFRP and one CFRP bar in the section considered), A_{GFRP} = 0.458 in.^{2}, A_{CFRP} = 0.1679 in.^{2}, E_{GFRP} = 5.92 x 10^6 psi, E_{CFRP} = 18 x 10^6 psi, f_c' = 6,000 psi, E_c = 2.96 x 10^6 psi (concrete properties based on actual tests, GFRP and CFRP properties based on manufacturer's test results supplied along with the rebars).

Based on these input parameters, the location of the neutral axis is computed from Eq. 8.8 as c= 1.43 in. (Note the c value again is larger than that obtained for service loads based on cracked elastic analysis). The corresponding value of ε_{GFRP} = 0.0092 ($\varepsilon_{fu\ (GFRP)}$=0.01064 after an environmental reduction factor of 0.7 is applied), and ε_{CFRP} = 0.0962 ($\varepsilon_{fu\ (CFRP)}$=0.0167 after an environmental reduction factor of 0.9 is applied). Given these observations, the failure at ultimate can be considered to be due to concrete crushing. The nominal moment capacity computed is 24.38 kip-ft. Even using a capacity reduction factor of

ϕ of 0.5, as recommended for failure by rupture of reinforcement, ϕM_n is 12.19 kip-ft., which is larger than the factored moment, M_u, requirements at the section of 10.08 kip-ft. (12.09 x 10/12 to account for the width b of 10 in. analyzed for the negative moment region). Hence the design provides for adequate moment capacity due to factored loads at ultimate conditions in both the positive and negative moment regions.

8.6 CRACK WIDTHS

ACI 440.1R-03 recommends that serviceability check on crack width be enforced using the equation:

$$w = \frac{2{,}200}{E_f} \beta\, k_b\, f_f \sqrt[3]{d_c A} \tag{8.11}$$

Where E_f and f_f are the elastic modulus of the FRP rebar, and stress in the FRP rebar at service loads, respectively. β, is the ratio of the distance from the neutral axis to the extreme tension fiber to the distance from the neutral axis to the center of the tensile reinforcement, k_b is a bond-dependent coefficient, d_c is the cover in in., from the extreme tension face to the center of the closest reinforcement, and A is the effective tension area of concrete, defined as the area of concrete having the same centroid as that of tensile reinforcement, divided by the number of bars, in^2. The direct validity of this expression originally empirically derived for steel reinforced concrete and later adapted for FRP (with empirical modifications) for hybrid reinforcement such as the one recommended here, is not entirely appropriate. However, estimated crack-widths can be computed independently for GFRP and CFRP reinforcement in the hybrid system, assuming each were acting alone (neglecting the obvious coupling effects that are likely as far as crack-widths are concerned).

Based on results from this investigation (Belarbi and Wang, 2005, Eq.5.8), have proposed:

$$w = \frac{1{,}700}{E_f} \beta\ f_f \sqrt[3]{d_c A} \tag{8.12}$$

For the GFRP computations, the following input is used:

c = 1.34 in. , β = 1.47 (h = 8 in., d_{GFRP} = 5.875 in.), f_{GFRP} = 14,608 psi, d_c = 2.125 in., A = 5 (8 – 1.34) = 33.3 in^2., yielding an estimated crack width of 0.025 in. (or 25 mils). All input parameters are identical to the ones earlier computed using working stress analysis for service loads.

For CFRP computations, the following input is used:

c = 1.34 in. , β = 1.42 (h = 8 in., d_{CFRP} = 6.015 in.), f_{CFRP} = 45,787 psi, d_c = 1.985 in., A = 5 (8 – 1.34) = 33.3 in^2., yielding an estimated crack width of 0.0248 in. (or 24.8 mils). All input parameters are identical to the ones earlier computed using working stress analysis for service loads.

These estimated crack widths are in the same range as allowed by ACI 440-1R-03 and the Canadian codes that the ACI 440-1R-03 document bases its recommendation for permissible crack widths on. It should be noted that crack-widths typically in a matrix reinforced with fibers are smaller than that observed in similar plain concrete matrices. It should also be noted that results from full-scale slab test reported in Chapter 7 confirmed that crack-widths in hybrid GFRP/CFRP reinforced slabs were finer and more in number than a “GFRP only” reinforced slab.

8.7 CREEP RUPTURE AND FATIGUE

Since working stress calculations for service loads presented earlier in Section 8.4 are identical in approach to those recommended for a check of creep rupture (with considerations of the fatigue regimen of loading), those calculations can be readily adapted for the check of creep rupture. The only difference would be that service moments in the stress calculations would be replaced by sustained moments during service (i.e only the dead load components of the service moments). Since the analysis is elastic, the stresses due to sustained service moments (only dead load components of the service moments) can be computed by using proportional scaling of those values obtained for total service moments in Section 8.4.

Sustained moments due to dead load are 20% or less of the total service moments listed in Table 8.1 in the positive moment and negative moment regions of the interior bay as well as the negative moment in the overhang. Hence the creep rupture stresses including the fatigue regime restrictions are less than 5% of $f_{fu(GFRP)}$ and less than 3.5% of $f_{fu(CFRP)}$ (where the limits specified in ACI 440.1R-03 are 20% for GFRP reinforcing and 30% for CFRP reinforcing, respectively).

8.8 SHEAR

The shear capacity of concrete for flexural members using FRP reinforcement has been recommended by ACI 440.1R-03 to be of the form:

$$V_{c,f} = \frac{\rho_f E_f}{90\beta_1 f'_c} V_c \tag{8.13}$$

where $V_{c,f}$ is the shear capacity of FRP reinforced concrete, V_c represents the nominal shear capacity of concrete when steel reinforcement is used, and ρ_f and E_f are the reinforcement ratio and elastic modulus, respectively of the FRP reinforcement. The basis for Eq. 8.13 is the assumption that shear capacity in concrete is proportional to the axial stiffness of the reinforcement. This shear capacity calculation is typically more appropriate for beam members or slabs that essentially behave like one-way slabs. In the case of a bridge deck this is not really true because bridge deck slabs typically act like two-way slabs and shear design is normally ignored because it is seldom of concern. The longitudinal reinforcement act to provide additional resistance to shear deformations. Local punching shear action is more likely in bridge deck slabs due to unanticipated large concentrated loads.

Using the same logic it is possible to derive the shear capacity of a hybrid GFRC/CFRP (one-way) flexural member as:

$$V_{c,f} = \frac{A_{GFRP} E_{GFRP} + A_{CFRP} E_{CFRP}}{bd} \frac{V_c}{90\beta_1 f'_c} \tag{8.14}$$

The d to be used in the above equation can be computed as the effective depth of the net tensile force at ultimate, d_{eff}, and can be computed by simple mechanics of the tensile forces at ultimate as:

$$d_{eff} = \frac{T_{GFRP} d_{GFRP} + T_{CFRP} d_{CFRP}}{T_{GFRP} + T_{CFRP}} \tag{8.15}$$

Based on these computations, the shear capacity of concrete using FRP reinforcement for transverse bending (one way action) is 2.2 kip/ft. (per ft. of the longitudinal direction). The ultimate shear capacity required from RISA 3D calculations (positive moment section, interior bay) is 4.7 kip/ft (again assuming one-way action). The longitudinal reinforcement provided in slabs typically contributes to shear resistance much similar to the way in which reinforcement transverse to the axis of bending (for e.g. shear stirrups in beams). In this particular slab design, there is an average of at least one GFRP and one CFRP bar at a spacing of at least 10 in. in the top and bottom mats (Table 3.9). These will collectively provide more than the capacity required.

8.9 TEMPERATURE AND SHRINKAGE REINFORCEMENT

ACI 440.1R-03 recommends that temperature and shrinkage reinforcement be provided to limit crack widths. In a bridge deck slab, this is provided along the longitudinal direction (in the top and bottom mats). The amount of reinforcement according to ACI 440.1R-03 is given by:

$$\rho_{f,ts} = 0.0018 \ \frac{60{,}000E_s}{f_{fu}E_f} \qquad (8.16)$$

For a hybrid GFRP/CFRP system using alternate bars of GFRP and CFRP, this can be applied using an effective strength and effective modulus approach based on law of mixtures (or iso-strain model). The effective design tensile strength, $f_{fu,\,eff}$ is computed as:

$$f_{fu,eff} = \frac{f_{fu(GFRP)}A_{GFRP} + f_{fu(CFRP)}A_{CFRP}}{A_{GFRP} + A_{CFRP}} \qquad (8.17)$$

Similarly, the effective modulus is given by $E_{f,eff}$:

$$E_{f,eff} = \frac{E_{GFRP}A_{GFRP} + E_{CFRP}A_{CFRP}}{A_{GFRP} + A_{CFRP}} \qquad (8.18)$$

Using $f_{fu,eff}$ and $E_{f,eff}$ instead of f_{fu} and E_f in Eq. 8.16, one gets $\rho_{f,ts}$ = 0.003.

Two (one top mat and one bottom mat) No. 6 GFRP bar at 20 in. spacing (GFRP bar to GFRP bar spacing) and two (one top mat and one bottom mat) No. 4 CFRP bar at 20 in. spacing (CFRP bar to CFRP bar) effectively provide a ρ_{GFRP} of 0.007 and a ρ_{CFRP} of 0.0026 independently. These quantities collectively far exceed the net temperature and shrinkage reinforcement required (even while reinforcement ratios of the two FRP rebars cannot be readily added, given the different material properties).

9. CONCLUSIONS AND RECOMMENDATIONS

9.1 SUMMARY OF CONCLUSIONS

A better understanding of the static and fatigue performance of FRP reinforced concrete members both with regard to fundamental characteristics such as bond and flexural behavior, in simple test configurations as well as more complex structural performance in a two-way composite slab was achieved. The influence of incorporation of discrete fibers on the performance and accelerated durability characteristics of such hybrid reinforced composite systems were also documented. In the opinion of the PIs, steel-free hybrid reinforced bridge deck slabs offer a technically viable option with regard to mitigation of the problem of corrosion in steel reinforced bridge deck slabs. While relative brittleness and tensile stiffness of the commercially available FRP reinforcing bars compared to conventional steel rebars is of some concern, it is still possible to engineer an adequately stiff bridge deck slab that performs as well as the conventional deck under normal service conditions. Design approaches to the new material must recognize the strengths and drawbacks of the innovative composite system as highlighted in this and other reports (ACI440.1R-03), and reflect the recent advances made towards implementing this new technology for practical use.

More specific conclusions with regard to each aspect of the test program are outlined in the next few sub-sections. Recommendations on the implementation on this technology in the field are included in the next section.

9.1.1 Bond Tests

Based on the bond studies carried out during this investigation in the three test configurations, including pullout bond, splitting bond and flexural bond tests, the following conclusions can be made:

- The addition of 0.5% volume fraction, 2-in. long, fibrillated polypropylene fibers improves the static bond-slip characteristics in the post-peak region. Little change as expected was observed for the static pre-peak behavior. The bond specimens that included fibers in the matrix failed in a more ductile fashion with a gradual descending portion. A significant fraction of the peak load could be sustained, even at large slip values. The bond specimens with a plain concrete matrix failed in a brittle fashion, exhibiting a brittle failure at peak load.

- Different bond mechanisms were observed for the CFRP and the GFRP specimens, largely attributable to their different surface treatments. Average bond strength of the GFRP specimens were about twice as that observed for the CFRP specimens. The GFRP specimens typically failed due concrete splitting; while the CFRP specimens failed by pull-out. This mechanism of failure provided for more structural ductility (toughening at the cost of strengthening).
- Fatigue loading, within the working stress range, was observed to increase bond stiffness and bond strength. The resultant behavior also made the overall bond-slip response more brittle with accompanying changes in some specimens of the failure mode from a pull-out failure to a splitting failure.
- Incorporation of 0.5% volume fraction of 2-in. long, fibrillated polypropylene fibers in the concrete matrix can effectively decrease the rate of bond degradation due to the fatigue loading in FRP reinforced systems. The addition of fibers in the bridge deck slab will serve two very valuable purposes, namely, improving the matrix quality, and bond performance of the FRP reinforced composite under both static and fatigue loads.
- Based on a semi-empirical approach, an equation has been proposed to predict the bond strength for FRP bars embedded in a fiber concrete matrix that exhibit matrix splitting failure.

9.1.2 Flexural Tests

Based on the flexural ductility studies during this investigation, the following conclusions can be made:

- The model proposed by Salib et al. (2004) yields reasonable predictions of the crack width for both the plain concrete beams and the FRC beams. The predictions by the ACI 440 were found to be conservative. A modified version of the equation proposed by ACI 440.1R-03 is proposed which is also used in the design example.
- The addition of fibers reduced the crack widths at the service load in the case of beams that had FRC matrices as compared to plain concrete matrices.

- Concrete strain measured at the extreme compression fiber of beams with FRC matrices was larger than those observed for beams that used plain concrete. The concrete compressive strains at peak load ranged from 4,000 μstrains to 5,500 μstrains, with an average of 4,500 μstrains for the FRC beams, while concrete strains, ranging from 2,700 μstrains to 3,300 μstrains, with an average of 2,950 μstrains, were measured for the plain concrete beams. The analysis procedures at ultimate should reflect this more ductile compressive behavior of the matrix when fibers are incorporated.
- With the addition of polypropylene fibers, the ductility indices increased by approximately 40% based on deformation based approach, which takes into account the strength effect as well as the deflection (or curvature) effect on determining the ductility. In addition, both plain concrete beams and FRC beams provided an adequate deformability level, as described by Jaeger, Tadros and Mufti (1995).

9.1.3 Durability Tests

Based on the accelerated durability component of this investigation including the bond and flexural performance of weathered specimens, the following conclusions can be drawn:

- Bond degradation in durability tests can be attributed to three reasons: (1) expansion of solution in the microvoids at the interface; (2) difference in the coefficient of thermal expansion between the rebar and concrete; (3) damage of the rebar, especially on the surface. The first two mechanisms function together and degrade the bond mainly at the interface. The third reason is attributed to damage of the rebar surface, resulting in separation between the rebar and concrete.
- Bond performance of weathered specimens significantly improved due to fiber addition, which contributed greatly to improved crack growth resistance of the matrix in the vicinity of the rebar. The loss of the ultimate bond strength of the FRP rebars in the plain concrete matrix due to weathering effects was found to be 28% on average, while only 6% reduction was observed in the specimens with FRC matrix. Similarly, bond stiffness exhibited a 26% average reduction in plain concrete specimens, while only 10% reduction was observed in the FRC specimens.
- The larger specimens with longer embedment length and relatively smaller exposed area to the solution of sodium chloride (NaCl) showed better performance.

- CFRP reinforced specimens exhibited superior bond performance as compared to the GFRP reinforced specimens. This may be attributed to the inherently more durable characteristics of the CFRP rebar.
- Both plain concrete beams and FRC beams exhibited a small reduction in ultimate flexural strength and ductility in the durability test. The degradation of concrete based matix was the main reason for the degradation in flexural performance of the composite beams.
- Compared to the plain concrete beams, FRC beams showed approximately 40% increase in ductility index based on deformation based approach both before and after the environmental conditioning.

9.1.4 Full-Scale Slab Tests

- The precracking stiffness of the three test slabs was nearly identical because at this stage of loading the concrete matrix primarily contributes to the flexural rigidity of the slab.
- The post-cracking stiffness of the GFRP and hybrid GFRP/CFRP slabs were significantly lower than that for the conventional steel reinforced slab as observed from the post-fatigue static test. The overall post-cracking stiffness of the GFRP and hybrid GFRP/CFRP slabs were nearly identical, even while the modulus of the CFRP bar is higher. This can be attributed to inferior bond for CFRP bars compared to GFRP bars and also to more number of finer cracks.
- Crack widths were smaller for hybrid slab than for GFRP slab. Crack widths for hybrid slabs were more readily comparable to that for steel reinforced slab, even while the global stiffness of the hybrid slab was more comparable to the GFRP slab. This anomaly can be explained by the presence of many finer cracks in the hybrid reinforced slab.
- FRP reinforced slabs used 0.5% by volume of polypropylene fibers unlike the steel reinforced slab which used plain concrete matrix. Fibers affect the near surface crack widths while being insignificant as far as global properties are concerned.
- Fatigue performance under service loads of cracked elastic FRP reinforced slabs is comparable to performance of similarly loaded steel reinforced slabs during the 1 million fatigue cycles. The degradation in normalized stiffness of the FRP reinforced slabs is no different from that in conventional slabs.

- Steel slab failed by punching shear failure. GFRP and hybrid slabs did not fail due to punching shear. Tests on these slabs had to be stopped due to the limiting load capacity of the hydraulic actuator and due to excessive displacements of the slab and the outer span support mechanism. At the time these tests were stopped, the GFRP slab exhibited extensive bond splitting type cracking (cracking patterns reflecting profile of lower reinforcement mat) indicating that the incipient failure would have likely been in the flexural mode. The difference in the types of failure can be attributed to a strong influence on concentrated loading configuration used and concrete slab strength used. Had the loading configuration involved uniformly distributed loading, punching shear failure observed in the steel reinforced slab may not have preceded a flexural failure.

9.2 RECOMMENDATIONS

Based on results from the investigation, the following recommendations are made:

- Steel-free FRP reinforced bridge deck slabs can be designed to meet service performance specifications of strength normally intended for conventional steel reinforced slabs. Post-cracking deflections and associated crack widths are expected to be larger than in conventional steel-reinforced bridge deck slabs and should be recognized as such. Despite this no significant difference in fatigue performance was observed in the full-scale slab tests.
- It is recommended that MoDOT consider a system of hybrid reinforcement comprising continuous GFRP and CFRP reinforcement for the top and bottom reinforcement mats in a polypropylene fiber reinforced matrix for the next phase of field implementation. CFRP bars are of higher modulus and strength, provide better fatigue performance and are inherently more resistant to environmental degradation. But these bars are also significantly more expensive than GFRP bars. It is hence recommended that CFRP bars be used where necessary to resist tensile cracking, limit crack widths and provide improved fatigue performance. While the slab tested in this investigation used alternate GFRP and CFRP bars in all four layers of reinforcement (longitudinal and transverse reinforcement in both the top and bottom mats), it is adequate to use CFRP bars only to resist cracking due to transverse bending in regions subjected to high tensile stresses.

GFRP bars can be used exclusively for the longitudinal bars which primarily are intended as temperature and shrinkage reinforcement.

- It is recommended that 0.5% volume fraction of 2-in. long polypropylene fibers be used in the concrete matrix. This greatly improves matrix quality and bond performance under both static and fatigue loads. Since the incorporation of polypropylene fibers increases the content of both entrained and entrapped air, strict limits on air content in the design mix should be enforced. Loss of strength and stiffness can result if strict control on air content is not enforced. The benefits of fiber incorporation in terms of significant improvements in mechanical performance under fatigue loads far outweigh the extra effort needed to ensure tighter specifications with regard to air content.
- It is recommended that flexural design of deck slabs be carried out using working stress approach with mandatory checks on ultimate capacity and mode of failure. This approach is more practically relevant for hybrid reinforced FRP slabs than the procedures based on ultimate design as recommended in ACI 440.1R-03.
- Since no bridge deck railing system has been tested or analyzed during this investigation it is recommended that the tried and tested conventional design used by MoDOT for bridge deck railings be incorporated with proper detailing to connect the railing to the hybrid reinforced FRP deck slab.

REFERENCES

AASHTO LRFD Bridge Design Specifications, American Association of State Highway and Transportation Officials, Washington, D.C., 1998, pp. 5-138.

ACI Committee 201, "*Guide to Durable Concrete*," ACI 201.2R-92, American Concrete Institute, Farmington Hills, Michigan, 1992, 39 pp.

ACI Committee 318. *"Building Code Requirements for Structural Concrete (318-02) and Commentary (318R-02),"* American Concrete Institute, Farmington Hills, Michigan., 2002, 443 pp.

ACI Committee 408, "*State–of–the–Art Report on Bond under Cyclic Loads*," ACI 408.2R-92 (Reapproved 1999), American Concrete Institute, Farmington Hills, Michigan, 1999, 32 pp.

ACI Committee 440, "*Guide for the Design and Construction of Concrete Reinforced with FRP Bars*," ACI 440.1R-03, American Concrete Institute, Farmington Hills, Michigan, 2003, 40 pp.

ACI Committee 440, 1996, "State-of-the-Art Report on Fiber Reinforced Plastic (FRP) Reinforcement for Concrete Structures," January 1, 1996.

ACI Committee 440, 2000, "Guide for the Design and Construction of Concrete Reinforced with FRP Bars," November 1, 2000.

ACI Committee 544, "*State–of–the–Art Report on Fiber Reinforced Concrete*," ACI 544.1R-96, American Concrete Institute, Farmington Hills, Michigan, 1996, 66 pp.

Admi, M.R., Rahman, A.H. and Benmokrane, B., "New Method for Testing Fiber-Reinforced Polymer Rods under Fatigue," *Journal of Composites for Construction*, Vol. 4, No.4, November 2000, pp. 206-213.

Al-Dulaijan S.U., Al-Zahrani, M., Nanni, A., Bakis, C., and Boothby, E., "Effect of Environmental Pre-Conditioning on Bond of FRP Reinforcement to Concrete," *Journal of Reinforced Plastics and Composites*, Vol. 20, No.10, pp. 881-900.

Alsayed, S.H., and Alhozaimy, A.M., "Ductility of Concrete Beams Reinforced with FRP Bars and Steel Fibers," *Journal of Composite Materials*, Vol. 33, No. 19, 1999, pp. 1792-1806.

ASTM A-944-99, "Standard Test Method for Comparing Bond Strength of Steel Reinforcing Bars to Concrete Using Beam-End Specimens," *Annual Book of Standards*, American Society for Testing and Materials, West Conshohocken, Pennsylvania, 1999.

ASTM C 1543-02, “Standard Test Method for Determining the Penetration of Chloride Ion into Concrete by Ponding,” *Annual Book of Standards,* American Society for Testing and Materials, West Conshohocken, Pennsylvania, 2002.

ASTM C 666-03, “Standard Test Method for Resistance of Concrete to Rapid Freezing and Thawing in Water,” *Annual Book of Standards,* American Society for Testing and Materials, West Conshohocken, Pennsylvania, 2003.

Bakht, B., and Mufti, A., “Five Steel Bridge Deck Slabs in Canada,” *Structural Engineering International*, Vol. 8, No.3, 1998, pp. 196-200.

Bakht, B., and Mufti, A., “FRC Deck Slabs without Tensile Reinforcement,” *Concrete International*, Vol.18, No.2, February 1996, pp. 50-55.

Bakis, C.E., AL-Dulaijan, S.U., Nanni, A., Boothby, T.E., and Al-Zahrani, M.M., “Effect of Cyclic Loading on Bond Behavior of GFRP Rods Embedded in Concrete Beams,” *Journal of Composites Technology & Research*, JCTRER, Vol. 20, No. 1, January 1998, pp. 29-37.

Balazs, G.L., and Borosnyoi, A., “Long-term behavior of FRP,” *Composites in construction: a reality, Proceedings of the International Workshop,* July 20-21 2001 Capri, (Italy) by Edoardo Cosenza, Gaetano Manfredi, and Antonio Nanni.

Bank, L.C., and Gentry, T.R., “Accelerated Test Methods to Determine the Long-Term Behavior of FRP Composite Structures: Environmental Effects,” *Journal of Reinforced Plastics and Composites,* Vol. 14, June 1995, pp. 559-587.

Bank, L.C., Puterman, M., and Katz, A., “The Effect of Material Degradation on Bond Properties of Fiber Reinforced Plastic Reinforcing Bars in Concrete,” *ACI Materials Journal*, Vol. 95, No. 3, May-June 1998, pp. 232-243.

Barker, R.M., and Puckett, J.A., *Design of Highway Bridges*, A Wiley-Interscience Publication, 1997

Batchelor, B. deV., and Kwun, M., “Shear in RC Beams without Web Reinforcement,” *Journal of the Structural Division,* ASCE, Vol. 107, No. 5, May 1981, pp. 907-921.

Belarbi, A., and Wang, H**.,** “Bond Splitting Behavior of FRP Reinforcing Bars Embedded in Fiber Reinforced Concrete,” *Proceeding for the 84th Transportation Research Board Annual Meeting,* 2005, Washington D.C.

Belarbi, A., and Wang, H., “Bond-Slip Response of FRP Reinforcing Bars in Fiber Reinforced Concrete under Direct Pullout," *Proc. of ICFRC--International Conference on Fiber Composites, High Performance Concretes, and Smart*

Materials, January 8-10, 2004, Chennai, India pp. 409-419, Ed. By V. S. Parameswaran

Belarbi, A., Chandrashekhara, C., and Watkins, S.E., "Performance Evaluation of Fiber Reinforced Polymer Reinforcing Bar Featuring Ductility and Health Monitoring Capability," *Fourth International Symposium on Fiber Reinforced Polymer for Reinforced Concrete Structures,* SP-188, American Concrete Institute, Farmington Hills, Michigan, 1999, pp. 1-12.

Benmokrane, B., Tighiouart, B., and Chaallal, O., "Bond Strength And Load Distribution of Composite GFRP Reinforcing Bars in Concrete," *ACI Materials Journal*. Vol. 93, No. 3, May-June 1996, pp. 246-253.

Berg, A.C., Bank, L.C., Oliva, M.G., and Russell, J.S., "Construction of FRP Reinforced Bridge Deck on US Highway 151 in Wisconsin," *Proceeding for the 84th Transportation Research Board Annual Meeting,* 2004, Washington D.C.

Boothby, T.E., Nanni, A., Bakis, C.E., and Huang, H., 1995, "Bond of FRP Rods Embedded in Concrete," Proceedings of the 10th ASCE Engineering Mechanical Specialty Conference, pp. 114-117.

Boyle, H.C, and Karbhari, V.M., 1994, "Investigation of Bond Behavior Between Glass Fiber Composite Reinforcements and Concrete," Polymer-Plastic Technology and Engineering, Vol. 33, No. 6, pp. 733-753.

Bradberry, T.E., "Concrete Bridge Decks Reinforced with Fiber-Reinforced Polymer Bars," *Transportation Research Record 1770,* 2001, pp. 97-104.

Bresler, B., *Reinforced Concrete Engineering,* John Wiley & Son, 1974.

Byars, E.A., Waldron, P., Dejke, V., Demis, S., and Heddadin, S., "Durability of FRP in Concrete--Current Specifications and a New Approach," *International Journal of Materials and Product Technology,* Vol. 19, No. 1-2, 2003, pp. 40-52.

Cairns, J., and Abdullah, R., "An Evaluation of Bond Pullout Tests and Their Relevance to Structural Performance," *Structural Engineer,* Vol. 73, No. 11, June 1995, pp. 179-185.

Cairns, J., and Plizzari, G., "Towards a Harmonized European Bond Test," *Materials and Structures,* Vol. 36, October 2003, pp. 498-506.

Campbell, T. I., Chitnuyanondh, L., and Batchelor B. deV., " Rigid-Plastic Theory V. Truss Analogy Method for Calculating the Shear Strength of Reinforced Concrete Beams," *Magazine of Concrete Research.* Vol. 32, No. 110, March 1980, pp. 39-44.

CAN/CSA-S6-00, 2000, “Canadian Highway Bridge Design Code,” Canadian Standard Association, Rexdale, Ontario, Canada, 190 pp.

Carrasquillo, R.L., Nilson, A.H., and Slate, F.O., “Properties of High Strength Concrete Subject to Short-Term Loads,” *ACI Journal*, Vol. 78, No. 3, May-June 1981, pp. 171-178.

CEB-FIP, *Model Code for Concrete Structures: CEB-FIP International Recommendations,* 3rd ed., Comité Euro-International du Béton, Paris, 1978, 348 pp.

Chaallal, O., and Benmokrane, B., “Pullout and Bond Glass-Fiber Rods Embedded in Concrete And Cement Grout,” *Materials & Structures.* Vol. 26, No. 157, April 1993, pp. 167-175.

Chen, Wai-Fah and Duan, Lian, *Bridge Engineering Handbook*, CRC Press, 1999

Chinn, J., Ferguson, P.M., and Thompson, J.N., “Lapped splices in reinforced concrete beams,” ACI *Journal*, Vol. 52, No.10, 1955, pp. 201-213.

Choi, O.C., and Lee, W.S., “Interfacial Bond Analysis of Deformed Bars to Concrete,” *ACI Structural Journal*, Vol.99 No.6, November-December 2002, pp. 750-756.

Clark, C.R., and Johnston, D.W., “Early Loading Effects on Bond Strength,” ACI Journal, Vol. 80, No. 6, November-December 1983, pp. 532-539.

Collins, M.P., and Mitchell, D., *Prestressed Concrete Structures,* Prentice-Hall, Inc., 1991, 753 pp.

Conrad, J.O., Bakis, C.E., Boothby, T.E., and Nanni, A., 1998, “Durability of Bond of Various FRP Rods in Concrete,” Proceedings of the First International Conference on Durability of Composites in Construction, B. Benmokrane and H. Rahman, Eds., Sherbrooke, Quebec, Canada, pp. 299-310.

Cosenza, E., Manfredi, G., and Realfonzo, R. “Behavior and Modeling of Bond of FRP Rebars to Concrete,” *Journal of Composites for Construction*, Vol. 1, No.2, May 1997, pp. 40-51.

Cosenza, E., Manfredi, G., Pecce, M., and Realfonzo, R., 1999, “Bond between Glass Fiber Reinforced Plastic Reinforcing Bars and Concrete -- Experimental Analysis,” ACI Special Publication, V. 188, August 1, 1999.

Cox, J.V., 1999, “Computational Models for the Bond between FRP Reinforcing Bars and Concrete,” Proceedings of the 13th ASCE Engineering Mechanics Division Conference, Dayton, OH, September 1999, pp. 618-627.

Cox, J.V., and Guo, J., "Modeling the Stress State Dependency of the Bond Behavior of FRP Tendons," ACI Special Publication, V. 188, August 1, 1999, pp 791-805.

Demers, C.E., “Fatigue Strength Degradation of E-Glass FRP Composites and Carbon FRP Composites,” *Construction and Building Materials*, Vol. 12, No. 5, July 1998, pp. 311-318.

Demers, C.E., “Tension-Tension Axial Fatigue of E-Glass Fiber-Reinforced Polymeric Composites: Fatigue Life Diagram,” *Construction and Building Materials*, Vol. 12, No.1, 1998, pp. 303-310.

Ehsani, M.R., Saadatmanesh, H., and Tao, S. “Bond Behavior of Deformed GFRP Rebars,” *Journal of Composite Materials*, Vol. 31, No. 14, 1997, pp. 1413-1430.

Ehsani, M.R.; Saadatmanesh, H.; and Tao, S., 1995, “Bond of Hooked Glass Fiber Reinforced Plastic (GFRP) Reinforcing Bars to Concrete,” ACI Materials Journal, V. 92, No. 4, pp. 391-400.

Ehsani, M.R.; Saadatmanesh, H.; and Tao, S., 1996, “Design Recommendation for Bond of GFRP Rebars to Concrete,” Journal of Structural Engineering, V. 122, No. 3, pp. 247-254.

El-Salakawy, E. and Benmokrane, A., “Serviceability of Concrete Bridge Deck Slabs Reinforced with Fiber-Reinforced Polymer Composite Bars,” *ACI Structural Journal*, Vol. 101, No. 5, September-October 2004, pp. 727-736.

Faza, S.S., and GangaRao, H.V.S., 1990, “Bending and Bond Behavior of Concrete Beams Reinforced with Plastic Rebars,” Transportation Research Record 1290, pp. 185-193.

Federal Highway Administration, “Deficient Bridges by State and Highway System,” http://www.fhwa.dot.gov/bridge/deficient.htm, Accessed in February 2005

Federal Highway Administration, “Innovative Bridge Research and Construction (IBRC) Program,” http://ibrc.fhwa.dot.gov , Accessed in February 2005.

Ferguson, P. M., and Thompson, J. N., “Development Length of High Strength Reinforcing Bars in Bond,” *ACI Journal*, Vol. 59, No. 1, January 1962, pp. 887-922.

Ferguson, P. M., Breen, J.E., and Thompson, J.N., “Pullout Tests on High Strength Reinforcing Bars,” *ACI Journal*, Vol. 62, No. 8, August 1965, pp. 933-950.

Gao, D., Benmokrane, B., and Masmoudi, R., “A Calculating Method of Flexural Properties of FRP-Reinforced Concrete Beam: Part 1: Crack Width and

Deflection," *Technical Report*, Department of Civil Engineering, University of Sherbrooke, Sherbrooke, Quebec, Canada, 24 pp.

Gergely, P., and Lutz, L.A., "Maximum Crack Width in Reinforced Concrete Flexural Members," *Causes, Mechanism, and Control of Cracking in Concrete*, SP-20, American Concrete Institute, Farmington Hills, Michigan, 1999, pp. 87-117.

Giernacky, R.G., Bakis, C.E., Mostoller, J.D., Boothby, T.E., and Mukherjee, A., "Evaluation of Concrete Beams Reinforced With Internal GFRP Bars: A Long-Term Durability Study," *Second International Conference on Durability of Fiber Reinforced Polymer (FRP) Composites for Construction*, Ed. Benmokrane, B., and El-Salakawy, E., 2002, Canada, pp. 39-50.

Gopalaratnam, V. S., El Shakra, Z. M., and Mihashi, H., "Confinement Analogy Model for the Bahavior of Fiber Reinforced Reinforced Concrete," *American Ceramic Society Special Publication*, January 2005.

Gopalararatnam, V.S., and Meyer, J.W., "Fatigue Response of Flexural Bond in FRP Reinforced Concrete," *Proceeding of ICFRC International Conference,* 8-10 January 2004, Chennai, India, pp. 363-373.

Gopalaratnam, V.S., Meyer, J.W., and DeYoung, K.L, "Non-Ferrous Hybrid Reinforcement Systems for Concrete Bridge Decks," *Proceedings of INCONTEST 2003*, 10-12 Sept. 2003, Coimbatore. India, pp. 10

Goto, Y, "Cracks Formed in Concrete Around Deformed Tension Bars," *Journal of the American Concrete Institute*, Vol. 68, No. 4, April 1971, pp. 244-251.

Guo, J., and Cox, J.V., 2000, "An Interface Model for the Mechanical Interaction between FRP Bars and Concrete," Journal of Reinforced Plastics and Composites, Vol. 19, pp. 15-32.

Gupta, S.D., *Bridge Manual*, Missouri Department of Transportation, 12/19/2001.

Gylltoft, K., Cederwall, K., Elfgren, L., and Nilsson., L., "Bond Failure in Reinforcement Concrete Under Monotonic and Cyclic Loading: A Fracture Mechanics Approach," *Fatigue of Concrete Structures, SP-75,* American Concrete Institute, Detroit, 1982, pp. 269-287.

Hamad, B.S., "Comparative Bond Strength of Coated and Uncoated Bars with Different Rib Geometries," *ACI Material Journal*, Vol. 92, No. 6, November-December 1995, pp. 579-591.

Harris, H.G., Somboonsong, W., and Ko, F. K., "New Ductile Hybrid FRP Reinforcing Bar for Concrete Structures," *Journal of Composites for Construction,* Vol. 2, No. 1, February 1998, pp. 28-37.

Hughes Brothers, 2001, “Aslan 100 Glass Fiber Reinforced Polymer (GFRP) Rebar – Specifications,” Hughes Brothers Inc.

Jaeger, G.L., Tadros, G., and Mufti, A.A., “Balanced Section, Ductility and Deformability in Concrete with FRP Reinforcement,” *Research Report* No. 2-1995, Industry Center for Computer-Aided Engineering, Technical University of Nova Scotia, Halifax, Nova Scotia, Canada, 1995, 29 pp.

Katz, A., “Bond Mechanism of FRP Rebars to Concrete,” *Materials and Structures*, Vol. 32, December 1999, pp. 761-768.

Katz, A., “Bond to Concrete of FRP Rebars after Cyclic Loading,” *Journal of Composites for Construction*, Vol. 4, No. 3, August 2000, pp. 137-144.

Katz, A., Berman, N., and Bank, L., “Effect of high temperature on bond strength of FRP rebars,” *Journal of Composites for Construction*, Vol. 3, No. 2, May 1999, pp. 73-81.

Keesler, R.J., and Power, R.G., “Corrosion of Epoxy Coated Rebars--Keys Segmental Bridge-Monroe County,” *Report No. 88-8A*, Florida Dept. of Transportation, Materials Office, Corrosion Research Laboratories, Gainesville, Fl, 1988.

Kemp, E.L., “Bond in Reinforced Concrete: Behavior and Design Criteria,” *ACI Journal*, Vol. 83, No. 1, January-February 1986, pp. 50-57.

Laboubi, K., El-Salakawy, E., Pigron, M., and Benmokrane, B., “Behavior of Concrete Beams Reinforced With GFRP under Sustained Load and Freeze/Thaw Cycles,” *Second International Conference on Durability of Fiber Reinforced Polymer (FRP) Composites for Construction*, Ed. Benmokrane, B., and El-Salakawy, E., 2002, Canada, pp. 453-464.

Li, V.C., and Wang, S., “Flexural Behaviors of Glass Fiber-Reinforced Polymer (GFRP) Reinforced Engineered Cementitious Composite Beams,” *ACI Materials Journal*, Vol. 99, No. 1, January-February 2002, pp. 11-21.

Malvar, L. J., 1995, “Tensile and Bond Properties of GFRP Reinforcing Bars,” ACI Materials Journal, V. 92, No. 3, pp. 276-285.

Malvar, L.J., Cox, J.V., and Cochran, K.B., “Bond between Carbon Fiber Reinforced Polymer Bars and Concrete. 1: Experimental Study,” *Journal of Composites for Construction*, Vol. 7, No.2, May 2003, pp. 154-163.

Mashima, M., and Iwamoto, K., “Bond characteristics of FRP rod and concrete after freezing and thawing deterioration,” *Fiber-Reinforced-Plastic Reinforcement for Concrete Structures - International Symposium*, SP 138, American Concrete Institute, Detroit, 1993, pp. 51-70.

Mashima, M., and Iwamoto, K., 1993, “Bond Characteristics of FRP Rod and Concrete after Freezing and Thawing Deterioration,” ACI Special Publication, V. 138, September 1, 1993.

Mathey, R., Wastein, D., “Investigation of Bond in Beam and Pull-Out Specimens with High-Yield-Strength Deformed Bars,” *ACI Journal*, Vol. 57, No. 3, March 1961, pp. 1071-1090.

Mays, G.C., and Tilly, G.P., “Long Endurance Fatigue Performance of Bonded Structural Joints,” *International Journal of Adhesion and Adhesives*, Vol. 2, No. 2, April 1982, pp. 109-113.

Micelli, F., and Nanni, A., “Durability of FRP Rods for Concrete Structures,” *Construction and Building Materials*, Vol. 18, 2004, pp. 491-503.

Naaman, A.E., and Jeong, S.M. “Structural Ductility of Concrete Beams Prestressed with FRP Tendons,” *Proc., 2nd Int. RILEM Symp. (FRPRXS-2), Non-Metric (FRP) Reinforcement for Concrete Structures*, RILEM, Bagneux, France, 1995, pp. 379-386.

Nanni, A., Al-Zaharani, M.M., Al-Dulaijan, S.U., Bakis, C.E., and Boothby, T.E., “Bond of FRP Reinforcement to Concrete-Experimental Results,” *Proceedings of the Second Int. RILEM Symp. (FRPRCS-2),* L. Taerwe, ed., 1995, pp. 135-145.

Nanni, A., Al-Zahrani, M.M., Al-Dulaijan, S.U., Bakis, C.E., and Boothby, T.E., 1995, “Bond of FRP Reinforcement to Concrete – Experimental Results,” Non-metallic (FRP) Reinforcement for Concrete Structures, L. Taerwe, Ed., E & FN Spon, London, 1995.

Nanni, A., and Faza, S., 2002, “Designing and Constructing with FRP Bars: An Emerging Technology,” Concrete International, Vol. 24, No. 11, pp. 53-58.

Nanni, A., Bakis, C.E., and Boothby, T.E., 1995a, “Test Methods for FRP Systems Subjected to Mechanical Loads: State of the Art Review,” Journal of Reinforced Plastics and Composites, Vol. 14, pp. 524-558.

Nanni, A., Nenninger, J., Ash, K., and Liu, J., 1997, “Experimental Bond Behavior of Hybrid Rods for Concrete Reinforcement,” Structural Engineering and Mechanics, V. 5, No. 4, pp. 339-353.

Park, R., and Paulay, T., *Reinforced Concrete Structures*, John Wiley & Sons, 1976, 769 pp.

Potter, R., and Ho, D., “Quality of Cover Concrete and Its Influence on Durability,” *Concrete Durability, Katharine and Bryant Mather, International Conference, SP100,* American Concrete Institute, Detroit, 1987.

Rasheeduzzafar, A., Dakhil, F., Basa, M., and Khan, M., "Performance of Corrosion-Resisting Steels in Chloride-Bearing Concrete," *ACI Materials Journal*, Vol. 89, No. 5, September-October 1992, pp. 439-448.

Rehm, G., and Eligehausen, R., "Bond of Ribbed Bars under High Cycle Repeated Loads," *ACI Journal*, Vol. 76, No. 2, February 1979, pp. 297-309.

RILEM 7-II-128 (Réunion Internationale des Laboratoires et Experts des Matériaux, Systèmes de Constructions et Ouvrages), "RC6: Bond Test for Reinforcing Steel. 1. Pull-Out Test," *RILEM Technical Recommendations for the Testing and Use of Construction Materials*, E & FN Spon, U.K. 1994, pp.102-105.

Rizkalla, S., Shehata, E., Abdelrahman, A., and Tadros, G., 1998, "The New Generation (Design and Construction of Highway Bridge)," Concrete International, V. 20, No. 6, June 1, 1998.

Salib, S.R., and Abdel-Sayed, G., "Prediction of Crack Width for Fiber-Reinforced Polymer-Reinforced Concrete Beams," *ACI Structural Journal*, Vol. 101, No. 4, July-August 2004, pp. 532-536.

Schutte, C.L., "Environmental Durability of Glass-Fiber Composites," *Materials Science and Engineering*, Vol. 13, No.7, 1994, pp. 265-324.

Sekijima, K., Otsuka, Y., and Konno, T., "Durability of Fiber Reinforced Polymer Reinforcement Embedded in Concrete," *Fourth International Symposium on Fiber Reinforced Polymer Reinforced Concrete Structures*, SP-188, American Concrete Institute, Farmington Hills, Michigan, 1999, pp. 501-513.

Sen, R., Mariscal, D., and Shahawy, M., "Durability of Fiberglass Prestensioned Beams," *ACI Structural Journal*, Vol. 90, No. 5, September-October 1993, pp. 525-533.

Sen, R., Shahawy, M., Sukumar, S., and Rosas, J., "Durability of Carbon Fiber Reinforced Polymer (CFRP) Pretensioned Elements under Tidal/Thermal Cycles," *ACI Structural Journal*, Vol. 96, No. 3, May-June 1999, pp. 450-457.

Shield, C.K., French, C.W., and Hanus, J.P., 1999, "Bond of Glass Fiber Reinforced Plastic Reinforcing Bar for Consideration in Bridge Decks," ACI Special Publication, V. 188, August 1, 1999.

Sippel, T.M., and Mayer, U., "Bond Behavior of FRP Strands Under Short-term, Reversed, and Cyclic Loading," Advanced Composite Materials in Bridges and Structures, M.M. El-Badry, Ed., Canadian Society for Civil Engineering, Montreal, Quebec, pp. 837-844.

Standard Specifications for Highway Bridges, 16th ed., American Association of State Highway and Transportation Officials, Washington, D.C., 1996.

Status of the Nation's Highways, Bridges, and Transit: 2002 Conditions and Performance Report. http://www.fhwa.dot.gov/policy/2002cpr/highlights.htm. Accessed July, 2004.

Tannous, F.E., and Saadatmanesh, H., "Environmental Effects on the Mechanical Properties of E-Glass FRP Rebars," *ACI Materials Journal*, Vol. 95, No.2, March-April 1998, pp. 87-100.

Theriault, M., and Benmokrane, B., "Effects of FRP Reinforcement Ratio and Concrete Strength on Flexural Behavior of Concrete Beams," *Journal of Composites for Construction*, Vol. 2, No. 1, February 1998, pp. 7-16.

Thorenfeldt, E., Tomaszewicz, A., and Jensen, J.J., "Mechanical Properties of High-Strength Concrete and Application in Design," *Proceedings of the Symposium "Utilization of High Strength Concrete,"* Stavanger, Norway, June 1987, Tapir, Trondheim, pp. 149-159.

Tighiouart, B., Benmokrane, B., and Gao, D., "Investigation of Bond in Concrete Member With Fiber Reinforced Polymer (FRP) Bars," *Construction and Building Materials*, Vol. 12, No. 8, December 1998, pp. 453-462.

Toutanji, H. A., and Saafi, M., "Flexural Behavior of Concrete Beams Reinforced with Glass Fiber-Reinforced Polymer (GFRP) Bars," *ACI Structural Journal*, Vol. 97, No. 5, September-October 2000, pp. 712-719.

Uomoto, T., and Nishimura, T., "Deterioration of Aramid, Glass, and Carbon Fibers Due to Alkali, Acid, and Water in Different Temperatures," *Fourth International Symposium on Fiber Reinforced Polymer for Reinforced Concrete Structures*, SP-188, American Concrete Institute, Farmington Hills, Michigan, 1999, pp. 515-522.

Uppuluri, V.S., Bakis, C.E., Al-Dulaijan, S.U., Nanni, A., and Boothby, T.E., 1996, "Analysis of the Bond Mechanism in FRP Reinforcement Rods: The Effect of Rod Design and Properties," Advanced Composite Materials in Bridges and Structures, M.M. El-Badry, Ed., Canadian Society for Civil Engineering, Montreal, Quebec.

Vijay, P.V., and GangaRao, H.V.S., "Bending Behavior and Deformability of Glass-Fiber-Reinforced Polymer Reinforced Concrete Members," *ACI Structural Journal*, Vol. 98, No. 6, November-December 2002, pp. 834-842.

Yonezawa, T., Ohno, S., Kakizawa, T., Inoue, K., Fukata, T., and Okamoto, R., 1993, "A New Three-dimensional FRP Reinforcement," Fiber Reinforced Plastic (FRP) for Concrete Structures: Properties and Applications, A. Nanni ed., Elsevier Science Publishers, pp. 405-418.

APPENDIX I
CONSTITUENT MATERIAL PROPERTIES

Table AI-1: Results from Tension Test of FRP Reinforcing Bars

Rebar Type	Specimen	Tensile Strength (ksi)	Strain at Ultimate (μstr)	Elastic Modulus (x 10^6 psi)
# 4 CFRP	1	276.48	12.33	17.08
	2	280.54	16.00	21.51
	3	301.55	17.50	18.72
	Average*	**286.19**	**15.27**	**19.10**
	Manufacturer	**300.00**	**17.00**	**18.0**
# 4 GFRP	1	79.86	17.76	4.14
	2	78.50	19.89	4.13
	3	81.03	20.89	4.13
	Average*	**79.80**	**19,51**	**4.13**
	Manufacturer	**100.00**	**15.00**	**5.92**
# 8 GFRP	1	65.53	11.80	5.56
	2	65.58	12.40	5.10
	3	65.00	15.80	4.10
	Average*	**65.37**	**13.33**	**4.92**
	Manufacturer	**80.00**	**15.00**	**5.92**

* *Since unavoidable eccentricities in loading were suspected in the tension test results reported above, nominal data provided by the manufacturer were used in all calculations for the design example*

Table AI-2: Typical Compression Test Results for Plain and Fiber Reinforced Concrete for Bond and Ductility Test Specimens

Mix ID	Specimen	Compressive Strength (psi)	Strain at Ultimate (in./in.)	Elastic Modulus (x 10^6 psi)
Plain concrete	1	6,888	0.0021	4.64
	2	6,841	0.0021	4.75
	3	6,957	0.0021	4.61
	Average	**6,895**	**0.0021**	**4.67**
Fiber reinforced concrete*	1	4,880	0.0021	3.36
	2	4,561	0.0024	3.46
	3	4,371	0.0019	3.57
	Average	**4,603**	**0.0021**	**3.46**

* *Several castings were made for the exhaustive laboratory test program. Values reported above are from one typical casting. FRC used initially for the bond and ductility test specimens had excessive air and hence typically were weaker and less stiff than plain concrete castings. Better air content control in FRC used for the slab casting reflects better mechanical performance (see Table A3)*

Table AI-3: Results From Compression Tests on Concrete Used for Full-Scale Slab Tests

Mix ID	Specimen	Compressive Strength (psi)	Strain at Ultimate (in./in.)	Elastic Modulus (x 10^6 psi)
Concrete mix for Steel Slab	1	5,914	0.0018	3.736
	2	5,751	0.0020	3.63
	3	5,841	0.0025	2.65
	Average	**5,835**	**0.0021**	**3.34**
FRC mix for GFRP Slab	1	6,181	0.0019	4.07
	2	5,309	0.0022	3.5
	Average	**5,745**	**0.0021**	**3.80**
FRC mix for Hybrid GFRP/ CFRP Slab	1	6,570	0.0031	2.84
	2	5,586	0.0022	3.08
	Average	**6,078**	**0.0027**	**2.97**